

X-ray Properties of Galactic Supernova Remnants

DISSERTATION

der Fakultät für Physik der Ludwig-Maximilians-Universität München
zur Erlangung des Grades
Doktor der Naturwissenschaften
Dr. rer. nat.

vorgelegt von

DANIEL SCHAUDEL

aus Ettenheim

München, den 18. Februar 2003

1.Gutachter: Prof. Dr. Joachim Trümper
2.Gutachter: Prof. Dr. Ralf Bender
Tag der mündlichen Prüfung: 8. Juli 2003

Summary

Galactic supernovae (SNe) are rare events, believed to occur at intervals of ~ 30 -50 years. However, in the past 2000 years, only seven Galactic SNe have been observed: SN 185 (RCW 86), SN 386 (G 11.2-0.3), SN 1006, SN 1181 (3C58), Crab SN, Tycho SN and Kepler SN. Most Galactic SNe go unobserved because of visible-band extinction by interstellar dust. Due to an average lifetime of supernova remnants (SNRs) of a few 10,000 to 100,000 years, about 15 000 SNRs are expected in our Galaxy, which exceeds the number of identified radio SNRs by almost a factor 70. These identified Galactic SNRs comprise an incomplete sample of SNR population due to various selection effects. ROSAT performed the first all-sky survey (RASS) with an imaging X-ray telescope, providing another window for searching for SNRs.

Performing a search for extended X-ray sources in the RASS database, 373 objects were identified as SNR candidates in recent years (Busser 1998). One of the main objectives of this work was to perform an identification campaign of these Galactic SNR candidates. The low exposure (\sim a few hundred seconds) and spatial resolution ($\sim 96''$) of the RASS data did not, in most cases, allow for a quantitative analysis of the SNR candidates in order to identify them by their X-ray morphology and spectral source properties. A few candidates from the sample were additionally located in the field-of-view of pointed ROSAT HRI and PSPC as well as Einstein and ASCA observations. The spatial resolution of the pointed ROSAT and Einstein observations and the spectral resolution capability of ROSAT PSPC, Einstein and ASCA allowed for a more detailed analysis and an identification of the sources in most cases. Studying their X-ray and radio morphology and correlating the results with radio databases like the NRAO/VLA Sky Survey (NVSS), Parkes-MIT-NRAO (PMN) survey, Molonglo and Effelsberg Galactic Plane Surveys and the optical DSS2red as well as with SIMBAD and NED allowed for discrimination between extragalactic background objects and SNR candidates, leaving 215 targets for subsequent identification. Fifty-nine of the 373 candidates (16 %) turned out to likely be galaxies or cluster of galaxies, and ~ 99 targets (27 %) were found to be spurious background features. The most promising candidates were subject of follow-up observations in the X-ray and radio band because of their distinct X-ray and radio morphology.

The SNR candidates 1RXS J161411.3-630657 and 1RXS J104047.4-704713 have been observed in the X-ray band with the Chandra observatory. These data do not support to further interpret this sources as SNR candidates. 1RXS J161411.3-630657 has a slight elliptical shape in X-rays and harbours a central cD galaxy. The entire spectrum is best described by the thermal bremsstrahlung model MEKAL which yields a temperature of $\sim 5.4 \times 10^7$ K, abundances of ~ 0.35 times solar and a redshift of the hot intracluster gas of ~ 0.048 , which is consistent with the measurements of optical redshifts of two galaxies in the same field within the errors. Optical data show many galaxies in the region where the X-ray emission peaks. The other source 1RXS J104047.4-704713 also has a slight elliptical shape and is centrally brightened in X-rays. In this case, a thermal bremsstrahlung model is also found to fit the data,

with a temperature of ~ 4.0 times 10^7 K, abundances of $\sim 0.75 \times$ solar and a redshift of the hot intracluster gas of ~ 0.075 . Both objects are therefore identified as clusters of galaxies.

The six SNR candidates G 6.1-1.3, G 38.7-1.4, G 39.9-2.8, G 75.8+8.1, G 80.7+6.8 and G 178.2-3.3 were selected for radio-continuum follow-up observations at 6 cm due to their radio morphology in the Effelsberg Galactic Plane survey. Only G 38.7-1.4 is identified as a SNR due to its polarized radio emission which has a spectral index $\alpha \approx -0.79$. The remaining sources are identified as a probable H II region (G 6.1-1.3), part of the large SNR W 50 (G 39.9-2.8), a spurious radio feature (G 75.8+8) and faint polarized radio sources with steep non-thermal spectral shapes (G 80.7+6.8 and G 178.2-3.3).

The candidates G 296.7-0.9 and G 308.3-1.4 have been observed with the Australia Telescope Compact Array (ATCA) at 13 cm and 20 cm. No polarization could be detected from either source, but G 296.7-0.9 shows bright extended radio emission with a spectral index $\alpha \sim -0.30$ at the location of an incomplete X-ray shell that was found in pointed ROSAT HRI and PSPC data. The X-ray spectrum is well described by a Raymond-Smith model with a temperature of 0.22 ± 0.13 keV and a galactic absorption $N_H = 1.42 \pm 10^{22} \text{ cm}^{-2}$. Based on these data G 296.7-0.9 is identified as a Galactic SNR. G 308.3-1.4 shows two radio arcs with spectral index $\alpha \sim -0.71$ matching well with a region of extended X-ray emission. But the nature of the X-ray source is still unclear. G 308.3-1.4 is still counted among the most promising SNR candidates.

The following summary gives a brief overview of the results from the re-analysis campaign of the original 373 RASS candidates:

- 2 targets can be identified as SNRs (G 38.7-1.4 and G 296.7-0.9)
- 9 targets are very promising SNR candidates
- 99 targets emerge as spurious background features
- 59 targets can be assigned mainly to extragalactic objects like clusters of galaxies
- 90 targets have extended X-ray emission but lack typical shell structure in X-rays/radio
- 114 targets show poor evidence of typical properties of SNRs and are located in crowded regions of X-ray and radio point sources.

Rejecting these 114 targets, only 2 candidates are found to be SNRs, leaving still 99 of the original 373 RASS targets as SNR candidates. A simulation of the theoretical distribution of SNe and their remnants in the Galactic plane was performed by Busser (1998) using canonical input values. His simulation predicted somewhat more than 200 SNRs to be detected in the RASS. A comparison of the results from the identification campaign with that of the simulation shows that in deed less SNR candidates are found in the RASS than is expected from his simulation. If the simulation accurately describes the physics of SNe and SNRs, indicating the distribution of Galactic

SNRs, the smaller number of Galactic SNRs signify either a lower Galactic SN rate, a lower explosion energy, higher interstellar density and/or lower ambient density at the location where the star exploded. However, these results do not allow for the determination of the individual physical parameters which have to be adopted to bring his simulation in agreement with the results of this work.

The second part of this thesis deals with the spatial and spectral analysis of three selected Galactic SNRs. They are RCW 103, G 21.5-0.9 and G 65.3+5.7.

- **XMM-Newton observation of RCW 103:**

RCW 103 is a shell-like SNR with a central compact X-ray source. The thermal X-ray spectrum, with prominent He α -like lines of Neon, Magnesium, Silicon, Sulphur and the Iron L complex, shows a low temperature component of ~ 0.3 keV and a high component of ~ 0.7 keV, varying slightly across the remnant. A belt of faint X-ray emission across the remnant is found to emerge from absorption and not from an intrinsic emission mechanism. It is not clear yet if RCW 103 originated from a SN Ia or a core-collapse SNR, but there are some indications supporting the core-collapse event. Constant radii of RCW 103 in different emission lines, as well as the low expansion velocity of light elements like Magnesium, are found, which are rather expected for core-collapse SNe. Finally, the existence of the central point source, which is a binary consisting probably of a neutron star and a low mass companion, is a strong argument for a core-collapse scenario (Garmire et al., 2001).

Deep optical observations are necessary to detect and characterize the assumed low mass companion of the neutron star.

- **XMM-Newton observation of G 21.5-0.9:**

G 21.5-0.9 was found to harbour a central compact object, probably a pulsar, which is embedded in a more extended synchrotron nebula. Recent Chandra data let assume that the faint extended halo further outside corresponds to an outer shell that was formed from the expanding ejecta (Slane et al. 2000). Data from a subsequent XMM-Newton observation show that the nebula of G 21.5-0.9 is best described by a power law continuum with an increase in photon spectral index from values of 1.72 at the center of G 21.5-0.9 to 2.43 at the edges of its halo.

In the case of thermal halo emission, the lack of line emission implies that the plasma is far from ionization equilibrium. Modelling with the thermal model NEI, a low ionization state of $n_e t \approx 3 \times 10^8 \text{ cm}^{-3} \text{ s}$ was found which corresponds to an electron density $n_e < 0.1 \text{ cm}^{-3}$, assuming a expansion velocity of $10,000 \text{ km s}^{-1}$ and a distance of 5 kpc to G 21.5-0.9. This low value of the electron density is not in agreement with the electron density determined from the observed X-ray luminosity, which is required for thermal bremsstrahlung radiation. The temperature derived for the continuum Bremsstrahlung emission is $\sim 5\text{-}6$ keV, which is rather hot, even for a very young SNR. The lack of limb brightening, the constant increase of the spectral index throughout the remnant and the

spherical symmetry suggest an interpretation of the outer halo as an extension of the central synchrotron nebula. Therefore G 21.5-0.9 is a Crab-like, rather than a composite, SNR.

- **ROSAT observation of G 65.3+5.7:**

The SNR G 65.3+5.7 with an extent of about 3 degrees, has been observed only in X-rays with the Einstein observatory while performing a count rate map. RASS data and 17 pointed ROSAT PSPC observations allowed a complete spatial and spectral analysis of the entire remnant. The X-ray spectrum of G 65.3+5.7 shows thermal X-ray emission described by a two-temperature Raymond-Smith plasma model with an average temperature of 0.20 keV and a low ambient density of $\sim 0.019 \text{ cm}^{-3}$. Performing a Sedov analysis and assuming a distance of 1 kpc based on radio observations, an age of $\sim 27,500$ years, explosion energy of 0.18×10^{51} erg and a luminosity $L_x \sim 9.9 \times 10^{34}$ erg is obtained. The spectral analyses of the pointed PSPC observations show that 65.3+5.7 has small variations in temperature and galactic absorption over the remnant and a slight increase of the plasma temperature towards the center.

The radio pulsar PSR J1931+30, which is located within G 65.3+5.7, is offset $\sim 45'$ from the geometrical center of the remnant. Unfortunately, the position of the pulsar is not very well determined and a first time derivative of the pulsar rotation period is not available either, leaving open the pulsar spin-down age, spin-down flux and magnetic polar field. An association of the pulsar with the remnant based on an age estimated from the radio data is therefore currently not possible. However, using the count rate upper limit and assuming a Crab-like spectrum, an X-ray flux of $f_x = 3.93 \times 10^{-13} \text{ erg cm}^{-2} \text{ s}^{-1}$ is obtained, yielding an X-ray luminosity of $L_x = 4.32 \times 10^{32}$ erg for the dispersion measure based distance of 3 kpc (Camilo et al. 1997). The luminosity is comparable to the luminosities of the recently discovered 65 ms pulsar PSR J0205+6449 in 3C58 (Murray et al. 2002) and B0833-45 in the Vela SNR (Becker & Pavlov 2002 and references therein). Based on the X-ray luminosity, a lower limit of the characteristic age τ could be determined to be 1400 years. Further radio observations are necessary to determine the pulsar spin down age and the accurate position in order to clarify whether the pulsar is associated with G 65.3+5.7 or not.

The objectives of this work were the X-ray studies of Galactic SNRs and candidates using different instruments in the X-ray and radio band in order to clarify the individual issues. The RASS allowed for searching SNR candidates in the X-ray band but did not allow for their identification due to the low exposure time and low spatial resolution. Subsequent source correlations with various databases and a few follow-up observations in the X-ray and radio band helped to identify some of the SNR candidates but not all of them. In future, many more follow-up observations are therefore necessary to clarify the nature of the remaining targets. Considering the long time period of submitting proposals and observing the targets (on average \sim one to sev-

eral years for Chandra and XMM-Newton, respectively), it is not possible to complete this work within three years. However, the results from this identification campaign show that less Galactic SNR candidates are found in the RASS than expected from a simulation which describes the distribution of SNe and their diffuse remnants in the Galactic Plane. It is not possible to find out to what extent the individual parameters contribute to the low number of SNRs. Some of the SNR candidates show very faint or no radio emission which can be explained by a weak magnetic field and/or low density of relativistic electrons if they are indeed SNRs. SNRs which are embedded in very dense regions like molecular clouds and H II regions should have a low density gradient between the dense surrounding and the ejecta and therefore perform a less efficient acceleration mechanism at the shock front. Therefore it is difficult to detect their radio-continuum. This type of radio-faint SNRs can be ascribed to a very dense ISM in which the progenitor star exploded earlier.

Compared to ROSAT, XMM-Newton allows for more detailed studies of SNRs due to its large effective area and the capability of spatially resolved spectroscopy. Observing the Galactic SNRs RCW 103 and G 21.5-0.9 with XMM-Newton it was possible to find indications for the progenitor star and to clarify the nature of the outer X-ray halo, respectively.

The future X-ray observatories like Constellation X and XEUS with high spatial resolution but also a maximum field-of-view of $8'$ and $10'$, respectively, will not only provide observations in the field of extragalactic astronomy but also will play an important role in the observation of Galactic SNRs. Due to the small field-of-view, only SNRs with small extent can be observed as well as interesting emission regions within large SNRs. The main objectives will be the observation of compact objects within SNRs like the interaction between pulsars and their environment.

Contents

Contents	I
1 Introduction	1
2 Non-Thermal and Thermal Radiation Processes and Acceleration Mechanisms	4
2.1 Non-thermal Radiation Processes	4
2.1.1 Synchrotron Emission Mechanism	4
2.1.2 Inverse Compton Scattering	6
2.2 Thermal Radiation Processes	7
2.3 The Acceleration of High Energy Particles	8
2.3.1 Fermi Acceleration Mechanisms	8
2.3.2 Particles Acceleration in Shell-Type SNRs	10
2.3.3 Particle Acceleration in Crab-like SNRs	11
3 Supernovae and Supernova Remnants	13
3.1 Supernovae	13
3.1.1 Final Evolution Stage of Stars	13
3.1.2 Classification of SNe	17
3.1.3 Galactic Supernova Rate	17
3.2 Supernova Remnants	19
3.2.1 Classification of Supernova Remnants	19
3.2.2 Evolution of Thermal Supernova Remnants	20
3.2.3 Supernova Remnants in Various Wavelength Bands	23
3.3 Distribution of SNRs in the Galaxy	31
3.4 Compact Objects Within Supernova Remnants	33
3.4.1 Young Neutron Stars	33
3.5 Neutron Star - Supernova Remnant Association	34
4 X-ray Observatories and Radio Telescopes	36
4.1 X-ray Observatories	36
4.1.1 ROSAT	36
4.1.2 The Chandra Mission	39
4.1.3 The XMM-Newton mission	42
4.2 Radio telescopes	45
4.2.1 Effelsberg 100-m radio telescope	48

4.2.2	Australia Telescope Compact Array (ATCA)	48
4.2.3	The Galactic Radio and Optical Surveys	49
5	Identification Campaign of SNR Candidates in the RASS	52
5.1	Analysis of the RASS Data	52
5.1.1	SNR Candidates with $D \leq 30'$	55
5.1.2	SNR Candidates with $D \geq 30'$	64
5.2	X-ray Follow-up Observation With Chandra	67
5.2.1	SNR Candidate 1RXS J161411.3-630657	67
5.2.2	SNR Candidate 1RXS J104047.4-704713	74
5.3	Radio Follow-up Observations With the Effelsberg 100-m Telescope	77
5.4	Radio Follow-up Observations With ATCA	83
5.4.1	G 296.7-0.9	84
5.4.2	G 308.3-1.4	88
5.5	X-ray Emission From the SNR G 67.7+1.8	91
5.6	Conclusion and prospects	92
6	SNRs With Compact Objects	97
6.1	RCW 103	97
6.1.1	X-ray Studies of the Remnant	98
6.1.2	The Mystery of the Compact X-ray Source	110
6.1.3	Conclusion	114
6.2	G 21.5.-0.9	114
6.2.1	Spatial Analysis	115
6.2.2	Spectral Analysis	116
6.2.3	Conclusion	120
6.3	G 65.3+5.7	120
6.3.1	Spatial Analysis	121
6.3.2	Spectral Analysis	122
6.3.3	Summary and Discussion	127
A	Source catalogues of the SNR candidates	129
B	RASS images of the SNR candidates	138
	Bibliography	188

Chapter 1

Introduction

Supernovae (SNe) and their remnants play a central role in the dynamics and evolution of the interstellar medium (ISM). Supernova explosions describe the powerful death of stars injecting massive amounts of energy ($\sim 10^{51}$ ergs) and heavy elements into the ISM, compressing the magnetic field and accelerating in their shock waves efficiently energetic cosmic rays as observed in the whole Galaxy. They are expected to leave behind compact, as well as diffuse, remnants. Depending on the mass of the progenitor star the compact remnants take usually the stage of neutron stars (NS) or black holes (BH). The expansion of the supernova remnant (SNR) illuminates the pre-existing structures in the ISM and forms new ones, transferring kinetic energy and material from the original supernova to the ISM and trigger star formation in nearby dense clouds. Supernovae therefore do not stand only for the end of stellar evolution but also act as a recycling machine, returning material to the ISM to form new stars. The recycled material is processed by the supernova explosion into iron and heavier elements which effect the energetics and chemical composition of the ISM and the next generation of stars which form out of it. The study of supernovae or supernova remnants of exploded stars is also essential for our understanding of the origin of life on Earth. The cloud of gas and dust which collapsed to form the Sun, Earth and other planets was composed mainly of hydrogen and helium with a small amount of heavier elements such as carbon, nitrogen, oxygen and iron which is required by complex life. The only place where these elements are produced by nucleosynthesis is deep in the interior of massive stars. They can only spread out in the ISM due to an explosion.

Despite the large number of stars in our Galaxy, SN explosions are rare events occurring only ~ 2 times per century (Dragicevich et al., 1999). Over the last two millennia the supernova explosions of about eight stars in our Galaxy have been observed (Tab 1.1). They include those observed in detail by Tycho Brahe in 1572 and by Johannes Kepler in 1604 and several ‘guest stars’ chronicled earlier in China, Japan and/or Korea. These historical observations are very useful for the modern astrophysical interpretation regarding the observations of the remnants which originate from these supernovae. The exact age, for example, of the remnants of these historical supernovae are useful to compare the observed parameters with its evolution phase (Woltjer, 1972). Comparing the number of historical SNe with the actual SN rate for

Year	Date	R.A.	DEC	mag	Observer	Remnants
185		14:43.1	-62:28	-2	Chinese	RCW 86
393/396		17:14	-39.8	-3	Chinese	3 candidates
1006	Apr 30	15:02.8	-41:57	-9	Chinese, Japanese, European	SNR 1006
1054	Jul 4	05:34.5	+22:01	-6	Chinese, Japanese, Arabic	Crab nebula
1181		02:05.6	+64:49	-1	Chinese, Japanese	3C 58
1572	Nov 6	00:25.3	+64:09	-4	Tycho Brahe	Tycho SNR
1604	Oct 9	17:30.6	-21:29	-3	Johannes Kepler	Kepler SNR
1667 ?		23:23.4	+58:50	6 ?	John Flamsteed ?	Cas A

Table 1.1: Complete list of the historical supernovae over the last two millennia (Clark & Stephenson, 1976). The last and youngest SN in this list is a candidate which is assumed to be observed by Flamsteed. Even for the 185 AD event, doubts have been brought up on its nature as a supernova (Chin & Huang, 1994). The meaning of the columns is as follows: Year/Date: Time of observation/occurrence, R.A./Dec: Right Ascension and Declination (2000.0), mag: estimated apparent magnitude in brightness maximum.

More information about the listed historical SNe and also candidates are available under http://www.seds.org/messier/more/mw_sn.html

the whole Galaxy and taking a lifetime of several 10^5 years for SNRs into account, it becomes clear that only a small number of SNRs has been observed till this day (cf. Green (2002)). In former times people could observe the sky only with the naked eye or small telescopes in the optical band. Unfortunately, optical emission from SNRs is often obscured by dust and gas in the galactic plane, so that only the brightest SNRs could be detected. SNRs, however, are strong radio emitters due to synchrotron radiation of relativistic electrons which are accelerated at the shock front and spiral in strong magnetic fields and also thermal X-ray emitters heating up the gas behind the shock wave to several million degrees. The beginning of radio astronomy in the early 40's and the opening of the X-ray window later on with ballon experiments and rocket flights in the 50's and 60's implicated consequently two useful and very important tools for searching and investigating SNRs. Nevertheless, till this day only 231 galactic SNRs are known (Green, 2002), most of them have been detected during radio surveys in the galactic plane. This raise instantly the question if the small number of SNRs is only ascribed to selection effects or lead to a new understanding of SN explosions mechanism and/or the evolution of SNRs in the Galaxy. The number of observable SNRs depends strongly on the physical conditions of the progenitor star and the region where the SN explosion has taken place.

The X-ray satellite ROSAT performed the first all-sky survey with an imaging X-ray telescope, and thus allows a systematic search for SNRs in the X-ray band. This survey data mark a starting point of an identification campaign of galactic SNR candidates which is described in this thesis. The subject of this identification campaign refers to the question, how many candidates are indeed SNRs or account for possible SNRs, respectively, based on 373 SNRs candidates found in the ROSAT all-sky survey (RASS) by Busser (1998). A re-analysis of the RASS data was performed with the

help of extensive databases and additional follow-up observations of SNR candidates in X-rays as well as in radio. This identification campaign allowed to restrict the number of possible SNRs and to compare them with the results from a simulation of the theoretical distribution of SNe and their remnants in the RASS (Busser, 1998).

The second part describes the X-ray study of three galactic SNRs. The SNRs RCW 103 and G 21.5-0.9 consist not only of a diffuse remnant but also of a compact X-ray source in their centers. They were observed with the X-ray observatory XMM-Newton which performed resolved spectroscopy with high photon statistics for the first time, and hence detailed X-ray studies of these two SNRs measuring fundamental properties like the temperature/spectral photon index distribution across the diffuse X-ray emission regions, abundances of nucleosynthesis products and density distribution of the diffuse ISM. RCW 103 is of particular interest since Tuohy & Garmire (1980) have discovered the compact X-ray source 1E 161348-5055 in the center of the remnant and considered it as one of the best candidates for a cooling neutron star. This picture changed by X-ray observations with ASCA and later with Chandra and XMM-Newton analysing the compact source in the center and the diffuse remnant. G 21.5-0.9 is a central brightened X-ray source which was found to belong to the group of Crab-like SNRs. Spatial and spectral analysis of XMM-Newton data allowed to characterize the nature of the SNR and to determine the spectral properties in more details. The SNR G 65.3+5.7, with an extent of about 3 degrees was only observed in the radio and optical wavelength band and in X-rays with the Einstein observatory which performed a count-rate map. Using ROSAT data from the all-sky survey and 17 pointed PSPC observations, spatial and spectral analysis of the diffuse remnant were performed for the first time determining basic characteristics like distance, age and ambient density according to the Sedov model.

The thesis is divided in the following way. An introduction to supernovae and supernova remnants as well as acceleration mechanism of high energy particles in supernova remnants is given in the chapter 2 and 3. Then, a brief description and specification of the X-ray (ROSAT, Chandra and XMM-Newton) and radio observatories (Effelsberg 100-m telescope and the Australia Telescope Compact Array (ATCA)) which have been used in the course of this thesis is presented in chapter 4. Chapter 5 devotes the description of the identification campaign and the associated analysis of the RASS data addressing the follow-up observations of the most promising SNR candidates with the Chandra observatory as well as the Effelsberg 100-m telescope and ATCA. Finally chapter 6 describes the X-ray studies of three well-known SNRs using data from XMM-Newton and ROSAT, respectively.

Chapter 2

Non-Thermal and Thermal Radiation Processes and Acceleration Mechanisms

2.1 Non-thermal Radiation Processes

2.1.1 Synchrotron Emission Mechanism

In the early days of radio astronomy, galactic radio sources were found showing brightness temperatures which exceeded 10^{12} K. It became immediately clear that they were not of thermal origin. Alfvén & Herlofson (1950) considered stellar models that might produce extremely high radio brightness temperatures and concluded that the most likely process was synchrotron radiation. Synchrotron radiation is emitted by very high energy charged particles spiraling in a magnetic field (Figure 2.1). Due to the low mass of electrons compared to protons, electrons are favoured to emit synchrotron radiation. For this reason, synchrotron radiation is one of the processes which dominates high energy astrophysics. The fact that synchrotron emission is a non-thermal radiation process is reflected in the energy spectrum, which is not Maxwellian.

The radiation loss rate in the rest frame of the electron is:

$$-\left(\frac{dE}{dt}\right) = 2 \cdot \sigma_T \left(\frac{v}{c}\right)^2 c U_{mag} \gamma^2 \sin^2\theta \quad (2.1)$$

where σ_T is the Thomson-cross section, $U_{mag} = \frac{B^2}{2\mu_0}$ the energy density of the magnetic field with the magnetic constant μ_0 , γ the Lorentz factor¹ and θ the pitch angle which describes the angle between the acceleration vector \vec{a} and the direction in which the radiation is emitted. In a uniform magnetic field, high energy electrons move in a spiral path at a constant pitch angle.

In the case of an isotropic distribution of pitch angles, the average energy loss rate is:

$$-\left(\frac{dE}{dt}\right) = \frac{4}{3} \cdot \sigma_T \left(\frac{v}{c}\right)^2 c U_{mag} \gamma^2 \quad (2.2)$$

¹Lorentz factor $\gamma = \sqrt{1 - (v/c)^2}$

The emission spectrum of electrons can be described by an energy distribution of power law form

$$N(E) dE \propto E^{-\alpha} dE \quad (2.3)$$

where $N(E) dE$ is the number of electrons per unit volume in the energy interval E to $E+dE$ and α the power law index.

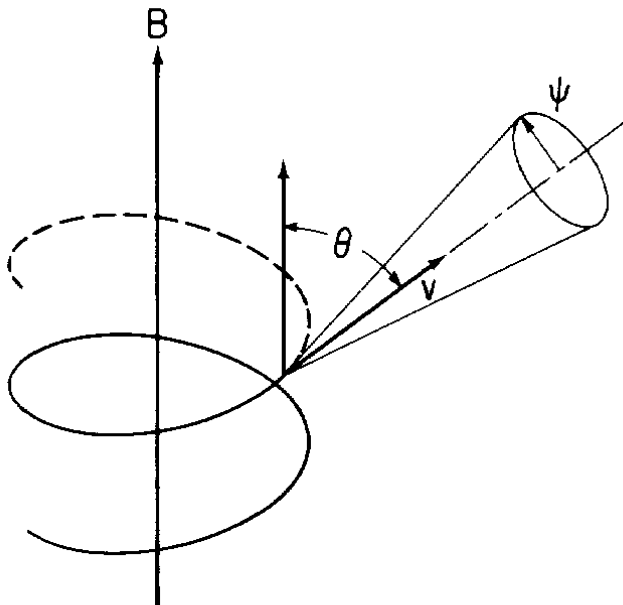


Figure 2.1: Electron spirals with the velocity \vec{v} around a magnetic field line \vec{B} and emits synchrotron radiation in a narrow cone of angle $\Psi = 1/\gamma$.

One of the basic features of the radiation of relativistic particles is that the radiation is beamed in the direction of motion of the particle. A significant amount of radiation is only observed if the trajectory of the electrons lies within the cone of angle $\Psi = 1/\gamma$ from the line of sight. Considering the case of only those electrons with velocity cones that lie precisely along the line of sight to the observer, the acceleration vector \vec{a} is in the direction $\vec{v} \times \vec{B}$ and the observed radiation is linearly polarised parallel to the direction $\vec{v} \times \vec{B}$ (i.e. lying in the plane perpendicular to the wave vector \vec{k}). When the electron is not pointing precisely towards the observer within the velocity cone there is also an acceleration component parallel to the magnetic field. The radiation from a single electron is elliptically polarised because the component parallel to the magnetic field has a different time dependence within each pulse compared with that of the perpendicular component. In the case of a distribution of pitch angles, all electrons with velocity cones within the angle $1/\gamma$ of the line of sight contribute to the intensity measured by an observer. These contributions are elliptically polarised in

opposite senses on both sides of the velocity cone. The total polarisation is found by integrating over all particles which contribute to the intensity. The beamwidth $1/\gamma$ is very small when the electrons are highly relativistic and therefore the components of elliptical polarisation parallel to the magnetic field lines cancel out and the resultant polarisation is linear. The fractional circular polarisation amounts to about $1/\gamma$ of the linear polarisation. The ratio of circular polarisation therefore provides information about the energies of the electrons emitting the synchrotron radiation.

In the non-relativistic case, i.e. $v \ll c$ and hence $\gamma \approx 1$, the energy loss rate of an electron becomes

$$-\left(\frac{dE}{dt}\right) = \frac{2 \cdot \sigma_T}{c} U_{mag} v_{\perp}^2 \quad (2.4)$$

and radiation is emitted at the gyrofrequency of the electron $\nu_g = \frac{e \vec{B}}{2\pi m_e}$, with m_e the mass of the electron. In the non-relativistic case there is no beaming effect, and the radiation of the electrons is circularly polarised.

2.1.2 Inverse Compton Scattering

Inverse Compton (IC) scattering occurs when highly relativistic electrons with energies $E = \gamma mc^2$, moving through a soft isotropic photon field, scatter some of these ambient soft photons to gamma-ray energies (Figure 2.2). For an isotropic photon distribution the energy loss rate by each electron, and thereby the increase of radiation, is

$$-\left(\frac{dE}{dt}\right) = \frac{4}{3} \cdot \sigma_T \gamma^2 c \left(\frac{v}{c}\right) U_{Photon} \quad (2.5)$$

where U_{Photon} is the initial photon energy density, σ_T the Thomson-cross section and γ the Lorentz factor. The above equation is similar to the loss rate given for synchrotron radiation except that the magnetic energy density has been replaced with the photon energy density. This depends, however, on the validity of Thomson scattering in the rest frame of the electron, i.e. $\gamma h\nu \ll mc^2$. In the case of an isotropic distribution of high energy electrons no polarization can be expected. The maximum energy of upscattered photons depends on the Lorentz factor γ of the scattering electrons so that

$$h\nu_{max} \approx 4 \gamma^2 h\nu_0 \quad (2.6)$$

The average energy of these photons is

$$h\nu_{average} \approx \gamma^2 h\nu_0 \quad (2.7)$$

This means that the energy gain of photons by IC scattering from relativistic electrons is roughly proportional to γ^2 of the electrons.

The isotropic microwave background provides low energy photons which can be upscattered by high energy electrons in SNRs as well as IR photons which are generated during grain heating in SNRs (de Jager, 1995).

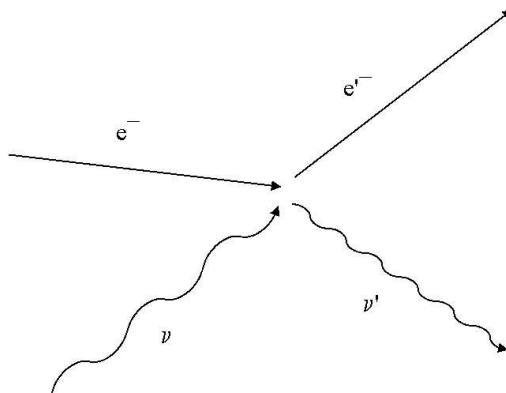


Figure 2.2: Inverse Compton scattering. A high energy electron e^- interacts with a photon of frequency ν . The scattered photon gains energy and thus has the frequency $\nu' > \nu$.

2.2 Thermal Radiation Processes

Apart from a few examples (i.e., emission from Crab-like SNRs and non-thermal radio emission), the main emission mechanism in SNRs in almost the entire frequency band is thermal due to forward and reverse shock heating of the interstellar material and ejecta, respectively. Thermal emission indicates that particles obey a Maxwellian distribution in energy and therefore are in the so-called thermal equilibrium. In SNRs, thermal emission comes from two radiative processes - continuum from thermal bremsstrahlung and line emission from electron-ion impact excitation, ionization and radiative capture of electron by ions. Thermal bremsstrahlung ('deceleration radiation') arise from electrons which are decelerated by a static electric field of atomic nuclei and therefore radiate energy (Fig. 2.3). The energy emitted by an accelerated particle is proportional to $1/m^2$, where m is the rest mass of the particle. Bremsstrahlung therefore plays a particularly important role for light particles such as electrons. At the critical energy for electrons $E_c \approx 500 \text{ MeV}/Z$, the average energy loss by radiation and by ionization is the same. In the non-relativistic case the radiation power is perpendicular to the acceleration direction and varies as $\sin^2 \theta$. For an isotropic distribution of electrons in a plasma the entire photon field is expected to be unpolarized. For a Maxwellian distribution of electron velocities $N_e(v) \propto \exp(-\frac{m_e v^2}{2kT})$ the total bremsstrahlung emission is:

$$\left(\frac{dP(T)}{dV} \right)_B = 1.4 \times 10^{-27} T^{1/2} n_e n_i Z^2 g(E, T) \quad [\text{ergs s}^{-1} \text{ cm}^{-3}] \quad (2.8)$$

where n_e and n_i are the electron and ion density, respectively, Z is the atomic number of the traversed material and $g(E, T) \approx (E/kT)^{-0.4}$ for

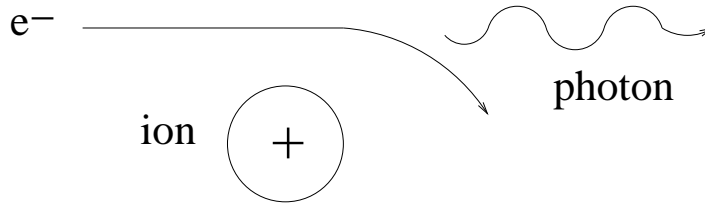


Figure 2.3: Bremsstrahlung - an electron is accelerated by the static electric field of an ion and emits a photon.

$E \sim kT$.

Bremsstrahlung occurs in optically thin thermal plasmas (i.e. the photons do not interact with the plasma after leaving the decelerated electrons and therefore carry the information directly from the production process, in contrast to blackbody radiation which is emitted from optical thick plasma). Non-thermal bremsstrahlung is the same process as thermal bremsstrahlung but originates from a suprathermal electron population that is beyond the Maxwellian distribution of energy. The spectrum is also described by a power law.

2.3 The Acceleration of High Energy Particles

One of the most fascinating problems in high energy astrophysics is that of the mechanisms by which high energy particles are accelerated to ultra-relativistic energies. (up to $E \sim 10^{15}$ eV in the case of Galactic cosmic rays). Terrestrial laboratories will never be able to produce such high energetic particles, but SNRs can accelerate particles up to $E \sim 10^{15}$ eV. The Galactic cosmic rays are generally supposed to originate in SNR shock waves through Fermi shock acceleration. The following sections describe the most important acceleration mechanisms.

2.3.1 Fermi Acceleration Mechanisms

Second-Order Fermi Acceleration

This mechanism was first proposed by Fermi (1949) as a stochastic process by which particles colliding with fast-moving clouds in the ISM could be accelerated to high energies. Charged particles are reflected from ‘magnetic mirrors’ associated with irregularities in the Galactic magnetic field. The mirrors (i.e. the clouds) are assumed to move randomly with typical velocity v , and Fermi showed that the particles statistically gain energy in these reflections. The particles undergo head-on collisions, when they travel towards the cloud, and following collisions when they travel with the cloud encountering the cloud from behind. If the particles remain within the acceleration region for some characteristic time, a powerlaw distribution of particle energies is found.

Because of scattering by hydromagnetic waves or irregularities in the magnetic fields, it is likely that the particles are randomly scattered in pitch angle. Supposing that the cloud is infinitely massive so that its velocity is unchanged in the collisions and that the particles are relativistic ($v \approx c$), the average energy gain per collision is

$$\left\langle \frac{\Delta E}{E} \right\rangle = \frac{8}{3} \left(\frac{V}{c} \right)^2 \quad (2.9)$$

where V is the velocity of the cloud. The equation shows that the average increase in energy is only second order in V/c . Due to the low velocities of interstellar clouds ($\sim V/c \leq 10^{-4}$) and the mean-free path of cosmic rays in the ISM on the order of 1 pc, the number of collisions should be roughly one per year, resulting in a very slow gain of energy by the particles. SNRs, however, are the ideal location of Fermi acceleration processes due to small-scale turbulences at the shock front.

First-Order Fermi Acceleration

First-order Fermi acceleration takes place in the strong shock waves which occur in SNRs. High energy particles which are present in front of and behind the shock wave propagate much faster than the shock itself. Since the thickness of the shock is much smaller than the gyroradius of high energy particles, the particles hardly notice the shock at all. Due to turbulences behind the shock front and irregularities ahead of it, when the particles propagate through the shock in either direction, they are scattered so that their velocity distribution becomes isotropic on either side of the shock front. It is easiest here to consider the frame of reference in which the shock front is at rest, and hence the upstream gas (gas beyond the shock) flows into the shock front at velocity $v_1 = u$ and leaves the shock with a downstream velocity v_2 (gas in front of the shock). Due to the conservation of mass through the shock (i.e. $\rho_1 v_1 = \rho_2 v_2$) and the compression ratio $\rho_2/\rho_1 = (\gamma+1)/(\gamma-1)$ in a strong shock (where γ is the ratio of specific heats of the gas) the downstream velocity arises to $v_2 = \frac{1}{4}v_1$, with $\gamma = 5/3$ for a monatomic or fully ionized gas.

Considering the frame of reference in which the flow of gas in front of the shock is stationary and the velocity distribution of the high energy particles is isotropic, the shock propagates through the medium at velocity u , but the gas behind the shock travels at a velocity $\frac{3}{4}u$ relative to the upstream gas. In the opposite process, the particles diffuse from behind the shock to the upstream region in front of the shock, with an isotropic velocity distribution of particles behind the shock. Crossing the shock front the particles hit the gas which moves towards the shock front with the same velocity $\frac{3}{4}u$. The particles undergo exactly the same process of receiving a small increase in energy ΔE on crossing the shock front from downstream to upstream as they do in the opposite process. There are never crossings in which the particles lose energy because there are only head-on collisions. The gas on the downstream side approaches the particles at a velocity $V = \frac{3}{4}u$ and this means that high energy particles which cross the shock front, obtain an average increase in energy

$$\left\langle \frac{\Delta E}{E} \right\rangle = \frac{2}{3} \left(\frac{V}{c} \right) \quad (2.10)$$

assuming a non-relativistic shock but relativistic particles.

The direction of propagation of the particles is randomized without energy loss by scattering in the downstream region, and hence, they recross the shock gaining another increase in energy $\frac{2}{3}(V/c)$, i.e. the average energy gain after one cycle is

$$\left\langle \frac{\Delta E}{E} \right\rangle = \frac{4}{3} \left(\frac{V}{c} \right) \quad (2.11)$$

Starting with the average energy of a particle after one collision and the probability $P=1-u/c$ that the particle remains within the acceleration region after one collision, the differential energy spectrum of the high energy particles becomes

$$N(E) dE \propto E^{-2} dE \quad (2.12)$$

which corresponds to a spectral index α of -0.5, where $S_\nu \propto \nu^\alpha$ is the so-called source function.

It is also essential to calculate the number distribution of repeated cycles before the particles escape the acceleration regions. These are determined by the shock speed, the compression ratio of the shock and the pitch angle distribution of particles at the shock crossing.

2.3.2 Particles Acceleration in Shell-Type SNRs

The first-order Fermi mechanism of diffuse shock acceleration is the most dominant process for particle acceleration in SNRs. Adiabatic deceleration and synchrotron radiation losses are the two major processes of momentum loss of relativistic electrons in SNRs. Momentum gain processes are restricted to 1st and 2nd order Fermi processes. The observed radio spectral indices are directly related to the compression ratio ($\rho_2/\rho_1=(\gamma+1)/(\gamma-1)$) yielding strong dependence on the dynamical evolution in an adiabatic shock wave. A strong adiabatic shock leads to a compression ratio of 4.0 (see therefore section 2.3.1) whereas an isothermal shock (in the case of thermal conduction from the hot interior of the remnant) leads to a lower compression ratio of about 2.4. Droege et al. (1987) showed that neglecting the 2nd order Fermi mechanism in the particles acceleration scheme could lead to much too high radio spectral indices and concluded that the adiabatic compression ratio must be less than 4 in order to obtain the observed radio spectral indices. However, the inclusion of the 2nd order Fermi acceleration into their calculations provided that the compression ratio lies somewhere between the two strong shock cases that of a strong adiabatic shock and a strong isothermal shock. A range in the compression ratio from 4 downwards together with the degree of the relative strength of 2nd order Fermi acceleration can explain both the mean and the dispersion of the radio spectral index distribution. The acceleration time scale for the 2nd order process must be shorter than or comparable to the time scale for the 1st order acceleration and also shorter than the time scale for the wave energy damping of the thermal plasma.

Ellison et al. (2000), on the other hand, assume a compression ratio greater than

4 in order to explain efficient particle acceleration. They use a simple model of non-linear diffuse shock acceleration to include the injection and acceleration of electrons and the production of photons from bremsstrahlung, synchrotron, inverse Compton and pion-decay processes. The density of the ambient ISM as well as the environmental magnetic field strength are the most interesting parameters in this regard. In addition, the ejecta mass, density profile and the explosion energy play an important role in the understanding of the emission processes. An important aspect of non-linear acceleration is that shock heating is linked to particle acceleration and thus to the broadband photon emission. The nature of X-ray emission depends significantly on density and magnetic field. As the density is increased for a given magnetic field strength, the keV X-ray emission shifts from synchrotron emission from relativistic electrons to quasi-thermal bremsstrahlung emission. In the case of increased magnetic field strength, the X-ray emission behaves in the opposite way. The results of Ellison et al. (2000) were in excellent agreement with the observations of SN 1006 (Koyama et al., 1995), where X-ray emission from the edges of the remnant shell is dominated by non-thermal radiation from electrons accelerated to energies of ~ 100 TeV within the shock front. The evidence for synchrotron emission in SN 1006 is supported by the strong correlation between the radio and X-ray surface brightness.

2.3.3 Particle Acceleration in Crab-like SNRs

The origin of relativistic electrons in pure shell SNRs is probably very different from that in the Crab-like SNRs. Crab-like SNRs possess a central young pulsar which powers a surrounding synchrotron nebula. The brightness distribution peaks in the center. Charged particles are accelerated in the neutron star magnetosphere along curved magnetic field lines and propagate into the surroundings emitting synchrotron radiation by spiraling around magnetic field lines in the nebula. The basic structure of a pulsar wind nebula is regulated by the input power from the pulsar and the density of the medium into which the nebula expands. The nebula radius itself results from the formation of a wind termination shock at which the highly relativistic pulsar wind is decelerated to $v \approx c/3$ in the postshock region where it finally merges with the particle flow in the nebula. The shock forms at the radius r_w at which the pressure of the wind is balanced by the internal pressure of the pulsar wind nebula (Slane, 2002):

$$r_w^2 = \dot{E}/(4\pi\eta cp) \quad (2.13)$$

where \dot{E} is the rate at which the pulsar injects energy into the wind, η is the fraction of a spherical surface covered by the wind and p is the total pressure outside the shock.

Wind particles are accelerated at the termination shock up to energies of the order of ~ 50 TeV, which cannot be explained by normal diffuse shock acceleration because the magnetic field at the termination shock must be nearly perpendicular to the flow. The acceleration of e^\pm is the result of resonant cyclotron absorption of low frequency electromagnetic waves which are emitted by ions gyrating in the compressed B-field of the postshock gas (Arons & Tavani, 1994). The magnetic field in the pulsar wind nebula strengthens with radius. The lifetime of the synchrotron emitting particles in

the nebula is:

$$t_{syn} = 5 \times 10^{11} B^{-3/2} \nu^{-1/2} s \quad (2.14)$$

where ν is the frequency of the synchrotron radiation and B the magnetic field. This results in a variation of the nebula radius with energy (e.g. in the Crab nebula, for which the radio size is larger than that seen in X-rays) or the radial variation of the powerlaw index, steepening with radius (e.g. in the Crab nebula and G 21.5-0.9).

Chapter 3

Supernovae and Supernova Remnants

This chapter illustrates the final stages of stellar evolution, describing the scenario of SNe Type Ia explosions as well as the gravitational collapse of massive stars resulting in Type II SNe. The Galactic SN rate and the further evolution stages of thermal SNRs are discussed in the classical picture of Woltjer (1972) in the following subsections. In the frame of multi-wavelength studies of SNRs presented in this PhD thesis, the observational properties of SNRs are illustrated in various wavelength bands focusing mainly the X-ray and radio band. Finally a brief introduction is given to compact objects which are born in supernova explosions and to NS/SNR associations.

3.1 Supernovae

The evolutionary end of massive stars is characterized by a supernova, a powerful explosion due to gravitational collapse, which disrupts almost the whole star leaving a gaseous SNR and, in some cases, a detectable stellar remnant such as a pulsar, neutron star or black hole. The situation is different when a White Dwarf (WD) is part of a binary system and accretes matter and angular momentum from its companion star. It is believed that at a certain point the WD is disrupted completely in a thermonuclear explosion leaving only a gaseous SNR (cf. Hillebrandt & Niemeyer (2000)). A SN explosion is usually associated with an increase of brightness on the order of 20 mag in the optical band, explaining the origin of the name ‘supernoava’ (lat. nova stella for ‘new star’), and near the maximum its luminosity is comparable with that of an entire galaxy.

3.1.1 Final Evolution Stage of Stars

SNe Ia

The currently accepted scenario of SNe Type Ia is a carbon/oxygen (C/O) WD in a close binary system which has already rejected its hydrogen envelope. It is pushed by accretion very near to the Chandrasekhar mass limit of $1.38 M_{\odot}$ ¹, and as the central

¹Solar mass $M_{\odot} = 1.9891 \times 10^{30}$ kg

density of the dwarf rises above 10^9 g cm^{-3} carbon ignites near the center resulting in an outward-propagating thermonuclear flame. This flame is Rayleigh-Taylor unstable and becomes turbulent leading to acceleration and therefore to an energetic explosion (Woosley & Weaver, 1986; Reinecke et al., 2002). Thus, the star is disrupted completely without leaving behind a stellar remnant. Recent progress in modeling Type Ia SNe is reported by Hillebrandt & Niemeyer (2000) who used numerical 3-D simulations making the models more realistic and reliable. But the physics leading to the explosion is not completely understood. The sub-Chandrasekhar-mass models are actually favored by the statistics of possible SN Ia progenitor systems (Yungelson & Livio, 1998) considering C+O white dwarfs below the Chandrasekhar mass. These dwarfs do not reach the critical density and temperature for explosive carbon burning by accretion and therefore need to be ignited by an external trigger. Detonation in the accreted He layer were suggested to drive a strong enough shock into the C+O core to initiate a secondary carbon detonation (Iben & Tutukov, 1984).

SNe II

SNe Type II belong to the collapse-driven supernovae which result from the death of a massive star with a main sequence mass $M_0 \geq 8 M_\odot$ (Hashimoto et al., 1993). During the evolution from the main-sequence to the SN explosion, massive stars strongly modify the ambient medium by ionizing emission and winds resulting in a surrounding of cavities and shells (D’Ercole, 1992). Massive stars undergo all the major burning stages up to silicon burning. Almost all stars start with hydrogen burning in the core via the pp-chain or CNO-cycle²(Fowler et al., 1975). This phase is the longest one in the life of a star due to the large initial abundance of hydrogen ($\sim 70\%$ by mass) and the high thermal yield for transformation of hydrogen into helium ($\sim 0.7\% mc^2$). In this phase the central temperature is less than $T=4 \times 10^7$ K. When the hydrogen is depleted, the pressure decreases and the core contracts, initiating helium burning at a temperature of $\sim 10^8$ K. The triple- α process is the most important of all helium burning reactions leading mainly to ^{12}C and ^{16}O formation which explains the high cosmic abundance of these two elements (Austin et al., 1971). The heavier elements ^{20}Ne , ^{24}Mg and ^{28}Si as well as ^{14}N , ^{18}F , ^{18}O , ^{22}Ne and ^{25}Mg , for temperatures slightly above 10^8 K, are also produced from He burning but at a much smaller production rate. The energy released per unit mass is about an order of magnitude less than in hydrogen burning. The fusion of heavy elements releases far less energy per unit mass of burnt material than fusion of light elements and therefore the nuclear fuels of the succeeding burning stages are very rapidly exhausted. For temperatures $T \geq 6 \times 10^8$ K carbon burning starts. This is followed by neon burning at temperatures $T \geq 10^9$ K, producing high energy photons and a background of e^\pm pairs. At $\sim T \geq 2 \times 10^9$ K oxygen burning sets in and produces elements like ^{24}Mg , ^{28}Si , ^{31}S , ^{31}P and ^{32}S . The final burning stage is reached with silicon burning at $T \geq 4 \times 10^9$ K (Bodansky et al., 1968) which produces elements up to iron, like ^{56}Ni , ^{56}Co and ^{56}Fe (Tab. 3.1). The star then consists of an iron core which is surrounded by shells with successively lighter elements

²Carbon, nitrogen, oxygen act only as catalysts and are not burned or produced

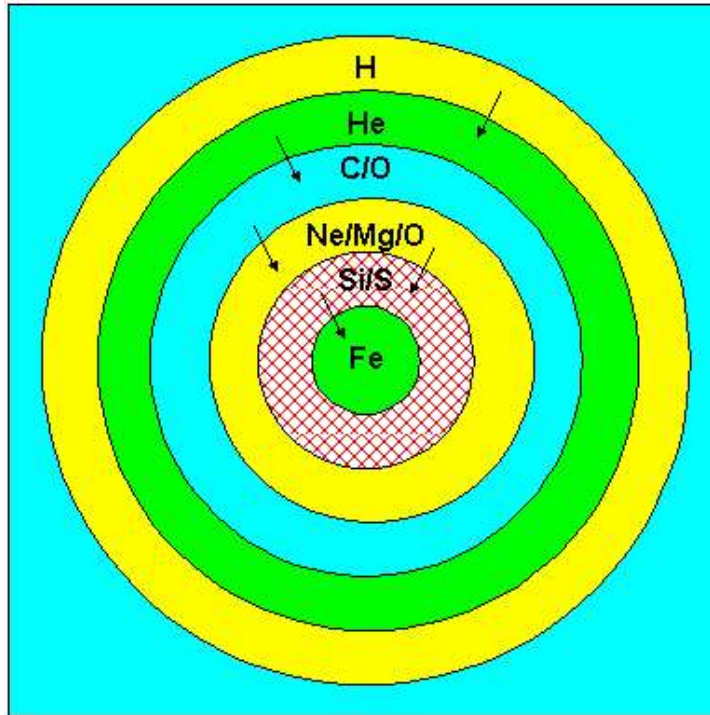


Figure 3.1: The onion skin model for SN type II illustrating the layered structure of massive stars with lighter gases on the outside and heavier gases on the inside through nuclear fusion.

and looks roughly like an onion with different shells (Fig. 3.1). Elements heavier than iron can only be produced during SN explosions in the r-process (r=rapid) or the s-process (s=slow) inside highly-evolved, late-type stars. The r-process occurs when two neutrons are captured almost simultaneously by the most massive nuclei and then decay into protons via β -decay. Hence, they form stable isotopes (Terasawa et al., 2001). The s-process (s=slow) occurs when a single neutron is added to the nuclei and the neutron subsequently undergoes a β -decay to change into a proton (Aufderheide et al., 1990). The neutron capture is a slower process than the β -decay.

Further increase in central density and temperature due to nuclear reaction outside the iron core will not lead to more nuclear energy generation in the interior. The star has exhausted all its energy sources as iron has the highest binding energy per nucleon (beyond the iron-group elements, all nuclear reactions are endothermic). Reaching the Chandrasekhar mass, the iron core contracts since the degeneration pressure of the electrons can no longer balance the gravitation. Energy loss from the core due to neutrinos leads to higher temperatures, which in turn cause even more neutrino losses (because the temperature rises to 10^9 K).

Moreover, the electrons are pushed into the nuclei via inverse β decay, following:



Fuel	T[K]	density ρ [g/cm ³]	time scale t[yr]	Nucleosynthesis Products
H	3×10^7	1	10^7	He
He	1×10^8	500	10^6	C, O
C	6×10^8	10^5	10^3	Ne, Mg
Ne	1.2×10^9	10^6	10	Mg, Si
O	2×10^9	10^7	1	Mg, Si, S, P
Si	3×10^9	10^8	hours	Ni, Co, Fe

Table 3.1: Overview on the different burning stages of a massive star. T and ρ are the required temperature and density of the star to start the corresponding burning. The time scale t refers to the duration of the individual burning stage. The Nucleosynthesis Products are the end products.

which is energetically favored. This process reduces the pressure in the star because electrons are consumed and energy is lost. The core continues to contract. The photons become so energetic that they start to disintegrate the nuclei which is an endothermal reaction. Temperature and pressure decrease dramatically, and the core collapse in free fall. The gravitational collapse releases $\sim 10^{53}$ ergs of energy whereof only about 1 % of the energy is transformed into electromagnetic radiation and the kinetic energy of the envelope. Once the density reaches $\rho \approx 10^{12}$ g cm⁻³, a large fraction of the core is already transformed into neutrons which can not escape anymore (Scheffler & Elsässer, 1990). For $\rho \approx 10^{14}$ g cm⁻³, the density of nuclear matter is reached. If $M_{core} \leq 3 M_{\odot}$ the quantum mechanical degeneracy of the neutrons stops the collapse and a new configuration of equilibrium is obtained (i.e. a neutron star is born). In the case of $M_{core} \geq 3 M_{\odot}$ the core collapses to a black hole.

If the core forms a neutron star, the compressibility becomes virtually infinite (nearly degenerate fermi gas with very strong repulsion at short distances between nucleons). The outer stellar material falling onto the neutron star (core bounce) is strongly shocked and heated up causing the explosive expansion of the envelope. The out-going shock wave loses a lot of energy to photo-disintegration of iron. The temperature of the neutron star reaches a temperature of a few 10^{11} K and cools down to a temperature of $\sim 10^9$ K within a few hours to days due to the emission of neutrinos. The mean birth velocity of a neutron star is about 500 km s^{-1} but higher velocities lead to the assumption that the collapse may occur asymmetrically; the neutron star may even be ejected from the envelope (Lorimer et al., 1997). The final breakthrough of the out-going shock wave through the outermost layers of the star, specifies the beginning of a SN explosion.

The non-spherical core collapse of a star is also expected to radiate gravitational waves (Thorne, 1997) opening a new window for investigations of the most powerful events in the universe. Plans are underway by several groups to observe such gravitational waves in the near future in order to study directly the processes of the gravitational collapse of a star (cf. Rüdiger (2000); Danzmann (2000)).

3.1.2 Classification of SNe

The observed SNe have been classified mainly into two types, on the basis of spectroscopic evidence. Type I includes all the SNe showing no obvious hydrogen lines near the maximum whereas Type II are rich in hydrogen. Type I SNe are further divided into three categories, namely Type Ia which are characterized by strong [Si II] absorption lines at $\lambda = 6717, 6731 \text{ \AA}$, Type Ib by strong [He I] lines at $\lambda = 5876, 7065$ and 66678 \AA and Type Ic if neither [Si II] nor [He I] lines are present (Matheson et al., 2001). The light curves of Type I are quite similar, rising steeply to a peak absolute blue magnitude of about -18.2^m for Type Ib/c and $-19.30^m \pm 0.03^m$ for Type Ia (Riess et al., 1999). The given error results in the 1σ fluctuation for a sample of six scarcely absorbed SNe Ia whose distance could be well derived from the Cepheids. Due to the small error in the brightness SNe Ia are also used as standard candles for distance measurements (Branch & Miller, 1993). Type Ia light curves decline by about 3 magnitudes in the first four weeks after maximum light, after which they decay more slowly with a rate of $\sim 0.02^m d^{-1}$. The light curves of Type Ib are similar to that of Type Ia but fall off more slowly. Type SNe II can be divided into two categories with respect to the shape of their light curves. There are Type II-L (linear) whose brightness fall off at a rate of $\sim 0.05^m d^{-1}$ after the maximum and after about 80 days decays linearly at $\sim 0.01^m d^{-1}$. The brightness of Type II-P (plateau), however, fall off at $\sim 0.03^m d^{-1}$ for the first 30 days after the maximum, then remain constant for about 50 days, followed by a steep decay of $\sim 0.05^m d^{-1}$ (Petschek, 1990). Four months after the maximum the brightness, they decline more slowly at a rate of $\sim 0.006^m d^{-1}$.

SNe II are the most common type of SNe and are not as bright as the SNe Ia, but they offer the potential to be used as distance indicators. Making use of the envelope expansion velocities of the plateau subclass which are highly correlated with their luminosities during the plateau phase, allows one to standardize the candles in order to derive distances with precisions comparable to those delivered by SNe Ia (Hamuy & Pinto, 2002). Type Ib/c and II events are found only in spiral or irregular galaxies and are mainly concentrated in spiral arms, whereas the Type Ia SNe also occur in elliptical galaxies and halos. Thus, Type Ib/c and II seem to be associated with Population I (young, massive) progenitors while Type Ia would be assigned to old objects of Population II. They appear in all kinds of galaxies (i.e. elliptical, spiral and irregular), but tend not to be found in the arms of spiral galaxies (McMillan & Ciardullo, 1996) whereas Type II SNe have never been observed in elliptical galaxies. They occur occasionally in irregular galaxies but more often in spiral galaxies, within the confines of the spiral arms (van den Bergh & Tammann, 1991).

3.1.3 Galactic Supernova Rate

There are three methods to estimate the galactic SN rate from the Galactic SNe data, historical data on SNe in the solar neighbourhood and data from external galaxies (Dragicevich et al., 1999). An overview of all methods and results of SN rates are summarized in Tab 3.2.

The Galactic SN rate can be estimated by using observations of Galactic SNRs,

theoretically from the mass spectrum of star formation and from modelling the chemical evolution of the Galaxy. The SN rate can not be deduced directly from SNRs because of the dependence of a remnant's lifetime on the ambient density and therefore on the distance from the Galactic plane (Tammann et al., 1994). Ratnatunga & van den Bergh (1989) used the mass spectrum of star formation to calculate the rate of massive star collapse (leading to SNe Type Ib/c and II) in the Galaxy. They obtained a total SN rate for the Galaxy of $1.2_{-0.7}^{+1.7}$ per century taking into account that core collapse SNe constitute 85 per cent of all SN events, the other 15 per cent being of Type Ia (van den Bergh & Tammann, 1991). Tsujimoto et al. (1995) investigated theoretically the relative frequencies of Type Ia and II SNe in the chemical evolution of the Galaxy which is in good agreement with the observational estimate by van den Bergh & Tammann (1991). Based on the different types of SNe and hence their progenitors, different heavy elements are produced on different time-scales during the chemical evolution of the Galaxy. The nucleosynthesis products of SN Ia and II and their roles in the chemical evolution of the Galaxy are considerably different (e.g. nucleosynthesis arguments indicate that Fe is mainly produced by SNe Ia while O is mainly produced by SNe II). This fact can also be used to determine the type of SN explosion from the observed element abundance in the X-ray spectra. Matteucci & Francois (1989) developed models of the chemical evolution of the Galaxy with respect to the temporal variation of the abundances of several elements. They yielded a SN rate of 1.9 and 2.5 SNe per century at the present epoch in different models.

The SN rate for the Galaxy can also be calculated using the historical records of SN sightings. One method is to assume that the historical sightings, after corrections for gaps in the historical record and for extinction toward the galactic center have been applied, are complete out to a horizon of 4 or 5 kpc from the solar system. The comparison of the surface area within this horizon with that of the Galactic disk enables the calculation of the SN rate. Another method is to assume that the historical records are complete for a sector of the Galaxy which contains the Solar system and in which the historical sightings occurred. Using the sector method a rate of 5.8 ± 2.4 per century was calculated (van den Bergh/Tammann 1991). Strom (1990) reported a rate of 3_{-1}^{+2} per century using the horizon method. Many estimates of the SN rate from historical SNe are based on the assumption of a uniform distribution of SNe across the Galactic plane although numerous studies of SNe in external spiral galaxies have shown that the surface density as a function of radius is not constant.

The third method is to determine the SN rate by SN discoveries in external spiral galaxies requiring knowledge of the Hubble constant H_0 , the spiral classification and the luminosity of our Galaxy. Using $H_0=75 \text{ km s}^{-1} \text{ Mpc}^{-1}$ and a galactic blue luminosity of $2.3 \pm 0.6 \times 10^{10} L_{B,\odot}$, Cappellaro et al. (1997) considered the SN rate that they found for spirals of subtype Sab, Sb and Sbc and thus obtained a SN rate of 1.3 ± 0.9 per century in our Galaxy. Based on the same parameters and the luminosity of our Galaxy, Evans (1994, 1997) found a galactic SN rate of 3.0 ± 1.5 SNe per century considering also the later type (Sc-Sd) galaxies which have relatively high SN rates. Assuming a lower value of the Hubble constant, the calculated SN rate would even be larger.

Year	Observer	SN rate	determination method
1989	Ratnatunga & van den Bergh	$1.2_{-0.7}^{+1.7}$	mass spectrum of star formation
1989	Matteucci & Francois	$2.2_{-0.3}^{+0.3}$	model of chem. evolution of the Galaxy
1990	Storm	3_{-1}^{+2}	historical sightings - horizon method
1991	van den Bergh & Tammann	$5.8_{-2.4}^{+2.4}$	historical sightings - sector method
1996	Cappellaro et al.	$1.3_{-0.9}^{+0.9}$	SN rate in external spiral galaxies
1997	Evans	$3.0_{-1.5}^{+1.5}$	SN rate in external spiral galaxies
1999	Dragicevich	2	SN rate in external spirals and historical

Table 3.2: The determined/calculated values of the SN rate in the last 13 years. The SN rate gives the number of SNe per century.

Dragicevich et al. (1999) shows that if the observed surface density function of SNe in external galaxies is used to calibrate the historical data on the SN rate in the solar neighbourhood, then the calculated total SN rate for the Galaxy is abnormally high due to the localization of galactic SNe near spiral arms and star-forming regions. In this picture one has the impression of a considerably higher SN rate than is valid for the Galaxy as a whole. Therefore the actual SN rate for the whole Galaxy is likely 2 per century.

3.2 Supernova Remnants

After a SN explosion the evolution of the possible compact as well as the diffuse and gaseous remnant continues until the SNR is diluted by the ISM. The complexity of SNR spectra relative to many other emission line nebulae results from non-equilibrium processes. The various types of SNRs as well as their evolution is described in the following sections which also address observable properties of SNRs in all wavelength bands.

3.2.1 Classification of Supernova Remnants

SNRs can be divided into four broad categories based on their radio and X-ray morphology. The first class, including most of the known SNRs, shows a shell-like structure in the X-ray and radio band. Prominent examples of these shell-like remnants are Tycho (SN1572), Kepler (SN1604), the Cygnus Loop and RCW 86 (SN185). The X-rays are produced in an optically thin plasma which has been heated up by shock waves to temperatures on the order of 10^{6-7} K. The majority of the X-ray emission is thermal, and only the high energy tail of the spectrum shows non-thermal X-ray emission which is believed to be produced by synchrotron radiation from TeV electrons accelerated by the remnant shocks (Ellison et al., 2001). The thermal X-ray spectra are dominated by strong line emission from highly ionized nucleosynthesis products. The X-ray band includes K shell emission lines from carbon through nickel and lines from the Fe L shell. As these lines originate from the shock-heated, low density ($\sim 1 \text{ cm}^{-3}$) plasma,

it is generally not in equilibrium ionization. In radio, the shell is characterized by non-thermal and partly polarized emission.

The second class contains the Crab-like remnants, also called plerions. Well known examples here are the Crab Nebula, G 21.5-0.9 and 3C58 (G 130.7+3.1). They show centrally peaked emission in both bands with spectral indices ≥ -0.3 (Weiler & Sramek, 1988) in radio. The morphology and radio spectral index are useful in separating plerion from the more numerous shell remnants. An active pulsar acts an energy source within the remnant and is inferred from the presence of a known central neutron star or from a bright synchrotron nebula indicating the presence of a hidden pulsar. The X-ray spectrum is described by a featureless power law due to synchrotron emission processes.

The third class combines elements of the previous two. Some remnants, such as Vela or CTB 80, possess both a thermal shell and a non-thermal synchrotron nebula, while others, like W 44 or KES 27, have a shell-like radio structure combined with a center-filled X-ray morphology that nevertheless arises from thermal X-rays. The latter SNRs emerge as a fourth class of remnants (Rho, 1996).

3.2.2 Evolution of Thermal Supernova Remnants

A SN explosion releases kinetic energy on the order of 10^{51} ergs in the form of ejected material expanding into the ISM. Considering ejected material with initial mass M_{ejecta} and total energy E_0 at the time $t=0$ which expands with an initial velocity v_0 into the rather cold and uniform ISM with density n_0 , Woltjer (1972) divided the evolution of SNRs schematically into four phases. In the case of SNe Ia, M_{ejecta} is the mass of the exploded star which amounts to about $1.4 M_{\odot}$ while for SNe Ib and II the mass of the rejected stellar envelope accounts for several M_{\odot} . Although SNRs are generally not spherical and do not usually interact with homogeneous and uniform surroundings, this scenario describes roughly the evolution of SNRs. The effects of relativistic particles as well as magnetic fields are neglected.

1) Free expansion

Since the ISM has a very low density, the SN blast wave expands very quickly and unimpeded. During the free expansion phase, the SNR radius increase linearly with time (i.e. $R_s = v_0 \cdot t$). At the beginning of the SNR evolution, the ejected mass M_{ejecta} dominates the swept-up mass ($M_{ejecta} \gg (4\pi/3) n_0 R_s^3$).

Assuming a density $n_0 \sim 1 \text{ cm}^{-3}$ for the ISM, the free expansion is still fulfilled for a maximal shock radius of about 2 pc. This shock radius is reached in about 200 years, taking a medium expansion velocity of 10^4 km s^{-1} into account. The speed of sound in the ISM is about 10 km s^{-1} and hence much less than the velocity of the expanding ejecta. A shock wave consequently forms at the contact discontinuity between shocked ejecta and shocked ISM. Atoms are ionized by the shock and the temperature increases to 10^7 to 10^8 K.

2) Sedov or Adiabatic Phase

When the accumulated ISM exceeds the ejected mass ($M_{ejecta} \ll (4\pi/3) n_0 R_s^3$), the SNR then enters the Sedov (or adiabatic) phase. Radiative losses are still negligible, i.e. the cooling time is long compared to the dynamical evolution timescale. Hence, the rate of expansion is only determined by its initial energy E_0 and the density n_0 of the ISM. A similar solution was obtained by Sedov (1959) for nuclear explosions applying for a gas with a ratio of specific heats $\gamma=5/3$.

The radius R_s of the blast wave is

$$R_s = 14 \cdot \left(\frac{E_0}{10^{51} \text{ ergs}} \right)^{1/5} \left(\frac{n_0}{\text{cm}^{-3}} \right)^{-1/5} \left(\frac{t}{10^4 \text{ years}} \right)^{2/5} \text{ pc} \quad (3.3)$$

and the shock velocity is given as

$$v_s = \frac{2}{5} \cdot \frac{R_s}{t} \quad (3.4)$$

The temperature behind the shock front arises to

$$T_s = \frac{3}{16} \frac{\mu}{k_B} v_s^2 \quad (3.5)$$

where μ indicates the mean molecular weight of the gas ($\mu \approx 0.6$).

Based on the X-ray data, the physical parameters of the remnant (the shock velocity v_s , the ambient density n_0 , the initial energy E_0 and the age t) can be derived. The observed parameters are the angular shock radius, the surface brightness and the temperature of the X-ray emitting gas.

Directly behind the shock front, the density is $4 n_0$ and decreases towards the center due to the gradual expansion of the SNR, while the temperature increases. The thickness of the expanding shell is about 10% of R_s . The kinetic energy of the swept-up ISM has been estimated by Chevalier (1974) as $E_{kinetic}^{ISM} = 1/2 M v^2 \sim 0.283 E_0$. Therefore, the kinetic energy is about 28% of the explosion energy and the rest of the explosion energy is thermal. Additionally, a reverse shock forms when the outer shells of the expanding sphere are decelerated and the material inside the sphere begins to catch up with the material in the outer layers. Therefore, the matter density begins to increase at the boundary of the expanding sphere. As the deceleration continues, the flow of gas into the outer layers becomes supersonic compared to the sound speed inside the sphere itself. A shock wave forms on the inner edge of the compressed outer layers and propagates back through the expanding gas towards the center, heating the ejected gas.

The end of the adiabatic phase can be estimated by comparing the cooling time of gas behind the shock with the age of the remnant (Blondin et al., 1998). The age for the transition into the radiative phase is then

$$t_{transition} \approx 2.9 \times 10^4 \left(\frac{E_0}{10^{51} \text{ ergs}} \right)^{4/17} \left(\frac{n_0}{\text{cm}^{-3}} \right)^{-9/17} \text{ years} \quad (3.6)$$

At this age the blast wave has reached a radius of

$$R \approx 19.1 \left(\frac{E_0}{10^{51} \text{ ergs}} \right)^{5/17} \left(\frac{n_0}{\text{cm}^{-3}} \right)^{-7/17} \text{ pc} \quad (3.7)$$

and has swept up a mass of

$$M \approx 10^3 \left(\frac{E_0}{10^{51} \text{ ergs}} \right)^{15/17} \left(\frac{n_0}{\text{cm}^{-3}} \right)^{-4/17} M_\odot \quad (3.8)$$

3) Radiative Phase

The remnant's age becomes comparable to the radiative cooling time scale of the shock, and the material behind the shock cools quickly. The remnant then consists of a dense, cool shell with a hot interior. As a consequence, pressure forces are no longer important and the shell moves at constant radial momentum (i.e. $(4\pi/3) R^3 n_0 v = \text{constant}$). This phase begins roughly when half of the thermal energy of the SNR has been radiated at time t_{rad} .

Cioffi et al. (1988) distinguish between two stages of evolution:

- **Pressure-Driven Snowplow (PDS)**

Since the density of the plasma at the shock front is very high and the temperature low, high radiation loss occur directly behind the shock front. A dense and cool shell comes up whose expansion pressure is sustained by the pressure of the hot interior. The cooler shell is pushed through the ISM like a snowplow.

The radius of the shock front and the shock velocity are given by Cioffi et al. (1988):

$$R_s = R_{PDS} \left(\frac{4t}{3t_{PDS}} - \frac{1}{3} \right)^{3/10} \quad (3.9)$$

$$v_s = v_{PDS} \left(\frac{4t}{3t_{PDS}} - \frac{1}{3} \right)^{-7/10} \quad (3.10)$$

where $R_{PDS} = 14 \cdot \left(\frac{E_0}{10^{51} \text{ ergs}} \right)^{2/7} \left(\frac{\zeta_m}{\text{dimless}} \right)^{-1/7} \left(\frac{n_0}{\text{cm}^{-3}} \right)^{-3/7} [\text{pc}]$,

$v_{PDS} = 413 \cdot \left(\frac{E_0}{10^{51} \text{ ergs}} \right)^{1/14} \left(\frac{\zeta_m}{\text{dimless}} \right)^{3/14} \left(\frac{n_0}{\text{cm}^{-3}} \right)^{1/7} [\text{km s}^{-1}]$,

$t_{PDS} = 1.33 \times 10^4 \cdot \left(\frac{E_0}{10^{51} \text{ ergs}} \right)^{3/14} \left(\frac{\zeta_m}{\text{dimless}} \right)^{-5/14} \left(\frac{n_0}{\text{cm}^{-3}} \right)^{-4/7} [\text{years}]$

and ζ_m gives the metallicity relative to the solar abundances which depends mainly on the ISM. ζ_m has no unity and is therefore indicated with “dimless”.

- **Momentum Conserving Snowplow (MCS)**

When most of the interior thermal energy has radiated and the pressure is decreased, the expanding shell can not be sustained any longer by the pressure and expands only due to conservation of radial momentum, i.e.

$$(4\pi/3) R^3 n_0 v = constant \quad (3.11)$$

The shock front then expands with $R_s \propto t^{1/4}$ (Oort, 1951).

4) Dissipation

When the expansion velocity of the remnant becomes comparable to the random motion of the interstellar gas (on the order of 10 km s^{-1} , i.e. the expansion velocity drops below the local sound speed), the remnant dissipates in the ISM.

The time of dissolution is given by Cioffi et al. (1988):

$$t_{merge} = 153 \left(\frac{E_0}{10^{51} \text{ ergs}} \right)^{1/14} \left(\frac{\zeta_m}{\text{dimless}} \right)^{3/14} \left(\frac{n_0}{\text{cm}^{-3}} \right)^{1/7} \left(\frac{\beta}{\text{dimless}} \right)^{-1} \left(\frac{v_{sonic}}{10^6 \text{ cm s}^{-1}} \right)^{-1} \right)^{10/7} \quad (3.12)$$

The shock velocity v_s was substituted by the ambient isothermal sound speed v_{sonic} ($\sim 10^6 \text{ cm s}^{-1}$) and a numerical factor β . Since v_s must exceed v_{sonic} in order to satisfy the validity of the analysis β must be larger than 1.

The maximum radius is then:

$$R_{merge} = 4.93 \left(\frac{E_0}{10^{51} \text{ ergs}} \right)^{1/14} \left(\frac{\zeta_m}{\text{dimless}} \right)^{3/14} \left(\frac{n_0}{\text{cm}^{-3}} \right)^{1/7} \left(\frac{\beta}{\text{dimless}} \right)^{-1} \left(\frac{v_{sonic}}{10^6 \text{ cm s}^{-1}} \right)^{-1} \right)^{3/7} \quad (3.13)$$

Assuming $v_{sonic} \approx 10^6 \text{ cm s}^{-1}$, $E_0 = 10^{51} \text{ ergs}$, $n_0 = 1 \text{ cm}^{-3}$ and setting $\beta \approx 2$, the maximum radius of a SNR is 51 pc, which will be achieved in about 7.5×10^5 years.

In the realistic picture, inhomogeneities of the ISM may distort a regular SNR shell, gradients in density of the ISM may cause an elliptical shape and low density bubbles may lead to so-called “break-out” phenomena. The structure of the ambient magnetic field also affects the shape of radio SNRs (van der Laan, 1962), indicating the direction and homogeneity of the ambient magnetic field.

3.2.3 Supernova Remnants in Various Wavelength Bands

After the SN fades, the shock waves of the remnant expand into the ISM, heating up the surrounding gas, and can therefore become visible in almost all frequencies from infrared to X-rays and gamma-rays. The radiation is observable until the SNR is completely diluted by the ISM. As an example of a SNR observed in four wavelength bands, namely radio, infrared, optical and X-rays, Cas A is shown in Fig. 3.2. For the sake of completeness the radiation properties and physical processes of SNRs are described covering the whole electromagnetic spectrum.

Radio

Galactic SNRs are largely observed as radio objects. Most of them were detected in this wavelength regime.

As mentioned above, radio emission from SNRs is believed to be synchrotron radiation which requires relativistic electrons and magnetic field. Generally, the central pulsar is thought to be the source of non-thermal radio emission, while for shell-type SNRs the non-thermal radiation comes from particle acceleration at the shock front and magnetic field amplification due to compression by the shock as well as particle acceleration behind the shock (Cowsik & Sarkar, 1984). The electrons can be accelerated in two ways: (i) either by turbulent acceleration at the unstable contact discontinuity (second-order Fermi acceleration) or (ii) acceleration in the shock front itself, which is described by first-order Fermi acceleration (cf. 2.3.1). The latter is more efficient (Droege et al., 1987; Reynolds & Ellison, 1992). The magnetic field strength can be determined for a few SNRs, like Cas A, by measuring the rotation measure of background radio sources and making use of the Zeeman splitting of OH maser lines (Brogan et al., 2000). The observationally deduced magnetic field strength for these SNRs are much too high to only be explained by compression. Polarization measure can be used to determine the magnetic field orientation, whereas the electric field component is measured in radio observations which consequently lies perpendicular to the magnetic field component (i.e. the 90° rotated view has to be taken for the magnetic field orientation). But the measured polarization suffers from Faraday rotation in the ISM. The rotation measure depends on the magnetic field strength, particle density and the index of refraction, which is proportional to the square of the wavelength (Simonetti, 1992). The rotation of the position angle is

$$\Delta\Psi = 0.81 \lambda^2 \int \frac{n_e}{\text{cm}^{-3}} \frac{B_{\parallel}}{\mu\text{G}} \frac{dz}{\text{pc}} \quad (3.14)$$

where n_e denotes the electron density and B_{\parallel} the parallel component of the magnetic field.

This rotation can be measured and the true position angles of the magnetic field lines can be determined by using measurements at three or more different wavelengths (Dickel, 1999). Young SNRs clearly show radially oriented magnetic fields, implying a stretching of the field lines as the remnant expands, whereas some of the very old remnants show magnetic field lines tangential to the brightest parts of the SNR shell, suggesting a possible compression of the surrounding field (Dickel & Milne, 1976). Lou (1994) suggested that magnetic fields in young SNRs could mainly originate from magnetized envelopes or magnetospheres of their progenitors, probably magnetic WDs, whereas Jun & Norman (1996) supposed that magnetic field amplification arises from Rayleigh-Taylor instabilities at the interface of the ejecta and the shocked surroundings. The non-thermal nature of radio emission due to synchrotron radiation is also evident by significant linear polarization (5-10 % for shell-type SNRs and up to 30% for Crab-like SNRs).

The radio morphology provides information about the SNR type and the interaction with the ambient ISM and with the ambient magnetic field. H II regions, however,

also show extended radio emission with morphologies similar to those of SNRs. For this reason, it is necessary to observe a SNR candidate at of least two frequencies, which allows for the determination of the spectral index. The detection of non-thermal radio emission (i.e. a negative spectral index) and the presence of polarization are used as adequate evidence to distinguish synchrotron sources from sources of thermal emission. Radio observations facilitate another useful indicator in discriminating between thermal and non-thermal radio emission from the ratio of 60 μm to 0.843 GHz flux densities (Broadbent et al., 1989; Whiteoak & Green, 1996). This method is especially suited for small-diameter sources (Whiteoak, 1992). SNRs generally have very low flux density ratios in the range of ≤ 50 and can be identified on this basis (for comparison extended H II regions have values ≥ 500 -1000). Typical spectral indices for thermal SNRs in the adiabatic phase are on the order of -0.5 for a compression factor of 4. Young (historical) SNRs show steeper spectra ($\alpha = -0.6$ to -0.8). Crab-like SNRs have flatter spectra, with indices which are on the order of ~ -0.1 to -0.3 .

Very young SNRs are first detected at short wavelengths (~ 1.3 cm), because the radio emission at longer wavelengths is strongly absorbed, as is expected for an optically thick source. The optical thickness, however, decreases with the expansion of the remnant and the SNR also become visible at longer wavelengths. In the case of SN 1993J, Pérez-Torres et al. (2001) modeled the radio light curves for a number of frequencies and found evidence for synchrotron self-absorption and free-free absorption.

An advantage of radio observations in the GHz-regime is the lack of interstellar absorption which allows observations in the whole Galaxy. Thermal emission diminishes at frequencies below ~ 1 GHz while non-thermal emission becomes stronger in this energy range. Low frequency observations, where the contamination from thermal emission is minimized, are therefore more suited for the study of SNRs. On the other hand, the angular resolution becomes worse at lower frequencies which is an important point in the identification of SNRs and for detailed studies. Since radio emission in the galactic plane occurs at all angular scales, it is important to be sensitive to small-scales as well as large-scale structures. In order to achieve high angular resolution with sensitivity to large-scale emission, observations of SNRs are performed either by using single dish instruments at high frequencies or interferometric radio telescope array which take advantage of different baselines.

Aside from investigations and diagnostics, radio observations offer the possibility to measure the distance to SNRs via main two methods. The most reliable distance determination, the so-called HI absorption technique, is based on the kinematical distances to clouds that absorb radiation from the SNR. This method provides a lower limit to the remnant's distance and is only as good as the knowledge of the galactic kinematics. Another technique is based on the relationship between surface brightness and remnant diameter (Σ -D) assuming the same radio luminosity at a given distance for all SNRs with a roughly uniform morphology. This method also requires the same supernova explosion mechanism and energy. The following relationship is given for shell-like SNRs and indicates an upper limit (Case & Bhattacharya, 1998):

$$\Sigma \propto D^{-2.64} \quad (3.15)$$

The error in the distance estimate for an individual SNR is found to be $\sim 40\%$ using this Σ -D relation. The third distance method is only applicable to a minority of SNRs that are associated with a pulsar. A pulsar dispersion measure (DM) is related to the distance, which can be derived:

$$DM = \int n_e dl \quad (3.16)$$

where n_e gives the electron density along the line of sight.

Infrared

Studying the infrared (IR) spectrum of radiative shocks can give interesting information on the metal abundances and can yield a direct measurement of the actual efficiency of grain destruction by the shock. The infrared atomic fine-structure lines are produced by gas behind the radiative shocks. The dense, shocked gas cools quickly down to temperatures in the range of $10^2 - 10^3$ K, where infrared transitions are excited (Reach & Rho, 2000). In addition, warm dust can radiate in the mid-infrared due to collisional heating by the hot electrons of the plasma filling the SNR. This plasma is thought to be generated by the secondary shocks driven into the dense clumps of circumstellar material by the SN blast wave (Douvion et al., 2001). The polarized continuum emission in the far-infrared and sub-millimeter arises from magnetically aligned, elongated dust grains (Tamura, 1999). The detection of polarized emission therefore provides information on the strength and alignment of the magnetic field in the vicinity of the SNR. The polarization observation measures the sum of all magnetic fields along the line of sight and therefore can be depolarized by Faraday rotation (like in the radio band). It is not known whether the dust grains were ejected by the star long before it exploded or during the explosion. The Crab Nebula, for example, shows that the overall IR radiation is dominated by thermal emission from cold dust at long wavelengths (60 and 100 μm) and by synchrotron radiation at shorter wavelengths (12 and 25 μm).

The advantages of infrared observations are that far-infrared fine-structure lines are not affected by extinction. Extinction effects are significant in the soft X-rays, ultraviolet (UV) and also optical, as well as near-infrared if the line-of-sight column density exceeds 10^{21} cm^{-2} . This fact causes source confusion with other bright IR sources if the SNRs are located close to galactic plane. Older SNRs show stronger IR emission in the 60 μm or 100 μm band than younger SNRs, which are more dominant in the 12 μm and 25 μm band due to a hotter plasma.

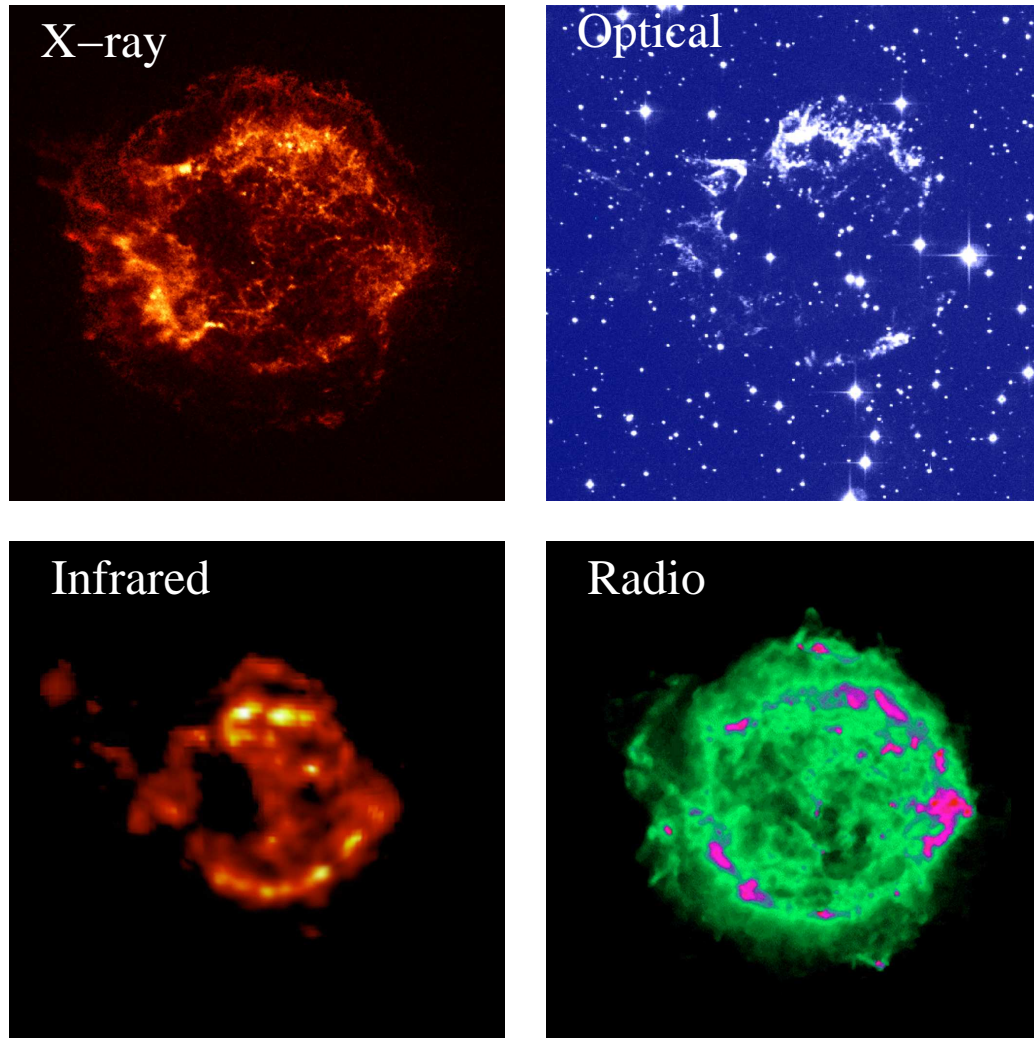


Figure 3.2: These images show Cas A as viewed at four different wavelengths (<http://chandra.harvard.edu/photo/0237/index.html>). The **X-ray** image was obtained with Chandra ACIS. Two shock waves are visible: a fast outer shock and a slower inner shock. The inner shock wave is believed to be the reverse shock, heating up the gas to a temperature of 10^7 K. The outer shock wave is due to the supersonic ejecta colliding with the ISM and possesses many bumps and protrusions that may be the result of convective instability. The faint point source near the center is probably an Anomalous X-ray Pulsar (AXP). The **optical** image shows matter with a temperature of about 10^4 K. Some of these wisps contain high concentrations of heavy elements and are thought to be dense clumps of ejected stellar material. This observation was performed with $H\alpha$ + $[N\text{ II}]$ and red continuum (7100 ± 100 Å) interference-filters. The **infrared** image shows dust grains that have been swept up and heated to several hundred Kelvin by the expanding hot gas. This observation was performed with the ISO satellite in the mid-infrared. The **radio** image shows synchrotron radiation which arises from high energy electrons moving in the magnetic field. This observation was obtained at a wavelength of about 21 cm with the VLA.

For a very long time only the small optical window was accessible to astronomical observations; and thus galactic SNRs were primarily detected and observed in this frequency band. Unfortunately, optical emission from SNRs is hampered by dust and gas in the galactic plane so that only optically bright SNRs can be detected. For this reason, only a small fraction of galactic SNRs is known in the optical band. Nevertheless, optical studies of SNRs provide important information on chemical abundances relative to hydrogen, expansion velocities, gas densities and temperature as well as the ejecta morphology and distribution. Bright optical emission arises from radiative shock waves (i.e. effective conversion of the thermal energy of the shocked gas into radiation). Young SNRs have been found to contain fast-moving oxygen-rich knots or filaments with high velocity dispersions in the order of $\sim 2000 \text{ km s}^{-1}$. The mechanism which excites the optical emission is generally assumed to be the propagation of a slow, radiative, reverse shock into the remnants (Dopita et al., 1984). Most of this emission originates from the cooling and recombination zones well downstream from the shock itself. Coulomb collisions bring the particles into thermal equilibrium by the time the gas cools.

Non-radiative shocks do not have time to produce much radiation, because the cooling time exceeds the age of the SNR. In this case, the optical as well as the ultraviolet (UV) emission is produced in a narrow zone just behind the shock where the gas passes rapidly through various stages of ionization. For fast shocks this zone is relatively narrow compared to the Coulomb equilibrium length scale and therefore it is possible to study the physical processes in the collisionless shocks. When a hydrogen atom or ion passes through a fast shock it suddenly reside in a hot plasma and becomes ionized which takes a finite time. This time is determined by the ratio of the excitation and ionization rate which depend on the temperature. Four neutral hydrogen atoms, for instance, produce about one $H\alpha$ photon (Raymond, 2001). The low abundances of metals relative to hydrogen make these emission lines faint. Non-radiative shocks in partially neutral gas are observed as faint filaments of pure Balmer line emission whereas spectra of radiative shocks are dominated by the forbidden lines [O II] and [O III] as well as [N III] and [S II]. The oxygen originates either from the stellar interior or from stellar winds which reject an oxygen-rich envelope before the SN explosion. Mathewson et al. (1983) have proposed a classification for SNRs according to their optical properties, namely the Balmer-dominated SNRs with prominent examples like the Tycho and Kepler remnants and Oxygen-rich SNRs like G 65.3+5.7.

The $H\alpha/[S II]$ ratio is a useful tool to discriminate remnants from H II regions (Fesen et al., 1985). The Balmer line profiles consist of a narrow component due to the thermal and turbulent velocities in a narrow region associated with the shock and a broad component that is Doppler shifted in the flow direction by the post-shock bulk velocity associated with the kinetic temperature of the post-shock protons, T_p . The intensity ratio of the narrow and broad components of $H\alpha$ provides an estimate of T_e/T_p just behind the shock, where T_e is the electron temperature. The efficiency of electron-ion equilibration decreases with shock speed whereas ion-ion equilibration

does not occur in fast shocks. UV lines have been detected from a few non-radiative shocks showing the resonance lines of the Li-like ions such as [C II] (1335 Å), [C IV] (1550 Å), and [O VI] (1034 Å). The brightness of these lines is reduced by scattering if the column density along the line of sight is sufficiently large. Radiative shocks show bright intercombination line emission such as [C III]. Over 60 UV lines have been detected and identified in Galactic and Magellanic Cloud SNRs. An overview of these lines is given by Fesen & Hurford (1996). UV observations can provide tests of models for the excitation and ionization of the ejected material by the shock waves or by photoionization (Blair et al., 1988). Ultraviolet emission lines in SNRs provide important clues to the shock velocities, densities, grain destruction, and thermal structure of the cooling regions in these objects.

The class of Crab-like SNRs is dominated by synchrotron continuum emission in the optical band powered by the central pulsar, but they also show line-emitting filaments like $H\alpha$ and [S II].

X-rays

The majority of SNRs emit thermal radiation from a hot, optically thin plasma with temperatures in the range of $10^6 - 10^7$ K. A small minority, the Crab-like and composite SNRs, show synchrotron emission which can be described by a powerlaw energy spectrum. The emission peaks at energies in the range of ~ 0.1 and a few keV, where interstellar photoelectric absorption is no longer negligible and limits the low energy flux.

The thermal spectrum of SNRs contains continuum and strong line emission from shock-accelerated electrons and highly ionized nucleosynthesis products, respectively. At early times, the X-ray spectrum is dominated by emission from the ejecta, while later, when the amount of swept-up material increases, the spectrum becomes dominated by emission from material with ISM abundances. The characteristic X-ray radiation includes K shell emission lines from carbon through nickel and also the Fe L band. The only mechanism for ionizing these atoms in a low density plasma is through collisions with electrons. These collisions are so infrequent that a long time is required for the ionization state of the gas to approach that expected for the temperature of the ions. Since the ionization potential of a He-like ion to its H-like state is high, it spends a relatively long time in the He-like state. The result is that the He-like ions dominate the spectra of SNRs in the X-ray band. The hot plasma is therefore in a non-equilibrium ionization state. The dynamics of SNR evolution are dominated by the ions, because they carry the bulk of the momentum while the electrons produce the continuum component that arises primarily from bremsstrahlung radiation. The shape of the continuum depends on the shock velocity v_s , the ionization time scale τ_0 , which is defined as the product of the remnants' age t_0 and the postshock electron number density n_e , and the extent of electron heating at the shock front. As typical for most X-ray emitting thermal plasmas, line strength depends on heavy-element abundances.

The X-ray emission from Crab-like SNRs, however, is non-thermal due to syn-

chrotron emission. This synchrotron emission is produced by highly relativistic electrons in the magnetic field of the nebula, originating from the central pulsar. The spectrum of these Crab-like SNRs is characterized by continuum emission and a lack of line emission that is described well by a power law. The Crab-Nebula, as well as the plerion G 21.5-0.9, show an increase of the power law index with radius, a so-called spectral softening, which reflects the impact of synchrotron radiation losses on very highly energetic electrons as they travel from the pulsar to the edges of the nebula (i.e. the energy losses are dominated by synchrotron emission and adiabatic expansion) (Willingale et al., 2001; Warwick et al., 2001).

X-ray spectroscopy offers the most direct tool to determine fundamental properties of SNRs. The shock velocity can be directly determined by measuring the temperature of the X-ray emitting gas. Spectral investigation also allows the measurement of the abundances of nucleosynthesis products and thus allows a determination of how enriched the shock-heated surroundings have become, or in evolved remnants, the composition of the gaseous ISM. In addition, X-ray spectroscopy allows density measurements of low density clouds and the dominant diffuse ISM, typically yielding densities in the range of $0.1-10 \text{ cm}^{-3}$. The new X-ray observatories Chandra and XMM-Newton provide spatially resolved X-ray spectroscopy as well, which allows for the investigation of density and abundance variations across and around the remnants. The broad bandpass ($\sim 0.1-10.0 \text{ keV}$) of these X-ray observatories additionally allows for the detection of hard X-rays which are not affected by the strong interstellar absorption (mainly in the galactic plane).

Gamma-rays

SNRs are believed to be the primary sources of galactic cosmic rays, produced by diffuse shock acceleration (1^{st} order Fermi acceleration) at the remnants' forward shock. Highly energetic γ -ray emission from SNRs is expected to be generated by cosmic ray interaction with the ambient ISM. Four major processes are responsible for γ -ray emission, namely π^0 production in ion-ion collision, bremsstrahlung emission from energetic electrons, inverse Compton scattering and synchrotron emission of background radiation in the SNR magnetic field (Baring et al., 1999).

The π^0 production in ion-ion collision is based on the reaction $p+p \rightarrow \pi^0 \rightarrow \gamma + \gamma$. The pion production is described using the isobaric and scaling models (Dermer, 1986a,b) which work very well at low and high energies, respectively. γ -ray emission from π^0 is dominant at the beginning of the Sedov phase and then slowly decays (Drury et al., 1994). The expected γ -ray spectrum is very hard, and therefore imaging Cherenkov telescopes, sensitive to γ -rays above $E_\gamma \geq 100 \text{ GeV}$, may be best suited to detect the γ -ray emission. Bremsstrahlung arises from particles decelerating in the electric field of one another. In the ISM which is mainly composed of hydrogen and helium as well as ionized gas, electron-nucleon bremsstrahlung plays a major role in γ -ray emission (rather than electron-electron and nucleon-electron bremsstrahlung). Inverse Compton scattering describes the interaction between highly energetic electrons and low energy background photons in which some part of the energy of the

electron is transferred to the photon. This process is well described by the Thomson cross section at lower energies and by the Klein-Nishina cross section in the relativistic case. Synchrotron radiation occurs when highly energetic electrons spiral in a magnetic field emitting in a narrow cone. A detailed collection of review papers can be obtained from Schönfelder (2001).

3.3 Distribution of SNRs in the Galaxy

Most galactic SNRs were identified at radio wavelength, and thus the identification is limited basically by two selection effects. The surface brightness Σ of the remnants must be above the sensitivity limit of the observations and be significantly discriminable from the Galactic background emission which increases towards the Galactic plane. On the other hand, the angular size of the remnants must be several times the resolution of the observations (Green, 1991, 1996). The low number of young SNRs can be explained due to expansion of the remnant in a low density region and consequently the low sensitivity of radio observatories and/or the large distant of these young SNRs lead to a low surface brightness. Old faint remnants, however, suffer from low surface brightness as the ejected material finally merges with the surroundings. Observations suggest that objects older than $\sim 50\,000$ years are not detectable with the current radio telescopes. Statistical studies of the distribution of Galactic SNRs suffer mainly from the Σ -selection effect which depends on Galactic coordinates and makes it difficult to distinguish this bias from intrinsic variation in the properties of SNRs with Galactic coordinates. Most of the 231 SNRs (Green, 2002) have been detected in the 2nd and 3rd quadrants ($90^\circ \geq l \geq 270^\circ$), because they are outside the Solar circle at large galactocentric radii and therefore do not suffer from high Galactic background emission (Fig. 3.3). An investigation of the radio surface brightness shows that there are many more faint remnants identified in the 2nd and 3rd quadrants than in either the 1st or the 4th quadrants (Green, 1991). Nevertheless, it is still unclear if this is a true excess or if it is the l -dependent Σ -selection effect.

In X-rays, the galactic absorption, mainly caused by photoelectric absorption of hydrogen, limits the view to objects which are located in the Galactic plane. Taking the interstellar photoelectric absorption into account, a useful approximation of the optical depth τ_x is given (Longair, 1994):

$$\tau_x \approx 2 \cdot 10^{-22} \left(\frac{h\nu}{1 \text{ keV}} \right)^{-8/3} \int N_H dl \quad (3.17)$$

where $\int N_H dl$ is the column depth, expressed in hydrogen atoms per square centimeter and $h\nu$ the energy of the X-ray photons in units of keV. The energy band of ROSAT (0.1-2.4 keV) therefore allows the detection of SNRs for an interstellar absorption which is below $\sim 3 \cdot 10^{22} \text{ cm}^{-2}$ (Aschenbach, 1996).

Previously, Ilovaisky & Lequeux (1972) used a derived luminosity distribution to correct for selection effects and suggested a flat SNR distribution out to 8 kpc and a sharp cutoff beyond 10 kpc. Recent observations have yielded radial SNR distributions

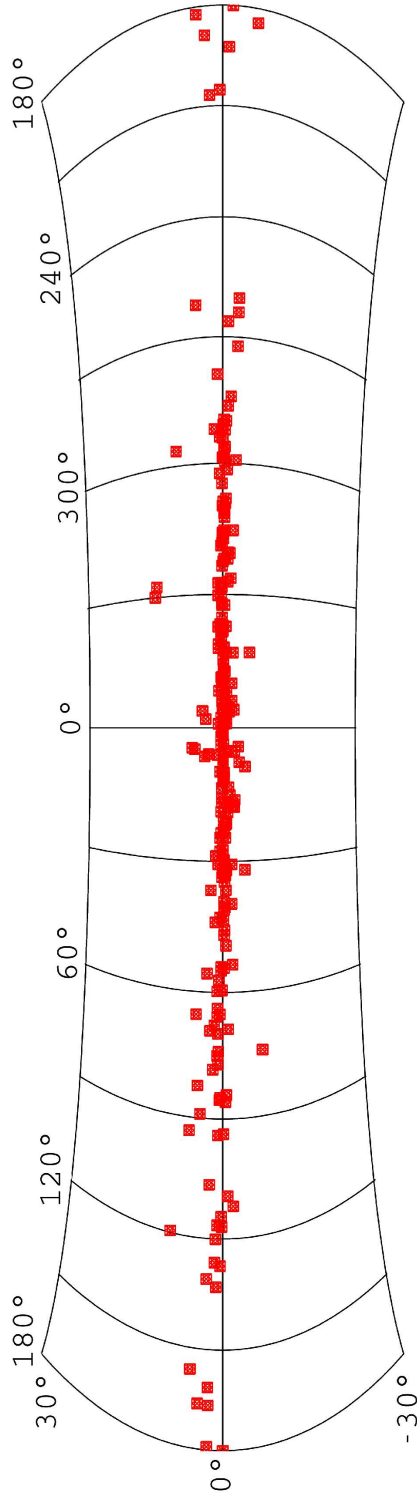


Figure 3.3: Distribution of the 231 Galactic SNRs across the sky (Green, 2001). The image is an Aitoff-Hammer projection in Galactic coordinates and show a strong concentration of SNRs towards the Galactic Plane as well as the Galactic Center.

peaked at small galactic radii (~ 5 kpc; Kodaira (1974)) or uniform concentration between $55^\circ \leq l \leq 345^\circ$ within a nuclear disk with $R=6.5$ kpc (van den Bergh, 1988), respectively. Analysing catalogs of SNRs, van den Bergh (1988) noted that SNRs are strongly concentrated to the Galactic plane with all remnants having $|b| \leq 15^\circ$ (corresponding to $|z_{max}| \sim 2.1$ kpc at an assumed distance of 8 kpc to the Galactic nucleus, Fig. 3.3).

Using the corrected distances from a sample of 36 SNRs and a new Σ -D relation, a modified galactic SNR distribution could be derived which peaks at ~ 5 kpc and has a scale length of ~ 7.0 kpc (Case & Bhattacharya, 1998).

3.4 Compact Objects Within Supernova Remnants

3.4.1 Young Neutron Stars

X-ray observations facilitate the search for SNRs as well as compact objects that may reside within them. Young radio pulsars can be divided in two groups according to their X-ray emission, i.e. the Crab-like and Vela-like pulsars. The radio-quiet neutron stars include anomalous X-ray pulsars (AXP), soft gamma-ray repeaters and quiescent neutron star candidates.

Crab-like pulsars are young rotation-powered pulsars whose radiation comes from charged particles accelerated in the neutron star magnetosphere travelling along the curved magnetic lines. The radiation of the Crab pulsar is characterized by a power law spectrum and shows two pulses per period. The Crab is also a bright optical, UV and gamma-ray source, covering at least 49 octaves in wavelength. Its pulsations from radio to gamma-rays are all phase-aligned (Becker & Pavlov, 2001), indicating that the emission in all frequencies has the same origin in the pulsar magnetosphere. The photon index of the pulsar spectrum slowly increase with energy, varying from $\alpha=1.1$ at $E \sim 1$ eV to $\alpha=2.1$ at $E \sim 10^{10}$ eV.

In X-rays, pulsars (PSR) with spin-down ages of $\sim 10^4 - 10^5$ years are often referred to as Vela-like pulsars, because of their similar emission properties. They differ from the Crab-like pulsars in the shape of the high energy spectra and their very faint optical emission. In addition, the pulses at different energies are not phase-aligned with each other (Becker & Pavlov, 2001). The soft X-ray spectrum of the Vela pulsar also has a thermal component with a temperature of 10^6 K that is buried by the strong non-thermalemission in the Crab-like pulsars. The spatial structure of the Vela plerion, however, is similar to that of the Crab nebula, consisting of a torus-like structure, inner ring and jets. The Vela as well as the Crab pulsar show that the direction of proper motion is remarkably close to the projected X-ray symmetry axis of the nebula and polar jet structures (Helfand et al., 2001). Spruit & Phinney (1998) suggested that the alignment of the rotation axes and direction of proper motion occurs from the kicks given to neutron stars when they are born.

Anomalous X-ray pulsars (AXPs) and soft gamma-ray repeaters (SGRs) are characterized by long periods in the range of $P=5-8$ s and very strong magnetic fields ($B \sim 10^{15}$ G). They are bright, quiescent X-ray sources with no infrared or optical

counterparts detected (Lorimer & Xilouris, 2000). Their typical X-ray luminosity is $L_x \sim 10^{34} - 10^{36} \text{ erg s}^{-1}$. The difference between both types of objects is that SGRs show soft gamma ray bursts in contrast to the AXPs (Zhang et al., 2000). The spectrum of the SRGs can be described by a powerlaw plus blackbody model, whereas the photon index range from $\alpha = 1-4$. The blackbody component can be characterized as thermal emission from the neutron star surface with an emitting area that is two orders of magnitude smaller than the neutron star surface area. Besides radio pulsars, it is believed that SGRs and AXPs are also associated with young SNRs, indicating an age of $10^3 - 10^4$ years (Gaensler et al., 2001).

3.5 Neutron Star - Supernova Remnant Association

PSR/SNR associations allow for constraints on remnant distance, age and the explanation of unusual remnant morphology or evolution. From the PSR point of view, the associations can prove the hypothesis of Baade & Zwicky (1934) and constrain the spin periods, luminosities, beaming fractions and space velocities of neutron stars as well as ages.

Most of the SN Ib/c and II are expected to form a neutron star (cf. 3.2.1 and 3.2.2). Therefore it is quite remarkable that, despite many radio searches, only a few of the 231 SNRs have yielded a neutron star candidate. As for SNRs, there are also selection effects that hamper radio searches for young neutron stars in them. There are mainly three factors which leave an incomplete and biased sample of neutron stars in SNRs (Johnston, 1994). First, the beaming fraction of young pulsars remains unknown; second, the luminosity function of pulsars is not well understood and third, the effects of interstellar scattering, mainly along the Galactic plane, lead to pulse broadening and loss of sensitivity concerning mainly the fast-spinning pulsars.

Kaspi (1996) proposed five criteria to evaluate PSR/SNR associations:

- Agreement on independent distance estimates of pulsars and SNRs
- Agreement on independent age estimates of pulsars and SNRs
- Reasonable transverse velocities of pulsars with respect to their birth places
- Evidence for any interaction between the pulsar and SNR (e.g. pulsar-driven nebula)
- Direction of the proper motion vector

There are only about a dozen cases in which such PSR/SNR associations can be seriously claimed (Kaspi, 1998). Proper motion measurements are crucial and allow one to disprove an association regardless the other criteria. Regarding the most secure associations, there is clear evidence that pulsars are born with large magnetic fields and short periods (Taylor et al., 1993). A large displacement of a neutron star from the geometrical center of the associated SNR, however, does not mean that the neutron star is moving with high transverse velocity (Gvaramadze, 2001). This could be explained,

if massive stars are fast enough to cross the wind-driven bubbles created during the main-sequence stage of their evolution, resulting in a significant offset of the SN explosion site from the center of the wind-driven bubble. X-ray observations of young SNRs could help to partly resolve this mystery, revealing X-ray bright, but radio-quiet compact objects at their centers (Gotthelf, 1998). Some of these sources have been found to be slowly rotating pulsars and are referred to as AXPs. There are currently more known slowly rotating, radio-quiet X-ray pulsars in the centers of SNRs than confirmed Crab-like radio pulsars. The enormous magnetic fields which have been postulated for these slow pulsars (Thompson & Duncan, 1995, 1996) could provide an explanation for their radio-quiet nature. Baring & Harding (1998) have proposed that such pulsars are radio-quiet, because of the suppression of electron-positron pair production in the magnetosphere by high magnetic fields ($\sim 10^{14} - 10^{16}$ G).

Chapter 4

X-ray Observatories and Radio Telescopes

The identification campaign of SNR candidates was performed with X-ray data from the huge archive of the ROSAT all-sky survey (RASS) and pointed observations. Follow-up observations of these candidates have been performed in X-rays with the Chandra observatory as well as in radio with the Effelsberg 100-m telescope in Germany and the radio interferometer ATCA (**A**ustralia **T**elescope **C**ompact **A**rray) in Australia. The three SNRs RCW 103, G 21.5-0.9 and G 65.3+5.7 have been studied with X-ray data from XMM-Newton and ROSAT, respectively.

The following sections give an overview on the ROSAT all-sky survey (RASS) and the two recently launched X-ray observatories, Chandra and XMM-Newton, focusing their individual advantages. Finally, a short introduction is given to radio observations with single dish and interferometric telescopes.

4.1 X-ray Observatories

4.1.1 ROSAT

On June 1, 1990 the X-ray observatory ROSAT (Truemper, 1982) was launched from Cape Canaveral and started its mission which lasted nearly eight years (Figure 4.1). ROSAT was equipped with an imaging X-ray telescope with a focal length of 2.4 m that covered the energy range from 0.1 to 2.4 keV (Aschenbach, 1987). Two redundant **P**osition **S**ensitive **P**roportional **C**ounters (PSPC_B and PSPC_C) with moderate energy resolution (Pfeffermann & Briel, 1986) and the **H**igh **R**esolution **I**mager (HRI) with high spatial but no energy resolution (Pfeffermann et al., 1987) were located in the focal plane of the telescope. Besides the X-ray telescope and detectors, ROSAT carried the **W**ide-**F**ield **C**amera (WFC) for observations in the extreme ultraviolet (0.017-0.2 keV).

Position Sensitive Proportional Counter (PSPC)

The PSPC_B (Pfeffermann & Briel, 1986) was chosen as the primary detector of the ROSAT mission and was used for the Performance-Verification and Calibration Phase

in the beginning and subsequently to perform the major part of the ROSAT all-sky survey (RASS). On January 25, 1991 the PSPC_B was destroyed by a pointing towards the Sun that was caused by an error in the Attitude and Control system. Hence, the following observations have been carried out with PSPC_C.

The functionality of the PSPC is based on the principle of a multiwire proportional counter that consists of a gas-filled chamber with gold plated wires as anodes and platinum iridium wires as cathodes. As an X-ray photon enters the detector, it is photo-electrically absorbed by the gas, producing a certain number of primary electrons which depends on the initial energy of the X-ray photon. These electrons will drift to the anodes where they gain kinetic energy and thus form a secondary electron cloud. The mean energy that is required to create a secondary electron is approximately constant over the energy range of the PSPC, and the number of electrons within the secondary electron cloud is approximately proportional to the energy of the incoming X-ray photon. This secondary electron cloud drift through the cathode grid towards the anode grid and causes another avalanche of charged particles. This avalanche of charge leads to a charge pulse at the anode and an induced signal at the cathodes, which are all registered by a charge-sensitive preamplifier. These signals allow for the determination of the position of the charge clouds and thus the position of the primary X-ray photon in the sky. The spectral information arises from the signals of the entire anode grid.

The PSPC provided modest energy resolution ($\Delta E/E=0.43 (E[\text{keV}]/0.93)^{-0.5}$) and a field-of-view (FOV) of 2° . The spatial resolution was about $25''$ FWHM.

High Resolution Imager (HRI)

The other instrument on board of ROSAT was the HRI which was very similar to the Einstein Observatory HRI and comprised of two cascaded microchannel plates (MCPs) with a crossed grid position readout system (Pfeffermann et al., 1987). The HRI provided a field-of-view of $38'$, and a spatial resolution of about $6'' - 8''$ (FWHM). The HRI had negligible energy resolution but provided relative time resolution down to 61 microseconds.

ROSAT all-sky survey (RASS)

As the primary objective ROSAT has performed the first all-sky survey with an imaging telescope in the soft X-ray band from 0.1 keV to 2.4 keV (Fig. 4.2). The main part of the RASS was carried out in 1990 and 1991 with the PSPC as the focal instrument and with ROSAT in scan mode. A small fraction of the sky remained with little or no exposure after the main RASS. In February 1997 the PSPC was switched on for 4 weeks after a period of 2.5 years in order to perform a number of important observations and to complete the RASS. Having mapped almost the whole sky, the observations had to be performed in the pointed mode using the PSPC as well as the HRI (High resolution Imager). The basic survey strategy of ROSAT was to scan the sky in great circles whose planes were oriented roughly perpendicular to the solar direction. The exposure times varied between ~ 400 s and 40,000 s in the ecliptic plane

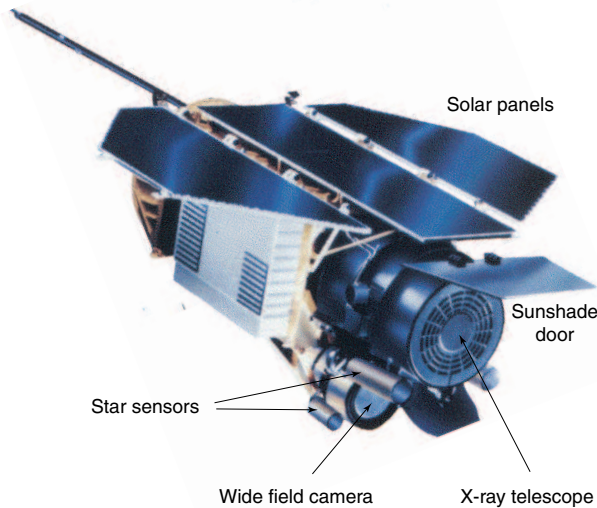


Figure 4.1: Artist view of the ROSAT observatory (courtesy NASA).

and poles, respectively. During the passages through the auroral zones and the South Atlantic Anomaly the PSPC had to be switched off, leading to a decrease of exposure time over certain parts of the sky. The first processing of the RASS (RASS-I) took place in 1991-1993 which was performed with the standard analysis software system (SASS). The processing was performed for strips of $2^\circ \times 360^\circ$ selecting contaminated data. The spatial resolution of the RASS is about a factor 4 lower than on-axis PSPC observations in the pointed mode, because the sources were not always in the centre of the field-of-view, where the detector had the best spatial resolution, as in pointed on-axis observations. Therefore the average spatial resolution in scan mode was $\sim 96''$, with a limiting survey sensitivity of $f_x \sim 5 \times 10^{-13} \text{ erg cm}^{-2} \text{ s}^{-1}$ (Voges, 1994).

In the following years, the RASS-II processing was carried out with the photons not collected in strips but merged in sky-fields with a size of $6.4^\circ \times 6.4^\circ$. A stricter selection of the data was performed to reduce the number of sources with erroneous position and morphology leaving behind voids and holes in the data. The subsequent RASS-III processing did not have such restricted selection criteria than the RASS-II processing in order to avoid the selection of too much data but still leaving voids and holes. The public RASS data were processed with the RASS-III processing¹. In order to retrieve the RASS-III data from the public archive, the RASS field(s) has/have to be selected first where the source of interest is located using an MPE tool that is implemented under <http://www.xray.mpe.mpg.de/cgi-bin/rosat/rass-fields>. Then the dataset of the specific sky field can be retrieved under <ftp://ftp.xray.mpe.mpg.de/rosat/archive/900000/>.

¹RASS-I and RASS-II data are not public domain

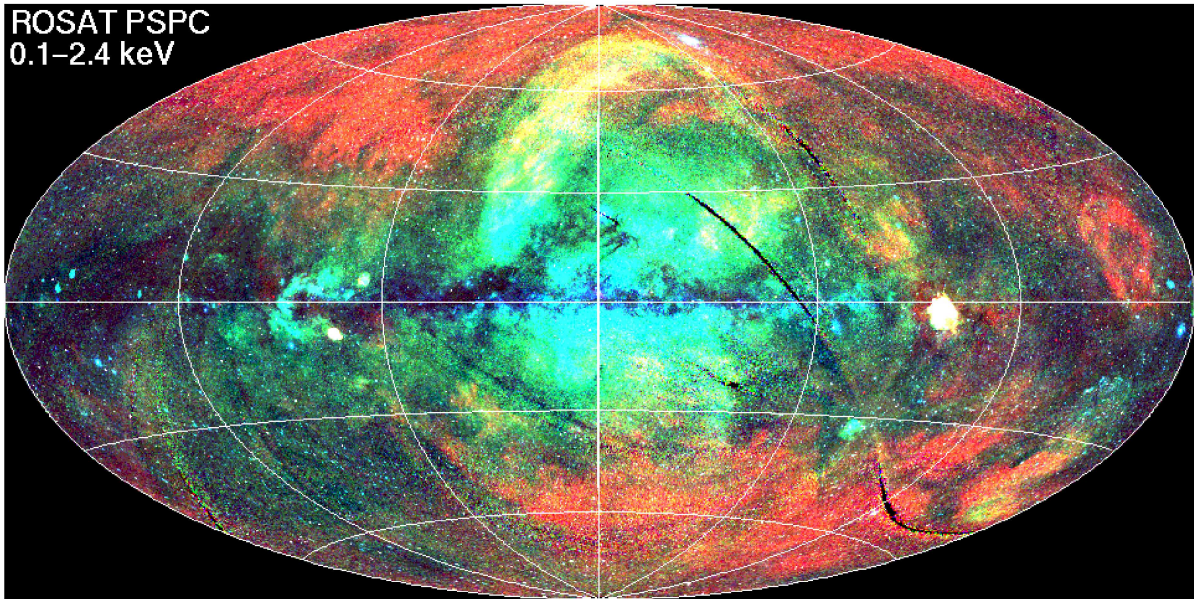


Figure 4.2: The distribution of diffuse X-ray emission across the sky, obtained from the ROSAT Survey. The low energy (0.1-0.4 keV) X-ray emission is presented by red, the intermediate energies (0.5 - 0.9 keV) by yellow-green and the high-energy radiation (0.9 - 2 keV) by blue colors. The image is an Aitoff-Hammer equal-area projection in Galactic coordinates with the Galactic centre at the origin and longitude increasing to the left (Voges, 1993).

4.1.2 The Chandra Mission

The Chandra X-ray observatory (AXAF²) was launched on July 23, 1999 by the space shuttle Columbia and later placed in its highly elliptical orbit of $\sim 140,000$ km apogee and $\sim 10,000$ km perigee yielding a high observing efficiency. The fraction of the sky that is occulted by the earth and the fraction of time when the detector background is high while dipping the Earth's radiation belts is small during most of the orbital periods. The Chandra spacecraft carries a high resolution four-nested mirror, two imaging detectors (ACIS and HRC), and two sets of transmission gratings (Fig. 4.3). Important Chandra features are: an order of magnitude improvement in spatial resolution (sub-arcsecond imaging) compared to previous X-ray observatories, good sensitivity from 0.1 to 10 keV, and the capability for high spectral resolution observations over most of the available energy range (Weisskopf et al., 2000).

High-Resolution Mirror Assembly (HRMA)

The HRMA consists of four nested grazing-incidence X-ray mirror pairs in the Wolter Type-I configuration (van Speybroeck, 1997). The front mirror of each pair is a

²AXAF was the former name for Chandra and renamed after the launch

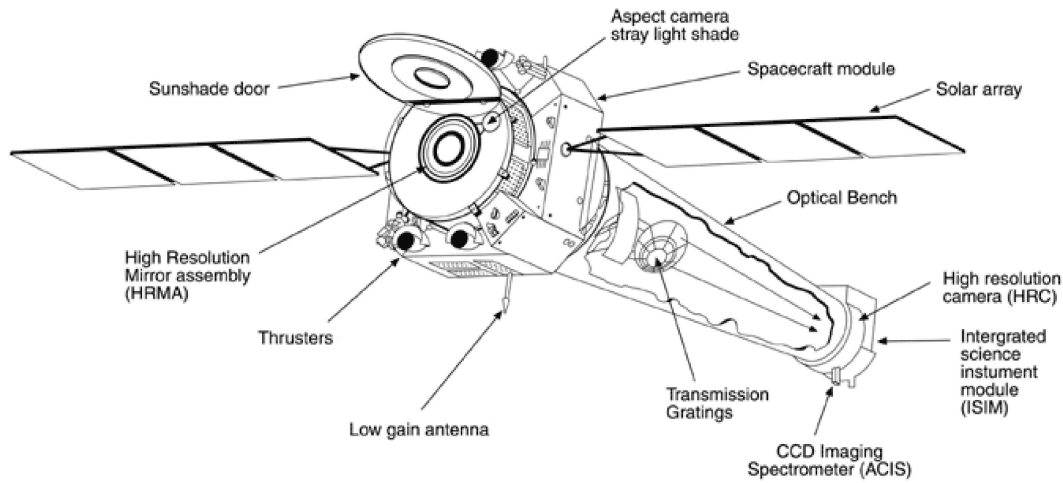


Figure 4.3: View of the Chandra observatory (courtesy NASA). The X-ray telescope consists of four nested grazing-incidence mirror followed by transmission gratings in the optical path. The detectors are situated in at the prime focus.

paraboloid and the back a hyperboloid in order to correct for aberration. A detailed overview on X-ray telescopes in general is given by Aschenbach (1985). The mirror pairs are made of Zerodur glass and coated with iridium. Their diameters range from about 0.65 m to 1.23 m. The focal length is ~ 10 m.

Advanced CCD Imaging Spectrometer (ACIS)

The ACIS offers the capability of high-resolution images and moderate resolution spectra (Garmire, 1997). It contains ten 1024×1024 pixel CCDs, four of which are arranged in a 2×2 array (ACIS-I) used for imaging, and six of which are arranged in a 1×6 array (ACIS-S) used either for imaging or as a readout of the gratings (Fig. 4.4). The two CCDs S1 and S3 are back-illuminated (BI) with the back side facing the HRMA, and the remaining eight are front-illuminated (FI) and have the gate structure facing the incident X-ray beam. Any combination of up to six CCDs can operate simultaneously. The field-of-view is $\sim 16.9' \times 16.9'$ for the ACIS-I array, which is comprised of four CCDs arranged in a square and $8.3' \times 50.6'$ for ACIS-S array, which is comprised of six CCDs lined up in a 1×6 configuration. In the full-frame mode the read-out time is 3.2 s, which can cause pile-up (i.e. when two or more photons are detected in the same pixel at the same time causing a single event) during observations of bright X-ray sources. Selecting subarrays (i.e. restricting the region of the CCD in which the data will be taken) yields a lower frame time and therefore also a lower pile-up ratio. Finally the continuous clocking mode provides a 3 ms timing which allows the investigation of very short time variability, obtaining $1 \text{ pixel} \times 1024 \text{ pixel}$ images. The point-source sensitivity in a 10 ks observation is $4 \times 10^{-15} \text{ ergs cm}^{-2} \text{ s}^{-1}$ in the (0.4-6.0) keV band.

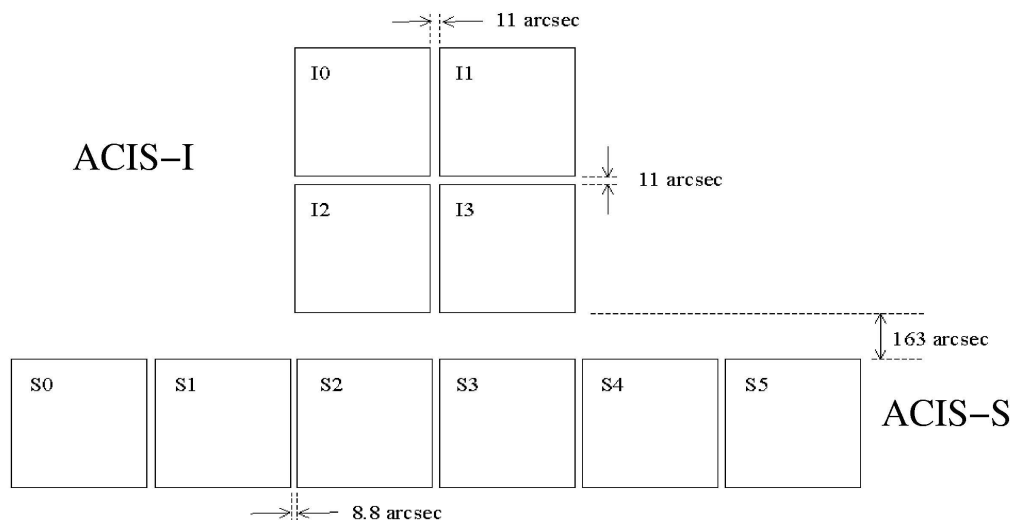


Figure 4.4: View of the ACIS array on board Chandra (courtesy Chandra X-ray Center). The ACIS-I configuration consists of four chips which are arranged in a 2×2 array and another two chips which belongs to the 1×6 array. The ACIS-S consists of six chips which are arranged in the 1×6 array. The CCDs S1 and S3 are back-illuminated.

High Resolution Camera (HRC)

The HRC is a microchannel plate instrument and in its functionality similar to the ROSAT HRI (Kenter et al., 1994). The HRC consists of two detectors, one optimized for imaging (HRC-I), and the other (HRC-S) serves as a readout for the Low Energy Transmission Grating (LETG). Nominally the HRC detectors should provide the best time resolution of about $16 \mu\text{s}$. A wiring error in the detector causes the time of an event not to be associated with that event but with the following event, which may or may not be telemetered. The result is an error in HRC event timing such that the accuracy is degraded from about $16 \mu\text{s}$ to about 4 ms. The HRC-S provides the largest field-of-view ($\sim 30' \times 30'$) on the observatory. Its spatial resolution achieves the subarcsecond range at about $0.4''$ (FWHM).

Low and High Energy Transmission Gratings (LETG/HETG)

The LETG provides high resolution spectroscopy ($E/\Delta E \geq 1000$) in the energy range 0.07-0.15 keV and lower resolving power for shorter wavelength. The HRC-S is the primary detector designed for use with the LETG.

The HETG is designed to provide high resolution spectroscopy at shorter wavelength (0.4-10.0 keV) with a resolution $E/\Delta E$ up to 1000. HETG is used in conjunction with the ACIS-S.

4.1.3 The XMM-Newton mission

XMM-Newton was launched on 10 December, 1999 on an Ariane-V and placed in a highly eccentric orbit of $\sim 114,000$ km apogee and $\sim 7,000$ km perigee, which is comparable to Chandra's. This implies the realization of uninterrupted exposures of about 65 ks. XMM-Newton carries three X-ray telescopes, which consist of 58 Wolter I mirrors leading to a large collecting area. At the prime focus of each of the telescopes is one of the three European Photon Imaging Cameras (EPIC), namely the EPIC-PN and two EPIC-MOS. For a complementary analysis of the spectrum, a grating structure on two mirror modules (den Herder et al., 2001) reflects about half of the incoming X-rays to a secondary focus, with its own CCD camera. An optical/UV monitor can simultaneously observe the same regions as the X-ray telescopes (Mason et al., 2001). Figure 4.5 shows a view of XMM-Newton. An overview of the XMM-Newton observatory is given by Jansen et al. (2001).

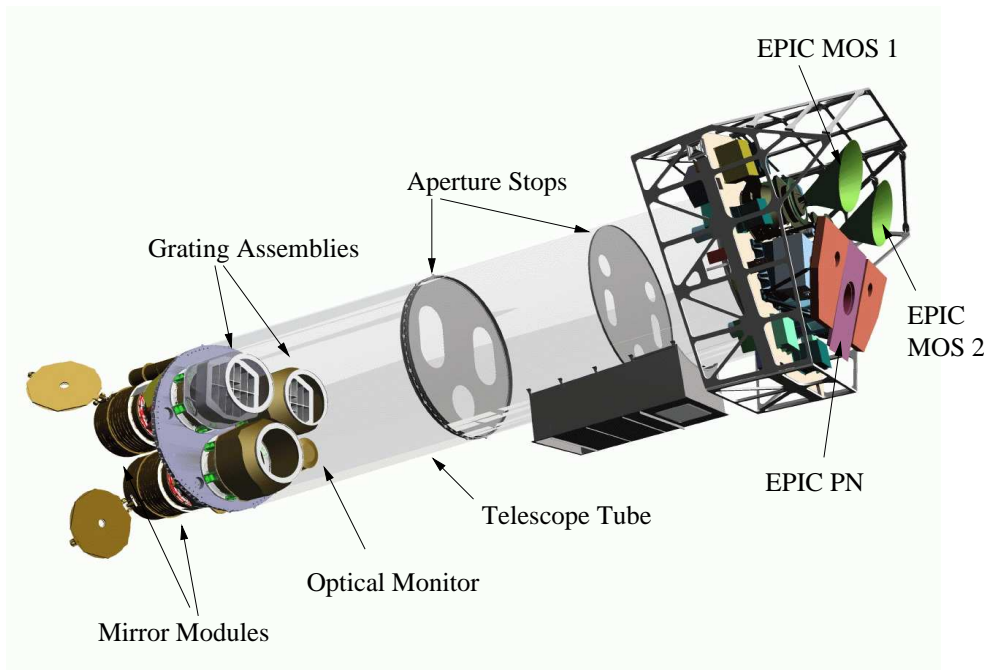


Figure 4.5: View of the XMM-Newton observatory with its three mirror modules, the gratings and the EPIC MOS and PN cameras at the prime focus (Jansen et al., 2001)

EPIC-PN camera

The EPIC-PN camera consists of 12 individually operating 3×1 cm² pn CCDs on a single wafer covering the energy band with high detection efficiency up to 15 keV (Strüder et al., 2001).

X-rays hit the detector from the back side and generate electrons and holes which

are separated by a strong electric field before they recombine. The electrons drift to the potential minimum and are stored under the transfer registers. They can be transferred towards the readout nodes, conserving the local charge distribution patterns from the former ionization process. The positively charged holes move to the negative back side where they are absorbed. Each CCD line has its own readout amplifier. Four individual quadrants, which consist of three pn CCD subunits, are operated in parallel (Fig. 4.6). In order to avoid an overlap of an X-ray photon with another in time and

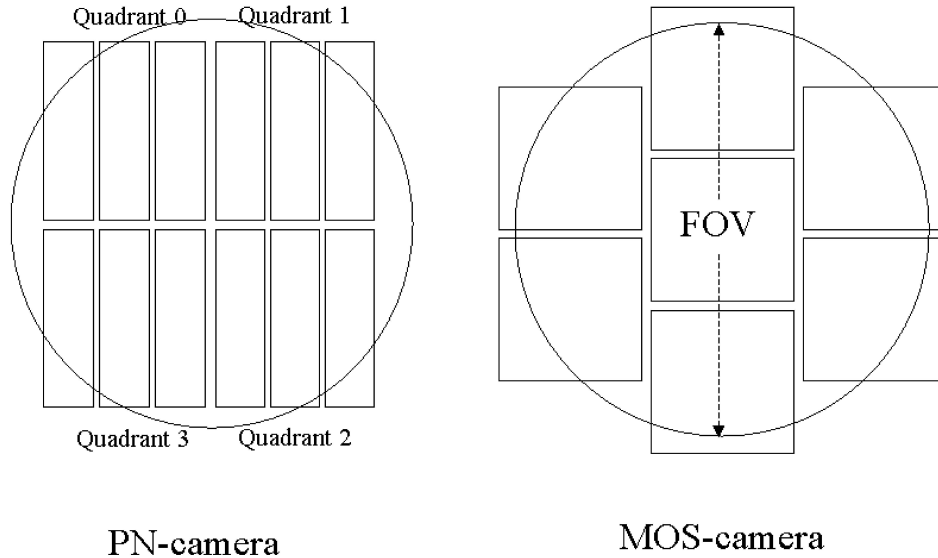


Figure 4.6: View of the EPIC PN- and MOS chips. The circle shows the field-of-view on the CCD devices (Jansen et al., 2001).

position on the detector, the X-ray camera read out mode can be adopted to the point source brightness. This can be achieved by shortening the integration time of the CCD camera by reducing the area to be read out. Five read out modes can be chosen.

The **full frame mode** includes a complete readout cycle which takes 73.3 ms for one individual CCD sub-unit. Within that time, 4.6 ms are needed for the readout itself leading to 6.2% so-called out-of-times events (i.e. events which hit the detector during readout and therefore are not recorded). In the **extended full frame mode** the integration time is 199.2 ms with again 4.6 ms readout, leading to 2.3% of out-of-time events. The extended full frame mode is ideal for the observation of extended objects. The **large window mode** uses only the inner half of the CCD for imaging, leading to a faster electron transfer towards the readout nodes. In this case, the time resolution is lowered to 47.7 ms and the number of out-of-time events is lower than 0.2%. The **small window mode** achieves a time resolution of 5.7 ms and a out-of-time event contribution of 1.1%, reducing the field-of-view to $4.4' \times 4.4'$ and operating only in one quadrant. CCD0 in quadrant 1 allows operation in the fast mode. The **timing mode** forms micro-pixels of 10×1 pixels. The position resolution is maintained

only in one dimension while the other 10 pixels are integrated along a column on the readout node. The time resolution then is 30 μ s. Finally the **burst mode** rapidly transfers 179 pixels and then reads out the content of CCD0 in the conventional way, resulting in a time resolution of 7 μ s (Strüder et al., 2001). The burst mode allows for observation of very strong sources up to 60,000 counts per second in the PSF (**P**oint **S**pread **F**unction). The duty cycle (life time) in this mode, however, is only 3%.

EPIC-MOS Camera

Each MOS camera consists of seven CCDs (Holland et al., 1996). The central CCD is at the focal point on the optical axis of the telescope while the outer six CCDs are stepped towards the mirror by 4.5 mm in order to follow the focal plane curvature. The design of the seven CCDs lead to an improvement of the focus for off-axis sources. The CCDs have a high quantum efficiency in the energy range 0.2-10.0 keV and cover a region of 28.4' diameter in the sky (Fig. 4.6). The basic readout speed of the MOS-CCDs is 2.6 s. In order to reduce the readout time the window mode can be applied to the central CCD. A window is defined on the CCD and rows and pixels outside this window are discarded on readout. There are two window sizes available, the small and the large window mode leading to 0.3 s and 0.9 s integration time, respectively. In the timing mode, 100 rows in the central window are compressed into one dimension, parallel to the CCD readout register. This mode gives a timing resolution of 1.75 ms per row. The choice of mode depends on the extent of the source and its brightness. The EPIC cameras are equipped with four light and UV blocking filters which should be used when a bright optical source is located in the field-of-view (Turner et al., 2001).

Table 4.1 gives an overview of the X-ray observatories ROSAT, Chandra and XMM-Newton and shows their individual power and characteristics. Figure 4.7 illustrates the different effective area of the discussed X-ray observatories.

Mirror Characteristic	ROSAT ¹	Chandra ²	XMM-Newton ³
Aperture diameter [cm]	83	120	70 (1 module)
Number of nested mirrors	4	4	58
Field of view [arcmin]	114	17	30
Unobscured geometric area [cm ⁻²]	1 140	1 145	6 000 (3 modules)
Focal length [m]	2.4	10.0	7.5
Energy resolution at 1 keV [eV]	500	56	55
Highest energy focused [keV]	2.4	10.0	12.0
On axis resolution [arcsec]	15	0.5	15

Table 4.1: Comparison of the X-ray observatories ROSAT, Chandra and XMM-Newton (¹ ROSAT PSPC, ² Chandra ACIS-I front, ³ EPIC MOS)

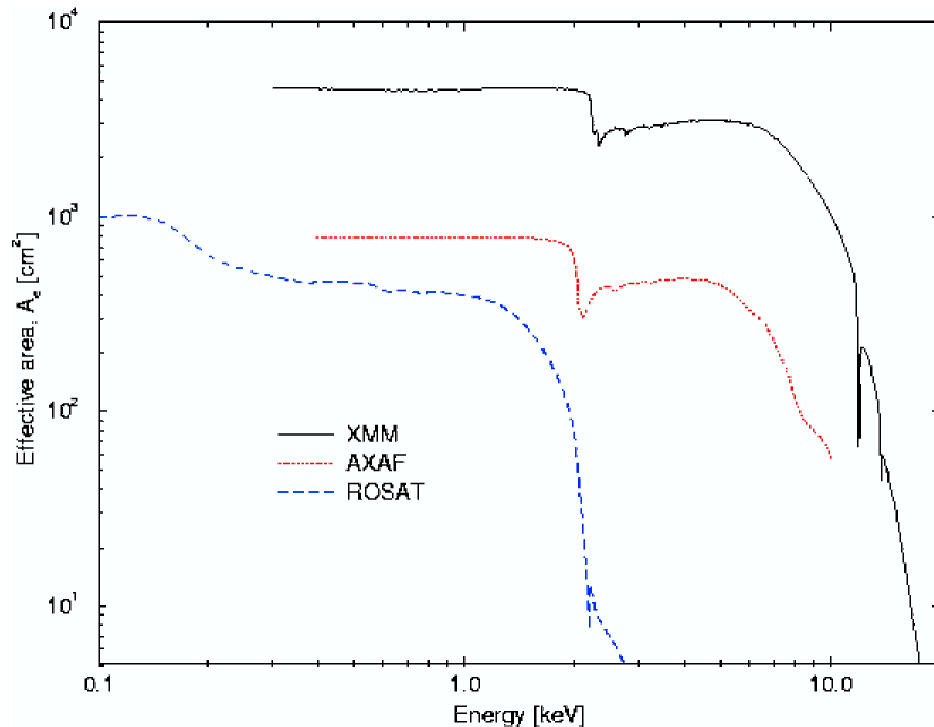


Figure 4.7: Energy dependent effective area of ROSAT (blue), Chandra (AXAF) (red) and XMM-Newton (black). The figure clearly shows the greater effective area and extended energy range of XMM-Newton compared to ROSAT and even Chandra (courtesy NASA).

4.2 Radio telescopes

Radio observations are performed from ground-based observatories, because they do not suffer from absorption in the terrestrial atmosphere. The radio window extends roughly from ~ 15 MHz to ~ 600 GHz depending on the geographical position and time. At the lower frequency limit the atmosphere ceases to be transparent because of absorption and reflection of radio waves in the ionosphere due to an electron-ion plasma. The high-frequency cut-off is related to the lowest rotation bands of molecules in the troposphere, mainly water vapor and oxygen. Nevertheless for the cm and mm wavelengths, and especially in the submillimeter range, tropospheric absorption has to be taken into account. Clouds of water vapor absorb and scatter radio waves even at frequencies as low as 6 GHz.

The state of polarized electromagnetic waves, which originate e.g. from synchrotron emission processes, is usually described by the Stokes parameters I , Q , U and V in a general way. The Stokes parameters are always non-negative, where I measures the total intensity of the radiation, Q and U together measure the linearly polarized intensity and V measures the circularly polarized intensity. For a partially polarized wave, the degree of polarization is

$$p = \frac{\sqrt{Q^2 + U^2 + V^2}}{I} \quad (4.1)$$

In contrast to X-rays, which are well described as photons, radio emission is treated as electromagnetic waves, which has consequences for the receiving of and detecting the radiation particularly in radio interferometry.

A single-dish radio telescope is usually an antenna with a parabolic shape that collects the radio waves from the celestial object and focuses them onto a sensitive radio receiver. Radio telescopes should have a large collecting area in order to make the beam pattern as small as possible (i.e. to achieve a high angular resolution), and to be sensitive to low flux radio sources. In order to resolve an image (i.e. produce a sharp image), the diameter of a telescope must be many times greater than the wavelength of the radiation it detects.

Using two or more separate radio telescopes and combining the signals they receive simultaneously from the same source allows for the detection of more detailed structures of radio sources (Fig. 4.8). This observation technique is called interferometry measuring the phase as well as the intensity of the radio waves. The radio waves from the same object reach the separated telescopes at slightly different times. These differences are correlated by computers, producing a composite signal. The maximum spacing of the separated radio telescopes determines the spatial resolution of the overall telescope array. The angular resolution of a radio telescope or an array of telescopes is $\delta \sim \lambda/D$ where δ is the smallest angular separation which two point sources can have in order to be recognized as separated objects, λ is the wavelength of the received radiation and D the diameter of a single-dish telescope or the maximum baseline of an interferometric telescope array. An array can yield images that reveal either large- or small-scale structure, using data from different sets of baselines. The study of large-scale structures, for example, requires lower resolution (i.e. more closely spaced radio antennas). The field-of-view is given by the observed wavelength ($\text{FOV} \sim \lambda$) and the diameter of the radio antenna ($\text{FOV} \sim 1/D$) but not by the individual spacing of antennas in interferometric arrays.

In radio interferometry, the observing plane that lies perpendicular to the direction from which the radiation is being received from the sky is called the u - v plane. In the simple case of two telescopes T_1 and T_2 separated by the distance \vec{d} , being sensitive only to radiation of the same state of polarization, an electromagnetic wave induces the voltage U_1 at the output of antenna T_1

$$U_1 \propto E \exp [i\omega t] \quad (4.2)$$

while at T_2

$$U_2 \propto E \exp [i\omega(t - \tau_d)] \quad (4.3)$$

where τ_d is the time delay caused by the relative orientation of the interferometer baseline \vec{d} with respect to the direction of the wave propagation. The measured correlation signal is then given by

$$R(\tau) \propto \frac{1}{2} E^2 \exp[i\omega\tau_d] \quad (4.4)$$

(i.e. the output signal varies periodically with the delay time τ_d). In the case of earth rotation, τ_d will vary and thus cause interference fringes as a function of time.

These interference fringes occur due to the coherence time $\tau_c \sim 1/\Delta\nu$ of the quasi-monochromatic radiation which can be larger or smaller than the delay time τ_d . The

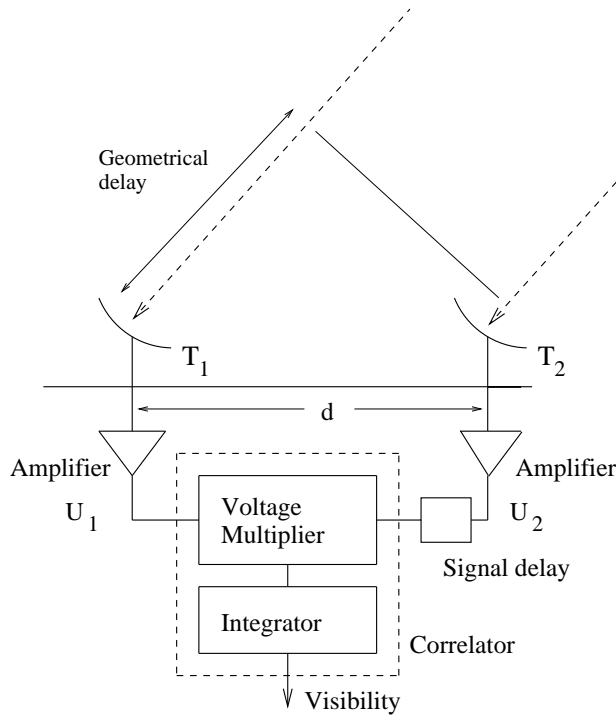


Figure 4.8: Schematic diagram of a two-element interferometer. The output of the telescopes T_1 and T_2 are U_1 and U_2 , respectively. Both outputs are first combined in the Voltage Multiplier and then integrated in the correlator. A signal delay after telescope T_2 is inserted so that the time delay between the radio telescopes is negligible. Thus, the loss of visibility can be avoided in the case of a large bandwidth which is desired to improve the sensitivity. For more details the lecture notes from Rohlfs & Wilson (1996) are recommended.

absolute value of the degree of coherence, the so-called visibility of the observed spatial interference fringes is measured with an interferometric telescope array. The visibility of an extended source is the sum of the visibilities of its components. The van Cittert-Zernike theorem gives a relation between the brightness distribution $I(x,y)$ and the complex visibility distribution $V(u,v)$ from a two-dimensional Fourier-transform:

$$I'(x, y) = A(x, y) I(x, y) = \int_{-\infty}^{+\infty} \int_{-\infty}^{+\infty} V(u, v) \exp[-i2\pi(ux + vy)] du dv \quad (4.5)$$

where $I'(x, y)$ is the intensity $I(x,y)$ as modified by the primary beam shape $A(x,y)$. If $V(u,v)$ is completely sampled, at least the Nyquist rate, the source brightness distribution $I'(x, y)$ can be recovered (Rohlfs & Wilson, 1996).

4.2.1 Effelsberg 100-m radio telescope

The Effelsberg 100-meter Radio Telescope is one of the world's two largest fully steerable instruments located near Bonn, Germany covering the northern sky down to a declination of -20° (Fig. 4.9). The radio telescope rotates on a circular track of 64 m in diameter, which rests on a solid concrete foundation. Within about 12 minutes, the telescope can be turned through 360° horizontally, and the dish can be tipped by 90° in less than 6 minutes (Hachenberg, 1970). Thus, practically the whole sky above the horizon can be scanned. A general limitation on the performance of large aperture antennas is imposed by the deformation of the paraboloid due to gravity. As the elevation angle of the telescope changes, the curve of the antenna will deform, degrading the antenna pattern. In the case of the Effelsberg radio telescope this problem is solved using the principle of 'homologous deformation' (i.e. maintaining a paraboloid at all elevations (von Hoerner, 1975)). In this scheme, the mechanical design of the telescope ensures that as the elevation angle is varied, the reflector shape deforms from one paraboloid curve to another, and the focal length also changes. The change of the focal length can be adjusted by shifting the main reflector or detectors, respectively. The deviation is typically 0.5 mm from its ideal shape of a paraboloid at medium vertical inclination, allowing this extreme-precision antenna to operate in the wavelength band from 73 cm (408 MHz) up to 3 mm (86 GHz). The 100-m reflector has a very short focal length of 30 m. All detectors for wavelengths larger than 11 cm are located in the prime-focus whereas the detectors for smaller wavelengths ($\lambda \leq 11$ cm) are located in the secondary focus.

In this study, data at 21 cm, 11 cm and 6 cm are used, where the 21 cm and 11 cm data were taken from the Effelsberg surveys in the public domain, and the 6 cm data were obtained during a pointed observation campaign in July 2001. The angular resolution (HPBW) at 21 cm, 11 cm and 6 cm is $9.4'$, $4.3'$ and $2.4'$, respectively. Two galactic plane surveys were performed with the Effelsberg 100-m telescope at 21 cm (Reich et al., 1990b, 1997) and 11 cm (Reich et al., 1990a; Furst et al., 1990). The 21 cm survey covers the sky at $357^\circ \leq l \leq 240^\circ$ and $-4^\circ \leq b \leq +4^\circ/5^\circ$, and the 11 cm covers the sky at $358^\circ \leq l \leq 240^\circ$ and $|b| \leq 5$.

4.2.2 Australia Telescope Compact Array (ATCA)

The Australia Telescope Compact Array (ATCA) is an earth-rotation aperture synthesis radio interferometer (Fig. 4.9). It is located at Culgoora in New South Wales, Australia, covering a major part of the southern hemisphere. The ATCA is part of the Australia Telescope National Facility (ATNF), which also operates the Parkes and the Mopra Observatories as well as The Australian Long Baseline Array. For full twelve hour syntheses, the array is limited to sources with declinations north of about -25° . ATCA is an interferometric telescope array consisting of six radio antennas 22-m in diameter, equipped with 6/3 cm and 13/20 cm receivers (Frater et al., 1992). They are mounted along the main optical axis which allows polarisation measurements with very low instrumental polarisation ($\sim 1\%$). Five of the six antennas lie along a three kilometer railway track, which is oriented east-west. The sixth antenna lies on a 75-m

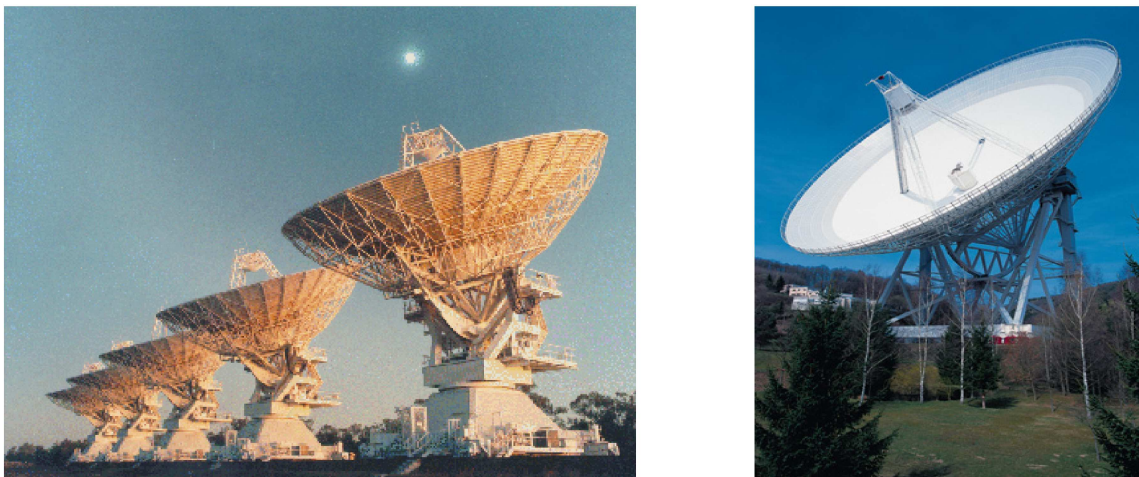


Figure 4.9: Left: Australia Telescope Compact Array (ATCA), Right: Effelsberg 100-m Telescope

rail-track three kilometers further west, thus allowing a maximum ATCA baseline of six kilometres. In total, 15 baselines are obtained from the six antennas leading to a good u - v coverage. Since data from the 20 cm and 13 cm observations were used, only the technical characteristics of these receivers are described in this section. The angular resolution (HPBW) of the primary beam, and therefore also the field-of-view, is $33'$ at 20 cm and $22'$ at 13 cm, and the 12 hour flux sensitivity at 20 cm is 0.022 mJy/beam and 0.029 mJy/beam at 13 cm.

4.2.3 The Galactic Radio and Optical Surveys

All data from the Galactic radio and optical surveys, described below are public domain and can be obtained via the world wide web.

NVSS

The NRAO/VLA (National Radio Astronomy Observatory/Very Large Array) is an interferometric radio array which is located on the plains of San Agustin near Socorro, New Mexico, USA. It consists of 27 radio antennas with a diameter of 25 m in a Y-shaped configuration. The antenna configuration in the survey mode had a maximum antenna spacing of 3.6 km and 1 km, to make 1.4 GHz continuum total intensity and linear polarization images, respectively. The NRAO/VLA Sky Survey (NVSS) covers the sky north of declination -40° . All images have a FWHM resolution of $45''$ and nearly uniform sensitivity (rms brightness fluctuations ≈ 0.5 mJy/beam and rms sensitivity of 2.5 mJy; Condon et al. (1998)). The NVSS is available at <http://www.cv.nrao.edu/nvss/postage.shtml>.

In comparison, the VLA high-resolution ($5''$ FWHM) 1.4 GHz survey, the so-called

FIRST survey, is optimized for faint compact radio sources and is therefore less sensitive to large-scale structures.

MOST

The Molonglo Observatory Synthesis Telescope (MOST) is located near Canberra, Australia and covers the sky south of declination -30° . The MOST consists of two cylindrical paraboloids, $778\text{ m} \times 12\text{ m}$, separated by 15 m and aligned in the east-west direction using rotational synthesis (Robertson, 1991). The observations were performed at 843 MHz with an rms sensitivity $\sim 1\text{-}2\text{ mJy/beam}$. The FWHM resolution of the synthesized beam is $43'' \times 43'' \cos \delta$ (R.A. \times Dec.) and the positional accuracy is about $1''$. The MOST Galactic Plane Survey (MGPS) covers the sky at $240^\circ \leq l \leq 365^\circ$ and $|b| \leq 10$ (Green, 1997). The MGPS is available at <http://www.astrop.physics.usyd.edu.au/MGPS/>.

PMN

The Parkes-MIT-NRAO (PMN) Survey was performed with the Parkes 64-m radio telescope, which is located approximately 365 km west of Sydney, Australia. The radio observatory is part of the ATNF. The principle institutions involved in the survey were the Parkes Radio Observatory, the Massachusetts Institute of Technology (MIT) and the National Radio Astronomy Observatory (NRAO). The southern sky was surveyed at a frequency of 4850 MHz between declinations of -87° and $+10^\circ$. The FWHM resolution is $4.2'$ with an rms sensitivity of 4.7 mJy (Griffith & Wright, 1993). The PMN survey is available at http://www.parkes.atnf.csiro.au/research_projects/surveys/surveys.html.

ESO Digitized Sky Survey

The ESO Digitized Sky Survey (DSS2) is an optical survey in the infrared, red and blue bands with different sky coverages. In this work optical data only from the DSS2-red survey were used, which covers about 98% of the whole sky (Lasker et al., 1998). The Digitized Sky Survey is a collection of (red) Schmidt plates (Palomar Sky Survey) that have been digitized. The plates for the southern data are from the SERC Southern Sky Survey and from the SERC J Equatorial extension. The DSS is available at <http://archive.eso.org/dss/dss>.

UKST/AAO $H\alpha$ Galactic Plane survey

The UK Schmidt Telescope (UKST) at the Anglo-Australian Observatory (AAO) have undertaken an $H\alpha$ survey ($6590 \pm 35\text{ \AA}$) of the Southern Galactic Plane (Parker et al., 1999). This survey covers the sky in the range of $-75^\circ \leq DEC \leq +2.5^\circ$ and Galactic latitude $|b| \leq 10^\circ$. This $H\alpha$ survey is available at <http://www-wfau.roe.ac.uk/~sss/>.

Instrument/survey	Frequency ν [GHz]	Sky Coverage
NVSS	1.4	north of -40°
MOST	0.843	south of -30°
PMN	4.85	-87° to $+10^\circ$
	Wavelength λ [\AA]	
ESO DSS2red	6500 ± 800	98% of the whole sky
UKST/AAO $H\alpha$	6590 ± 35	$-75^\circ \leq \delta \leq +2.5^\circ$ and $ b \leq 10^\circ$

Table 4.2: Summary of the Galactic radio and optical surveys giving the frequency range and sky coverage.

Chapter 5

Identification Campaign of SNR Candidates in the RASS

Currently, 231 Galactic SNRs are known and listed in the Catalogue of Galactic SNRs by Green (2002). Assuming a Galactic SN rate of about 2 SNe per century (Dragicevich et al., 1999) and an evolution time of thermal SNRs in the order of 7.5×10^5 years, about 15,000 SNRs are expected in our Galaxy. Due to the low sensitivity and poor spatial resolution of Galactic Plane surveys in searching for SNRs at X-ray, radio and optical wavelengths, a great deficit of SNRs seems to exist. This deficit can either be ascribed to selection effects in all wavelength bands or a different theory of SNe and the evolution of their diffuse remnants.

5.1 Analysis of the RASS Data

About 70% of the identified galactic SNRs have been discovered in the radio band (Green, 2002). Identified radio supernova remnants (SNRs) in the Galaxy, however, comprise an incomplete sample of the SNR population due to various selection effects (cf. 3.3). The ROSAT all-sky survey (RASS) offers another window for searching for SNRs in the Galaxy. Although this energy band is not free of selection effects (e.g. interstellar absorption, cf. equation 3.17) it provides important information on possible SNRs because of their strong X-ray emission from shock-heated gas. In X-rays, galactic SNRs are mainly identified by their size (larger than a few arcmin), morphology (shell-like, center-filled or irregular), and energy spectrum which is either characterized by thermal continuum and strong line emission (shell-like SNRs), non-thermal continuum without line emission in the case of Crab-like SNRs or a thermal shell and a synchrotron nebula in the case of composite SNRs (cf. 3.2.1). The resulting value of the interstellar absorption in a spectral fit allows the discrimination of galactic and extragalactic objects compared to the Galactic N_H in the direction of the appropriate object. But the relatively low exposure (\sim few hundred seconds) and the relative poor spatial resolution of the RASS data ($96''$), in most cases, do not allow for a quantitative spectral analysis of the SNR candidates (cf. 4.1.1). For this reason, only a qualitative study could be performed to discriminate between e.g. extragalactic

background objects, H II regions and SNR candidates.

Busser (1998) performed a search for extended (≥ 5 arcmin) X-ray sources in the RASS database at $b \leq \pm 15^\circ$. Looking over the RASS-I maps with the naked eye, Busser concentrated his attention on objects with typical morphologies of SNRs as shells, rings or arcs and found 454 of them. Correlating the data with extragalactic databases as well as catalogues of H II regions, clusters of stars and planetary nebula, about 373 objects were left as SNR candidates. Although a simulation could show that the number of SNR candidates is in agreement with the number of expected SNRs (Busser, 1998), no statement was made about the goodness of these candidates.

In order to restrict the number of SNR candidates a re-analysis of the archival RASS-I data was performed. Source properties of the SNRs candidates, like position, count rate, source extent in X-rays and the hardness ratio HR 1 and HR 2 (cf. A.1 and A.2) in the standard ROSAT soft, medium and hard bands (i.e. the hardness of emission in different energy bands) were determined. In the case of bright RASS sources, the hardness ratio is a useful tool to constrain spectral properties for various spectral models. All sources were correlated with the extragalactic database NED (**N**ASA **E**xtragalactic **D**atabase) which contains over 3.3 million unique objects with 4.2 million cross-identifications (Mazzarella et al., 2001) and SIMBAD which provides basic data, cross-identifications and bibliography for astronomical objects outside the solar system (Wenger et al., 2000). Thus, 59 candidates can probably be ascribed to extragalactic objects, i.e. clusters of galaxies, or X-ray bright stars in the Galaxy. In addition, the SNR candidates were correlated with radio databases like the Effelsberg Galactic Plane Surveys and NVSS for objects in the northern hemisphere as well as the PMN survey and the MOST Galactic Plane survey for objects in the southern hemisphere (cf. 4.2.3). The results from these correlations were of great importance because the presence of radio emission and hence the radio morphology could help to clarify the nature of the X-ray source. In the case of strong and extended radio emission the corresponding SNR candidates were selected for follow-up observations in the radio band. On the other hand radio point sources in the NVSS and MOST data indicate possible radio galaxies due to their high angular survey resolution. The existence of such extragalactic objects can only be confirmed by source correlation with NED and SIMBAD, respectively or the determination of the radio spectral indices.

The SNR candidates with an extent smaller than $30'$ were additionally correlated with the optical database DSS2red (cf. 4.2.3). The region of X-ray selected SNRs with a diameter of less than $10'$ have been inspected to determine if a bright optical source could hold as a counterpart of the X-ray emission or if strong H II regions are located nearby. The DSS2red, however, do not allow the detection of optical filaments. Optical filaments can only be observed using specific filters like an $H\alpha$ filter or filters in other prominent emission lines which are typically expected for SNRs (cf. 3.2.3). Therefore, optical data from the UKST/AAO $H\alpha$ survey were used in order to trace the SNR candidates in the optical band. For this reason, pointed observations of the SNR candidates in the northern hemisphere were also performed in the optical with a $H\alpha + [N II]$ filter using the 30 cm telescope at the Skinakas observatory in Crete. No

significant filaments could be detected at the location of the X-ray sources (F. Mavroumatakis, private communication).

Making use of the very large database of pointed ROSAT HRI and PSPC observations, a few SNR candidates which were situated in the field-of-view of such pointed observations could be investigated in more detail. The better spatial resolution (e.g. a pointed ROSAT HRI observation has 18 times higher angular resolution compared to the survey observation) and longer exposure times allow to resolve the X-ray morphology, as well as to extract a spectrum with higher photon statistics. The position of the smaller SNR candidates (extent less than $30'$) has also been correlated with the pointing directions of the archival data of Chandra, XMM-Newton, as well as past missions like ASCA¹ and the Einstein observatory². None of the candidates were located in the field-of-view of Chandra and XMM-Newton observations but four of them were found in the ASCA and Einstein data. Finally, a correlation with the Third EGRET catalog (3EG) (Hartman et al., 1999) which contains 271 high-energy gamma-ray sources (≥ 100 MeV) was performed. Seventy-four sources, out of this sample, with $b \leq \pm 10^\circ$, were unidentified. One of them was found in the field of a SNR candidate. EGRET is a telescope on board the Compton Gamma Ray Observatory. The field of view of EGRET extends $\sim 30^\circ$. The point spread function is energy dependent, having a FWHM of $\sim 6^\circ$ at 100 MeV within an 1σ confinement angle and smaller values at higher energies (0.5° at 5 GeV). In some cases, infrared databases were also used, especially at $60 \mu\text{m}$, estimating the ratio of $60 \mu\text{m}$ to 843 MHz flux densities (cf. 3.2.3).

The whole sample of SNR candidates was divided into four categories according to their size which allowed for a specific source analysis (Table 5.1). Source confusion is significant for those SNR candidates which have an extent less than $30'$. Targets

extent D [arcmin]	Number of sources
$5 \leq D \leq 30$	229
$30 \leq D \leq 60$	16
$60 \leq D \leq 120$	9
$120 \leq D$	18

Table 5.1: The number of RASS SNR candidates according to a specific size. Most candidates have an extend below $30'$. Only 30 are between $30'$ and 2° . Only 18 candidates have a size of more than 2° .

with an extent larger than $30'$ often suffer from poor X-ray and radio morphologies. Hence, all 229 SNR candidates with small extent ($D \leq 30'$) have been investigated in more detail and split up into several subclasses regarding mainly the goodness of the X-ray and radio morphology. The source properties of all SNR candidates are listed in Appendix A, whereas the X-ray images are shown in Appendix B.

¹Advanced Satellite for Cosmology and Astrophysics (1993-2001)

²First fully imaging X-ray telescope put into space (1978-1981)

5.1.1 SNR Candidates with $D \leq 30'$

All SNR candidates with an extent below $30'$ have been divided in four different categories according to the selection criteria being a SNR candidate of high or low priority. These selection criteria comprise the X-ray and radio morphology as well as the results from the correlation procedure with the X-ray, radio, optical and gamma ray databases which are described above. Making also use of NED and SIMBAD allowed to further constrain the number of candidates.

Most promising SNR candidates

This class of targets contains the most promising SNR candidates showing strong and extended radio emission (Fig. 5.1-5.3). Most of them show hard X-ray emission in the ROSAT band according to their hardness ratio implying that the targets are either more absorbed and/or have temperature higher than a few 10^6 K. No significant optical counterparts in the R-band could be found which would lead to source confusion with extragalactic objects or stars which could also cause the X-ray emission. These candidates were also correlated with the UKST/AAO $H\alpha$ survey data, but no significant optical filaments could be found in the region of these X-ray sources. They are good candidates for follow-up studies in X-ray and radio.

- **G 254.8-7.0** has a bright X-ray emission region in the north and seems to consist of an incomplete shell towards the south. PMN radio data show irregular radio emission close to the center of G 254.8-7.0.
- **G 286.6-15.2** seems to consist of two bright X-ray emission regions which are orientated in north-west south-east direction. An irregular radio source in the PMN data overlaps very well with the X-ray source.
- The SNR candidate **G 309.9-2.5** consists of a bright radio shell in the east and the smaller embedded X-ray emission region.
- **G 321.8-3.5** has an incomplete X-ray shell matching very well with the region of radio emission in the north.
- **G 322.5+6.3** shows center-filled X-ray emission and an arc shows up in the north-west in the PMN data.
- **G 332.5-5.6** is remarkable by its shell-like X-ray morphology which matches very well with the PMN survey and ATCA radio data (Fig. 5.2, 5.3). This target is also listed as a SNR candidate by Duncan et al. (1997) due to its radio morphology. Archival ATCA data at 13 cm and 20 cm do not show any evidence of significant polarization in the region of G 332.5-5.6. Both radio datasets show almost the same morphology as the MOST data do. The ATCA data show varying spectral indices across the radio sources. The radio emission region in the north-east has a spectral index $\alpha = -0.70 \pm 0.37$ whereas the close-by

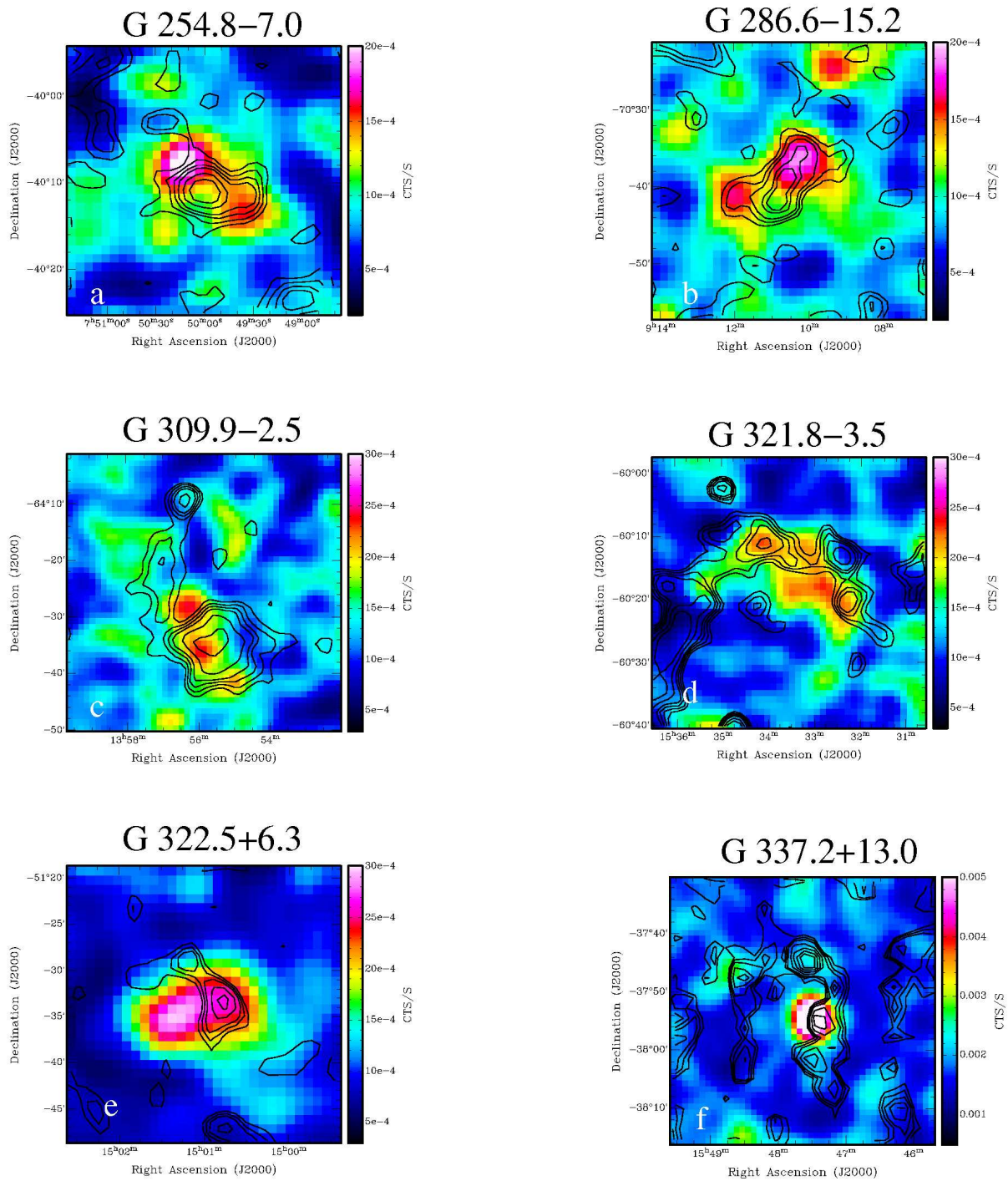


Figure 5.1: RASS images of very promising SNR candidates overlaid with PMN radio data with following contour lines: **a)** 10, 20, 30, 40, 50, 80 mJy; **b)** 5, 10, 15, 25, 30 mJy; **c)** 20, 30, 40, 50, 70, 100 mJy; **d)** 15, 20, 25, 30, 40, 50 mJy; **e)** 10, 15, 20, 30, 40, 50, 60 mJy.

bright radio point source in the north (R.A.= $16^h43^m15^s$ and DEC= $-54^\circ18'00''$ (J2000.0)) has a spectral index $\alpha = +0.58 \pm 0.37$ indicating thermal radio emission. There is neither an X-ray nor bright optical counterpart. The central radio emission region which matches with the extended X-ray source has a steep non-thermal radio continuum with a spectral index $\alpha = -1.07 \pm 0.37$ which seems to be too high for SNRs and is rather typical for extragalactic objects like galaxy clusters. The radio emission region in the south-west has a spectral index

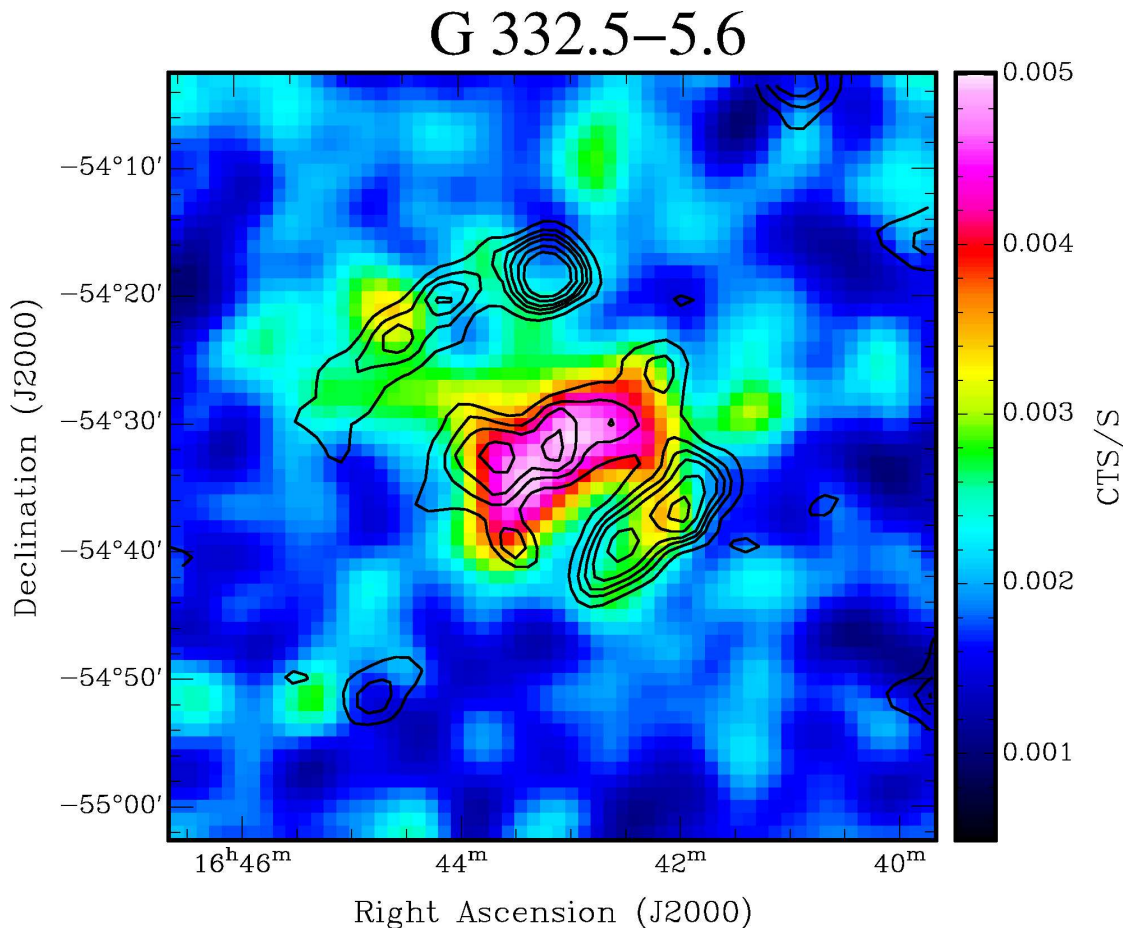


Figure 5.2: Pointed RASS image of G 332.5-5.6 overlaid with PMN radio data at 4.85 GHz. The countour levels are: 25, 40, 50, 60, 75 and 90 mJy (resolution $4.2'$ (FWHM)). In X-rays, the source shows an irregular shape which matches very well the shell-like radio emission region.

$\alpha = -0.70 \pm 0.37$. A pointed 3 ks ROSAT PSPC observation shows an elongated X-ray source ($\sim 20' \times 10'$) but very faint X-ray emission at the position of the radio arc in the south-west (Fig. 5.3). A spectral analysis of the pointed ROSAT PSPC data of G 332.5-5.6 was performed with ~ 1200 source counts using the X-Ray Spectral Fitting Package XSPEC. A Raymond-Smith model with reduced

$\chi^2=0.98$ is found to describe the data best resulting in a Galactic absorption $N_H = (0.53 \pm 0.27) \cdot 10^{21} \text{ cm}^{-2}$ and temperature $kT=0.27 \pm 0.05 \text{ keV}$. The hydrogen column density through the Galaxy in the direction of G 332.5-5.6 exceeds the best fit N_H almost by a factor of 5. The X-ray point source which is located in the radio arc in the north-east does not have enough photons for a proper spectral analysis. An analysis of the hardness ratio HR 1 and HR 2 shows that this X-ray point source has almost the same strength as the extended X-ray emission in the center of G 332.5-5.6. On the other hand, this X-ray point source appears as the central source of two possible radio jets. There is only a faint optical counterpart in the DSS2red. G 332.5-5.6 seems, therefore, to be a complex

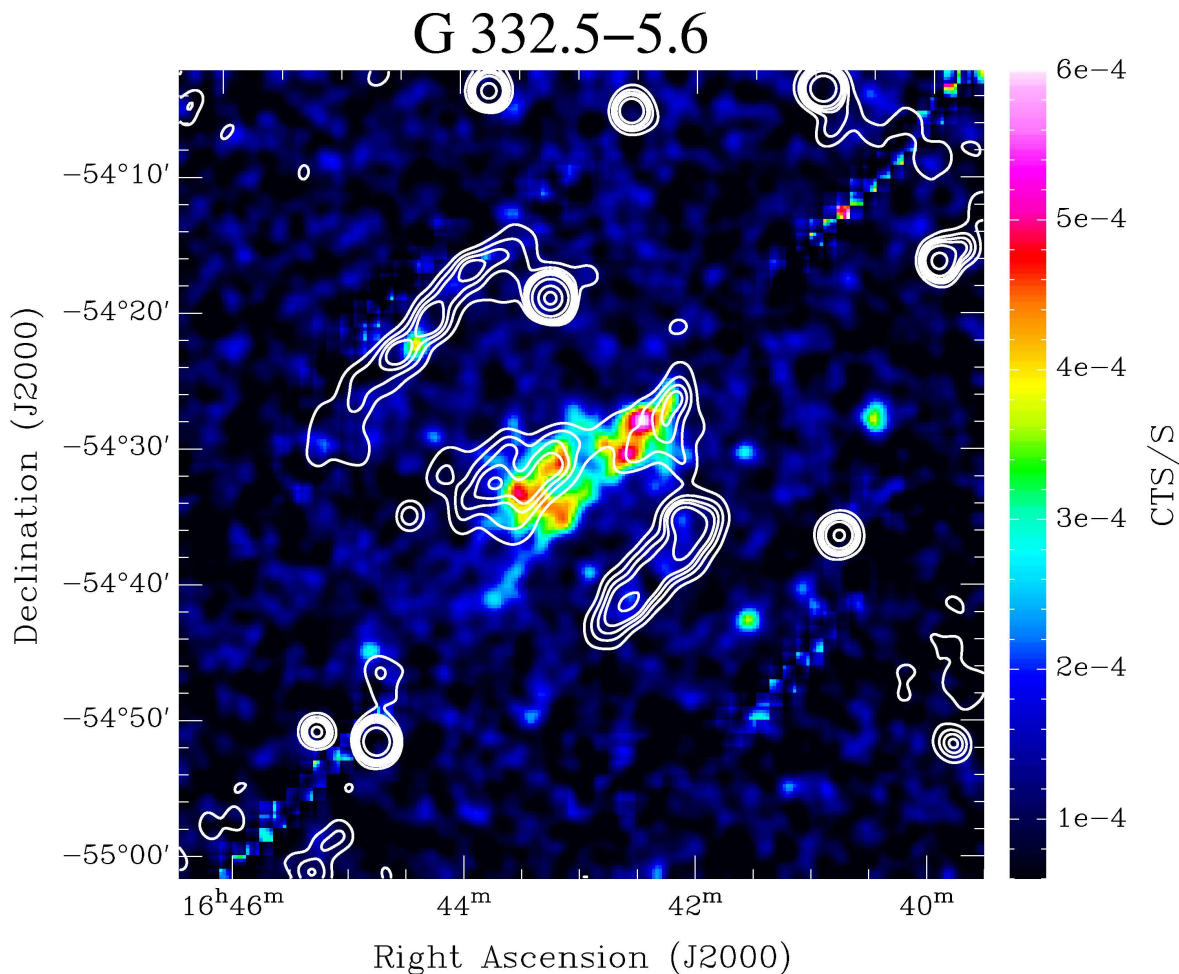


Figure 5.3: Pointed ROSAT PSPC image of G 332.5-5.6 overlaid with ATCA contour lines at 13 cm. The contour levels are: 5, 10, 15, 20, 30, 60, 150 and 250 mJy (synthesised image resolution of $105''$). The X-ray source has an irregular and elongated morphology in east-west direction but only very faint emission in the radio arc in the south-west. Remarkable is the X-ray point source which is located directly in the center of the radio arc in the north-east.

region of X-ray emission and thermal and non-thermal radio emission. There are two plausible explanations for this scenario: (i) a supernova remnant with the two outer radio arcs which have the same spectral indices $\alpha = -0.70 \pm 0.37$ or (ii) an X-ray and radio bright galaxy cluster due to the irregular X-ray and radio morphology and the steep index in the radio spectrum. But the X-ray spectral properties in are not consistent with an extragalactic source. The extended radio source in the north-east could also be taken by an extragalactic radio jet originating from the X-ray point source. No clear and consistent picture emerges from the X-ray and radio data. Further X-ray observations would be helpful to clarify the nature of the X-ray emission in the field of G 332.5-5.6.

- **G 337.2+13.0** is a candidate at an extreme high Galactic latitude. It appears center-filled in X-ray and shows shell-like radio emission in the PMN data at 4.85 GHz.

Good SNR candidates

These objects are good SNR candidates. No extragalactic objects or optical bright stars coincide with the X-ray sources. They are characterized by no or very faint radio emission and therefore have no extended radio structures. On average their X-ray count rate in the ROSAT band is lower than that in the previous category.

The SNR candidate **G 31.9-1.1** was situated in the pointing direction of an ASCA observation at an off-axis angle of $\sim 14'$ (PI: Dr. Michael G. Watson), therefore the source appears elongated in the ASCA data whereas it appears circular in the RASS data. The source has a total of ~ 1100 counts which allows for a detailed spectral analysis. Figure 5.4 shows the ASCA GIS image of G 31.9-1.1 and the spectrum fitted with a single power law. No significant radio emission could be found in the NVSS data. Because of only ~ 1100 source counts the spectrum was grouped with a signal to noise (SN) ratio of at least 4σ . Various models have been fitted to the X-ray data. Only the fit results with reduced $\chi^2 < 1.5$ are given in Tab. 5.2. The

Model	N_H [10^{22} cm $^{-2}$]	kT [keV]/ Γ	reduced χ^2 (dof)
Power law	$0.098^{+0.16}_{-0.10}$	$1.84^{+0.23}_{-0.21}$	0.86 (40)
MEKAL	$0.047^{+0.16}_{-0.05}$	$5.23^{+1.88}_{-1.35}$	0.84 (40)

Table 5.2: Spectral fit results of the X-ray source G 31.9-1.1.

spectrum shows no significant line emission and can be best described either by an absorbed power law model or the thermal model MEKAL which describes an emission spectrum from hot diffuse gas based on the model calculations of Mewe et al. (1995) and Kaastra (1992) with Fe L calculations by Liedahl et al. (1995). The model includes line emissions from several elements. The low Galactic N_H which is obtained in both models compared to the Galactic N_H through the Galaxy in the direction of G 31.9-1.1 (Dickey & Lockman, 1990) indicates a Galactic origin of the candidate. The symmetric

G 31.9–1.1

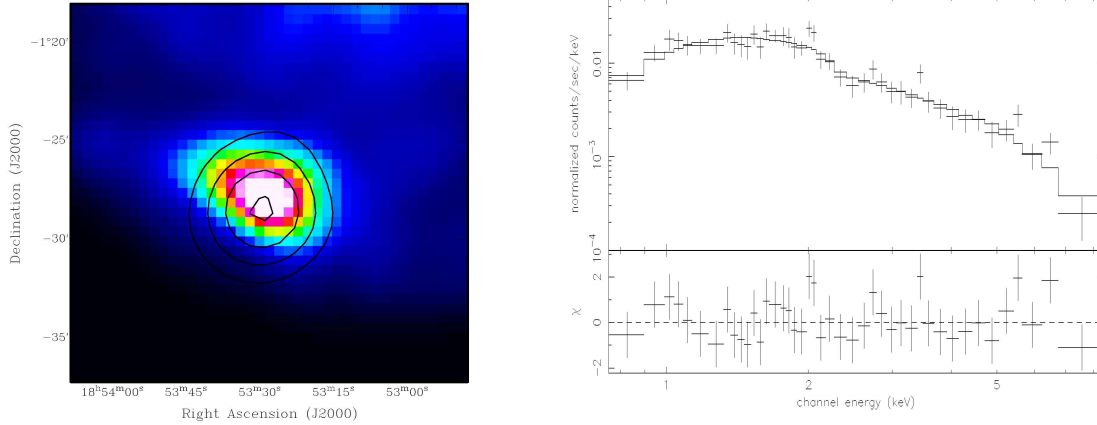


Figure 5.4: On the left side the smoothed ASCA GIS image of G 31.9-1.1 is shown overlaid with the contour lines of the RASS data. On the right side the corresponding ASCA spectrum is shown fitted with a single power law model.

and central brightened X-ray morphology and the fitted power law strongly support the interpretation of a Crab-like SNR, but no radio emission was detected at the position of the candidate.

Despite the lack of radio emission G 31.9-1.1 is a good candidate of a center-filled or Crab-like SNR which requires follow-up observation in X-rays.

Targets with poor evidence for SNRs

The majority of the sources in the catalogue of SNR candidates by Busser (1998) belongs to this group. A search in radio databases was performed but no extended radio sources could be found consistent with the position of the targets. The SNR candidates of this class show no uniform morphology in X-rays and are often located in a complex region of X-ray emitting objects, resulting in source confusion. Some of them contain one or several radio point sources indicating a possible radio-loud galaxy which could cause the X-ray emission. In many cases they are also located close to known galaxies and therefore it's rather difficult to distinguish between these targets and the extragalactic objects.

Three SNR candidates were also found in pointed Einstein and ASCA observations. All of them were located significantly off-axes resulting in a much lower exposure time.

- The candidate **G 305.5-1.9** was observed with the IPC detector in a ~ 1300 s Einstein observation. The Einstein data show several resolved X-ray sources at the position of G 305.5-1.9 which do not seem to correlate with the RASS data (Fig. 5.5). An elongated PMN radio source is situated relatively close to the center of G 305.5-1.9, but with an east-west orientation. In the Einstein data,

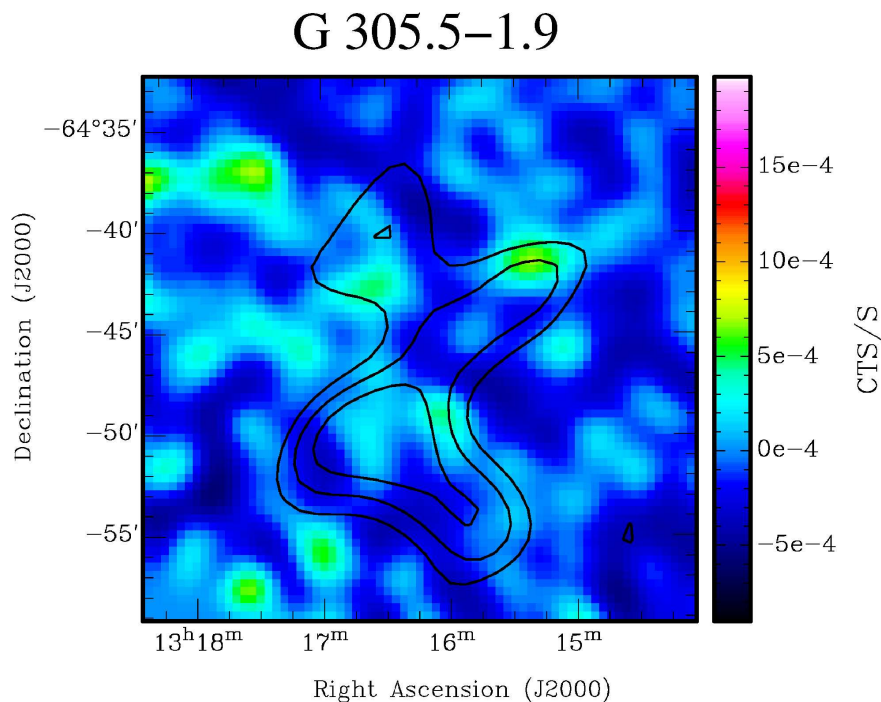


Figure 5.5: Exposure-corrected Einstein IPC image of G 305.5-1.9 overlaid with contour lines from the RASS data. The ROSAT PSPC contour levels are: 1.15 , 1.25 and 1.35×10^{-3} cts/s/arcmin. No extended X-ray counterpart is seen in the Einstein IPC data.

G 305.5-1.9 seems to appear as an accumulation of several independent X-ray sources rather than the fragments of an X-ray shell of a SNR.

- **G 315.4+0.4** was observed with ASCA for ~ 11.6 ks (PI: Dr. S.R. Kulkarni). The ASCA GIS data show several resolved X-ray sources in the field of G 315.4+0.4 which do not show a contiguous structure like shells or arcs (Fig. 5.6). Therefore no spectral analysis of the ASCA data could be performed in the region of G 315.4+0.4. A radio source in the PMN data emerge in the central-east part of the X-ray candidate without any significant correlation with the ASCA data. The X-ray morphology does not support the SNR interpretation.
- **G 353.7+16.0** was observed with ASCA (PI: Dr. N. Hirano) for 34.9 ks resulting in ~ 1600 source counts. The source appears elongated due to the large off-axes angle of $\sim 8'$. In addition, the ASCA data show two X-ray emission peaks whereas the brighter peak matches the center of the RASS source. The question is whether both X-ray sources in the ASCA data belong to G 353.7+16.0 or not. A spectrum of the source was extracted, grouped with a SN ratio of at least 5σ due to a higher photon statistics (Fig. 5.7). Various spectral models have been fitted to the X-ray data. The fit results with reduced $\chi^2 < 1.5$ are

G 315.4+0.4

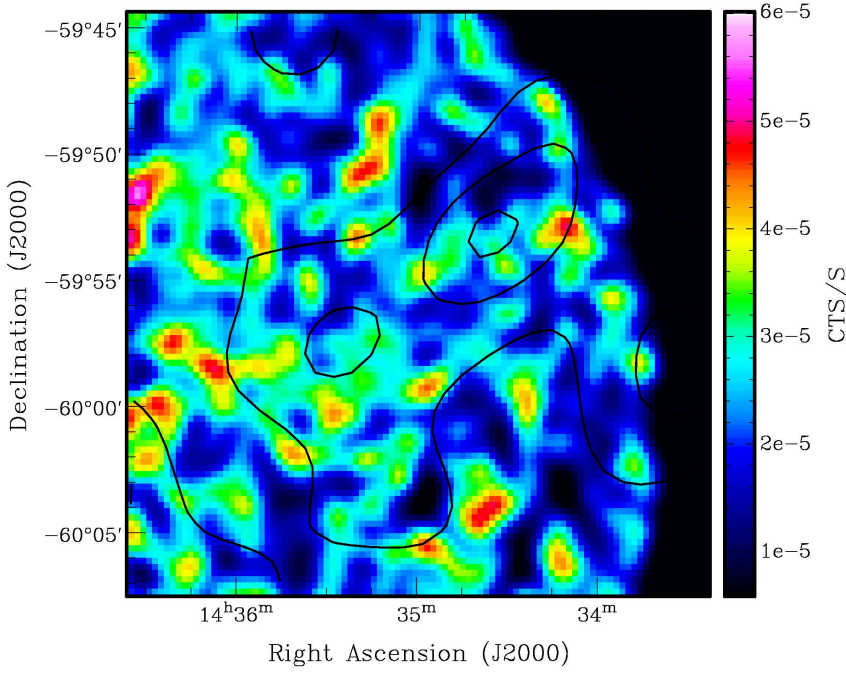


Figure 5.6: Vignetting-corrected ASCA GIS image of G 315.4+0.4 overlaid with contour lines from the RASS data. The contour levels are: 5.7 , 7.5 and 8.8×10^{-4} cts/s/arcmin. The extended RASS source appears as single resolved X-ray sources in the ASCA data.

given in Tab. 5.3. The spectrum of G 353.7+16.0 do not show significant spec-

Model	N_H [10^{22} cm $^{-2}$]	kT [keV]/ Γ	reduced χ^2 (dof)
Power law	$0.088^{+0.148}_{-0.088}$	$2.42^{+0.23}_{-0.20}$	1.14 (50)
MEKAL	$0.091^{+0.123}_{-0.091}$	$2.59^{+0.47}_{-0.38}$	1.21 (49)

Table 5.3: Spectral fit results of the X-ray source G 353.7+16.0. The model **MEKAL** provided also a redshift $z = 0.094^{+0.26}_{-0.025}$ with fixed solar abundances.

tral features. A simple power law and the thermal model **MEKAL** with a redshift $z = 0.094^{+0.26}_{-0.025}$ provide a very good fit to the data. The Galactic N_H in both models is in the order of the Galactic N_H through the Galaxy in the direction of G 353.7+16.0 (Dickey & Lockman, 1990) indicating an extragalactic object. The model **MEKAL** provides a redshift of $z = 0.094^{+0.026}_{-0.025}$ which would support the Galaxy cluster interpretation. The temperature of the hot gas, however, would be very low for a galaxy cluster. A radio point source emerges in the NVSS data at the position of the bright X-ray peak in the north-east of G 353.7+16.0.

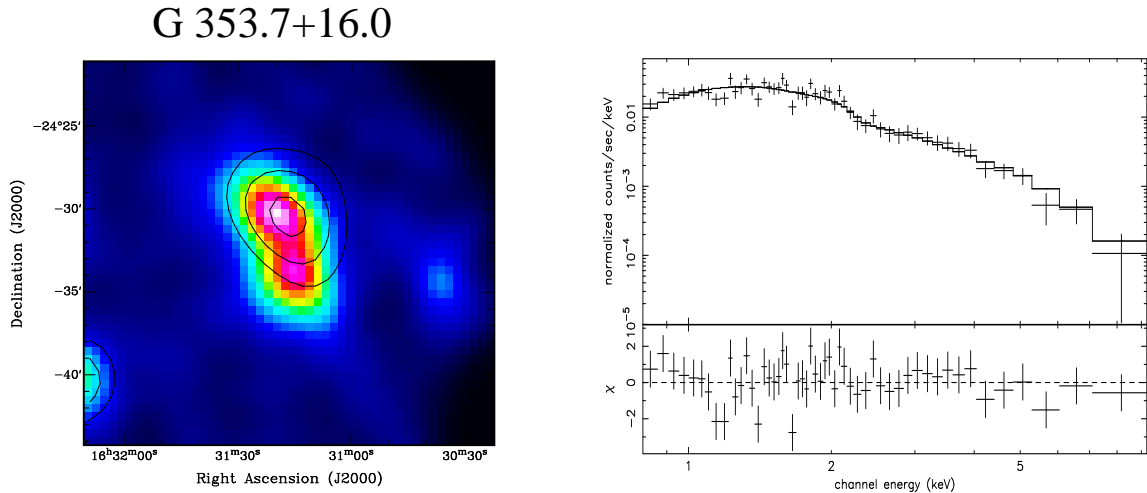


Figure 5.7: On the left side the smoothed ASCA GIS image of G 353.7+16.0 is shown overlaid with the contour lines of the RASS data. On the right side the corresponding spectrum is shown fitted with the model MEKAL.

The interpretation of the X-ray as well as the radio data favour rather a Galaxy cluster than a SNR. There is no evidence for a shell or plerionic structure neither in X-ray nor radio. At such high galactic latitude of +16.0, galaxy clusters are more likely than Galactic SNRs. Further follow-up observations in X-rays are needed to clarify the real nature of G 353.7+16.0.

Targets which are identified as extragalactic objects and stars

These targets are likely extragalactic objects like galaxies, clusters of galaxies or X-ray bright stars in the Galaxy. Correlating the positions of the targets with radio databases like NVSS, PMN, Molonglo and Effelsberg and the optical DSS as well as SIMBAD and NED allowed to ascribe them to extragalactic background objects or X-ray bright stars. They show, at least, one galaxy or a bright optical star in the region where the X-ray emission peaks. To be interpreted as a X-ray bright star, the target should consist of a spherical shape, small extent in X-rays, and coincide with a bright optical counterpart. The identification campaign was additionally supported by archival ROSAT PSPC and HRI data as well as follow-up observations with CHANDRA ACIS-I, resolving the diffuse X-ray emission regions in point sources and allowing spectral analysis (cf. 5.2). Follow-up observations in the radio with the Effelsberg 100-m telescope (cf. 5.3) and optical observations from the Keck telescope by Ebeling (H. Ebeling, private communication) helped to identify some of the targets as extragalactic background objects, H II regions or stars. The Galactic absorption in the direction of these targets (Dickey & Lockman, 1990) is at least a factor of 6 lower than the amount of Galactic hydrogen which provides the detection threshold in the ROSAT energy band (cf. 3.3).

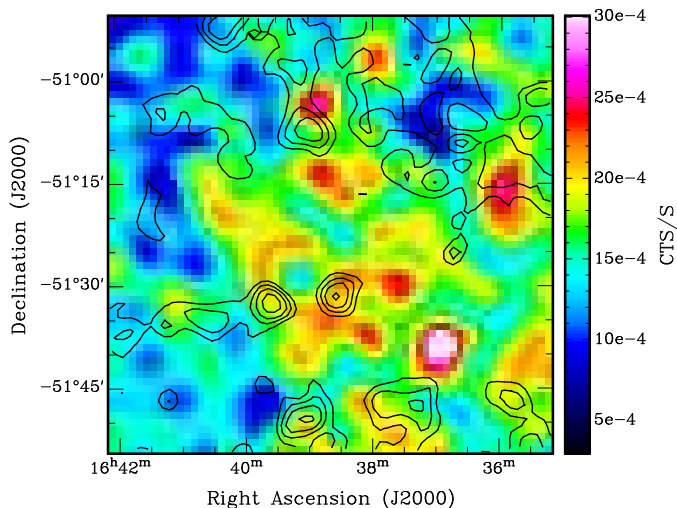


Figure 5.8: Exposure-corrected and smoothed RASS image of G 334.44-3.19 overlaid with radio contour lines from the PMN survey. The contour lines are: 10, 25, 40 and 60 mJy. G 334.44-3.19 shows extended X-ray emission but no indication of extended radio emission in the region of the X-ray source.

5.1.2 SNR Candidates with $D \geq 30'$

A detailed investigation of the large SNR candidates ($D \geq 30'$) as has been performed for the smaller objects, was not possible. The presence of known extragalactic objects and/or X-ray bright stars in the region of the SNR candidates do not come into consideration for the extended X-ray or radio emission regions due to the large size. Correlating the RASS data with radio databases which are sensitive to large scale structures, e.g. the Effelsberg Galactic Plane surveys, PMN and Molonglo survey, and the Third EGRET catalog provide important information about the nature of the sources.

SNR Candidates with $30' \leq D \leq 60'$

While the extent of these objects is not too large they have been correlated with the databases NED and SIMBAD as well as the radio surveys. Two objects could be identified as possible clusters of galaxies and 24 objects were found to be spurious background features leaving still 16 targets as SNR candidates.

The following SNR candidates **G 24.07-0.28**, **G 104.74+9.91**, and **G 335.56-1.59** distinguish themselves from the other candidates by their significant X-ray morphology. But no distinct radio morphology could be found. A fourth SNR **G 334.44-3.19** lies partly within the 1σ contour lines in the field of the unidentified γ -ray source 3EG J1638-5155 (Torres et al., 2001). Figure 5.9 shows the γ -ray source 3EG J1638-5155 overlaid with the SNR candidate G 334.44-3.19 (dashed line). The SNR candidate itself, however, shows extended X-ray emission but without any regular structure and a poor radio morphology and therefore probably do not stand for an extended SNR (Fig. 5.8). The remaining SNR candidates show patchy X-ray emission which gives the impression of an overall extended X-ray source. They can be considered as unresolved X-ray point sources. But no significant radio morphology was found. The nature of these targets is still unclear.

SNR candidates with $60 \leq D \leq 120$

All objects have been correlated with the radio databases which are described in the previous subsection. A few objects, showing strong brightening parts have been correlated with the databases SIMBAD and NED identifying subsequently two targets as complex regions of star clusters, H II regions and galaxies. Seventeen targets were found to be spurious background features leaving still 9 targets as SNR candidates.

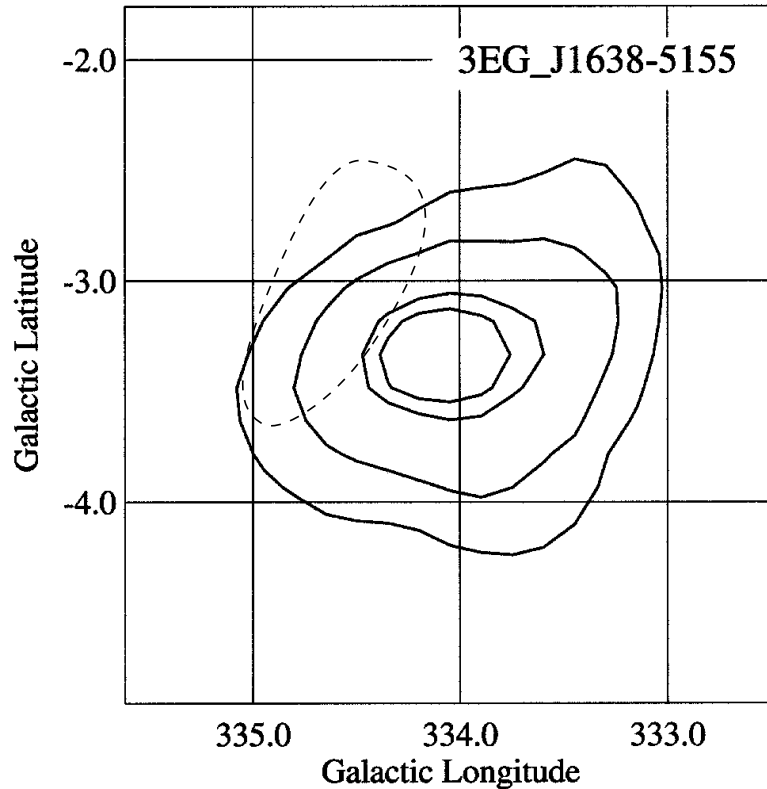


Figure 5.9: EGRET likelihood map from the γ -ray source 3EG J1638-5155. The contour lines indicate the 0.6σ , 1σ , 2σ and 3σ statistical probability that a source lies within that contour (Mattox et al., 1996). The shape of the SNR candidate G 334.44-3.19 is indicated by the dashed line.

The remaining candidates show poor evidence to be classified as SNRs according to their X-ray and/or radio morphology, therefore they are SNR candidates of low priority.

SNR candidates with $D \geq 120'$

The SNR candidates have been correlated with radiobases like the Effelsberg Galactic Plane surveys and PMN survey, respectively. No target out of this sample could be identified as a SNR or an extragalactic object, but 26 targets were found to be spurious background features, leaving still 18 targets as SNR candidates.

The following six SNR candidates **G 1.85-2.52**, **G 12.71+8.28**, **G 26.73-3.61**, **G 312.09+4.20**, **G 331.13-4.84** and **G 343.75+3.99** show extended spherical or elongated shapes and significant enhancement in the X-ray emission compared to the surroundings, but no significant radio morphology could be found matching the X-ray sources. The remaining 12 SNR candidates do not show such clear morphology neither in X-rays nor in radio. No unidentified Γ -ray source was found in the field of all these SNR candidates.

In the east of G343.75+3.99 an incomplete spherical radio shell **G 313.36+3.77** with a diameter of about 3° shows up in the PMN survey data with two bright radio point sources in the imaginary center. But there is no significant X-ray emission in this region where the radio emission dominates. Another radio SNR candidate **G 321.28-3.93** shows up in the PMN survey data with an incomplete shell which has a diameter of about 1.4° . No significant X-ray emission is found in the region of the incomplete radio shell because there is a strip of very low exposure time in the RASS data covering this field. Both radio candidates are shown in Fig. 5.10.

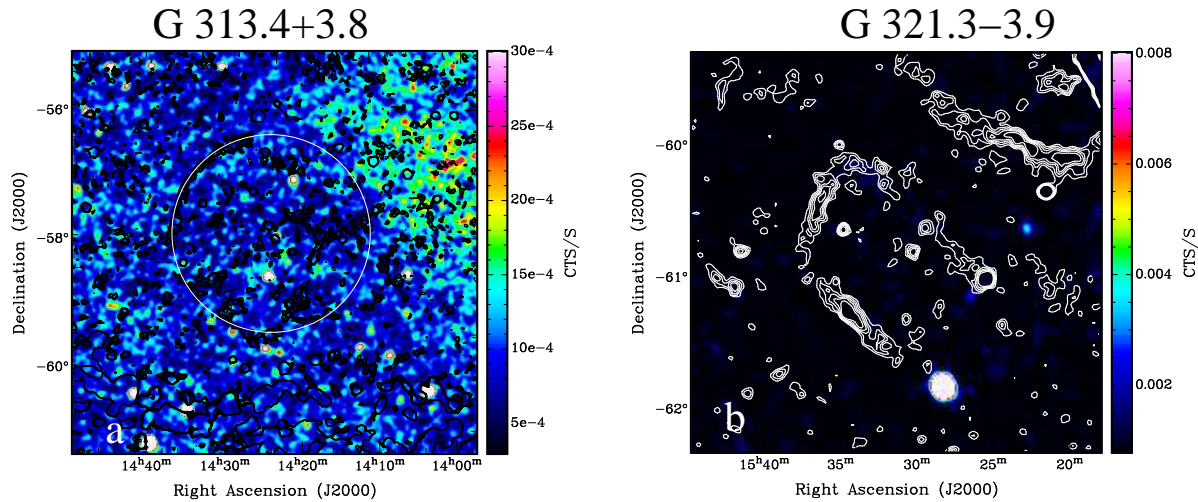


Figure 5.10: Smoothed RASS count rate images overlaid with radio contour lines from PMN survey data. **a)** The incomplete radio shell G 313.36+3.77 is indicated by a white continuous line. In the north-west the extended X-ray emission of G 321.28-3.93 is partly seen. The radio contour levels are: 10, 12.5, 15, 17.5, 20, 25, 30, 35 mJy. **b)** The radio SNR candidate G 321.33-3.75 which is located in the north of the bright Low Mass X-ray Binary V* KY TrA (Liu et al., 2001). The radio contour levels are: 15, 25, 35, 45 60 mJy.

5.2 X-ray Follow-up Observation With Chandra

The two SNR candidates 1RXS J161411.3-630657 (G 323.6-8.7) and 1RXS J104047.4-704713 (G 292.5-10.6) were selected due to their X-ray and radio morphology for a follow-up observation with the Chandra X-ray observatory. The data analysis was performed using the Chandra Interactive Analysis of Observations (CIAO) software version 2.2 and the Chandra Calibration Database (CALDB) version 2.12.

In the beginning of the Chandra mission, mainly the front-illuminated (FI) CCDs in the ACIS detector were damaged in the environment of the Earth's radiation belts, causing charge traps that result in enhanced charge transfer inefficiency (CTI) during parallel readout. Thus CTI changes the gain across the device and causes spatial redistribution of charge in the pixel neighborhood of an event, as charge traps capture electrons and release them on short timescales during the readout process. This results in charge being redistributed in surrounding pixels within the region recognized as a single event. Due to the unanticipated forward scattering of charged particles which are probably high energy protons around 100 keV (Prigozhin et al., 2000) by the Chandra mirrors onto the ACIS CCDs, the FI devices suffered degraded performance on-orbit, most pronounced near the aimpoint of the imaging array. For these reasons, Townsley et al. (2000) developed a phenomenological model of the CTI for the FI CCDs which reproduces the spatially-dependent gain, grade distribution and the row-dependent energy resolution seen in the FI devices.

A so-called 'CTI corrector' was applied to all the Chandra data in order to remove partially CTI effects from ACIS data and to improve the spatial as well as spectral performance. By the time of this PhD thesis no so-called 'closed observations' or 'dark moon observations' with Chandra were available for level 1 event files which are used for the CTI corrector software. Therefore it was not possible to determine the instrumental background which is enhanced incorrectly in the case of vignetting-corrected background spectra which were extracted considerably offset from the aimpoint. The enhanced background affects only the high energy tail of the spectra where the source count rate converts towards the background count rate.

5.2.1 SNR Candidate 1RXS J161411.3-630657

The RASS data show the candidate 1RXS J161411.3-630657 as an extended hard X-ray source with a size of about $10' \times 10'$. In addition, the PMN survey data show an extended radio source which is elongated in the north-south direction and peaks at two positions (Fig. 5.11). The good agreement of X-ray and radio data prompted a follow-up observation with the Chandra observatory in X-rays.

The SNR candidate 1RXS J161411.3-630657 was observed by Chandra at two epochs, on 21th October 2001 and 6th January 2002, using the ACIS-I detector with the CCD configuration 0-1-2-3-4-9.

The exposure times of the first and second observation were ~ 23.9 ks and ~ 9.0 ks, respectively. While soft proton flares could increase significantly the count rate above 10 keV, both observation were checked for this contamination. Selecting

1RXS J161411.3–630657

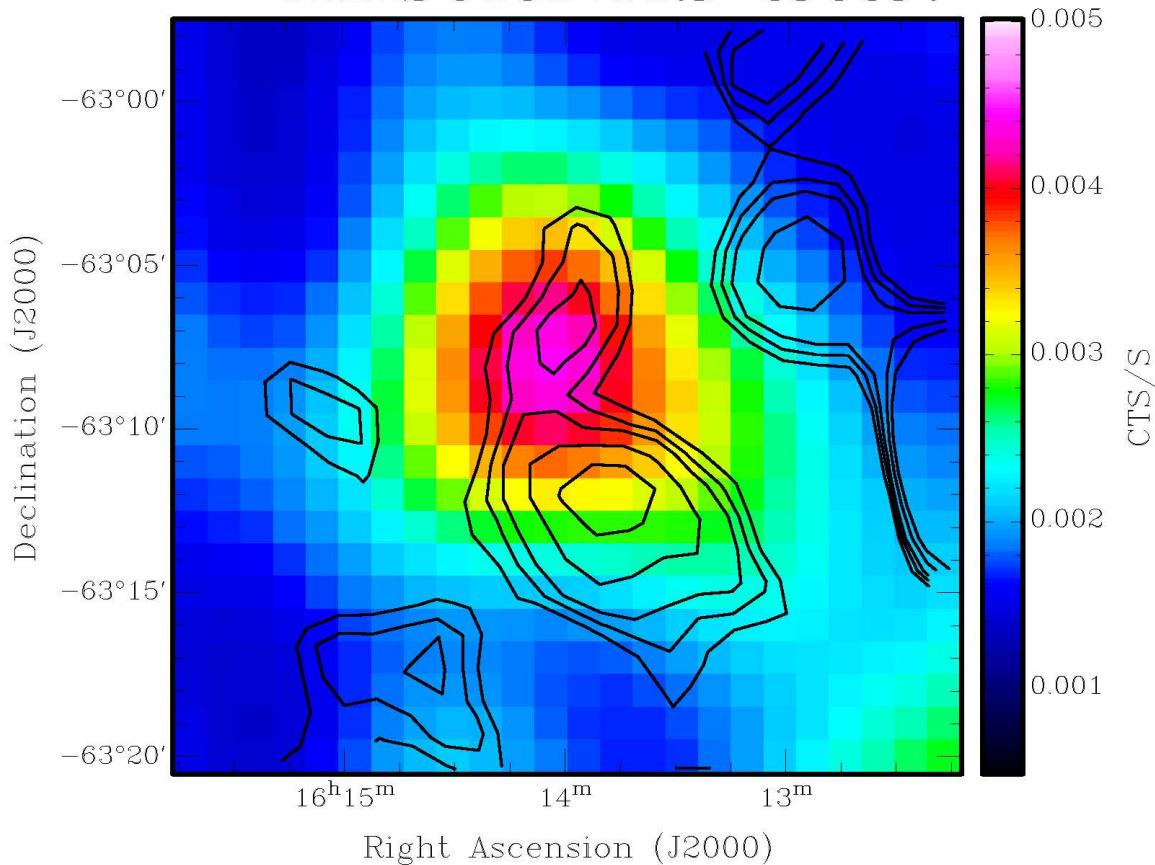


Figure 5.11: Smoothed and vignetting corrected RASS image (Gaussian filter with a width of $\sigma=3$ pixel, pixel size = $1'$) of 1RXS J161411.3-630657 overlaid with radio contours from the PMN survey. The contours are at 5, 7.5, 10, 15 and 20 mJy.

all photons above 10 keV, an increase in the count rate by a factor 2-3 was found 15 ks after the start of the first observation in October 2001. The second observation was 'uncontaminated' showing no significant variation or increase in the count rate. Selecting just the 'good time intervals' a total exposure time of ~ 23 ks remained.

Spatial analysis

1RXS J161411.3-630657 is an extended X-ray source and has its brightness center at R.A.= $16^h14^m05.7^s$ and DEC= $-63^\circ08'30.8''$ (J2000.0). A X-ray point source which is located exactly in the center coincide with the optical cD galaxy WKK 98 6203 (Woudt & Kraan-Korteweg, 2001). This X-ray counterpart has a significance of 7.8σ and an extent of $5.4''$. There are about 70 ± 12 source counts corresponding to $3.1 \pm 0.5 \times 10^{-3}$ cts/s. In the radio MOST data, there is a bright point source at the position of the central cD galaxy. The extended X-ray source is surrounded by a faint X-ray halo

which reaches out $6'$ - $10'$. Two other point sources with a significance $\sigma > 3$ are situated within 1RXS J161411.3-630657 which do not have known counterparts in the optical or radio band. There are further known galaxies in the region of 1RXS J161411.3-630657, i.e. WKK 986194 (Woudt & Kraan-Korteweg, 2001), which is close to the center. Figure 5.14 shows an optical image of the field of 1RXS J161411.3-630657.

In order to get an estimate for the extent, the source was smoothed with a Gaussian filter with a width of $\sigma=3$ pixels, applying the tool `ASMOOTH` on the exposure corrected image and fitted with a gaussian to determine the source position and size (Fig. 5.12). The extent is about $2' \times 3'$ at a 3σ significance level whereof most of the source is located on CCD #2 overlapping CCD #1 and #3. The source is central brightened and has a somewhat elliptical shape in east-west direction. The morphology does not show any shell structure neither in X-rays nor in radio. The source count rate is about 0.14 ± 0.01 ctst/s resulting in a total of about 3200 source counts in the full energy band (0.5-10.0 keV). A pointed radio observation in the MOST data shows a relatively bright

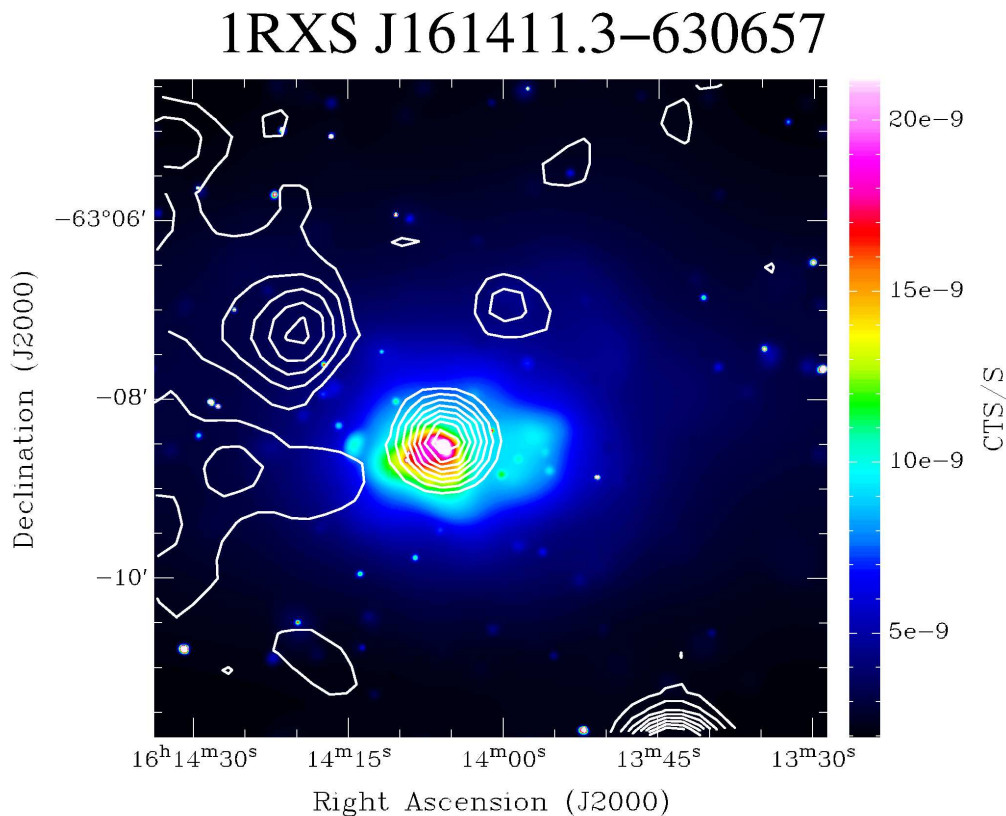


Figure 5.12: Smoothed (Gaussian filter with width $\sigma=2$ pixels) and vignetting corrected X-ray image of 1RXS J161411.3-630657 overlaid with radio contours lines from the MOST. The contours are at 2, 4, 6, 8, 10, 12, 14 and 16 mJy. The radio emission peaks at the position of the central cD galaxy WKK 98 6203 (Woudt & Kraan-Korteweg, 2001).

radio point source at the position of the central cD galaxy WKK 98 6203. Fainter radio

emission is outside the 3σ X-ray image. The PMN survey data show more extended and diffuse radio emission because the beam pattern³ is a factor ~ 6 larger than that of the MOST. Therefore the MOST allows to resolve the central radio point source. For this reason, a proper flux determination of the central radio source is not possible. But both datasets show in the central region of 1RXS J161411.3-630657 that the radio emission is much stronger at lower frequencies, indicative of non-thermal radio emission. The strong radio point source in the MOST data which is located in the south-west of 1RXS J161411.3-630657 coincides with the southern peak of the elongated radio source in the PMN survey data. This bright radio source has an X-ray counterpart in the Chandra data which does not allow for further analysis because of insufficient photon statistics.

Spectral analysis

The source spectrum and the background were extracted from CCD #2 neglecting the other two CCDs because almost all source counts are located on CCD #2. In addition, merging and weighting problems of the Response Matrice Files (RMF) and Auxiliary Response Files (ARF) from different CCDs could be avoided. The background spectrum was extracted from a region outside the faint diffuse X-ray halo which did not contain point sources or diffuse emission from other objects. The source as well as the background spectra were extracted from the CTI corrected data, using the RMF from the CTI product package and calculating the weighted ARF for the extended source and background region.

The source spectrum was grouped with a SN ratio of at least 5σ . Various models have been fitted to the X-ray data using the X-ray Spectral Fitting Package XSPEC. The fit results are given in Tab. 5.4, including only the models with reduced $\chi^2 < 2$.

Model	N_H [10^{22} cm $^{-2}$]	kT [keV]/ Γ	reduced χ^2 (dof)
Powerlaw	$2.54^{+0.39}_{-0.37}$	$1.98^{+0.10}_{-0.10}$	1.10 (108)
Bremss.	$1.66^{+0.28}_{-0.27}$	$4.55^{+0.82}_{-0.64}$	1.07 (108)
MEKAL	$1.69^{+0.27}_{-0.29}$	$4.57^{+0.80}_{-0.53}$	1.00 (106)

Table 5.4: Spectral fit results of 1RXS J161411.3-630657 using Chandra ACIS-I data. All models are with reduced $\chi^2 < 2$ are listed in this table. In addition, the model MEKAL provided a solar abundances of $0.35^{+0.35}_{-0.19}$ and a redshift $z = 0.048^{+0.029}_{-0.025}$.

1RXS J161411.3-630657 has been investigated whether the X-ray emission is thermal due to diffuse hot intracluster gas or non-thermal due to synchrotron or inverse Compton radiation (Takizawa, 2002) fitting a power law model as well as various thermal single-temperature models. Fitting an absorbed (Wilms et al., 2000) two-component model consisting of a Bremsstrahlung and a power law model could not improve significantly the spectral fit. Regarding the reduced χ^2 , the spectral model MEKAL best fits the data (Fig. 5.13). The best fit parameters are $N_H = 1.69^{+0.27}_{-0.29}$ cm $^{-2}$,

³In optics and in X-rays the beam pattern is called 'point spread function'

temperature $T = 5.36_{-0.62}^{+0.94} \times 10^7$ K, solar abundances of $0.35_{-0.19}^{+0.35}$ and a redshift $z = 0.048_{-0.025}^{+0.029}$ corresponding to a distance of 288_{-150}^{+174} Mpc⁴. The X-ray flux is $f_x = 1.68 \times 10^{-12}$ ergs cm⁻² s⁻¹ in the energy band 0.3-8.0 keV leading to an X-ray luminosity of $L_x = 1.67_{-1.29}^{+2.62} \times 10^{43}$ ergs. The spectrum also shows the redshifted iron line complex at 6 keV which is typical for clusters of galaxies. But no prominent emission lines in the spectra have been found which are expected for thermal SNRs. Only a Crab-like SNR could come into consideration due to the central X-ray point source and the central brightening and the well fitted absorbed power law model with a spectral index of $\Gamma = 1.98_{-0.10}^{+0.10}$.

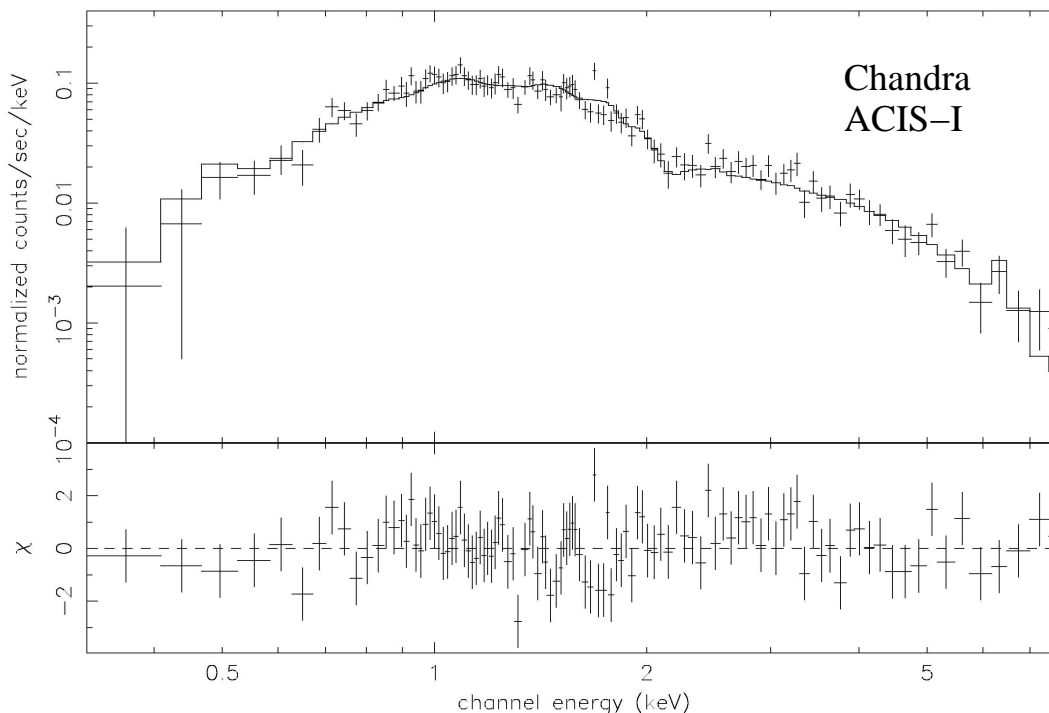


Figure 5.13: Spectrum of 1RXS J161411.3-630657 fitted with the model MEKAL.

Temporal analysis

Both observations were performed in the full frame mode and therefore provide a time resolution of 3.2 s. A light curve was created with data bins of 1000 seconds showing a constant flux of the source within the statistical fluctuations.

⁴using the Hubble constant $H_{50} = 50 \frac{km}{s Mpc}$

Optical emission

An optical observation in the R-band with an exposure time of 10 min was performed in the field containing 1RXS J161411.3-630657 in May 2000 at the ESO Danish 1.5 telescope by Schücker & Komossa. The optical image shows a field of about $6.5' \times 6.5'$ with the cD galaxy WKK 98 6203 in the center (Fig. 5.14). Many galaxies are located around this central cD galaxy within the X-ray countour lines from Chandra ACIS-I (P. Schuecker, private communication). The Chandra contour lines show only the inner

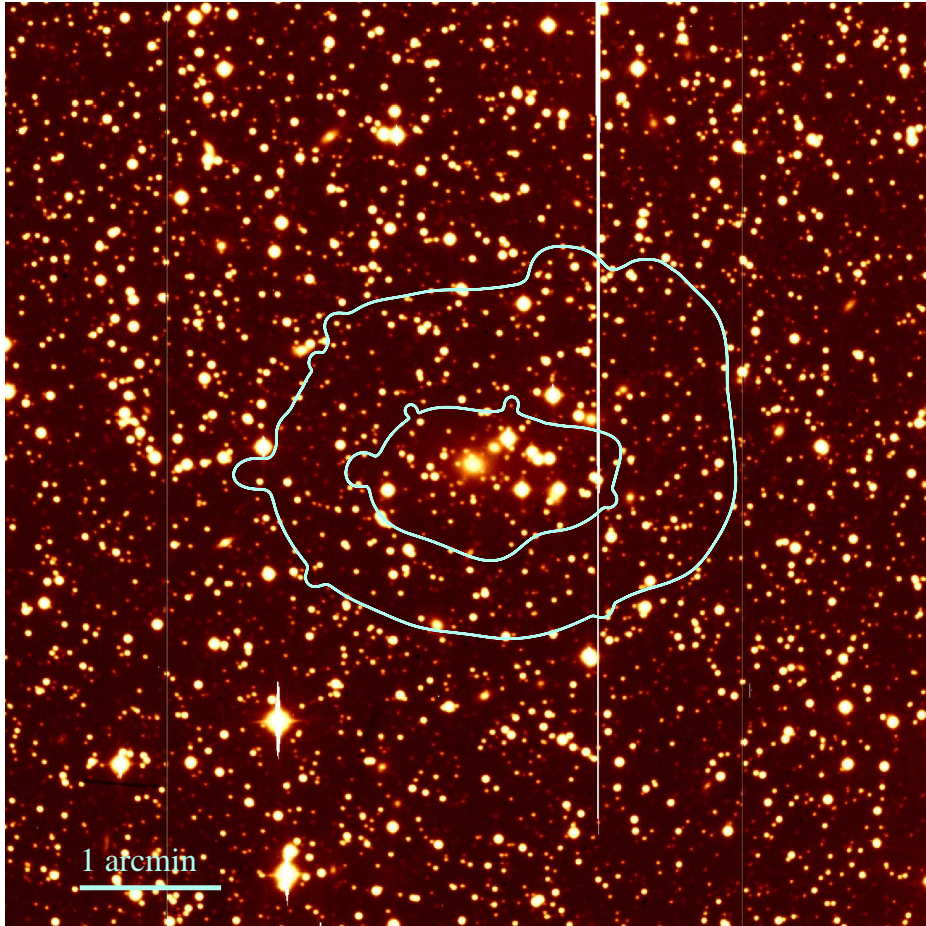


Figure 5.14: Optical image (R-band) from the central region of 1RXS J161411.3-630657 (courtesy P. Schuecker) overlaid with Chandra contour lines (6.0×10^{-5} , 1.2×10^{-4} cts/s/arcmin). The central cD galaxy WKK 98 6203 depicts the center of this image at R.A. = $16^h 14^m 05.7^s$ and DEC = $-63^\circ 08' 30.8''$ (J2000.0). The strong white line crossing the image is due to pile-up of a bright star. The image shows many galaxies around the central galaxy (P. Schücker, private communication).

part of the assumed cluster of galaxies. Two of these galaxies have a redshift $z = 0.062$ and $z = 0.059$, respectively (P. Woudt, private communication). The difference in redshift of these galaxies is in agreement with the velocity dispersion in the galaxy cluster. Due to the relative low Galactic latitude many of the bright stars are seen in

the image which make the identification of the galaxies difficult. The results from the spatial and spectral analysis do not show any evidence of a supernova remnant neither in X-rays nor in radio, but there are strong arguments which favour the interpretation of a galaxy cluster:

- The best fit to the data is obtained with an absorbed, single-temperature model MEKAL, yielding a temperature of $5.36_{-0.62}^{+0.94} \times 10^7 \text{K}$ which is in the typical range for thermal emission from diffuse hot intracluster gas (Smith et al., 2002).
- The fitted model MEKAL provides a galactic absorption $N_H = 1.69_{-0.29}^{+0.27} \times 10^{22}$ which is in the order of the Galactic N_H through the Galaxy in the direction of 1RXS J161411.3-630657 (Dickey & Lockman, 1990) favouring an extragalactic object.
- The solar abundances have a value of $0.35_{-0.19}^{+0.35}$ which is expected for galaxy clusters (Ohashi et al., 2000).
- The redshift in the X-ray data $z = 0.048_{-0.025}^{+0.029}$, is consistent with the measurements of optical redshifts ($z = 0.059$ and $z = 0.062$) of two galaxy in the same field of 1RXS J161411.3-630657 within the errors.
- The presence of the cD galaxy WKK 98 6203 in the center of 1RXS J161411.3-630657 which exists only in clusters and groups and never in the field (Oegerle & Hill, 2001).
- An optical observation of the field of 1RXS J161411.3-630657 shows many galaxies around the central cD galaxy WKK 98 6203. Two galaxies have a redshift of $z = 0.059$ and $z = 0.062$, respectively.
- Strong radio emission at the central position of 1RXS J161411.3-630657 matching very well with the position of the cD galaxy WKK 98 6203. A comparison of both radio datasets, i.e MOST and PMN survey data, indicates rather non-thermal radio emission.
- Constant X-ray flux of 1RXS J161411.3-630657 which is expected from diffuse hot intracluster gas.

Conclusion

Apart from its extent, 1RXS J161411.3-630657 does not show any characteristics of a supernova remnant. The source morphology does not show a shell structure neither in X-ray nor in radio, but is central brightened in both bands and has a slight elliptical shape. There are a few spectral models like a thermal Bremsstrahlung or a powerlaw model fitting the dataset very well with almost the same goodness, most notably the model MEKAL. Leaving the redshift and the solar abundances variable in the model MEKAL similar fit parameters are found which are typical for clusters of galaxies. The presence of the cD galaxy WKK 98 6203 in the center of 1RXS J161411.3-630657 where

the X-ray emission peaks and the measurement of the redshift of two galaxies at optical wavelength within the region of the extended X-ray source does conclusively identify the source as a cluster of galaxies. In this case, the galaxy cluster 1RXS J161411.3-630657 is located remarkable close to the Galactic Plane at low redshift.

Further follow-up observations in the optical would be useful to determine the redshifts of the other galaxies in the region of the extended X-ray source in order to confirm finally, 1RXS J161411.3-630657 as a galaxy cluster.

5.2.2 SNR Candidate 1RXS J104047.4-704713

The candidate 1RXS J104047.4-704713 has a size of about $9' \times 9'$ in the RASS data and shows strong X-ray emission in the hard ROSAT energy band above 1 keV. The position of the Parkes-survey radio source PMN J1040-7048 matches the location of 1RXS J104047.4-704713 very well (Fig. 5.15a). The radio source PMN J1040-7048 was observed twice in an interval of about five month during the survey observation (Gregory et al., 1994). No flux variability could be found within the error bars. The radio flux amounts to 69 mJy at 4.85 GHz. The good correlation of diffuse and extended X-ray and radio emission at the position of 1RXS J104047.4-704713 prompted a follow-up observation in X-rays with the Chandra observatory (Fig. 5.15 a).

The SNR candidate 1RXS J104047.4-704713 was observed by Chandra on 11th September 2001 using the ACIS-I detector with the same CCD configuration 0-1-2-3-4-9. The whole observation remained unaffected by soft proton flares leading consequently to a total exposure time of 12.8 ks.

Spatial analysis

1RXS J104047.4-704713 is an extended X-ray source which overlaps all four ACIS-I detector chips. The geometrical center is at R.A.= $10^h40^m43.2^s$ and DEC= $-70^\circ47'03.5''$ (J2000.0). The source has an extent of about $3' \times 2.5'$ at a 3σ significance level and is central brightened with an slight elliptical shape (Fig. 5.15 b). The X-ray as well as the radio morphology do not show any evidence of a shell-like structure. In addition, the extended X-ray source is surrounded by a faint X-ray halo which has a size of about $9' \times 7'$.

Nine X-ray point sources have been detected at the location of 1RXS J104047.4-704713 within its faint X-ray halo with a significance $\sigma > 4$. In X-rays, the central part of 1RXS J104047.4-704713 is dominated by a point source which is located very close to the geometrical center with a source significance of $\sigma=10$ containing ~ 150 source counts. A pointed MOST observation shows a bright radio source in the center of 1RXS J104047.4-704713 which is a possible radio counterpart of the X-ray source within the position accuracy. Another bright radio source is located in the south-west about $85''$ from the geometrical center which coincides with a bright X-ray source at R.A.= $10^h40^m32^s$ and DEC= $-70^\circ48'09''$ (J2000.0) and a source significance $\sigma=20$. The optical database DDS2red shows only a very faint source in this region. The central part of 1RXS J104047.4-704713 was observed with the 40-inch Anglo-Australian Observatory in the optical and five bright optical sources were found matching very

well the central position of the X-ray and radio point source, but the nature of these sources is still unclear (M. Filipovic & A. Tennant, private communication).

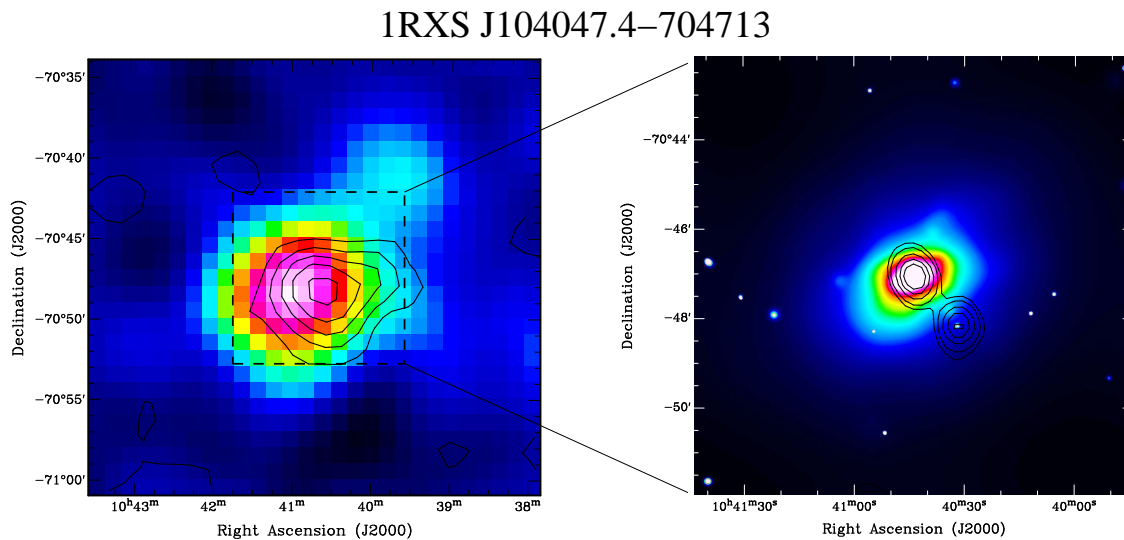


Figure 5.15: **a)** Smoothed and vignetting corrected RASS image (Gaussian filter with width $\sigma=3$ pixels, 1 pixel = $1'$) of 1RXSJ104047.4-704713 overlaid with radio data from the PMN survey (4.85 GHz). The contours are at 10, 20, 30, 40 and 50 mJy. **b)** Smoothed (Gaussian filter with width $\sigma=3$ pixels, 1 pixel = $0.5'$) and exposure corrected Chandra ACIS-I image of 1RXS J104047.4-704713 overlaid with radio contours lines from the MOST (0.843 GHz). The contours are at 5, 10, 20, 30 and 40 mJy.

Spectral analysis

The extended source overlaps all four ACIS-I chips with a concentration on chip ACIS-I3, so that the source spectra and their corresponding background were extracted from each CCD individually creating four single spectrum files from the CTI corrected event files, weighted Response Matrice Files (WRMF) and Auxiliary Response Files (WARF). The background spectra were extracted from a region outside the faint diffuse X-ray halo. Due to the low photon statistics on ACIS-I0, ACIS-I2 and ACIS-I1, only events from ACIS-I3 have been used to perform a spectral analysis. The spectral results from ACIS-I2 agree with them from ACIS-I3 within the errors. Subsequently, these files were used for individual spectral model fitting in XSPEC.

The source spectra were grouped with a SN-ratio of at least 5σ . The X-Ray Spectral Fitting Package XSPEC was used to fit various spectral models for the data. The fitting results are given in the Tab. 5.5 including the models with reduced $\chi^2 < 2$. Various spectral models have been fitted to the data showing no significant evidence for non-thermal X-ray emission. The best fit to the data is obtained with an absorbed, single-temperature model MEKAL, yielding a temperature of $3.39^{+0.46}_{-0.35}$ keV corresponding to $3.98^{+0.54}_{-0.41} \times 10^7$ K, a galactic absorption $N_H = 1.72^{+0.33}_{-0.34} \times 10^{21}$ cm $^{-2}$ and a redshift

Models	N_H [10^{21} cm $^{-2}$]	kT_1 [keV]/ Γ_1	kT_2 [keV]/ Γ_2	red. χ^2 (dof)
BB+Powerlaw	$4.48^{+4.15}_{-0.51}$	$0.16^{+0.02}_{-0.07}$	$2.13^{+0.46}_{-0.10}$	1.48 (62)
Brems+Brems	$6.56^{+3.76}_{-1.64}$	$0.25^{+0.06}_{-0.09}$	$3.58^{+1.06}_{-0.93}$	1.44 (62)
MEKAL	$1.72^{+0.33}_{-0.34}$	$3.39^{+0.46}_{-0.35}$		1.06 (61)
BB+BB	$3.06^{+1.76}_{-1.35}$	$0.22^{+0.05}_{-0.04}$	$0.84^{+0.11}_{-0.09}$	1.48 (62)

Table 5.5: Spectral fit results of 1RXS J104047.4-704713. In the model MEKAL the solar abundances was fixed at 1 and the redshift was left open.

$z = 0.076^{+0.013}_{-0.009}$ corresponding to a distance of $\sim 456^{+78}_{-54}$ Mpc 5 . The solar abundances has a value of $0.76^{+0.42}_{-0.21}$. An X-ray flux $f_x = 1.72 \times 10^{-12}$ ergs cm $^{-2}$ s $^{-1}$ is obtained in the energy band 0.3-8.0 keV leading to an X-ray luminosity of $L_x = 4.30^{+1.57}_{-0.98} \times 10^{43}$ ergs. The spectrum of the core region of 1RXS J104047.4-704713 is shown in Fig. 5.16.

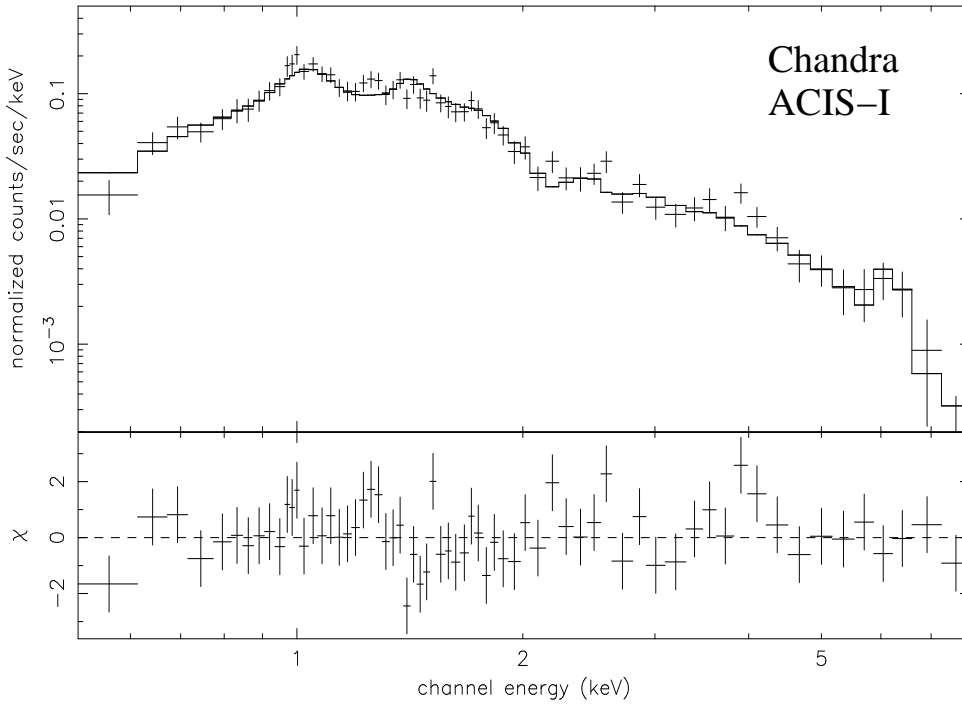


Figure 5.16: Count rate spectrum for the core region of 1RXS J104047.4-704713 on ACIS-I3. The best fit model MEKAL is represented by the solid histogram.

The fitted spectrum of 1RXS J104047.4-704713 shows also the blend of the redshifted lines Fe lines at around 6.5 keV, mainly from Fe XXIV and Fe XXV which are

5 using the Hubble constant $H_{50} = 50 \frac{km}{s Mpc}$

typical in Galaxy clusters.

The analysis of the X-ray data do not show any evidence for a thermal supernova remnant, but strongly support the interpretation of a galaxy cluster. The arguments favouring a galaxy cluster rather than a Crab-like SNR are very similar to the previous source 1RXS J161411.3-630657:

- Slight elliptical shape and central brightened in X-rays with a bright radio point source in the center.
- The spectral model **MEKAL** gives the best fit to the X-ray data with a temperature of $\sim 4 \times 10^7$ K, abundances of $\sim 0.75 \times$ solar and redshift $z \sim 0.075$ corresponding to a distance of ~ 460 Mpc.
- The galactic absorption N_H which is obtained from the spectral analysis exceeds the Galactic N_H through the Galaxy in the direction of 1RXS J104047.4-704713 (Dickey & Lockman, 1990) by almost a factor of two.
- No radio shell structure but a strong central radio point source at the position of an X-ray point source which also coincide with four optical sources.

Conclusion

In fact, the central brightened X-ray source 1RXS J104047.4-704713 with the central radio point source could be considered as a Crab-like SNR, but arguments from spatial and spectral analysis argue for a cluster of galaxies. Fitting various spectral models to the X-ray data, a simple **MEKAL** model is found to describe the data best (χ^2) resulting in $N_H = (1.4-2.0) \times 10^{21} \text{ cm}^{-2}$ which exceeds the intrinsic value through the Galaxy by almost a factor of two, temperature $T = (3.5-4.5) \times 10^7$ K, a solar abundances of (0.55-1.18) and a redshift $z = (0.067-0.089)$. The X-ray spectrum reflects the X-ray emission from diffuse hot gas with line features from Fe XXIV and Fe XXV. The slight elliptical morphology and central brightening in X-rays reflect the gravitational potential of the hot intracluster gas.

For a final conclusive identification of a galaxy cluster the redshifts of a few optical galaxies in the gravitational potential of the cluster have to be in agreement with the redshift of the hot gas.

5.3 Radio Follow-up Observations With the Effelsberg 100-m Telescope

The six SNR candidates, G 6.1-1.3, G 38.7-1.4, G 39.9-2.8, G 75.8+8.1, G 80.7+6.8 and G 178.2-3.3 were selected for radio-continuum follow-up observation at 6 cm due to their radio morphology in the Effelsberg Galactic Plane survey. The observations were carried out to study the radio morphology in more detail, to determine the spectral

indices and to search for polarized emission which directly proves a SNR identification. The direction of the polarization vectors shows the electric components, i.e the magnetic field components are orientated perpendicular to them. The observations were performed on 25th July 2001 with an exposure time of 1-2.5 hours depending on the size of the sources (Tab. 5.6).

Source	RA (J2000) hh:mm:ss	DEC (J2000) dd:mm:ss	source size arcmin	field size arcmin	exposure time hours
G 6.1-1.3	18:04:14	-24:21:44	35 × 25	40 × 30	2.5
G 38.7-1.4	19:06:59	04:29:20	22 × 22	30 × 30	1.8
G 39.9-2.8	19:14:12	04:57:37	28 × 18	35 × 25	1.8
G 75.8+8.1	19:50:51	40:58:52	7 × 6	15 × 15	1.0
G 80.7+6.8	20:14:48	47:11:23	6 × 6	15 × 15	1.0
G 178.2-3.3	05:28:37	28:39:54	8 × 7	15 × 15	1.0

Table 5.6: Source properties of the SNR candidates and 6-cm observational parameters.

The sources were scanned along constant Galactic latitude as well as along constant Galactic longitude with a scanning rate of about 1° per minute. Due to ground radiation, weather conditions and receiver instabilities, base levels of individual scans are not necessarily constant, appearing scanning effects like elongations of contour lines in the scan direction on a final map. In order to remove the baseline distortions, the method of unsharp masking was applied (Sofue & Reich, 1979). Finally, the two maps observed in orthogonal directions for each of the stokes parameters have been added using the PLAIT program (Emerson & Graeve, 1988), which minimize the effects of baseline drifts on raster-scanned data. In addition, all observations were performed almost during the night in order to avoid distortions in both the total intensity and the polarization data due to contribution of solar emission to the far sidelobes of the telescope (Kalberla et al., 1980).

- **G 6.1-1.3**

Although several H II regions are located in the field of G 6.1-1.3 (Lockman, 1989; Walsh et al., 1998) this sources was selected for a radio follow-up observation due to its strong radio emission overlapping very well with an X-ray source with an extent of about $22' \times 10'$ (Fig. 5.17 a). It is not unusual that SNRs are embedded in H II regions (Rosado et al., 1994) but it is very difficult to detect them due to the contamination of thermal radio emission from H II regions. Integrating the radio fluxes at 21 cm and 11 cm, the spectral index $\alpha = +1.37$ could be derived indicating thermal radio emission which is rather assigned to radio continuum from free-free emission. In addition, no polarized radio emission could be measured in the 6 cm observation indicating that the strong radio source corresponds to a H II region. This diffuse X-ray emission may come from star clusters (Sung et al., 2000) which are embedded in the H II regions (Corcoran, 1999). However, data from the IRAS survey at $60 \mu\text{m}$ show a bright infrared

source at the location of the extended X-ray source with almost the same morphology (Fig. 5.17 b). The infrared flux is 7760 Jy at $60\ \mu\text{m}$ and the radio flux 209 Jy at 21 cm (1.4 GHz) which leads to a $60\ \mu\text{m}/1.4\ \text{GHz}$ ratio of about 37 (cf. 3.2.3). Compared to the $60\ \mu\text{m}/0.843\ \text{GHz}$ ratio this analysis favours the SNR interpretation, but it is still an open question if there is SNR embedded in the H II regions or not.

G 6.1-1.3

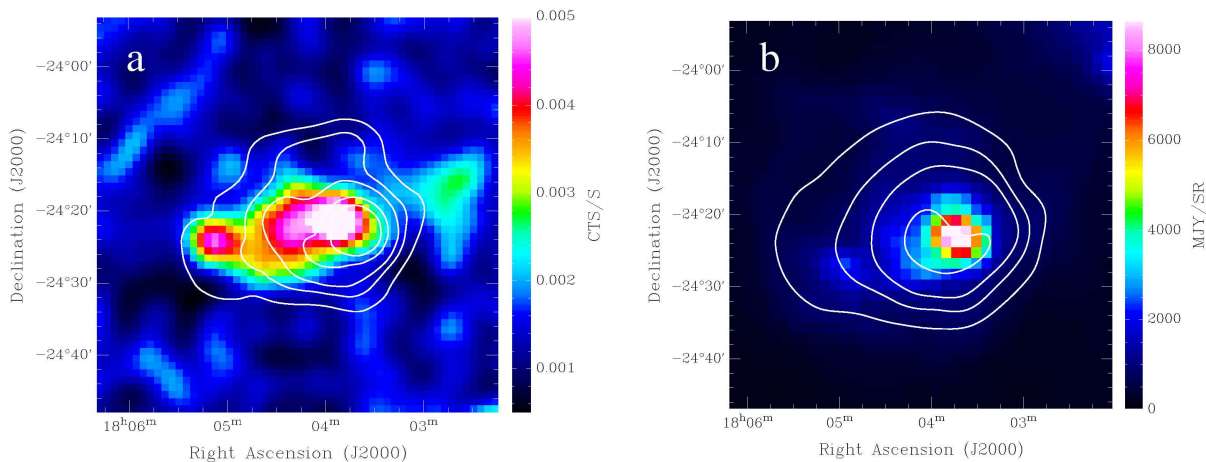


Figure 5.17: **a** Smoothed and vignetting corrected RASS image of G 6.1-1.3 overlaid with radio data from the Effelsberg 11 cm survey. The contour levels are: 2, 3.2, 4.4, 8.0, 12.0 and 19.9 Jy. **b** IRAS map at $60\ \mu\text{m}$ overlaid with radio data from the Effelsberg 21 cm survey with contour levels at 5, 10, 15 and 25 Jy. The X-ray and infrared emission region are matching very well.

- **G 38.7-1.4**

This candidate shows X-ray emission in the RASS with an extent of about $12' \times 8'$, surrounded by an incomplete and strong radio shell in the Effelsberg Galactic Plane 11 cm-survey data (Fig. 5.18 a). The distinct X-ray and radio morphology prompted a follow-up observation with the Effelsberg 100-m telescope at a wavelength of 6 cm in order to clarify the nature of the radio source. The total flux amounts to 1.64 ± 0.3 Jy in the 11 cm band. Using the data from the 6 cm observation as well the spectral index $\alpha = -0.79 \pm 0.23$ has been derived indicating non-thermal radio emission. In order to establish better the spectral index of the remnant, the 'T-T' method was used (Anderson & Rudnick, 1993). This technique determines the spectral index from the slope of the flux density S_1 versus S_2 within a specified region of the source by computing a linear regression between the intensities at two frequencies. Constant instrumental or real contamination effects are therefore reduced. The radio spectral index of -0.79 indicates that G 38.7-1.4 is a young SNR (while old shell SNRs tend to have

flatter spectra). The existence of polarization in the radio shell directly proves the SNR interpretation (Fig. 5.18 b). The central part of the incomplete radio shell shows strong radio emission at 6 cm as well as in the NVSS data at 20 cm. The spectral index of this compact radio source is $\alpha \sim -1.1$ indicating rather an extragalactic radio source. The polarized emission from this region is very faint and also shows a different orientation of the magnetic field lines compared to the remaining shell. The 11 cm survey data show additionally a second, fainter, incomplete radio shell in the west resulting in a total size of the radio remnant of $\sim 45' \times 30'$.

G 38.7-1.4

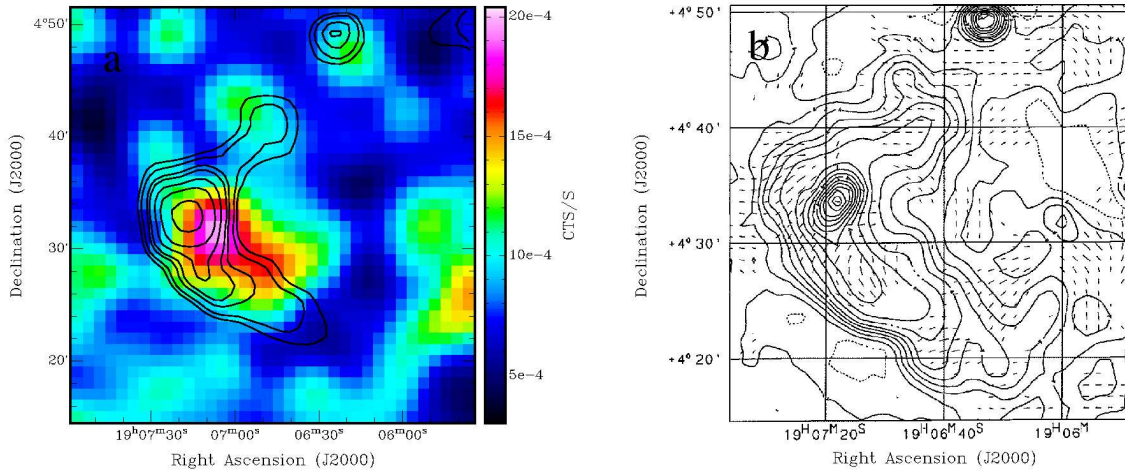


Figure 5.18: **a** Smoothed and vignetting corrected RASS image of G 38.7-1.4 overlaid with radio data from the Effelsberg 11 cm survey. The contour levels are: 80, 90, 105, 115, 135, 160 and 200 mJy. **b** 6 cm Effelsberg intensity map overlaid with polarization bars showing strong polarization over the entire radio shell. The contour levels are: -2, 4, 10, 16, 22, 30, 40, 50 and 60 mJy.

- **G 39.9-2.8**

This source was selected for a follow-up observation because of its strong X-ray emission which is correlated with radio emission at 11 cm, but G 39.9-2.8 is part of the large SNR W50 and therefore, probably does not account for a new SNR.

- **G 75.8+8.1**

The X-ray source has an extent of about $9' \times 7'$ and is close to the noise level. The region of radio emission in the NVSS data is located in the south-west of the X-ray source (Fig 5.19 a). A faint radio point source is located close to the center of the extended X-ray source. The Effelsberg survey data at 11 cm and 21 cm as well as a much deeper follow-up observation at 6 cm could not detect

significant radio emission in the field of G 75.8+8.1 (Fig. 5.19 b). Because of the missing radio emission in the 6 cm Effelsberg data the NVSS data are likely spurious radio features due to scanning effects during the survey.

G 75.8+8.1

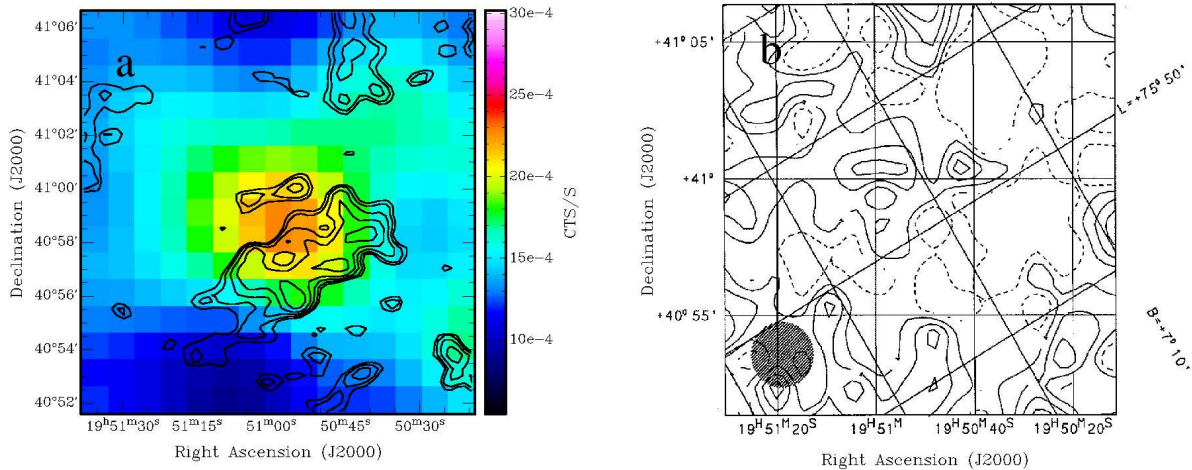


Figure 5.19: **a** Smoothed and vignetting corrected RASS image of G 75.8+8.1 overlaid with radio data from the NVSS survey. The contour levels are: 1.0, 1.4, 2.0, 2.8 and 4.0 mJy. **b** Intensity map of the 6 cm Effelsberg data showing no polarization at all. The contour levels are: -0.75, -0.25, 0.25, 0.75 and 0.125 mJy

- **G 80.7+6.8**

The small X-ray source with an extent of about $8' \times 8'$ is surrounded by an incomplete radio shell in the NVSS data at 20 cm (Fig. 5.20 a). A faint radio point source is located very close to the central brightened X-ray source. The radio flux of G 80.7+6.8 is marginally above the noise level in the NVSS data as well as in the Effelsberg data at 6 cm (Fig. 5.20 b). Using both data sets the spectral index could be determined as $\alpha \approx -0.9$ with high uncertainty due to small flux values. No significant amount of polarization could be detected. Although non-thermal radio emission was detected, the nature of G 80.7+6.8 is still unclear.

- **G 178.2-3.3**

This source is a central brightened X-ray source with an extent of about $9' \times 9'$. An elliptical region of radio emission at 11 cm is overlapping the X-ray source very well (Fig. 5.21 a). A follow-up observation at 6 cm could resolve the radio source into three separated radio sources, one of them showing two peaks (Fig. 5.21 b). The spectral indices are varying from +0.36 to -1.29 showing an reverse spectrum of thermal and non-thermal radio emission. The 6 cm radio map shows

G 80.7+6.8

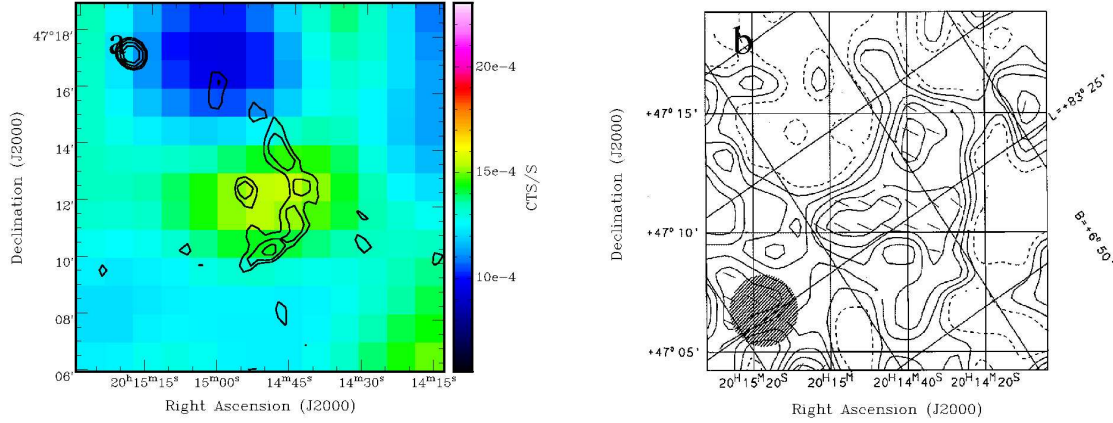


Figure 5.20: **a** Smoothed and vignetting corrected RASS image of G 80.7+6.8 overlaid with radio data from the NVSS survey. The contour levels are: 1.0, 1.4, 2.0 and 2.8 mJy. **b** Intensity map of the 6 cm Effelsberg data showing faint polarization across the radio source. The contour levels are: -1.25, 1.25, 3.75, 6.25 and 11.25 mJy.

polarization in all three radio sources but rotated relatively with 90° in the sources which are located west and north-west of the central bright radio source. G 178.2-3.3 can probably be attributed to independent galactic and/or extragalactic sources rather than a radio SNR.

G 178.2-3.3

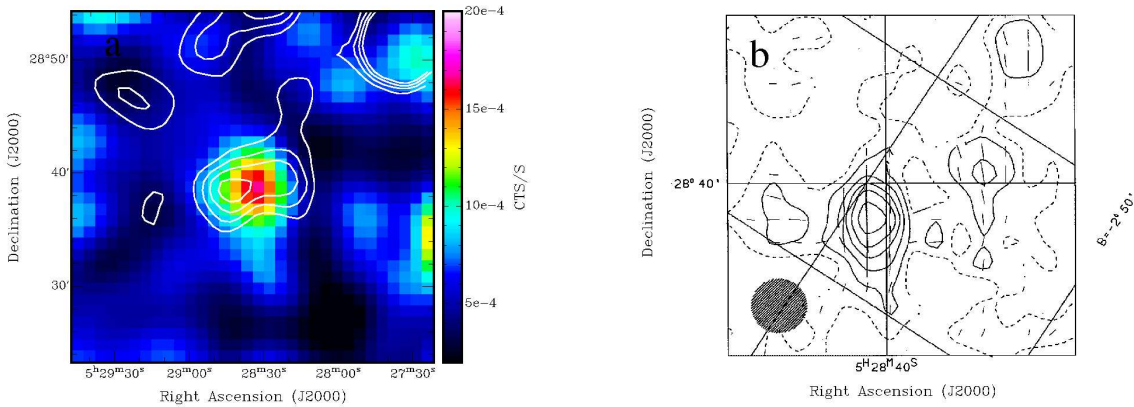


Figure 5.21: **a** Smoothed and vignetting corrected RASS image of G 178.2-3.3 overlaid with radio data from the Effelsberg 11 cm survey. The contour levels are: 12, 24, 36 and 48 mJy. **b** Intensity map of the 6 cm Effelsberg data showing the radio source resolved into three separated sources where the direction of polarization is rotated with 90° against each other. The contour levels are: 0.25, 0.75, 1.50, 2.25, 3.00 and 4.00 mJy.

5.4 Radio Follow-up Observations With ATCA

Two X-ray selected SNR candidates, G 296.7-0.9 and G 308.3-1.4, were observed on 1st and 2nd September 2001 with ATCA. A technical problem with one antenna and bad weather on the second observation day prevented the completion of the proposed observations. Subsequently, these two SNRs were proposed for radio-continuum observations once more and also accepted for observations with ATCA on 10th and 11th January 2002.

High-resolution radio-continuum observations at $\lambda=20+13$ cm were performed, measuring, additionally, the polarization of the radio emission. The exposure time of each source was 13 hours. The 750 m configuration was used in order to achieve a resolution of 45'' at $\lambda=20$ cm and 25'' at $\lambda=13$ cm. The primary beam at $\lambda=20+13$ cm (33'/22') is larger than the angular size of the SNR candidates, and thus completely covers both sources.

The data reduction is more complicated for interferometric radio telescopes due to the incomplete measurement of the u-v plane. First, scanning and self-interference effects as well as fluctuations in the instruments have to be removed before continuing with the calibration of the telescopes. During an observation period, a primary and secondary calibrator source is observed in addition to the source field of interest. Since the Stokes parameters of the calibrator sources are known, the first calibrator source which is usually a strong and unpolarized source is used to calibrate the total flux density whereas the second calibrator source determines all the calibration quantities except the absolute flux density (Hamaker & Bregman, 1996; Rohlfs & Wilson, 1996). ATCA samples the u-v plane at discrete points, i.e. there is incomplete knowledge about the Fourier transform of the source intensity distribution, and thus the images ('Dirty Maps') have to be 'cleaned' using a deconvolution algorithm in order to remove the sidelobes of the dirty beam. Two techniques exist, namely CLEAN (Marsh & Richardson, 1987) and the maximum entropy method (MEM; Cornwell & Evans (1985)). The final step of the data reduction procedure is the application of the so-called self-calibration technique. Since the basic calibrator gains do not determine the antenna gains perfectly at each time stamp due to atmospheric turbulences which cause phase and amplitude shifts, the self-calibration technique is used to find antenna gains which minimize the difference between the measured and the model visibilities. This procedure had to be performed iteratively until no improvement in the image quality can be done using a model visibility which is generally derived from a model image.

All data reduction steps regarding ATCA data were performed using the 'Multi-channel Image Reconstruction, Image Analysis and Display' package MIRIAD⁶ (Sault et al., 1995).

⁶<http://www.atnf.CSIRO.au/computing/software/miriad/>

5.4.1 G 296.7-0.9

G 296.7-0.9 was observed during the ROSAT all-sky survey for about 375 s and shows a compact or center-filled X-ray source which has an elongated shape. It is located in the H II region [CH87] 296.593-0.975 (Russell, 1997) which is partly overlapping with the area of radio emission. The source has an extent of about $15' \times 10'$ in X-rays and at radio wavelength and has its geometrical center at R.A.= $11^h 55^m 54^s$ and DEC= $-63^\circ 05' 51.''$ (J2000.0). A pointed ROSAT HRI observation shows an incomplete shell in the east, supporting strongly the SNR interpretation. This can also be confirmed by two pointed observations with the PSPC providing additionally spectral information.

X-ray emission

In 1998, ROSAT performed a pointed HRI observation with an exposure of ~ 28.2 ks and two pointed PSPC observations with a total exposure of ~ 9.7 ks. Both data sets show an incomplete bright X-ray shell in the east. Figure 5.22 shows the ROSAT HRI image overlaid with radio contour lines from the MOST.

After merging both PSPC data sets a spectral analysis of the X-ray bright shell could be performed with relatively high photon statistics. The background was extracted from a region close to the remnant with the same exposure time. The spectrum has been fitted with a single-temperature Raymond-Smith and Bremsstrahlung model. Both models provide acceptable fit results according to reduced χ^2 . The results are listed in Table 5.7. The local density can be calculated from the distance d and the

Models	N_H [10^{22} cm $^{-2}$]	kT [keV]	Flux	red. χ^2
Raymond-Smith	1.42 ± 0.33	0.22 ± 0.13	0.92	1.16
Bremsstrahlung	0.62 ± 0.30	0.33 ± 0.15	0.97	1.16

Table 5.7: Spectral fit results of G 296.7-0.9. The flux is in the unit [10^{-12} erg cm $^{-2}$ s $^{-1}$] and refers to the full energy band [0.1-2.4 keV].

emission measure (EM) which can be derived as a fit parameter from the corresponding Raymond-Smith model. The fit parameter K which includes the emission measure is generally given as:

$$K = \frac{EM}{10^{14} 4 \pi d^2} = \frac{\int n_e n_H dV}{10^{14} 4 \pi d^2} \quad (5.1)$$

with d the angular size distance to the source follows:

$$n_e = \sqrt{\frac{3.6 \cdot 10^{14}}{d \cdot \tan^3(\phi)}} \quad (5.2)$$

ϕ describes the half angular extent of the source. Describing the spectrum with a Raymond-Smith model, the best fit yield an emission measure $EM=0.12$ cm $^{-5}$. The emission measure gives the electron density, assuming a uniform sphere of emission,

G296.7-0.9

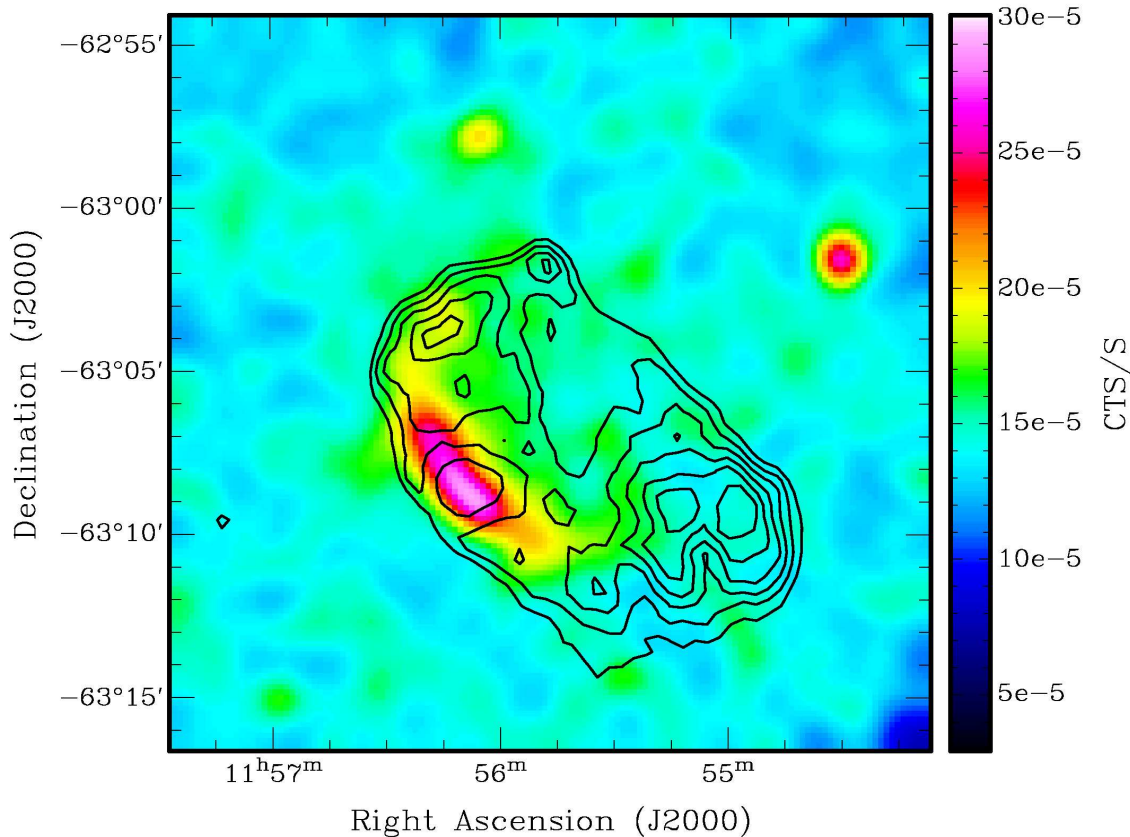


Figure 5.22: Exposure-corrected ROSAT HRI image of G 296.7-0.9 overlaid with MOST survey data at 843 MHz with a half-power beamwidth of $43''$. The MOST contour lines correspond to 10, 15, 20, 25, 30 and 35 mJy. The incomplete X-ray shell in the east shows a very good correlation with the radio emission. The bright X-ray point source in the north-west is positionally coincident with the star HD 103442.

of $n_e=0.375 \text{ cm}^{-3}d^{-1/2}$, with d the distance in kpc. A Sedov model with Raymond-Smith emissivity has been used to reproduce the observed brightness, temperature and angular size of G 296.7-0.9. The explosion energy is taken as a free parameter in the

E_0 [10^{51} erg]	d [kpc]	r [pc]	v [km/s]	t [10^3 yr]	n_0 [cm^{-3}]
0.10	1.8	7.9	440	4	0.27
1.00	4.5	19.8	440	10	0.18

Table 5.8: Spectral solutions of the Sedov model for G 296.7-0.9 using different initial explosion energies (cf. 3.2.2).

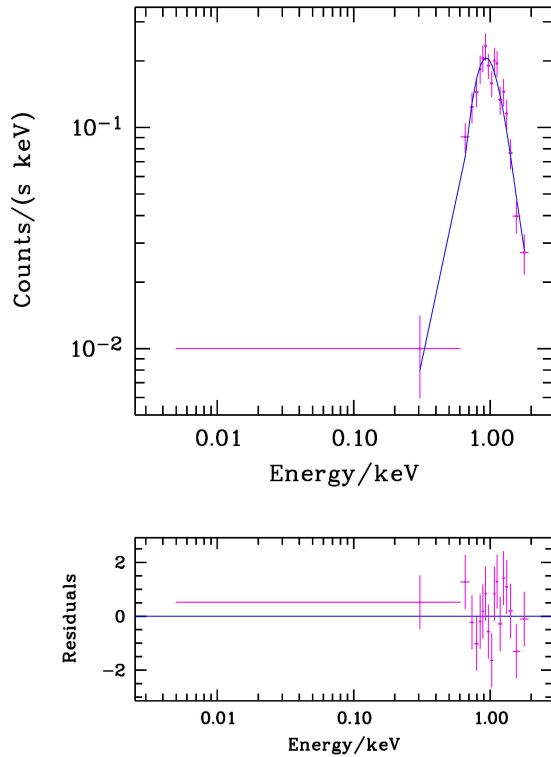


Figure 5.23: Count rate spectrum of G 296.7-0.9 from two merged PSPC datasets fitted with a Raymond-Smith model. The residues are shown below.

Sedov model (cf. 3.2.2) in the range of $0.1-1.0 \times 10^{51}$ erg. The Sedov parameters for the energy range $0.1-1.0 \times 10^{51}$ erg are given in Tab. 5.8. The X-ray data are indicating that G 296.7-0.9 is a relatively young SNR with an age between 4,000 and 10,000 years and a minimum distance of about 1.8 kpc.

Radio emission

In radio, G 296.7-0.9 was observed with ATCA at 13 and 20 cm. The 13 cm data, unfortunately, could not be used because of calibration problems. Figure 5.24 shows the ATCA image at 20 cm. No significant polarized emission could be detected at 20 cm. Nevertheless the MOST survey data at 843 MHz have been used to determine the spectral indices of the bright radio emission region in the north-east as well as the south-west. The radio emission region in the south-west of G 296.7-0.9 correspond very well with the H II region [CH87] 296.593-0.975 which is confirmed through a spectral index of $\alpha \sim +1.46$. The major part of the radio emission therefore originates from the continuum from free-free emission. The radio emission region in the north-east which matches very well the incomplete X-ray shell has a spectral index $\alpha \sim -0.30$. Worth mentioning is that a radio point source appears close to the center of G 296.7-0.9 at R.A. = $11^h 55^m 43.3^s$ and DEC = $-63^\circ 06' 57.7''$ (J2000.0). This radio source, however, has no X-ray counterpart in the ROSAT HRI data, but two faint optical counterparts in the DSS2red (Fig. 5.25).

G 296.7–0.9

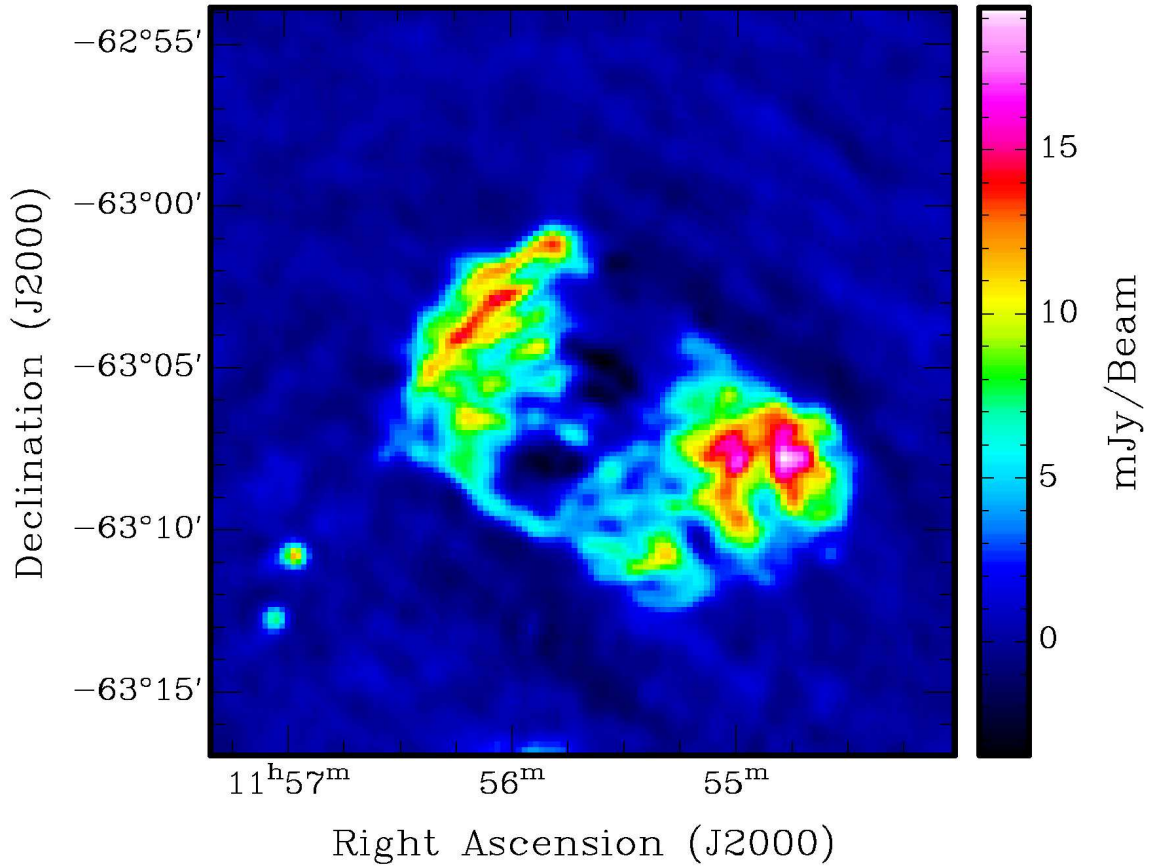


Figure 5.24: ATCA image at 20 cm with a half-power beamwidth of $43''$. The colour bar shows the radio flux distribution across the remnant. A radio point source shows up close to the center of G 296.7-0.9.

Optical emission

No filaments in $H\alpha$ could be found in the field of G 296.7-0.9 using the UKST/AAO $H\alpha$ Galactic Plane Survey. The high galactic absorption (Tab. 5.7) could be the reason that no filaments in $H\alpha$ could be found.

Conclusion

In X-rays, G 296.7-0.9 was first observed during the ROSAT all-sky survey showing an extended X-ray source which matches very well with radio emission using the MOST. Pointed X-ray observations with ROSAT HRI and PSPC reveal an incomplete and extended X-ray shell and provide a temperature $kT = 0.22$ keV and an X-ray flux $f_x = 0.92 \times 10^{-12}$ erg cm^{-2} s^{-1} indicating a new supernova remnant. A Sedov analysis

G 296.7-0.9

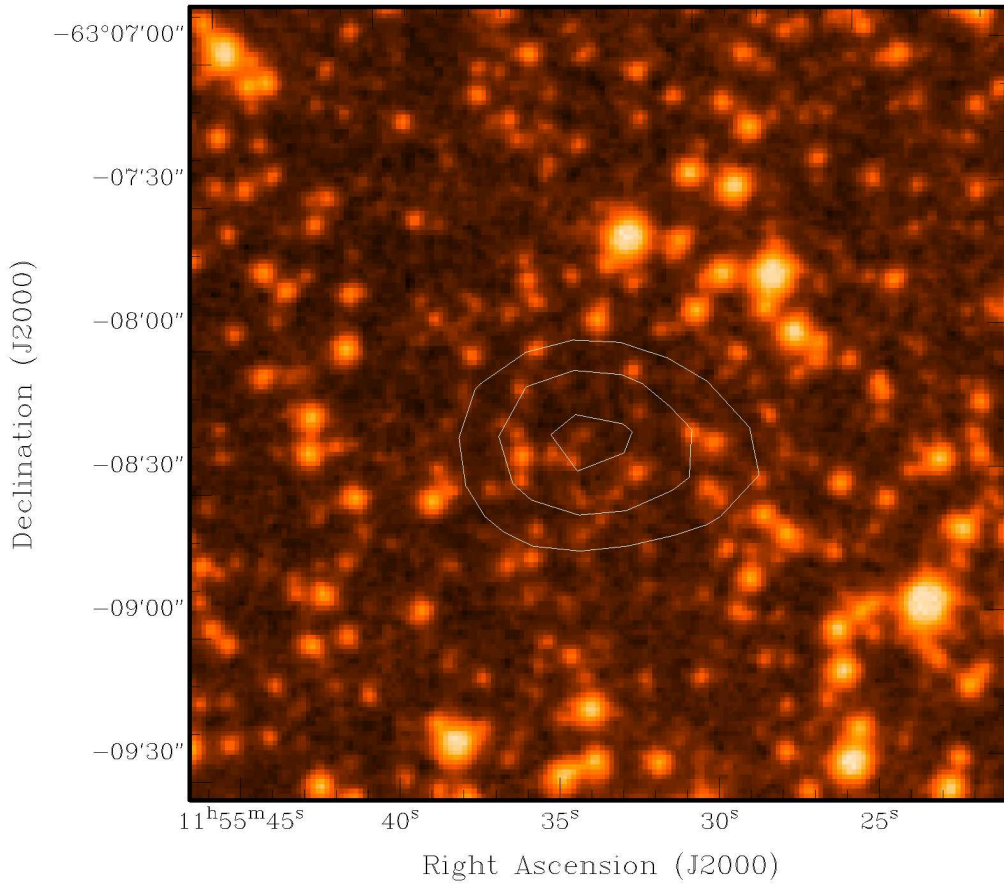


Figure 5.25: Optical DSS2red image from the central part of G 296.7-0.9 overlaid with ATCA data at 13 cm. The contour levels are: 2, 3 and 4 mJy. Two faint sources in the optical wavelength appear at the location of the central radio point source.

could restrict the SNR parameter which point to a young SNR with an age between 4,000 and 10,000 years. The radio data from MOST and ATCA exhibit thermal radio emission from the H II region [CH87] 296.593-0.975 in the south-west of G 296.7-0.9 and non-thermal radio emission with $\alpha = -0.30$ in the north-east where the incomplete X-ray shell is located. The X-ray as well as radio data leave no doubts about the presence of a young supernova remnant. The lack of significant H α emission in the region of G 296.7-0.9 can be explained by strong interstellar absorption.

5.4.2 G 308.3-1.4

G 308.3-1.4 was observed during the ROSAT all-sky survey for about 240 s and appears as a spherical center-filled X-ray source partly overlapping with the two radio arcs

(Fig. 5.26). It is listed as a possible SNR in the MOST supernova remnant catalogue (Russek, 1997) based on the composite radio morphology and the ratio of $60\ \mu\text{m}$ to 843 MHz flux densities (Whiteoak & Green, 1996).

X-ray emission

In X-rays, G 308.3-1.4 shows a spherical center-filled X-ray source with a diameter of about $10'$. The measured ~ 110 X-ray source counts from G 308.3-1.4, however, do not allow a proper spectral analysis and therefore the identification of the X-ray source. More than half of the source photons have energies larger than 1 keV indicating a hard X-ray source which is also expressed by the hardness ratio $\text{HR}1 = +0.95$ and $\text{HR}2 = +0.43$ (cf. A.1). The hard X-ray emission can be ascribed to the

G 308.3–1.4

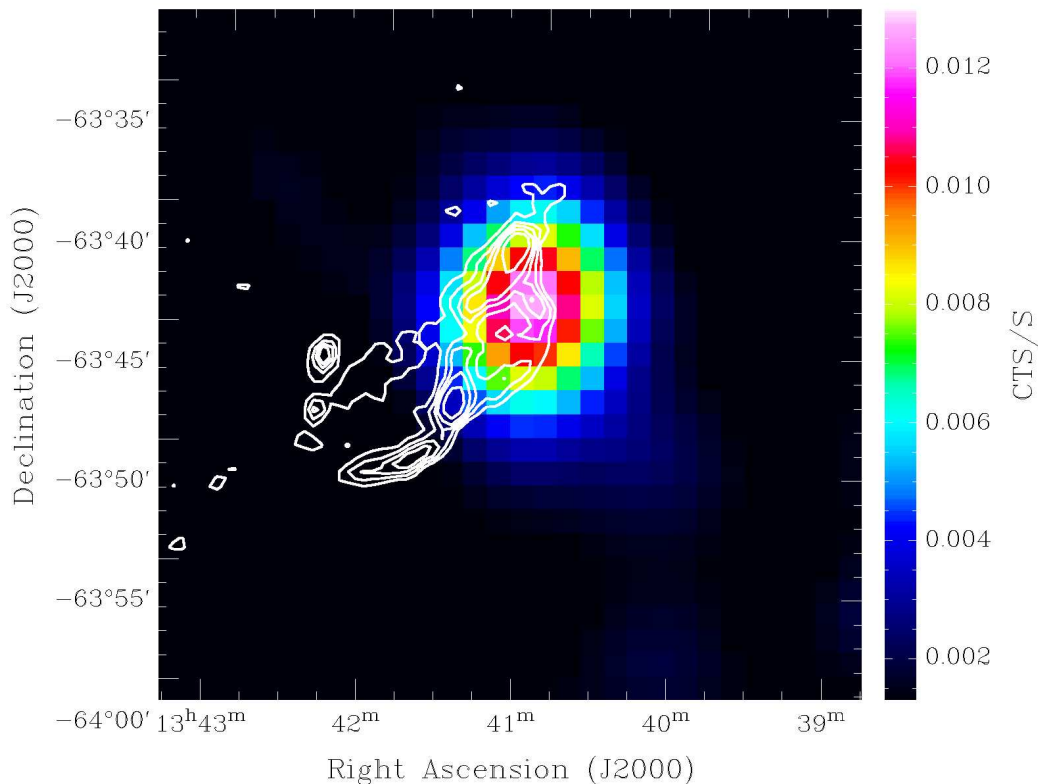


Figure 5.26: ROSAT RASS image of G 308.3-1.4 overlaid with MOST survey at 0.843 GHz. The half-power beamwidth of the radio telescope is $43''$. The MOST contour lines correspond to 4, 8, 12, 16 and 25 mJy. The radio emission consists of two incomplete arcs matching with the extended X-ray emission.

high Galactic absorption of $N_H = 1.64 \times 10^{22}\ \text{cm}^{-2}$ in the direction of G 308.3-1.4 (Dickey & Lockman, 1990) which absorbs the soft X-ray photons or a very hot plasma

with temperature $T > 6 \times 10^6$ K. There are two explanation of this scenario, whereas one of them favours a very young supernova remnant with hard X-ray emission whose origine is from a hot plasma and the other a highly absorbed X-ray source which is possibly located at the edge of the Galaxy or even of extragalactic origin.

Radio emission

The radio morphology in the MOST data shows two radio arcs which can be confirmed in the ATCA data at 13 cm as well as 20 cm (Fig. 5.27). Using the ATCA data at both frequencies, the spectral index $\alpha = -0.71 \pm 0.34$ could be derived indicating non-thermal radio emission which extend in two arcs. The two radio bright knots within the arc structures have spectral indices $\alpha = -0.05 \pm 0.34$ (northern knot) and $\alpha = -0.12 \pm 0.34$ (southern knot), respectively. No significant polarized radio emission could be detected.

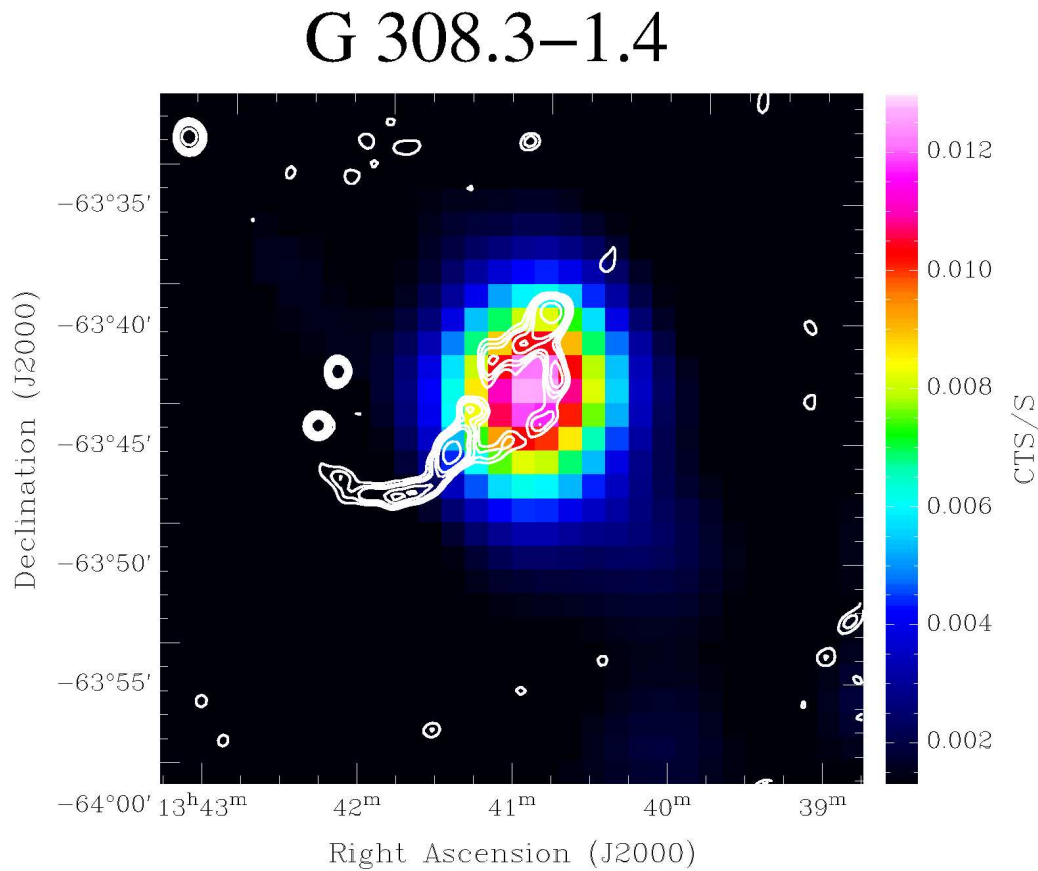


Figure 5.27: ROSAT RASS image of G 308.3-1.4 overlaid with ATCA data at 20 cm (1.4 GHz). The half-power beamwidth of the radio telescope is $43''$. The ATCA contour lines are 2, 3, 4, 6, 8 and 15 mJy. The radio emission consists of one incomplete arc matching with the extended X-ray emission.

Conclusion

The MOST as well as the ATCA radio data favour the SNR interpretation due to the morphology of the two extended radio arcs and the spectral index of $\alpha = -0.71 \pm 0.34$. The two radio bright knots do not have bright optical or X-ray counterparts and do not seem to be of extragalactic nature due to their very flat non-thermal spectrum. The X-ray data, however, do not allow an accurate interpretation of G 308.3-1.4 whereas the X-ray source can be possibly of different source origin than the two extended radio arcs. Further X-ray observations are necessary to identify the spherical X-ray source and to determine if the X-ray source is associated with the radio arcs or not.

5.5 X-ray Emission From the SNR G 67.7+1.8

The SNR G 67.7+1.8 was first detected in a galactic plane radio survey at 327 MHz by Taylor et al. (1992) using the Westerbork Synthesis Radio Telescope. It is characterized by an angular diameter of $\sim 9'$, a flux of $\sim 1.2 \times 10^{-21}$ at 1 GHz (Taylor et al., 1992) and a distance of ~ 7 -27 kpc through the Σ -D relation. Filamentary and diffuse emission have been discovered from optical imaging and spectroscopic observations (Mavromatakis et al., 2001).

A search in the RASS data shows X-ray emission at the same location of the radio remnant and optical filaments (Mavromatakis et al., 2001). This part of the sky was observed with a total exposure time of ~ 530 s. About 73 events above the background level have been detected in a circular area of $4'$ radius at energies higher than 0.5 keV. The region of the X-ray emission is very well correlated with the 1.4 GHz NVSS survey. In X-rays, G 67.7+1.8 shows strong emission in the hard energy band of ROSAT and has shell-like morphology with central brightening, suggesting the existence of a central neutron star or synchrotron nebula. According to the NVSS data (Fig. 5.28), two faint radio sources appear close to the center of G 67.7+1.8 where the X-ray emission peaks. These sources could be indicative of emission from a young neutron star. The sensitivity and spatial resolution in the RASS data preclude a further statement on the nature of the central brightening of the X-ray emission. Lorimer et al. (1998) searched for radio emission from a pulsar within G 67.7+1.8, using the Jodrell Bank Radio facility. No radio pulsar was detected down to a level of 0.8 mJy.

G 67.7+1.8 is a very interesting SNR showing some characteristics of Crab-like SNRs in X-rays but also clear evidence of a shell-like morphology according to the radio data. Due to the X-ray and radio morphology, G 67.7+1.8 seems to belong to the class of mixed morphology which combines elements from the shell-like and Crab-like remnants. The nature of the central part of the remnant is still unclear and requires subsequent high-resolution radio as well as X-ray observations.

G 67.7+1.8

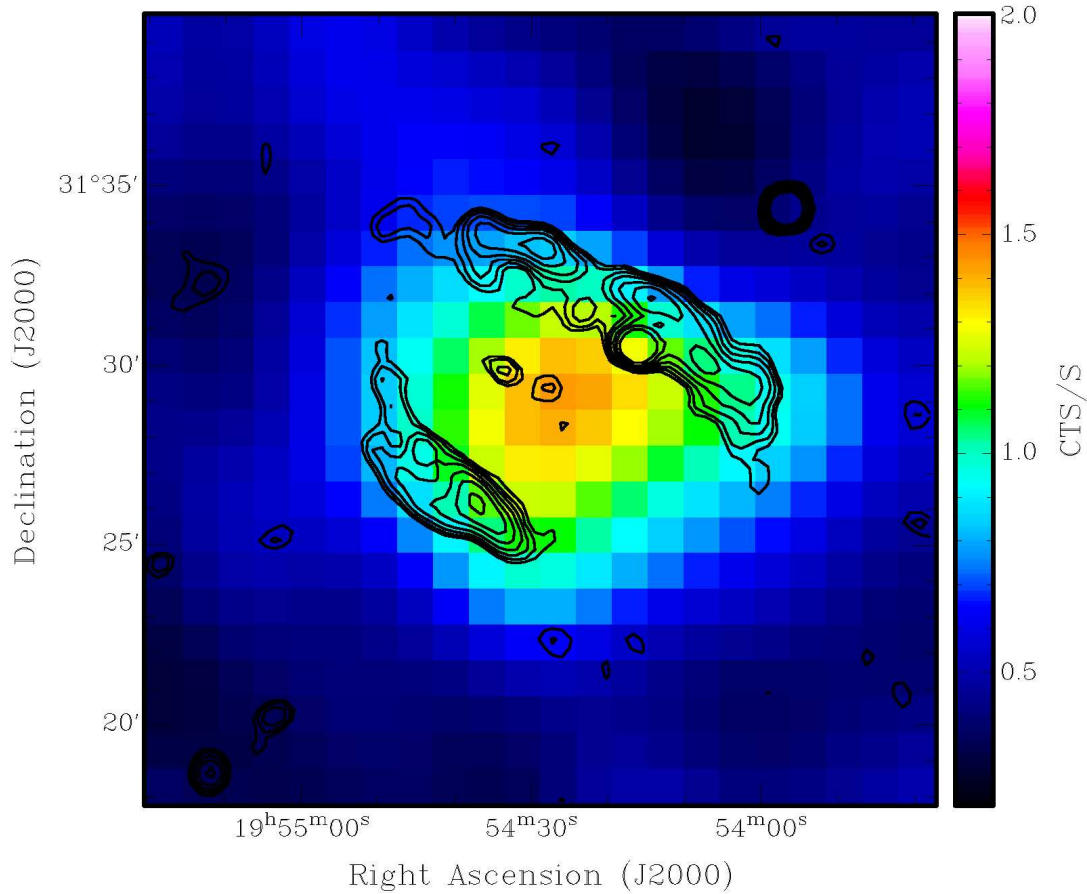


Figure 5.28: Exposure-corrected and smoothed ROSAT PSPC image of G 67.7+1.8 overlaid with radio contour lines from the NVSS at 1.0, 1.4, 2.0, 2.8, 4.0, 5.6 and 8.0 mJy. The X-ray image has a bin size of $1'$. The target appears center-filled in X-rays and has a bilateral radio arc structure. Two radio point sources turn up close to the geometrical center of the remnant.

5.6 Conclusion and prospects

Starting from originally 373 targets which were proposed to be SNR candidates in X-rays (Busser, 1998), many of the smaller targets ($5' \leq D \leq 30'$) could be identified by correlating them with various source catalogues but the nature of the larger candidates ($D \geq 30'$) is still unclear. All targets inclusive their source properties are listed in the appendix A whereas the images are shown in appendix B.

The following summary gives an brief overview of the results from the re-analysis campaign of the original 373 RASS candidates:

- 2 targets could be identified as SNRs (cf. Tab. A.1)

(G 38.7-1.4 and G 296.7-0.9)

- 9 targets are very promising SNR candidates (cf. Tab. A.2)
- 99 targets emerge as spurious background features
- 59 targets could be assigned mainly to extragalactic objects like clusters of galaxies (cf. Tab. A.5)
- 90 targets with extended X-ray emission but without typical shell structure in X-rays/radio (cf. Tab. A.3)
- 114 targets show poor evidence of typical properties of SNRs and lie in complex and crowded regions of X-ray and radio sources (cf. Tab. A.4)

The re-analysis of the RASS data shows that most of the SNR candidates which were found by Busser (1998) are spurious background features, targets which were assigned to extragalactic objects and X-ray bright stars or targets which show insufficient evidence in the X-ray and radio data to be classified as SNRs. Only two targets could be identified as SNRs due to their specific properties in the X-ray and radio data leaving 90 targets of originally 373 sources which are still possible candidates of SNRs.

Figure 5.29 depicts the distribution of the 373 RASS SNR candidates, plotted according to their position in Galactic coordinates. The distribution of the candidates shows a roughly uniform distribution of the SNR candidates. The two identified SNRs, as well as the most promising SNR candidates, are located near the Galactic plane in the 2nd and 3rd quadrants, respectively, where most of the known Galactic SNRs (from Green (2002)) are situated. The less significant candidates are distributed roughly uniformly across the sky with a slight concentration towards the Galactic center. They do not follow the distribution of the known Galactic SNRs and would therefore verify the l -dependent Σ -selection effect of the radio SNRs in the case they can be identified indeed as SNRs. The targets which have been identified as extragalactic objects are also distributed almost uniformly across the sky, but are situated more distant from the Galactic plane as expected.

Busser (1998) performed a simulation of the theoretical distribution of SNe and their remnants in order to estimate the number of X-ray SNRs which should be detectible in the ROSAT all-sky survey. The Galactic model which was used for the simulation describes the spatial structure of the Galaxy taking the distribution of the progenitor stars of SNe Ia in the disc and halo/bulge as well as the distribution of the core-collapse SNe (type Ib and II) in two spiral arms into account. In order to simplify the simulation, the density distribution of the ISM was approximated by an exponential decrease while increasing the radial distance from the Galactic center and increasing the distance from the Galactic plane. Busser also chose 1 particle cm^{-3} as the local density at the location of our sun and an initial explosion energy of 10^{51} ergs for all SNRs (canonical values). The total Galactic SN rate was assumed to be 2.5 SNe century⁻¹ according to Tammann et al. (1994). Finally, he fixed a diameter $\geq 15'$, a significance $\geq 2\sigma$ compared to the background and ≥ 50 recorded counts as a criterium

of observability. Smaller SNRs have been accepted with more than 1000 counts, thus, Busser could find about 215 SNRs in his simulation fulfilling the conditions which are described above. Based on the re-analysis of the RASS data, 215 targets belong to the category of identified or possible SNRs even though most of them show poor evidence of typical properties of SNRs. This number is in best agreement with the results from the simulation. As mentioned above the majority of SNR candidates, however, do not allow any predictions on their nature and therefore could also be assigned to extragalactic objects. This means that the probable number of observable X-ray SNRs seems to be much smaller than determined in the PhD thesis of Busser (1998). The new assumption of less SNRs, resulting from this re-analysis, is not inconsistent with the simulation because the variation in interstellar absorption, initial explosion energy or geometrical factor which determines the geometrical distribution of X-ray emitting gas and thus the phase of the SNR evolution increase or decrease significantly the number of observable SNRs. For example, the increase of the interstellar density in the order of 10% lead to 6% less X-ray SNRs in the simulation. The reduction of the initial explosion energy of a factor 2 decrease even the number of X-ray SNRs by 24%. Taking all variation effects into account and considering only the decrease of observable X-ray SNRs about 100 SNRs are expected from the simulation. However, it is not possible to clarify, which physical parameter is responsible for the lower number of observed SNRs and which physical parameter can be restricted.

Concluding the identification campaign of Galactic SNRs in the ROSAT all-sky survey, only a total of two targets have been identified as SNRs whereas 59 targets have been identified as extragalactic objects or X-ray bright stars. A smaller number of targets, only 99 objects, is still expected to be SNRs from the re-analysis of the RASS data disregarding the spurious background features and the targets which show poor evidence of typical properties of SNRs. Nevertheless the results from the simulation do not conflict with the observed SNR candidates and seem to specify the lower number of SNRs. A smaller number of Galactic SNRs could therefore indicate a lower average explosion energy, a smaller Galactic SN rate than 2 events per year (Dragicevich et al., 1999) and/or higher interstellar density. The results of the identification campaign finally show that less candidates are present and therefore less SNRs are expected compared to previous assumptions.

Some SNR candidates show very faint or no radio emission which can be explained in the case of an identification as a SNR by a weak magnetic field and/or low density of relativistic electrons. SNRs which are embedded in very dense regions like molecular clouds and H II regions should have a low density gradient between the dense surrounding and the ejecta and therefore a less efficient acceleration mechanism at the shock front. Therefore it is difficult to detect their radio-continuum. This type of radio-faint SNRs can be ascribed to a very dense ISM in which the progenitor star exploded earlier.

The ROSAT all-sky survey, the foundation of this identification campaign, will also be in future, a powerful database to search for further unidentified and extended X-ray

sources. After the failure of the X-ray satellite ABRIXAS a new X-ray observatory has been proposed, called ROSITA⁷ (Röntgen Survey with an Imaging Telescope Array) with the scientific goal of surveying the whole sky in an energy range up to 10 keV with an average sensitivity of 6×10^{-14} erg cm⁻² s⁻¹ (0.5-7.0 keV) for point sources. With its seven individual mirrors an angular resolution of 1' can be achieved. The detectors will consist of an advanced version of the pn-CCD which is successfully in operation on XMM-Newton. It is planned to install ROSITA on the International Space Station (ISS). The large energy range and higher sensitivity compared to the RASS would allow to detect high absorbed galactic X-ray sources and to perform highly resolved spectral analysis due to the pn-CCD. ROSITA should consequently reveal many more (highly absorbed) SNRs and SNR candidates in X-rays and allow a more detailed analysis of the source properties. The launch of the ROSITA is planned for 2009, if the mission is approved by ESA.

In the radio band the next generation radio telescope with sensitivity in the order of two magnitude higher than any existing telescope is planned, called the Square Kilometer Array (SKA) with an effective collecting area of 1 square-kilometer (Ekers, 1999). The SKA will be an interferometric array of individual 100m-antennas performing high angular resolution (0.1'' at 1.4 GHz) and high imaging dynamic range. It would allow to detect old and therefore very faint SNRs as well as young SNRs which occurred in low density regions of the ISM and thus are faint and/or resolve the distant and thus angularly small objects. The SKA is expected to be completed in the decade 2010-2020.

The realization of ROSITA as well as SKA would signify a large step in identifying new SNRs and studying the known remnants in more detail. A better understanding of the dynamic evolution of SNRs would also lead to more accurate estimates of existing SNRs in our Galaxy.

⁷Proposal available at: http://wave.xray.mpe.mpg.de/rosita/proposal/rosita_esa_proposal_8.pdf

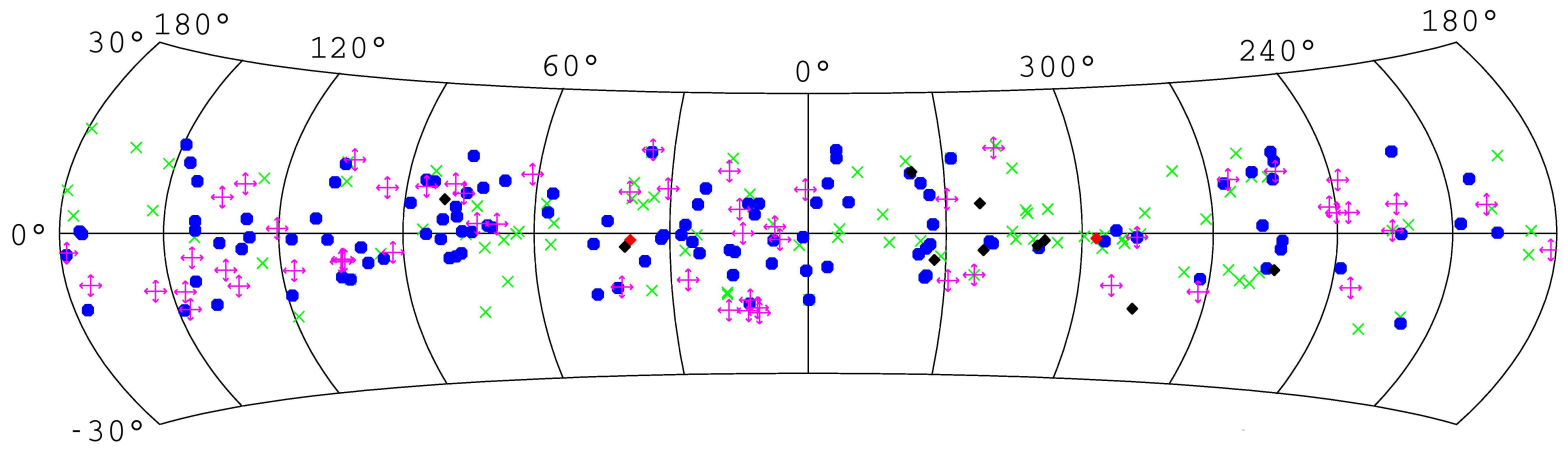


Fig 5.29: The distribution of 274 targets (excluding the 99 spurious background features) across the sky, obtained from the ROSAT all-sky survey. The two identified SNRs are presented by red diamonds, the most promising candidates by black circles, the good candidates by green crosses, the candidates of poor evidence for SNRs by blue circles and finally the targets which are probably of extragalactic origin by violet crosses. The image is an Aitoff-Hammer projection in Galactic coordinates.

Chapter 6

SNRs With Compact Objects

In this chapter the X-ray properties of three well-known SNRs, which have been observed with ROSAT, Chandra and XMM-Newton are described. RCW 103 and G21.5-0.9 are small diameter SNRs harbouring a compact object almost in the center of the remnant. G65.3+5.7, however, is a large extended SNR which was first discovered in radio and later mapped completely in X-rays using the ROSAT all-sky survey and 17 pointed PSPC observations.

6.1 RCW 103

RCW 103 (G 332.4-0.4) is a shell-type SNR with a central compact X-ray source (Garmiere & Tuohy, 1979). The remnant shows emission over a large frequency band from radio up to X-rays. It has a diameter of $\sim 9'$ in X-rays as well as in radio. It was first observed in the radio band by Shaver & Goss (1970) detecting a non-thermal radio shell traced by the optical filaments (van den Bergh, 1978). Further high-resolution radio observations with ATCA show an almost complete and circular shell which is weakly polarized at only a few spots (Dickel et al., 1996). The mean spectral index of the radio spectrum of the whole remnant is -0.56. ISO infrared observations indicate that the remnant appears to be interacting with a molecular cloud on the southern side (Oliva et al., 1999). Optical filaments exist in the south-east and north-west parts of the remnant. Four pointed observations were performed using the Einstein Solid State Spectrometer (SSS) to map the whole remnant (Nugent et al., 1984). Despite the low sensitivity and spectral resolution of the Einstein SSS a NEI (non-equilibrium ionization) model could be applied resulting in a low and high electron temperature of 0.51 keV and ≥ 6 keV, respectively. The galactic absorption was determined to be $5.9 \times 10^{21} \text{ cm}^{-2}$. The initial explosion energy could be adopted to be $\leq 6 \times 10^{50}$ ergs and thus it was assumed that RCW 103 originates from a Type Ia SN. The age of the remnant is assumed to be ~ 2000 years and the distance to be 3.3 kpc.

RCW 103 is of particular interest since Tuohy & Garmire (1980) have discovered the compact X-ray source 1E 161348-5055 in the center of the remnant using the Einstein Observatory. Its location, coupled with the lack of optical and radio emission prompted them to suggest 1E 161348-5055 to be an isolated cooling neutron star.

6.1.1 X-ray Studies of the Remnant

RCW 103 was observed with XMM-Newton on 3rd/4th September 2001 using the MOS 1 and 2 in the full window mode and the PN in the small window mode. In all three cases a medium optical blocking filter was used. RCW 103 was observed for 20 ks and additionally 30 ks but 7' off-axis aimed to observe the 69 ms Pulsar PSR J161730-505505 which is located north of RCW 103. Only the 20 ks on-axis observation has been used for the source analysis performing sufficiently high photon statistics. Due to soft proton flares causing flux variabilities in the hard energy band above 10 keV and occasional higher background level a dataset of ~ 16.0 ks was available for the following analysis.

Spatial analysis

RCW 103 is a nearly circular SNR with a diameter of $8' \times 9'$. The MOS datasets show strong X-ray emission in the south and south-east and also a bright X-ray emission region in the west (Fig. 6.1,6.2). The compact X-ray source 1E 161348-5055 is situated in the geometrical center of RCW 103 at $R.A. = 16^h17^m36^s$ and $Dec. = -51^\circ02'23''$. In addition, Fig. 6.1 shows the energy distribution of X-ray photons across the remnant in three different energy bands.

Most of the X-ray emission of the remnant is relatively soft, i.e. below 2 keV, except for the X-ray photons from the central point source which are detected up to ~ 8 keV. The radio emission of RCW 103 at 13 cm is also highest in the south, south-east and in the west, corresponding to the brightest knots of X-ray emission (i.e. the synchrotron emission from non-thermal electrons which forms the radio shell matches very well with the bright region of X-ray emission (Fig. 6.2,6.3)).

Beside the bright X-ray emission in the south and south-east, the remnant also shows a lack of bright X-ray emission in a small strip which extends from the south-west to the north-east across the remnant. This fact can be ascribed to interstellar absorption of soft X-ray photons or to the specific emission mechanism of the remnant itself. Wilson et al. (1970) report from the existence of the H II region [WMG 70] 332.4-0.4 which is located at $R.A. = 16^h17^m31^s$ and $Dec. = -51^\circ04'15''$ (J2000.0) with an extent of $5.5'$ in R.A. and $6.8'$ in Dec. Figure 6.16 shows the energy distribution of X-ray photons from the entire remnant within the energy range 1.0- 1.8 keV.

Spectral analysis

The spectral analysis of RCW 103 was performed using both MOS cameras. The X-ray spectra of the whole remnant were obtained using a circular extraction region which covers the whole remnant and excludes the central point source 1E 161348-5055. The background spectra were extracted close to the remnant on one of the neighbouring MOS CCDs. Due to the large extent of the remnant all selected photons have to be corrected for vignetting in order to avoid an underestimate of the flux of photons which are off-axis. The background region, however, consists of two indistinguishable components, one is the sky background and the other one the internal background

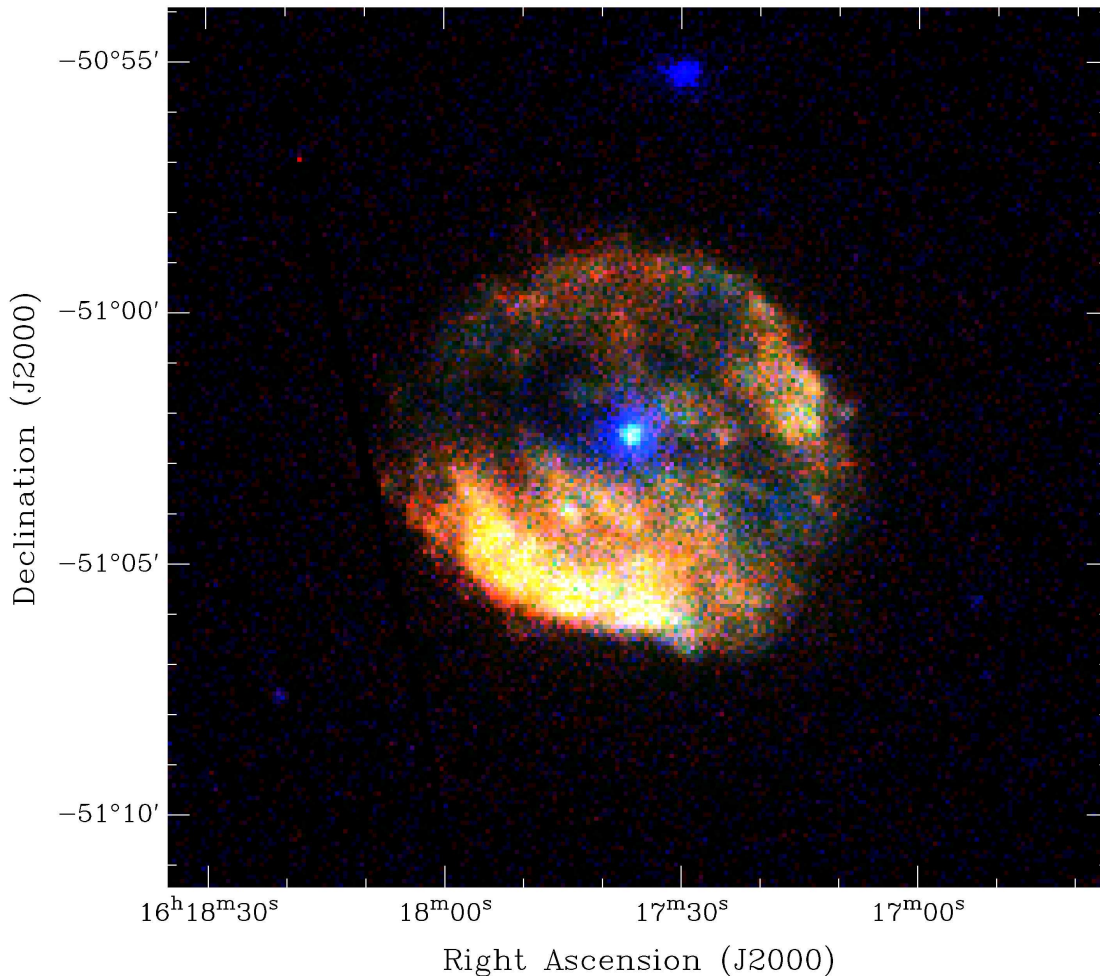


Figure 6.1: MOS1/2 false colour image of RCW 103. The red colour describes the X-ray emission in the 0.3-0.7 keV band, green corresponds to 0.7-2.0 keV and blue to 2.0-10.0 keV. The central point 1E 161348-5055 source shows up as the hardest source in RCW 103. The 69 ms Pulsar PSR J1617-5055 is located north of RCW 103 with a distance of 7'.

caused by fluorescent emission from particles crossing the detectors. The background which is off-axis (as well as the remnant due to its large extent), also have to be corrected for vignetting, i.e. each event detected with energy E at location (x,y) is weighted by a coefficient $w(x,y,E)$ which is the ratio of the effective area at position (x,y) to the central effective area for the energy E . Thus, the internal background component is wrongly enhanced, it has to be corrected once more. In order to estimate the effect of enhanced internal background due to vignetting correction, corrected and uncorrected background spectra were extracted from a 'closed observation' where the telescope aperture is closed and only photons are detected which are produced by particles crossing the detectors. The result was a flux variation of factor $\sim 3-4$ necessitating a more complex correction. This can be done by using such a 'closed ob-

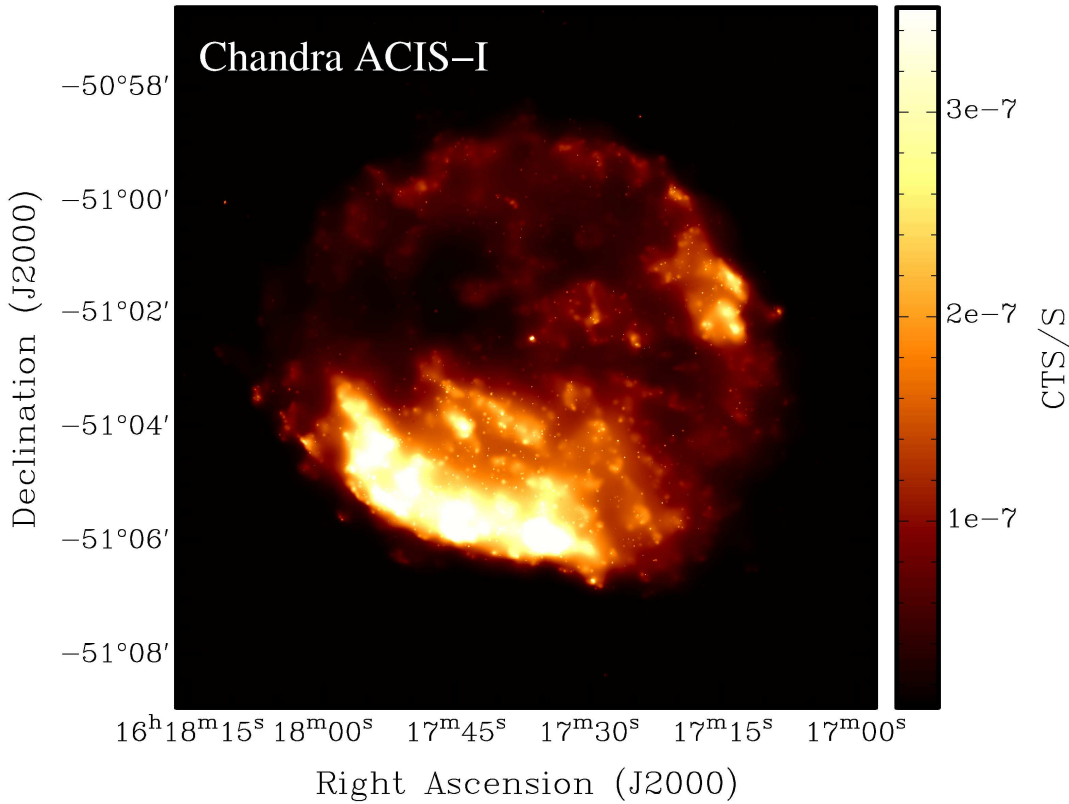


Figure 6.2: Vignetting-corrected Chandra ACIS-I image of RCW 103 showing clumps of bright X-ray emission on small scales. The gaps are due to the spacing between the four CCDs of the ACIS-I detector.

servation' assuming a constant flux of cosmic particles over a large period of time. The 'closed observation' was performed on 31st January 2002 in the full frame mode with an total exposure time of ~ 24 ks. These data are public domain and available under http://xmm.vilspa.esa.es/external/xmm_data_acc/xsa/index.shtml. The accurate background correction was done in the following way: At first a vignetting corrected background spectrum has to be extracted where the internal background is overestimated due to the vignetting correction. For this reason a corresponding background spectrum has to be extracted, corrected for vignetting in a 'closed observation' and subtracted from the original background spectrum. Finally the source spectrum has to be corrected for the vignetting corrected internal background by performing the same subtraction.

Figure 6.4 shows the overall spectrum of RCW 103 without its central point source. The most prominent lines in the MOS spectra are the He α -like lines of Neon, Magnesium, Silicon and Sulphur and a Iron XVII line in the Iron L complex as well as the Neon x Ly α . No Iron He α -like line could be identified because of a too low plasma temperature which does not reach this ionization state. Images have been created selecting the photons in narrow energy bands corresponding to the main line features.

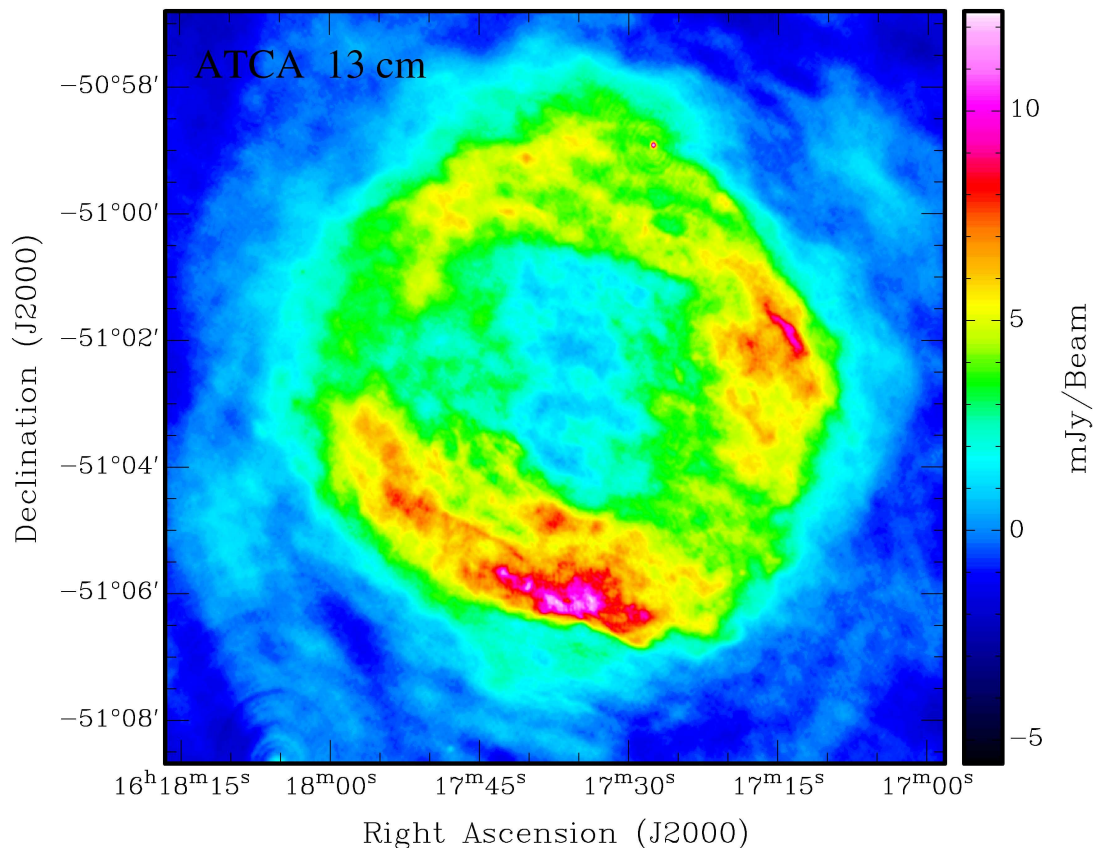


Figure 6.3: ATCA radio-continuum image at 13 cm (courtesy J. Dickel). The half-power beamwidth is $4.5''$. The radio emission region of RCW 103 matches very well with the extent of the X-ray emission (cf. Fig. 6.2).

In all cases the continuum had to be subtracted due to the relatively low S/N ratio of the lines above the continuum. Therefore, the ratio of the continuum at the line energy to the continuum in the close-by energy bands on both sides of the line, which were free of contamination by line emission, had to be derived. The continuum at the line was estimated in each spatial bin using the flux in the close-by energy bands as well as the defined ratio. No line emission is expected from the compact X-ray source 1E 161348-5055 in the center and thus the disappearance of the X-ray point source is a good test of accurate continuum subtraction. Figure 6.5 shows the spatial distribution of the four strongest emission lines in the X-ray shell of RCW 103, namely Neon, Magnesium, Silicon and Sulphur. The radius of the shells in the different emission lines is almost the same, i.e. the size of RCW 103 in the four resolved emission lines does not vary with increasing atomic number. In contrast to Tycho's supernova remnant (Stadlbauer & Aschenbach, 2001) this would rather indicate a collapse driven supernova remnant which led to the mixture of the elements. The intensity distribution of neon, magnesium, silicon and sulfur matches the morphology of the remnant in the whole energy range. Spectra were extracted from the region where the harder

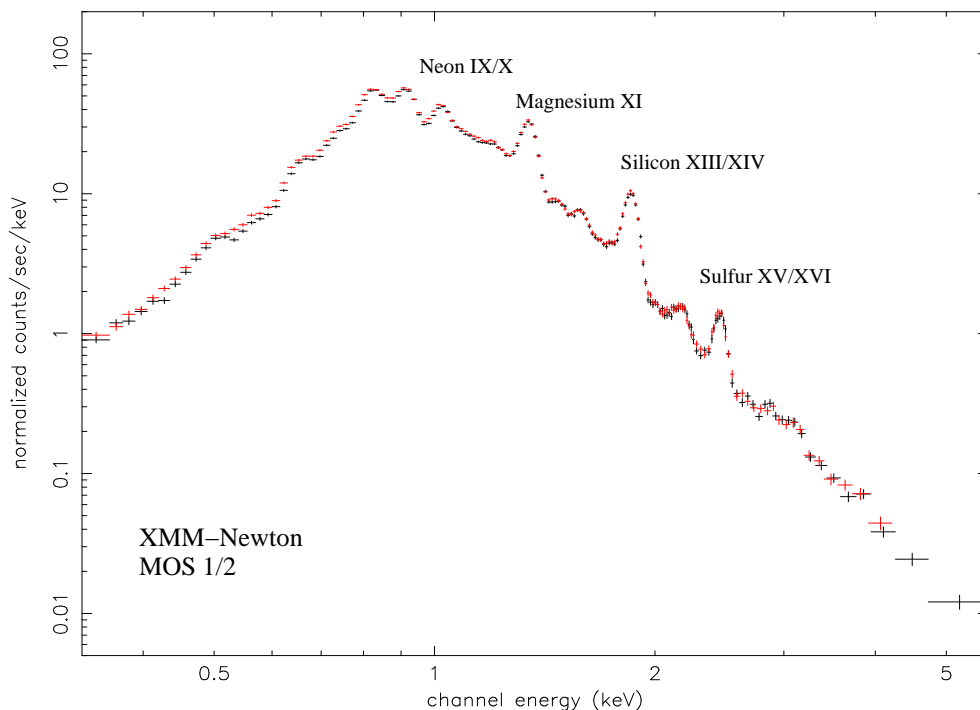


Figure 6.4: The observed MOS 1 and MOS 2 count rate spectra of the entire SNR RCW 103 without the central point source. The He α -like lines of Neon, Magnesium, Silicon and Sulphur are very prominent.

X-rays come from in the north-east and from a region at the rim of the shell in the north. After aligning the amplitudes of both spectra, they show the same shape above 1.1 keV. Below this energy the amplitude of the spectrum from the region of harder X-ray emission is a factor ~ 2 smaller indicating the partly absorption of soft X-ray photons (Fig. 6.7).

Spectral analysis of selected regions

A more detailed spectral analysis of six small regions (Fig. 6.8) within RCW 103 was performed. The source and background spectra have been first corrected for the instrumental background and then binned to a minimum of 50 counts per spectral channel. The spectra have been fitted with different models. One-component models could not fit the spectra whereas two-component models provided adequate fit results. Two-component CIE (collisional ionisation equilibrium) models like VMEKAL with variable solar abundances have been used but provided only poor fits to the data. Testing two-temperature non-equilibrium ionization collisional plasma model, the double VNEI was found to describe the data best. This model assumes a constant temperature and single ionization parameter. Leaving the element abundances of Oxygen, Neon, Magnesium, Sulfur, Silicon and Iron variable the data were fitted with the two-component

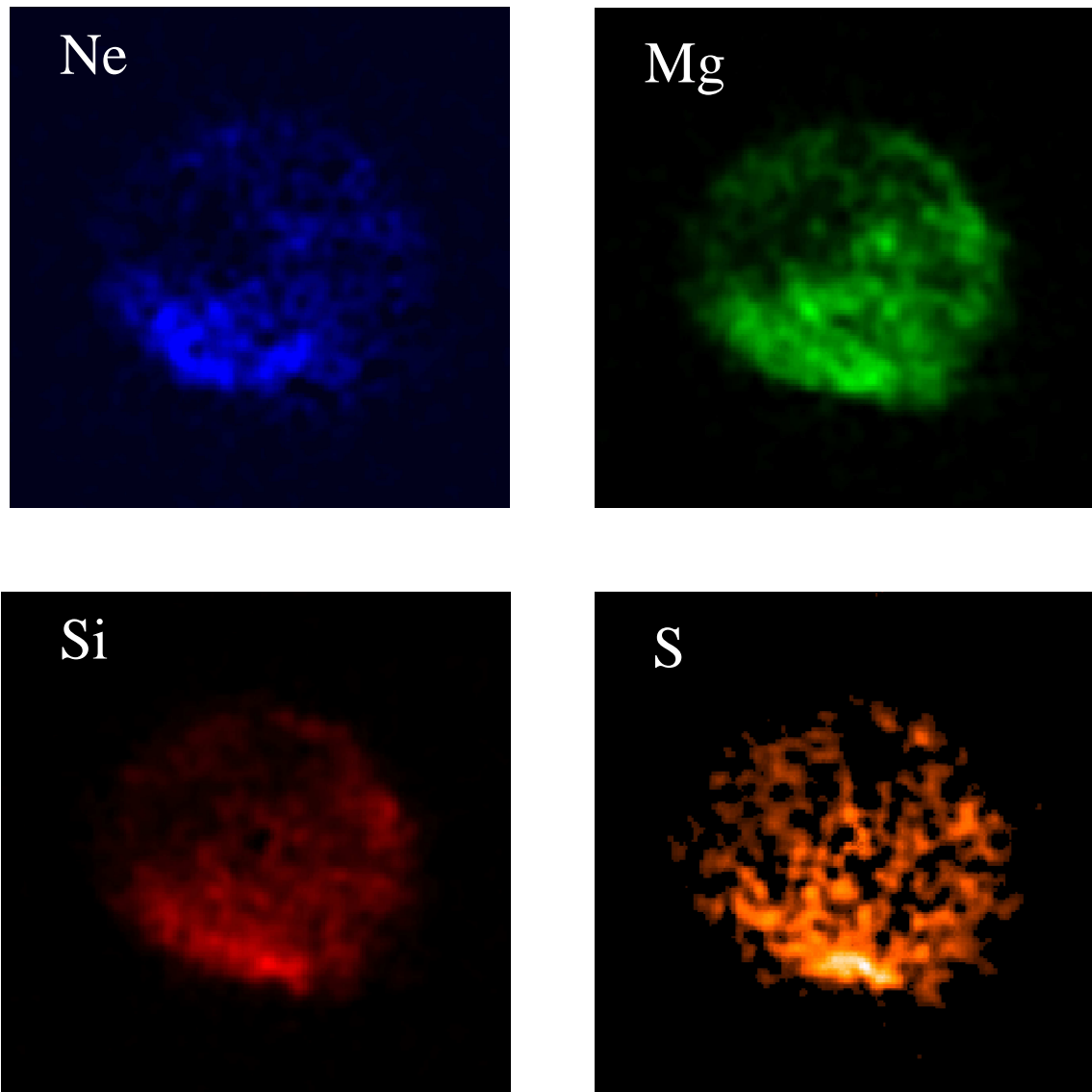


Figure 6.5: The XMM-Newton MOS 1+2 images of RCW 103 resolved in the prominent emission lines of Ne, Mg, Si and S. The sub-images are at the same scale. The extent of the shells in the different emission lines does not vary with increasing atomic number.

non-equilibrium model VNEI and the two-component CIE model MEKAL.

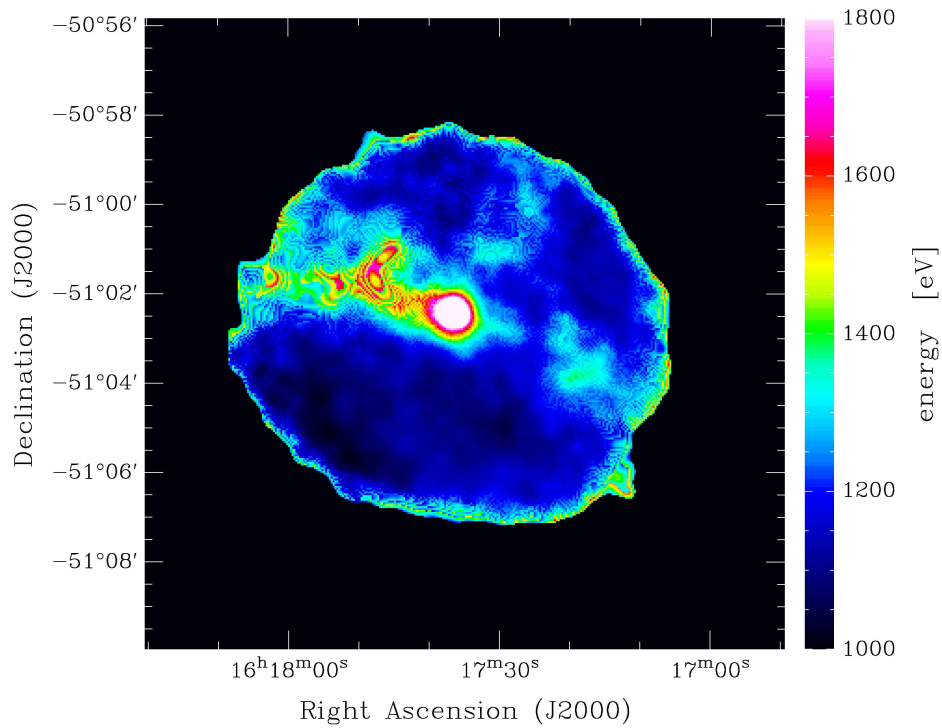


Figure 6.6: Energy image of RCW 103 from the combined MOS1/2 in the energy range 1.0-1.8 keV. Harder X-ray emission extends along a belt from the south-west towards the north-east across the remnant which originates from interstellar absorption.

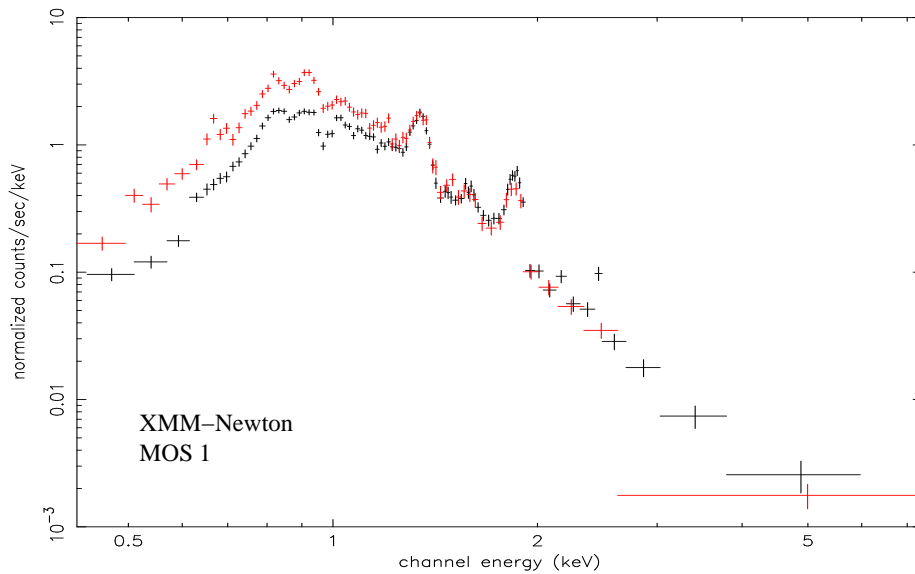


Figure 6.7: Two MOS1 spectra from the region of the harder X-ray emission (black) and from a close-by region (red). The soft X-ray emission below 1.1 keV is absorbed (black).

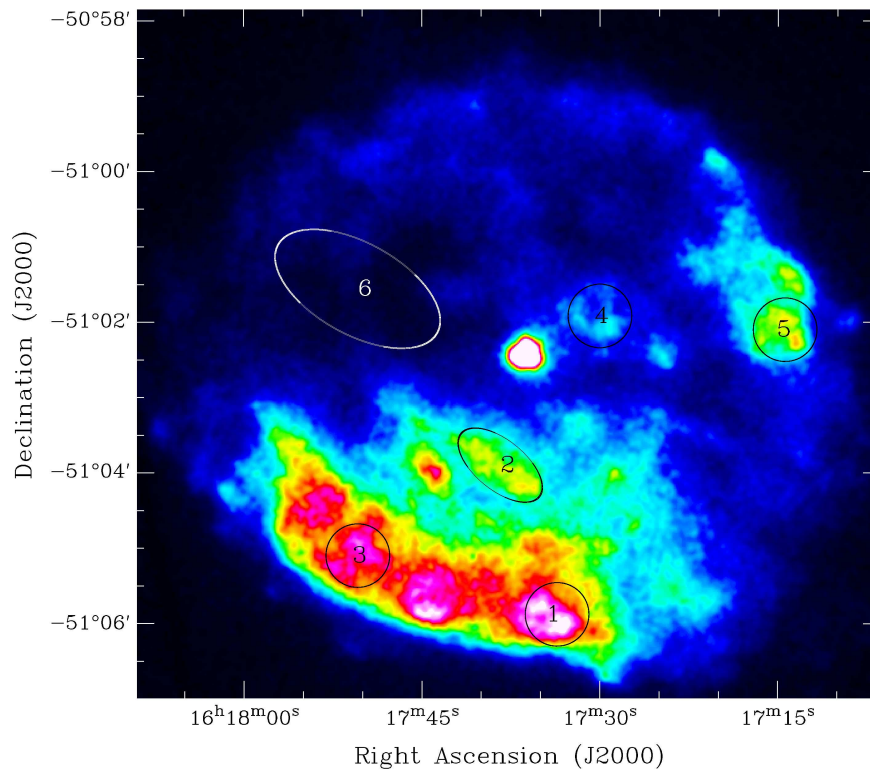


Figure 6.8: Combined MOS1/2 intensity image of RCW 103 with the marked regions which have been selected for the spectral analysis (cf. 6.9).

Region 1

parameter	vnei + vnei value	vmekal vmekal+ value	unit
N_H	7.94	7.58	10^{21} cm^{-2}
1. component			
kT_1	0.28	0.25	keV
τ_1	4.04		$10^{12} \text{ s cm}^{-3}$
EM_1 (frac.)	0.09	0.11	10^{58} cm^{-3}
Neon abundance	3.2	3.1	
Magnesium	1.6	5.4	
Silicon	4.8	7.6	
Sulfur	5.9	0	
Iron	3.7	2.6	
2. component			
kT_2	0.71	0.66	keV
τ_2	0.08		$10^{12} \text{ s cm}^{-3}$
EM_2 (frac.)	0.05	0.04	10^{58} cm^{-3}
red χ^2	1.26	2.64	

Region 2

parameter	vnei + vnei value	vmekal vmekal+ value	unit
N_H	7.79	5.71	10^{21} cm^{-2}
1. component			
kT_1	0.34	0.27	keV
τ_1	0.13		$10^{12} \text{ s cm}^{-3}$
EM ₁ (frac.)	0.1	0.03	10^{58} cm^{-3}
Neon abundance	1.3	1.7	
Magnesium	1.7	9.3	
Silicon	0.9	3.4	
Sulfur	0	0.1	
Iron	2.1	2.3	
2. component			
kT_2	0.68	0.62	keV
τ_2	0.43		$10^{12} \text{ s cm}^{-3}$
EM ₂ (frac.)	0.03	0.03	10^{58} cm^{-3}
red χ^2	1.04	1.93	

Region 3

parameter	vnei + vnei value	vmekal vmekal+ value	unit
N_H	6.21	6.01	10^{21} cm^{-2}
1. component			
kT_1	0.27	0.27	keV
τ_1	3.75		$10^{12} \text{ s cm}^{-3}$
EM ₁ (frac.)	0.23	0.10	10^{58} cm^{-3}
Neon abundance	1.4	2.9	
Magnesium	1.1	5.2	
Silicon	2.5	6.0	
Sulfur	0	3.6	
Iron	1.5	2.6	
2. component			
kT_2	0.62	0.71	keV
τ_2	0.4		$10^{12} \text{ s cm}^{-3}$
EM ₂ (frac.)	0.05	0.03	10^{58} cm^{-3}
red χ^2	1.19	2.64	

Region 4

parameter	vnei + vnei value	vmekal vmekal+ value	unit
N_H	8.92	7.83	10^{21} cm^{-2}
1. component			
kT_1	0.27	0.22	keV
τ_1	0.17		$10^{12} \text{ s cm}^{-3}$
EM ₁ (frac.)	0.19	0.46	10^{58} cm^{-3}
Neon abundance	2.1	0.9	
Magnesium	3.2	3.2	
Silicon	0.8	2.3	
Sulfur	0	0	
Iron	1.7	0.6	
2. component			
kT_2	0.60	0.63	keV
τ_2	0.3		$10^{12} \text{ s cm}^{-3}$
EM ₂ (frac.)	0.07	0.05	10^{58} cm^{-3}
red χ^2	1.00	1.80	

Region 5

parameter	vnei + vnei value	vmekal + vmekal value	unit
N_H	7.15	5.58	10^{21} cm^{-2}
1. component			
kT_1	0.29	0.34	keV
τ_1	1.53		$10^{12} \text{ s cm}^{-3}$
EM ₁ (frac.)	0.03	0.02	10^{58} cm^{-3}
Neon abundance	3.4	0.2	
Magnesium	5.6	6.4	
Silicon	7.3	4.0	
Sulfur	0	0	
Iron	3.7	0.4	
2. component			
kT_2	0.59	0.59	keV
τ_2	0.4		$10^{12} \text{ s cm}^{-3}$
EM ₂ (frac.)	0.05	0.04	10^{58} cm^{-3}
red χ^2	1.64	2.90	

Region 6

parameter	vnei + vnei value	vmekal vmekal+ value	unit
N_H	10.02	9.13	10^{21} cm^{-2}
1. component			
kT_1	0.28	0.21	keV
τ_1	0.62		$10^{12} \text{ s cm}^{-3}$
EM ₁ (frac.)	0.09	0.22	10^{58} cm^{-3}
Neon abundance	3.2	1.5	
Magnesium	3.8	5.7	
Silicon	9.9	12.4	
Sulfur	35	0	
Iron	2.9	1.4	
2. component			
kT_2	0.75	0.61	keV
τ_2	0.05		$10^{12} \text{ s cm}^{-3}$
EM ₂ (frac.)	0.023	0.040	10^{58} cm^{-3}
red χ^2	1.18	1.76	

The spectral analysis of all selected regions within RCW 103 shows that there are small variations in temperature and Galactic absorption across the remnant. The low temperature component is in the range of 0.27-0.34 keV and the high temperature component in the range 0.62-0.75 keV, respectively. The higher temperature and Galactic absorption in Region 6 confirms the higher absorption along a belt of faint X-ray emission (cf. Fig.6.16). There are large variations of element abundances depending on the temperature and ionization timescale which do not allow a proper statement if the elements are overabundant or not. But the spectrum of Region 4 shows a strong magnesium line with abundances of 3.2 solar. Calculations of the error ellipse of magnesium versus temperature, ionization timescale τ_1 as well as the adjacent element abundances of Neon and Silicon confirm the overabundances within the 3σ errors and therefore the origin from a SN explosion (Fig. 6.10). A range of the expansion velocity of magnesium can be calculated taking a distance of 3.3 kpc and an age of 2000 years into account. Due to the projection effect the emitting magnesium region can be located on the outer shell which is turned to the observer or close to the center of the remnant, yielding a velocity range of about 700 to 2100 km/s. This low expansion velocity of Magnesium is comparable with element velocity profiles from model calculations for core-collapse SNe (cf. Shigeyama et al. (1996)).

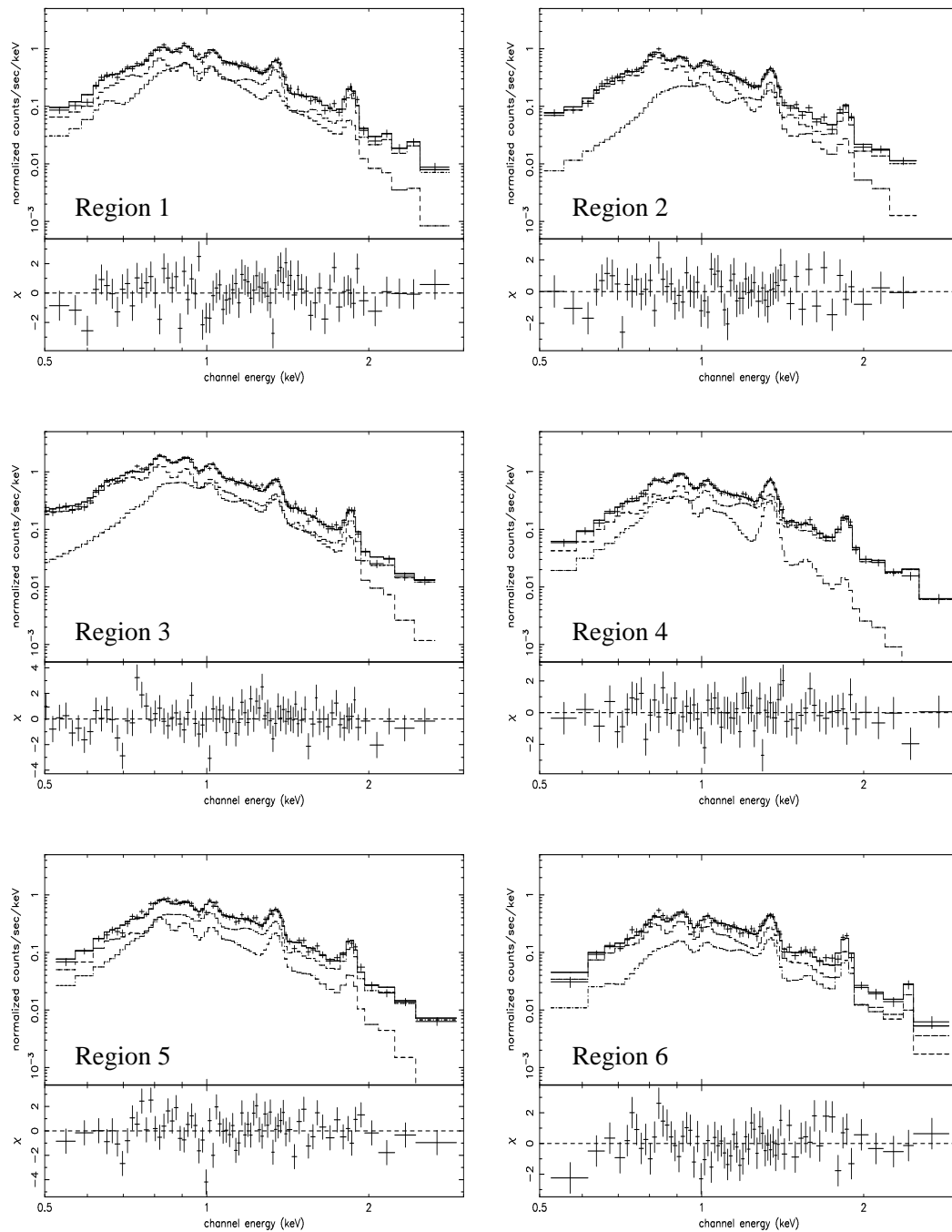


Figure 6.9: MOS spectra of selected regions of RCW 103 modeled with two vnei models. The dashed line shows the first (lower temperature) and dashed-dotted line the second VNEI component (higher temperature).

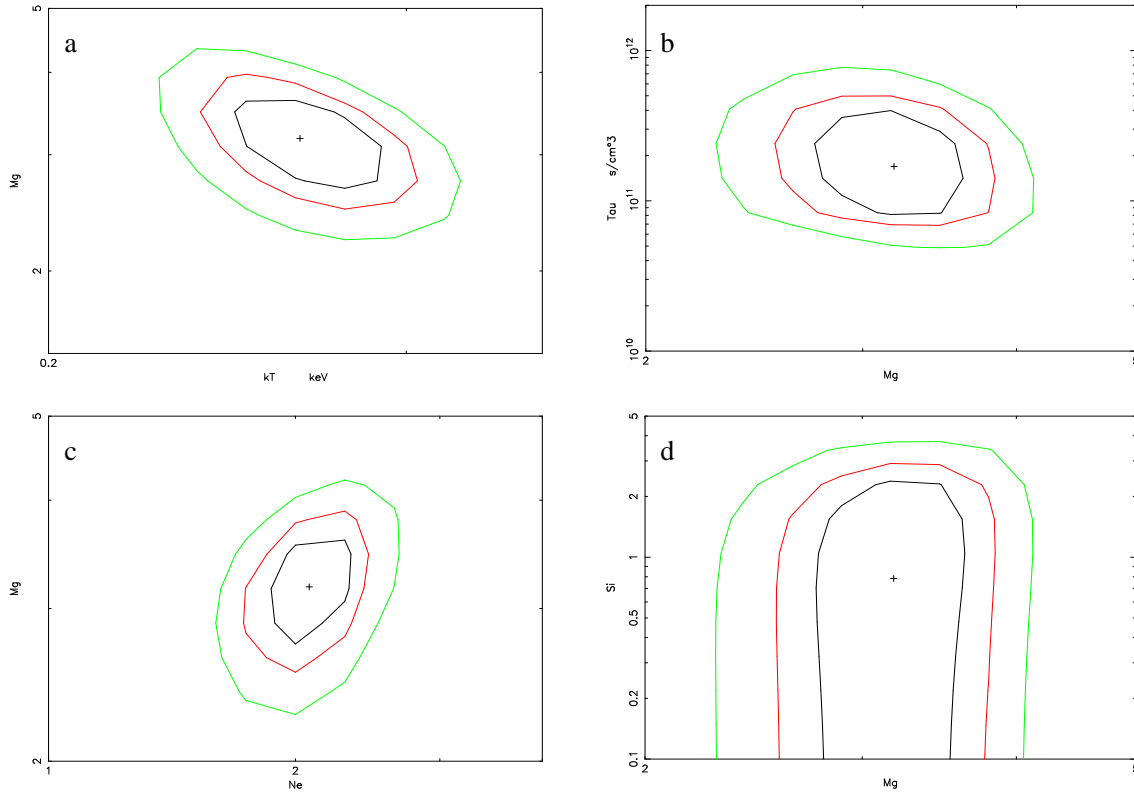


Figure 6.10: Error in abundances of Magnesium in region 4 (cf. Fig. 6.8, 6.9) depending on **a** temperature, **b** ionization timescale τ , **c** abundances of Neon and **d** Silicon. The significance of the contour levels are 1σ , 2σ and 3σ .

6.1.2 The Mystery of the Compact X-ray Source

Spectral analysis of 1E 161348-5055

The energy image of the remnant (cf. Fig. 6.16) shows only high energy X-rays (above 2 keV) from the point source 1E 161348-5055 and therefore is significantly harder than the remnant.

The spectral characteristics of 1E 161348-5055 were investigated using the data from the MOS cameras. The X-ray spectrum was obtained extracting a region of radius $15''$ at the position of the point source. The background spectrum was extracted in a ring around 1E 161348-5055 taking the diffuse emission of the remnant into account. Various spectral models have been fitted to the MOS data. A single power law model gives an acceptable fit but with high photon spectral indices of $4.10^{+0.15}_{-0.15}$ (MOS 1) and $3.90^{+0.19}_{-0.19}$ (MOS 2) which seem to be unphysical. The best fit is obtained with an absorbed two-temperature blackbody model (Table 6.1 resulting in two different temperatures according to two emission regions on the compact object of $R_1 = 1.16$ km and $R_2 = 320$ m assuming a distance of 3.3 kpc. Figure 6.4 shows the observed count

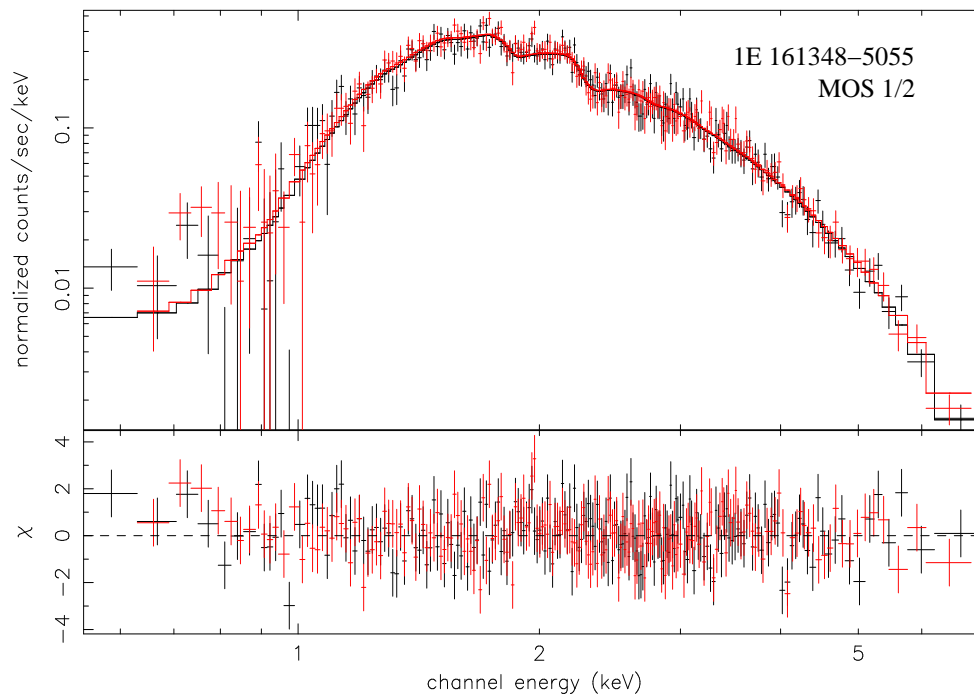


Figure 6.11: The observed MOS1/2 count rate spectra for the compact object 1E 161348-5055 in the center of RCW 103. The spectrum is fitted with a two-component blackbody model. In this spectrum the MOS 1 data are red whereas the MOS 2 are black.

rate spectrum for both MOS cameras together with the corresponding best-fitting model spectra.

The total X-ray integrated flux within $15''$ radius, corrected for the line-of-sight absorption, is $\sim 5.9 \times 10^{-12} \text{ erg cm}^{-2} \text{ s}^{-1}$ in the energy range 0.5-2.0 keV.

Flux variation on long time scale (years)

The compact X-ray source in the center of the SNR RCW 103 was believed to be a cooling neutron star for a long time (Tuohy & Garmire, 1980). In order to identify the nature of the central point source RCW 103 was observed several times with ROSAT at the beginning of the 90's. In 1991 the first image with the ROSAT HRI

Camera	N_H [10^{22} cm^{-2}]	kT_1 [keV]	kT_2 [keV]	red. χ^2
MOS 1	$1.35^{+0.10}_{-0.10}$	$0.46^{+0.02}_{-0.03}$	$0.86^{+0.15}_{-0.12}$	1.05 (197 dof)
MOS 2	$1.31^{+0.10}_{-0.10}$	$0.46^{+0.03}_{-0.02}$	$0.88^{+0.06}_{-0.06}$	0.94 (200 dof)

Table 6.1: Best-fitting spectral parameters for 1E 161348-5055

was performed, but the source was not detected. Also a follow-up observation with the PSPC did not detect the point source. A series of HRI observations in 1994 and 1995, especially the deep ROSAT HRI image (Becker, 1995), detected the point source in the center of RCW 103. Further observations with ASCA in the years from 1993 to 1997 (Petre & Gotthelf, 1998), however, revealed a flux variability of about a factor ten times higher than in previous observations. Gotthelf et al. (1997) suggested from observational arguments that 1E 161348-5055 is likely not a cooling neutron star, an accreting binary with high-mass companion or a plerion but a radio-quiet neutron star which is believed to account for hidden neutron stars associated with SNRs. Popov (1998) concluded from theoretical arguments that 1E 161348-5055 could be an accreting neutron star in a binary system with a young compact object born in the recent SN explosion that produced the observed SNR RCW 103.

Three observations were recently performed with the Chandra ACIS in September 1999, February 2000 and March 2002 and two observations with XMM-Newton in September 2001.

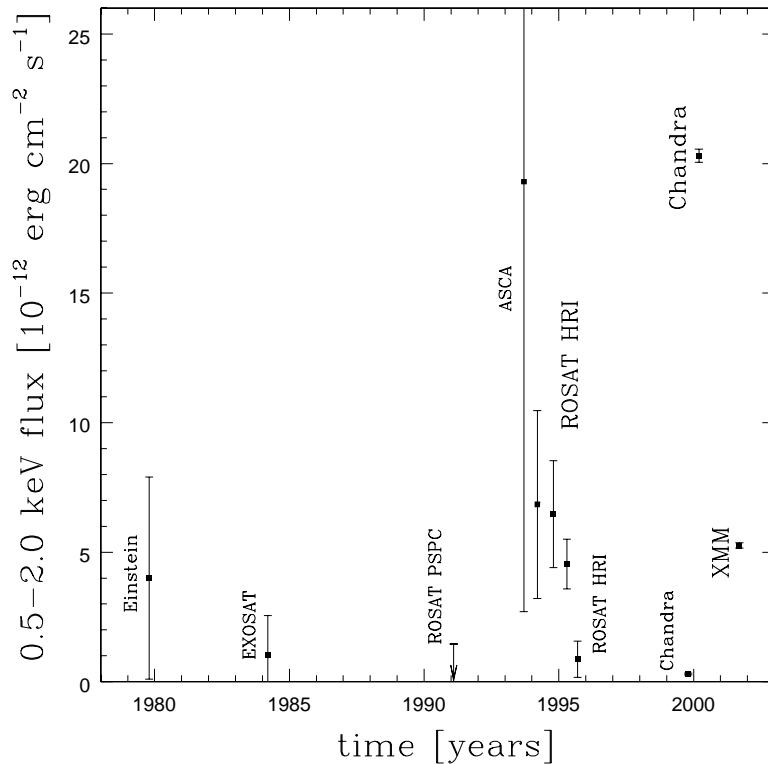


Figure 6.12: Long-term light curve for 1E 161348-5055. The error bars indicate combined contributions from 68% confidence and additional systematic uncertainties due to a high and inhomogeneous background. Because of a spatial resolution of $\sim 3'$ the flux value of the ASCA observation has a larger error.

Due to the discovered flux variability of 1E 161348-5055 (Petre & Gotthelf, 1998), a systematic reanalysis of all archival X-ray data from RCW 103 was performed in 2000. The energy band from 0.5-2.0 keV was selected in order to specify the flux, because it is common to all instruments. The fluxes were calculated using the best fit power law model of the ASCA observation with a power law index of 3.5. Taking additionally systematic uncertainties into account due to a high and inhomogeneous background the measured flux rate variability of Petre & Gotthelf (1998) could be confirmed but with reduced significance. Subsequent Chandra observations yielded a flux variation of a factor 20. The low errors in the flux values confirm the flux variability over a period of more than 20 years. The first two Chandra observation as well as the XMM-Newton observation are included in the plot shown in Fig. 6.12.

Flux variation on short time scales (hours)

The Chandra ACIS observation which was performed on 26th September 1999 gave the first indication of a $5.97^{+0.47}_{-0.44}$ hour period by observing the fragment of a sinusoid (Garmire et al., 2001). For this reason the ASCA GIS data above 3 keV were re-analyzed confirming a sinusoidal light curve with a period of (6.76 ± 0.30) hours. The observation extended to more than two cycles.

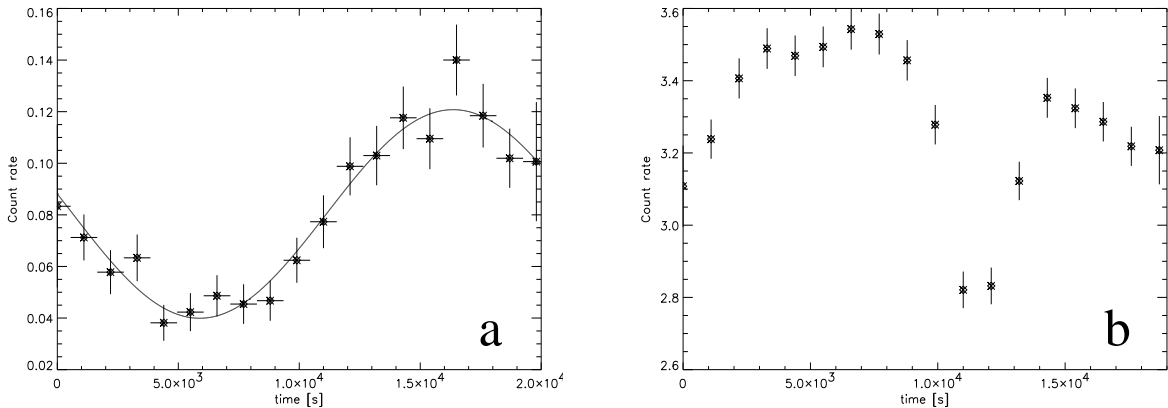


Figure 6.13: **a:** Light curve from a Chandra observation obtained in September 1999. The corresponding best-fitting period is represented by a solid sinusoidal curve. **b:** Light curve from the XMM-Newton observation obtained in September 2001. The light curve shows a ~ 6.6 hour period with a strong dip or eclipse.

A reanalysis of the Chandra ACIS data from September 1999 yielded a period of (5.82 ± 0.15) hours using a binning of 1100 s. This result is consistent with that of Garmire et al. (2001) within the errors. The Chandra data which were taken on 8th February 2000 could not confirm the ~ 6 hour period. The XMM-Newton data, however, showed for the first time a ~ 6.57 hour period with a deep dip or eclipse in one cycle (Becker & Aschenbach, 2001). Consequently, this source variability indi-

cates that it is powered by accretion, likely from a low-mass companion in a binary star. This result could also be confirmed by an observation performed with Chandra in March 2002. Deep near-IR observations of the source with VLT suggest a potential counterpart of the compact object about $2''$ from the nominal Chandra position (Sanwal et al., 2002).

6.1.3 Conclusion

The supernova remnant RCW 103 has a thermal X-ray shell with prominent He α -like lines of neon, magnesium, silicon, sulphur and the iron L complex. The low temperature component is about 0.3 keV and the high component about 0.7 keV, varying slightly across the remnant. The belt of faint X-ray emission across the remnant emerges from absorption rather than an alternative emission mechanism. It is not clear yet if RCW 103 originated from a SN Ia or a core-collapse SN, but there are some indications supporting the core-collapse event. Constant radii of RCW 103 in different emission lines as well as the low expansion velocity of light elements like magnesium are expected for core-collapse SNe. Finally, the existence of the central point source, which is a binary, consisting probably of a neutron star and a low mass companion, is a strong argument for a core-collapse scenario.

6.2 G 21.5.-0.9

G 21.5-0.9 is a typical Crab-like SNR showing strong linear polarization and centrally peaked emission in the radio band (Morsi & Reich, 1987) and a similar morphology in X-rays (Becker & Szymkowiak, 1981; Slane et al., 2000). From neutral hydrogen absorption measurements a distance of ~ 5.0 kpc could be adopted (Davelaar et al., 1986). There has been no detection of pulsed emission in X-rays as well as in radio (Biggs & Lyne, 1996; Slane et al., 2000). X-ray observations made by Chandra could locate precisely the position of the pulsar, a compact central core on a scale of $\sim 2''$ embedded within a more extended ($\sim 30''$ radius) synchrotron nebula (Slane et al., 2000).

G 21.5-0.9 was observed on-axis as a calibration target at the beginning of the XMM-Newton mission by the EPIC PN and MOS cameras giving a total accumulated exposure of ~ 30 ks (Warwick et al., 2001). All three EPIC cameras were operated in the full-frame mode with the medium filter selected. The events were screened, however, with the updated XMM Science Analysis Software SAS 5.3.3 and using the latest PN and MOS response matrices. Investigation of the count rate above 10 keV revealed a number of soft proton flares during the observation. The background itself shows strong variations selecting events only in the low-background period which lead to effective exposure times of ~ 16.7 ks and 13.6 keV for the MOS and PN cameras, respectively.

G 21.5–0.9

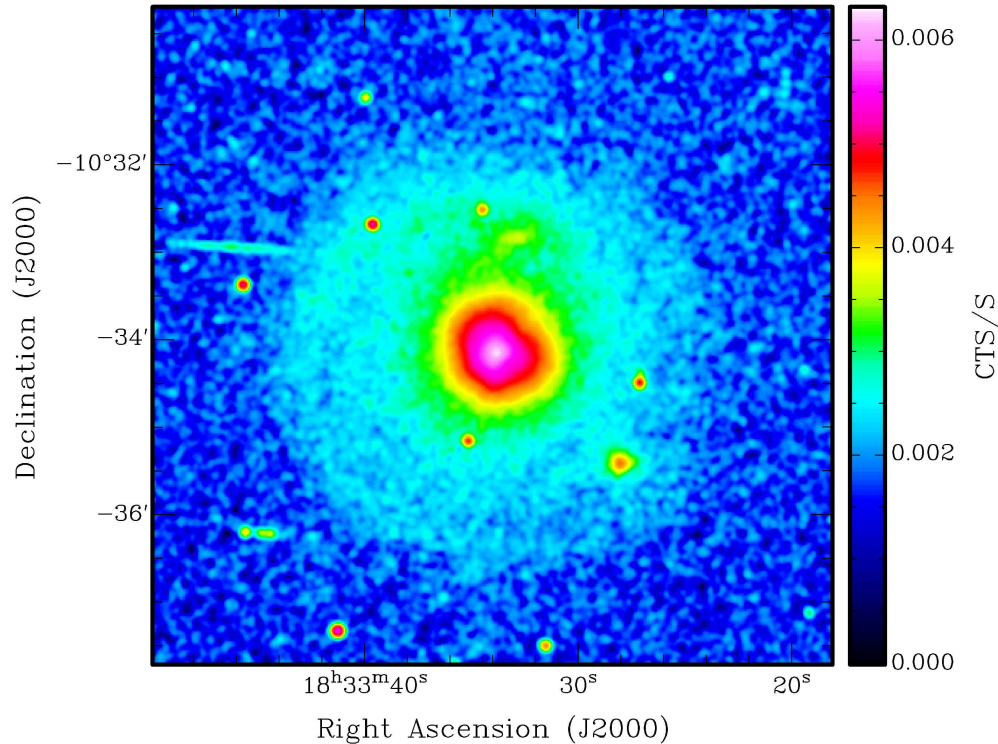


Figure 6.14: Vignetting-corrected image of G 21.5-0.9 from the merged EPIC MOS1 and MOS2 data. The pixel size is $1''$ and the image has been smoothed with a Gaussian filter with width $\sigma=2$ pixel. The central bright synchrotron nebula is the most prominent feature which is surrounded by a low surface brightness emission region. A remarkable “spur” extends from the center towards the north.

6.2.1 Spatial Analysis

The bright synchrotron nebula at the center of this remnant is the most prominent feature of the image, although the central core is clearly surrounded by a more extended low surface-brightness emission region shown in Fig. 6.14. A point source is located $\sim 2'$ to the south-west of the center of the remnant.

The bright center of the synchrotron nebula, i.e. the region within $r \approx 30''$, shows deviations from circular symmetry, mainly in the north-west. These spatial features match well to similar structures seen in the higher spatial resolution images from Chandra. A low surface brightness halo appears well out to $r \approx 150''$ with a near perfect circular symmetry. A remarkable ‘spur’ shows up at a lower level of surface brightness which extends from the core region towards the north. Bandiera & Bocchino (2003) note that this feature resembles a partial shell which can be described by a power law and an additional thermal component.

6.2.2 Spectral Analysis

An energy image was produced in the energy range 2.5-3.7 keV where most of the X-ray emission originates (Fig. 6.16). The colours indicate the energy per pixel. It shows that the core of the nebula is significantly harder than the low-surface brightness halo.

The spectral characteristics of the core of G 21.5-0.9 have been investigated using the data from both the PN and MOS cameras. The X-ray spectrum of the core of the nebula was obtained using a circular extraction region of radius $48''$ centered on the position of peak surface brightness. The background spectra were extracted from a region far-off the extended SNR including no point sources or diffuse X-ray emission. The source spectra were grouped with a SN ratio of at least 4σ .

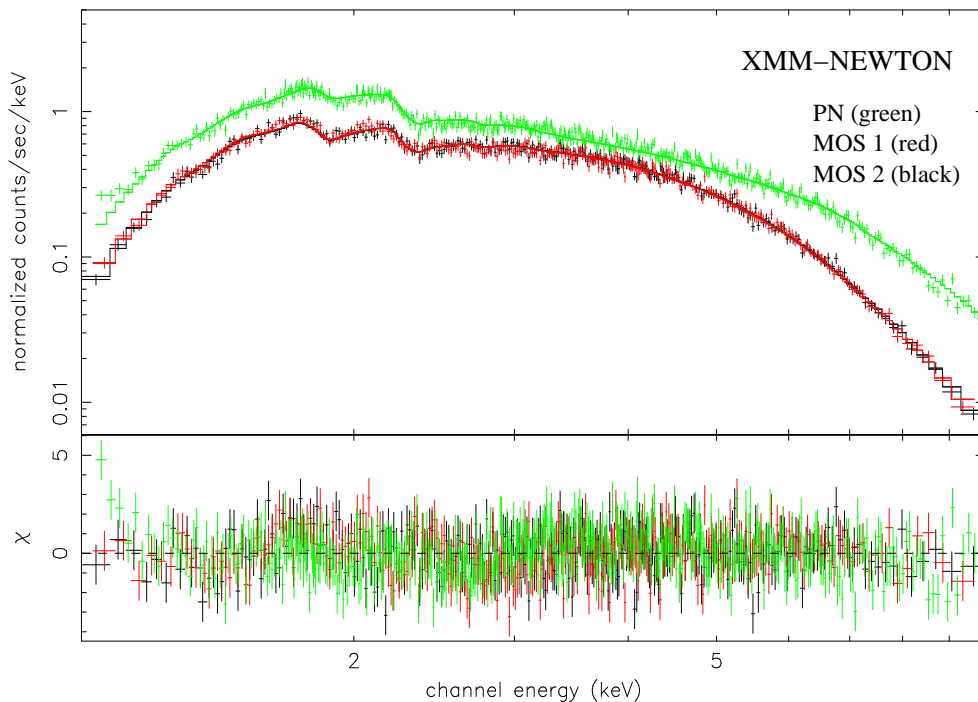


Figure 6.15: The observed PN (green), MOS 1 (red) and MOS 2 (black) count rate spectra of the core region of G 21.5-0.9. In each case the corresponding best fitting spectral model is represented by the solid histogram. ALL three datasets are modeled with an absorbed power law model.

The spectral modelling assumed an absorbed power law continuum. Figure 6.15 shows the observed count rate spectra for the PN, MOS 1 and MOS 2 detectors together with the corresponding best-fitting model spectra. The best-fitting spectral parameters obtained for separate fits to the PN and MOS spectra are summarised in Tab. 6.2, where the errors are quoted at a 90% confidence level. The simple absorbed power law model

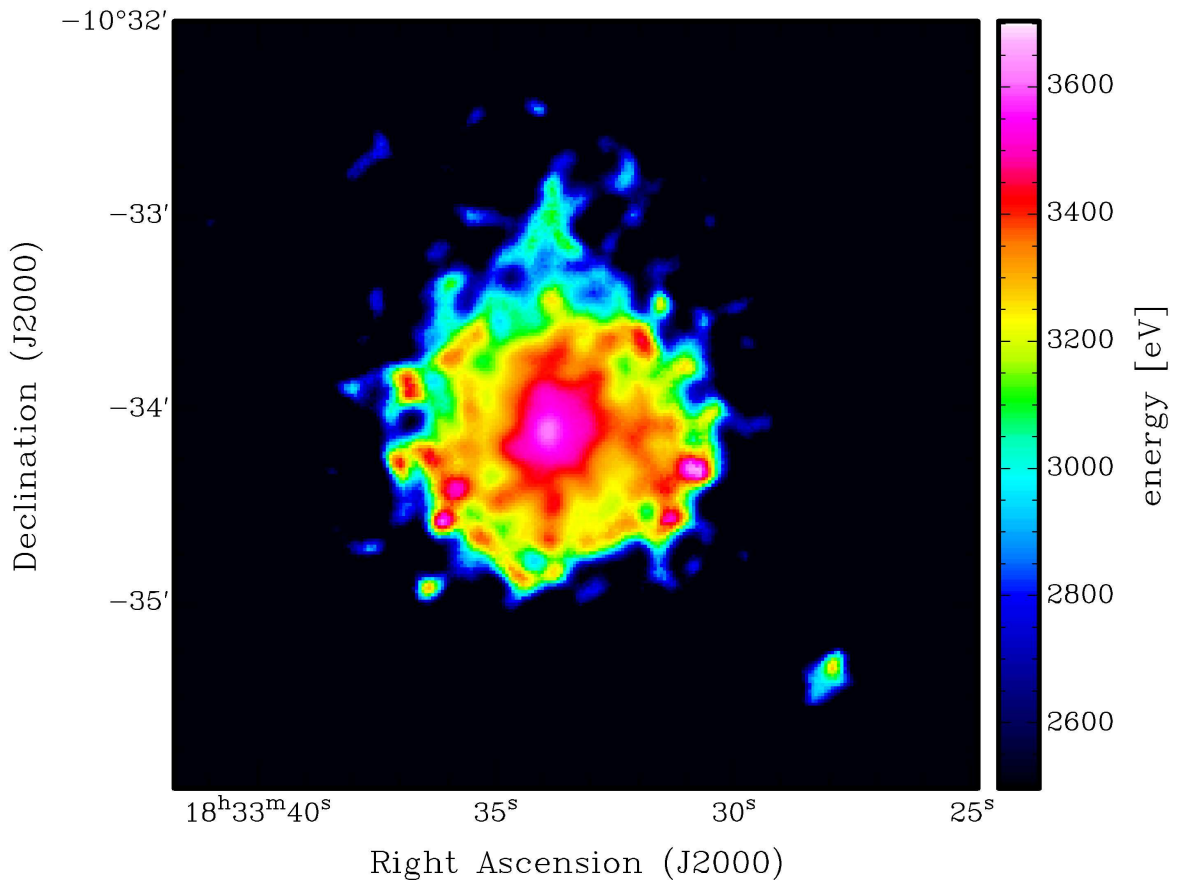


Figure 6.16: Energy image of G 21.5-0.9 from the MOS 1+2 datasets. The image was initially binned with $1''$ and smoothed with a Gaussian filter ($\sigma=3''$). The colour bar on the right side indicates the average energy per pixel. The image shows decreasing energy from the center outwards.

provides a very good fit to all three data sets.

The total X-ray flux of G 21.5-0.9 within a radius of $144''$ is $5.5 \times 10^{-11} \text{ erg cm}^{-2} \text{ s}^{-1}$ in the 1.0-10 keV band resulting in an X-ray luminosity of $1.62 \times 10^{35} \text{ erg s}^{-1}$ at an assumed distance of 5.0 kpc (Davelaar et al., 1986). The spectral variations were investigated by extracting spectra from the PN dataset in a set of annular regions centered

Camera	N_H [10^{22} cm^{-2}]	Γ	red. χ^2
PN	$2.17^{+0.05}_{-0.05}$	$1.89^{+0.03}_{-0.03}$	1.04 (1130 DOF)
MOS 1	$2.22^{+0.05}_{-0.06}$	$1.87^{+0.03}_{-0.04}$	1.03 (436 DOF)
MOS 2	$2.09^{+0.05}_{-0.06}$	$1.82^{+0.04}_{-0.03}$	1.04 (426 DOF)

Table 6.2: Best-fitting spectral parameters for the core of G21.5-0.9

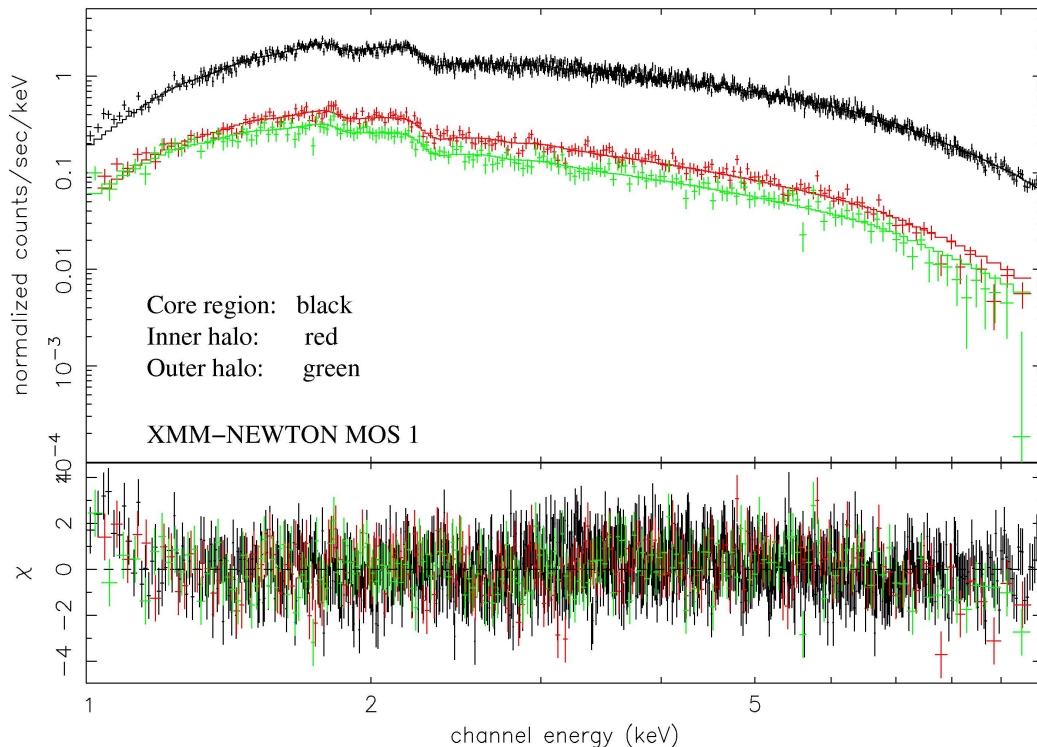


Figure 6.17: The observed count rate spectra and best-fitting absorbed power law model for the core ($r \leq 48''$), inner ($48'' < r < 96''$) halo and outer ($96'' < r \leq 144''$) halo regions using XMM-Newton MOS 1 data.

on the point of peak surface brightness. The resulting spectra were then fit as before with a simple absorbed power law model. The N_H was fixed at the value obtained for the core region.

The derived photon spectral index shows a steady increase with radius from a value of 1.71 ± 0.04 at the center to 2.42 ± 0.08 at the outer edge ($r = 150''$) of the low surface brightness halo (Fig. 6.18).

In order to check if there is evidence for thermal emission from the halo component, the PN spectrum, extracted from the outer ($r = 96'' - 144''$) annular region, was investigated. A two-component model was fit, comprising a power law and a thermal component, i.e. MEKAL. The result was a modest improvement in the χ^2 with respect to the single powerlaw model. The putative thermal component accounts for only $\sim 1\%$ of the observed flux. The lack of line features in the X-ray spectrum of the outer halo is evident in Fig. 6.17 which shows the fitting residuals to a simple power law spectral model. A reason for the lack of line emission is the fact that shocked-heated X-ray emitting gas in the halo G 21.5-0.9 did not have time to reach a state of ionization equilibrium. Therefore the non-equilibrium ionization model NEI was fit to the data. The NEI model provides only a poor fit to the data when the column density is constrained to the value measured for the core of G 21.5-0.9. A rather better result is obtained when N_H is allowed to vary freely (cf. Tab. 6.3).

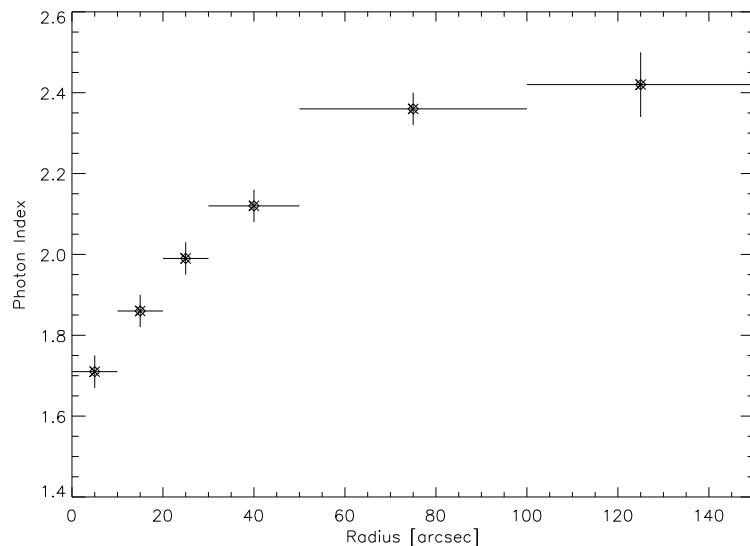


Figure 6.18: The observed variation in the photon spectral index versus radius as measured in the PN data. The synchrotron nebula of G 21.5-0.9 shows spectral softening with radius which reflects the impact of synchrotron radiation losses on very high energy electrons as they flow from the termination shock around the pulsar to the edges of the nebula.

Model	N_H [10^{22} cm^{-2}]	Γ	kT [keV]	$n_e t$ [$10^8 \text{ cm}^{-3} \text{ s}$]	red. χ^2 (dof)
PL	2.17^a	$2.46^{+0.06}_{-0.06}$	—	—	1.14 (208)
2-Comp	2.17^a	$2.28^{+0.10}_{-0.10}$	~ 0.74	—	0.98
NEI	2.17^a	—	$11.6^{+1.35}_{-1.20}$	347	2.42 (207)
NEI	$1.31^{+0.08}_{-0.09}$	—	$5.37^{+0.57}_{-0.53}$	$6.25^{+2.62}_{-4.49}$	1.00 (206)

Table 6.3: Best-fitting spectral parameters for the outer halo of G21.5-0.9; a fixed parameter

Finally the spectral properties of the south-west point source have been considered. Using the PN data, the source photons were extracted in a cell of $16''$ radius and the complementary background spectrum was taken on the same CCD using a cell with the same size which was located equidistant from the center of G 21.5-0.9. The spectral fit indicated a relatively hard spectrum (i.e. $\Gamma = 1.45^{+0.50}_{-0.41}$ or $kT \sim 6.5 \text{ keV}$) and a column density of $0.53^{+0.41}_{-0.31} \times 10^{22} \text{ cm}^{-2}$. Because of the column density which is about a factor 4 lower than the derived N_H of G 21.5-0.9 the point source is assumed to be a foreground object with respect to the SNR. This point source is positionally coincident with the emission-line star SS 397.

6.2.3 Conclusion

The observation with XMM-Newton shows that the nebula of G 21.5-0.9 shows a power law continuum without any significant line features. In the case of thermal halo emission, the lack of line emission implies that the plasma is far from ionization equilibrium. The NEI modelling confirms a low ionization state with $n_e t \approx 3 \times 10^8 \text{ cm}^{-3}\text{s}$. The temperature which is derived for the continuum Bremsstrahlung emission is $\sim 5\text{-}6 \text{ keV}$ which is rather hot, even for a very young SNR. Assuming a distance of 5.0 kpc (Davelaar et al., 1986) and a maximum expansion velocity of 10 000 km/s for the shell lead to about 100 years since the X-ray emitting gas was shock heated. Applying the ionization timescale $n_e t \approx 6 \times 10^8 \text{ cm}^{-3}\text{s}$ then gives $n_e < 0.2 \text{ cm}^{-3}$ which seems to be very low. In the case of a thermal Bremsstrahlung radiation the observed X-ray luminosity would require a higher electron density of a least $n_e \sim 0.6 \text{ cm}^{-3}$ performing a simulation¹ of the spectrum. But there is a high discrepancy in the electron density if the extended X-ray emission would be interpreted as a thermal shell. The lack of limb brightening, the constant increase of the spectral index throughout the remnant and the spherical symmetry suggest an interpretation of the outer halo as an extension of the central synchrotron nebula. Therefore G 21.5-0.9 is a Crab-like rather than a composite SNR.

The spectral softening with radius in G 21.5-0.9 reflects the impact of synchrotron radiation losses on very high energy electrons as they flow from the region of the termination shock around the pulsar to the edges of the nebula. The variation in photon spectral index is similar to the index range seen in the Crab nebula (Willingale et al., 2001). The major difference between both plerions is the near spherical symmetry in G 21.5-0.9 and absence of pulsed X-ray emission from the central pulsar (Warwick et al., 2001). This can be explained if our line of sight is reasonably aligned with the spin axis of the pulsar.

6.3 G 65.3+5.7

G 65.3+5.7 is a shell-type SNR which belongs to the class of very large extended SNRs with a diameter of ~ 3 degree. It was first discovered during an emission-line survey of the Milky Way in the optical, revealing a nearly complete 3.3×4.0 degree filamentary shell on the O III plate (Gull et al., 1977). Mavromataki et al. (2002) presented the first CCD mosaic of G 65.3+5.7 in the optical emission lines of O II and O III showing the presence of small and large scale inhomogeneities. Subsequent Effelsberg 100-m observations at 1420 MHz showed intense radio ridges which appear to coincide with bright optical filaments (Reich et al., 1979). Comparison with existing data at 408 MHz indicated that the radiation at 1420 MHz is mainly nonthermal resulting in a spectral index of $\alpha=0.61\pm 0.25$. Fesen et al. (1983) report from their optical observation a distance of ~ 1 kpc.

In X-rays, G 65.3+5.7 was first observed with the Einstein observatory providing an image and a count rate (Seward, 1990). During the ROSAT all-sky survey (RASS)

¹WebSpec (available at <http://heasarc.gsfc.nasa.gov/webspec/webspec.html>)

which was performed between July 1990 and January 1991 the remnant was fully mapped for the first time. In addition, 17 pointed PSPC observations were performed between September 1993 and May 1994 covering the whole remnant. The exposure time of the various pointed observations is in the range of 0.6 to 5.9 ks, providing a more detailed spatial and spectral analysis of the remnant in respect to what is available from the ROSAT all-sky survey.

6.3.1 Spatial Analysis

The ROSAT survey data show a rough circular remnant with an extent of 3.0×3.2 degrees in X-rays (Figure 6.19) which is smaller than the optical shell with 3.3×4.0 degrees (Gull et al., 1977) and radio with 4.0×5.2 degrees (Reich et al., 1979). In X-rays, the remnant has its geometrical center at $R.A. = 19^h33^m57^s$ and $Dec. = +31^\circ18'19''$ (J2000.0) and a count rate of (41 ± 0.5) cts s^{-1} resulting in a total of ≈ 21000 cts in the energy band 0.1-2.4 keV.

Correlating the X-ray data with databases like NVSS and the optical DSS2 as well as with SIMBAD and NED and calculating the hardness ratio HR1 and HR2 in the standard ROSAT soft, medium and hard bands (cf. A.1 and A.2) allowed the identification bright X-ray sources within the remnant (Tab. 6.4).

The radio pulsar PSR J1931+30 is situated in the south-west of G 65.3+5.7 at $R.A. = 19^h31^m11^s$ and $Dec. = +30^\circ34'58''$ (J2000.0) with an error circle of 5 arcmin (indicated by a cross in Fig. 6.19a). It was observed with Arecibo at 430 MHz and has a period of $P=0.582219 \pm 0.000001$ s and dispersion measure $DM= 56.0 \pm 11.0$ $cm^{-3}pc$ resulting in a distance of 3.03 ± 0.65 kpc (Camilo et al., 1996). In the ROSAT data the region of PSR J1931+30 is mainly dominated by X-ray emission from the remnant. Due to the off-axis position of PSR J1931+30 on the detector and the resulting large point spread function of ROSAT PSPC no X-ray point source could be detected. For this reason a 3.1σ count rate upper limit was determined by summing all photons within a radius $r = 2.5 \times FWHM$ at the position of PSR J1931+30. Another object is the radio-loud galaxy CGMW 5-10975 which is located on the northern edge of G 65.3+5.7 at $R.A. = 19^h33^m45^s$ and $Dec. = +32^\circ55'03''$ (J2000.0) and depicted as source I in Fig. 6.19. The source shows hard X-ray and radio emission (Roman et al., 2000). Source II is a X-ray source of ~ 10 arcsec diameter at $R.A. = 19^h37^m01^s$ and $Dec. = +31^\circ47'20''$ (J2000.0) and characterized by the hardness ratio $HR 1 \sim +0.02$ and $HR 2 \sim -0.15$. Its optical counterpart is the star GSC 02655-01741 of spectral type M. The values of the hardness ratio are in good agreement with that of M stars in the Pleiades except for HR1 which is marginally lower than that of the sample of M stars (Gagne et al., 1995). The $\log[f_x/f_v]$ relation of Maccacaro et al. (1988) was used to derive the ratio of X-ray to optical flux as ~ -2 . This is well within the range expected for M stars. The results are all consistent with the identification of this object as a star of spectral type M.

G 65.3+5.7

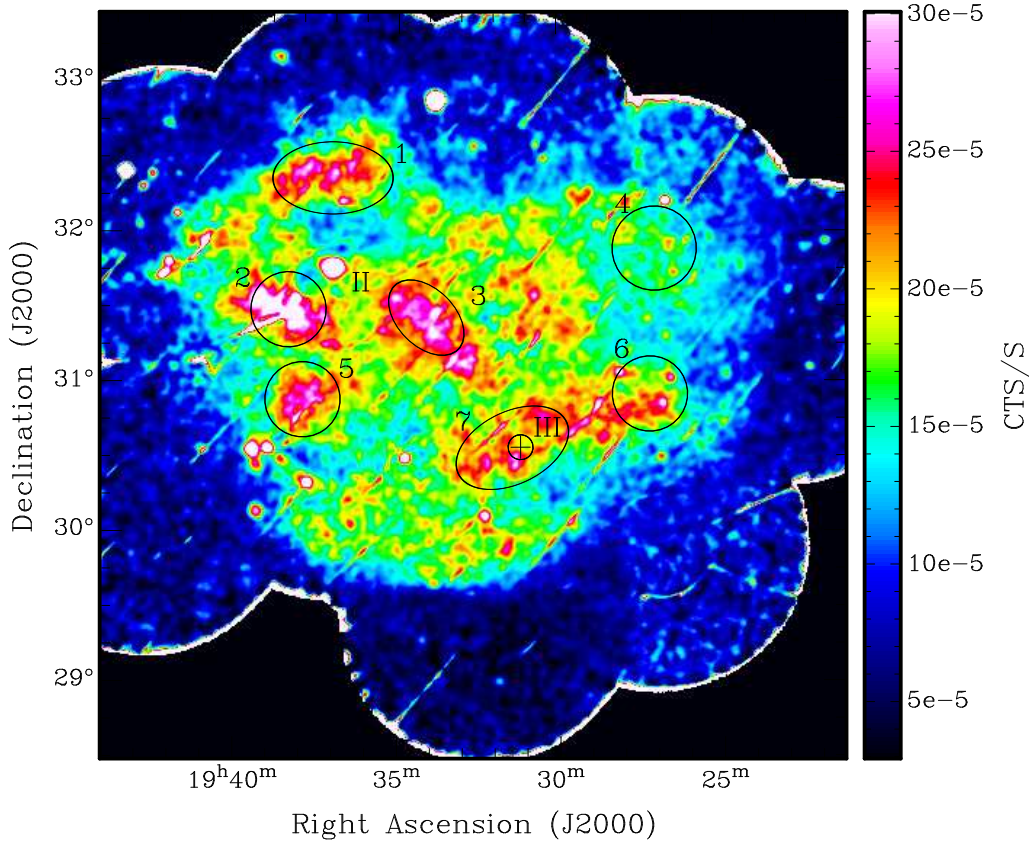


Figure 6.19: Vignetted and smoothed X-ray image of G 65.3+5.7 in the energy range 0.1 - 2.4 keV consisting of 17 merged ROSAT PSPC pointings. The circles mark the regions from which individual spectra were extracted. The cross with the small circle indicates the position and the position error of the Pulsar PSR J1931+30. The roman numbers refer to the sources specified in the text.

6.3.2 Spectral Analysis

A spectral analysis of the whole supernova remnant was performed using the RASS-III data. The emission region of the galaxy CGMW 5-10975 and other point sources were excluded (cf. Tab. 6.4). The background was extracted from a region close to the remnant. The PSPC spectrum of the entire remnant has been fit with single-temperature or power law and two-component models. Figure 6.20 shows the ROSAT PSPC spectrum of the entire remnant fitted with a two-temperature Raymond-Smith model. The best fit results are listed in Tab. 6.5. A two-temperature model, consisting of two Raymond-Smith models, describes the spectral nature of G 65.3+5.7 in the best way

Nr.	source	R.A. hh:mm:ss	DEC dd:mm:ss	count rate cts/s	HR1	HR2
1	CGMW 5-10975	19:33:45	+32:55:03	0.31±0.01	0.96±0.10	0.27±0.07
2	GSC 02655-01741	19:37:01	+31:47:20	0.41±0.01	0.02±0.05	-0.15±0.05
3	2E 1937.0+3027	19:39:02	+30:34:36	0.05±0.01	0.60±0.23	0.19±0.20
4	IRAS 19327+3024	19:34:45	+30:31:05	0.032±0.004	0.90±0.38	-0.26±0.14
5	V853 Cyg	19:26:32	+32:13:45	0.026±0.002	0.92±0.29	0.01±0.34
6	PSR J1931+30	19:31:17	+30:32:18	0.016±0.005	–	–

Table 6.4: X-ray point sources in the region of G 65.3+5.7 (Fig. 6.19). The position of the pulsar PSR J1931+30 results in a maximum likelihood detection within the error circle of the radio data.

according to the reduced χ^2 . A powerlaw model with an spectral index $\Gamma \geq 3.5$ seems to be unphysical indicating rather a steep drop-off of thermal emission. Archival data from 17 pointed observations with ROSAT PSPC provided a more detailed spectral analysis of the remnant. Excluding point sources, spectra were extracted from different regions of the remnant with high photon statistics. The extraction region are shown in Fig. 6.19. The spectra were fit with a single-temperature Raymond-Smith

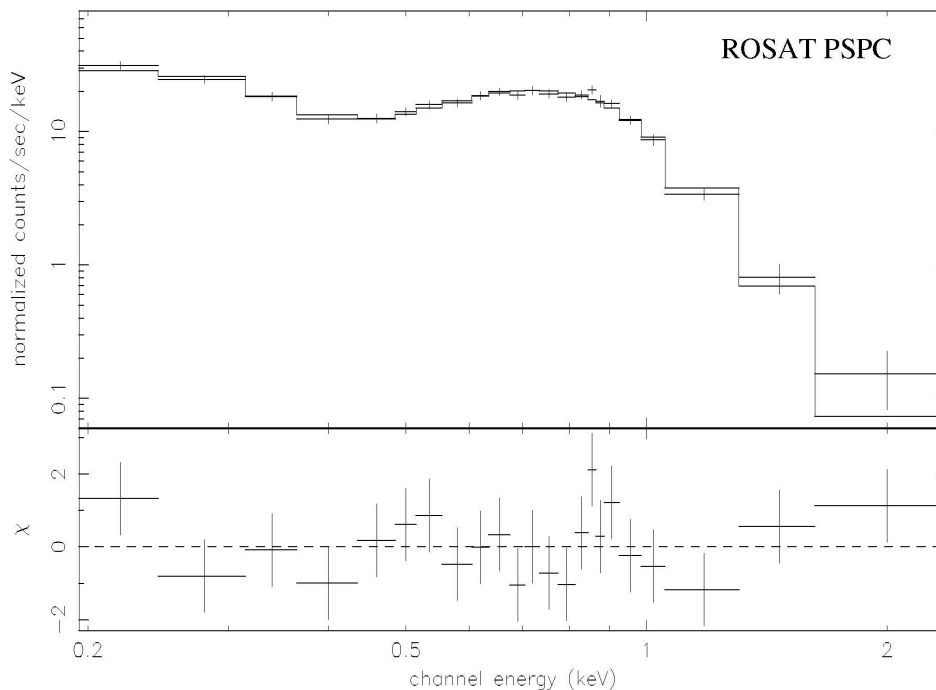


Figure 6.20: RASS spectrum of the entire remnant fitted with a two-temperature Raymond-Smith model.

Model	kT_1 [keV]	kT_2 [keV]	Γ	N_H [10^{20} cm^{-2}]	Flux [$\text{ergs cm}^{-2} \text{ s}^{-1}$]	red. χ^2
RS* + RS	0.11 ± 0.10	0.29 ± 0.10	–	(4.43 ± 8.28)	8.26×10^{-10}	1.065
RS + Pl**	0.24 ± 0.01	–	6.43 ± 3.70	(6.80 ± 3.83)	1.61×10^{-8}	1.16

Table 6.5: Results from the spectral analysis of the whole remnant using the RASS data. Flux refers to the unabsorbed flux in the 0.1-2.4 keV energy band. Raymond-Smith model is indicated by * and a power law by **.

Region	kT [keV]*	N_H [10^{20} cm^{-2}]*	red. χ^2 *	kT [keV]**	N_H [10^{20} cm^{-2}]**	red. χ^2 **
1	0.13 ± 0.06	5.91 ± 2.83	1.49	0.14 ± 0.05	2.91 ± 2.85	1.30
2	0.29 ± 0.13	5.00 ± 3.16	1.18	0.29 ± 0.11	0.65 ± 1.43	0.72
3	0.34 ± 0.06	5.37 ± 0.97	2.32	0.31 ± 0.03	0.95 ± 0.50	1.14
4	0.03 ± 0.05	351 ± 758	0.78	0.24 ± 0.04	6.56 ± 7.39	0.89
5	0.26 ± 0.05	6.11 ± 1.20	1.05	0.24 ± 0.03	1.87 ± 0.78	2.00
6	0.20 ± 0.03	6.93 ± 0.91	1.93	0.20 ± 0.01	2.63 ± 0.70	1.10
7	0.24 ± 0.01	6.56 ± 0.85	1.35	0.22 ± 0.01	1.82 ± 0.39	1.25

Table 6.6: Spectral fit results from seven regions within G65.3+5.7 (Fig. 6.19). Thermal Bremsstrahlung model is indicated by *, Raymond-Smith plasma model by **.

and thermal Bremsstrahlung model. The results are listed in Tab. 6.6. The reduced χ^2 specifies the goodness of fit and should approach the value 0.96. The spectral analysis shows a variation of factor ~ 2 in temperature for both models and a marginal variation in N_H using the Bremsstrahlungs model and a larger variation of factor ~ 4 using the Raymond-Smith model.

Another possibility to look for spectral and temperature variations across G 65.3+5.7, is the creation of an energy image (Fig. 6.21), where the colour of each pixel corresponds to the mean energy of photons in that pixel. The majority of the X-ray emission is below 0.9 keV. The entire rim, mainly the north-eastern part is characterized by soft X-ray emission below 0.5 keV (red colour) whereas the interior part shows harder emission indicated by the green colour which refers to 0.52 - 0.90 keV. This is in agreement with the fact that the plasma temperature decreases with radius from 0.29 keV to 0.22 keV (Fig. 6.22). Therefore, the remnant was divided in concentric shells from 0.4 to 1.6 degree radius with a step size of 0.3 degree from the rim to the interior. For each shell a spectrum was extracted and fit with a single Raymond-Smith model. The hard X-ray emission above 0.90 keV peaks in three regions located at $R.A. = 19^h 39^m 02^s$ and $Dec. = +30^\circ 34' 36''$ (J2000.0) coinciding with the X-ray variable binary stars 2E 1937.0+3027 (Kashyap & Drake, 1999), the radio-loud galaxy CGMW 5-10975 at $R.A. = 19^h 33^m 45^s$ and $Dec. = +32^\circ 55' 03''$ (J2000.0) and an extended X-ray source at $R.A. = 19^h 37^m 02^s$ and $Dec. = +31^\circ 47' 37''$ (J2000.0). The spectrum of this source fit a thermal bremsstrahlung model with a temperature of (1.02 ± 0.41) keV and $N_H = 0.8 \pm 0.3 \times 10^{20} \text{ cm}^{-2}$.

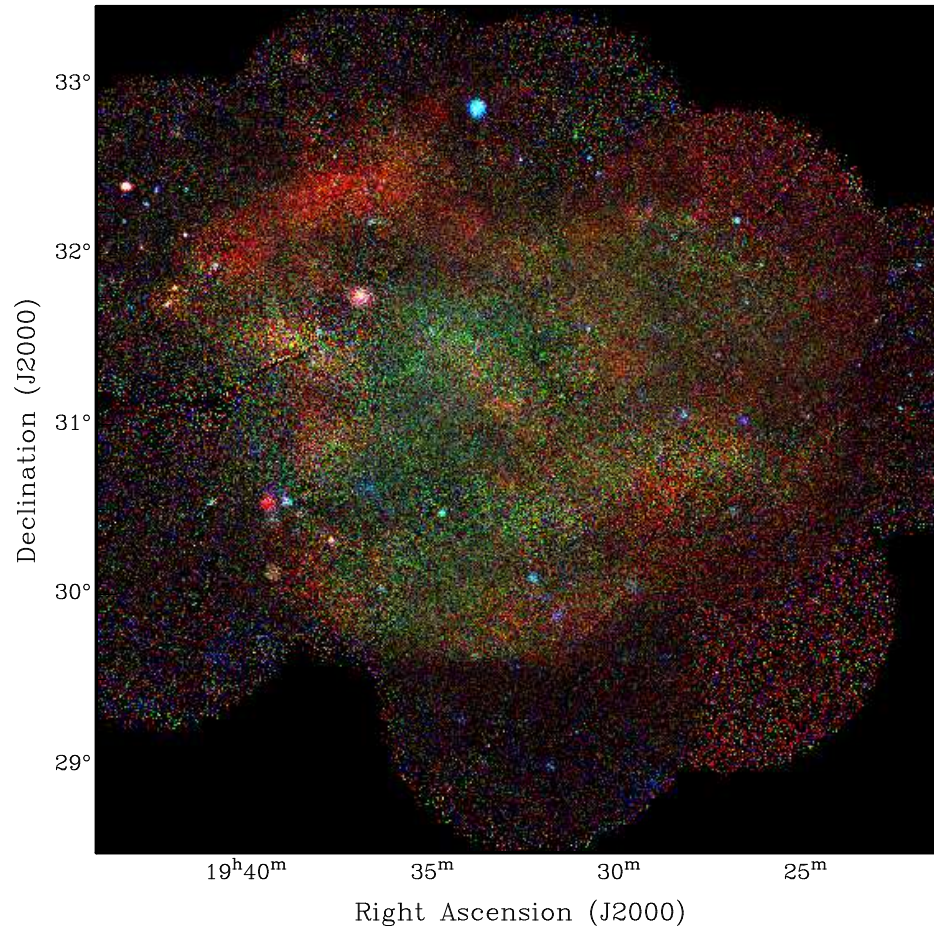


Figure 6.21: False colour image from the merged ROSAT PSPC pointings. The colour coding indicates the different energy bands as follows: red (0.11-0.41 keV), green (0.52-0.90 keV) and blue (0.91-2.01 keV). G 65.3+5.7 shows very soft X-ray emission throughout the remnant, indicated by the red and green colour.

Supernova remnant model for G 65.3+5.7

The spectrum of the whole supernova remnant G 65.3+5.7 is described by a Raymond-Smith model for hot, diffuse gas with an emission measure $EM=0.081 \text{ cm}^{-5}$. The emission measure gives the electron density $n_e=0.019 \text{ cm}^{-3} \text{ d}^{-1/2}$, with d the distance in kpc (cf. equations 5.1 and 5.2).

While the Sedov model is simplified and ignores magnetic effects and relativistic particles, it does properly explain many observed SNRs. A Sedov model with Raymond-Smith emissivity has been used to reproduce the observed brightness, temperature and angular size of G65.3+5.7. The explosion energy is taken as a free parameter in the Sedov model (cf. 3.2.2) in the range of $0.1 - 1 \times 10^{51} \text{ erg}$. (Tab. 6.7). In comparison, Gull et al. (1977) have noted that the expansion velocity is $v_{exp} \geq 50 \text{ km s}^{-1}$ in order to produce the observed strong O III lines. Recent optical observations

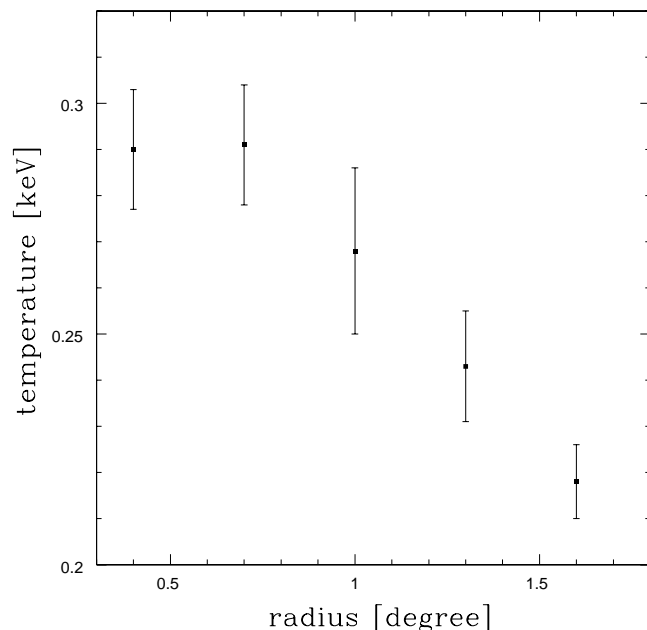


Figure 6.22: Variation of the plasma temperature with radius for G 65.3+5.7.

E_0 [10^{51} erg]	d [kpc]	r [pc]	v [km/s]	t [10^3 yr]	n_0 [cm^{-3}]
0.10	0.79	22	420	21.6	0.021
0.18	1.00	28	420	27.5	0.019
1.00	2.00	56	420	55.1	0.013

Table 6.7: Solution of the Sedov model for G 65.3+5.7 using different distances (cf. 3.2.2).

suggest shock velocities in the range of 90-140 km s^{-1} (Mavromatakis et al., 2002). A radius $r=38_{-13}^{+25}$ and distance $d=0.9_{-0.3}^{+0.6}$ could be adopted from radio observations using the Σ -D relation (Reich et al., 1979). In the case of a magnetic field $B_0=3 \times 10^{-6}$ Gauss which can be assumed due to non-thermal radio emission, Canto (1977) derived an empirical relation between linear radius r, ambient density n_0 and expansion velocity v_{exp} . Using his Fig. 3 (Canto, 1977) and the radius of the remnant, Reich et al. (1979) found $n_0 \leq 9_{-7}^{+21} \text{ cm}^{-3}$ yielding $E_0 \sim (13 \pm 2) \times 10^{51}$ erg.

The parameters from optical and radio observations seem to be consistent with the X-ray data, except for the velocity measurements from optical emission which is produced by collisionally ionized elements such as O III, N III and S II representing a lower limit of the expansion velocity when the shock wave interacts with a denser environment and therefore is slowed down. The Sedov parameters were adopted for a distance of 1 kpc regarding the radio data (Reich et al., 1979) and therefore the

following physical characteristics were obtained: radius ~ 28 pc, shock velocity ~ 420 km s $^{-1}$ age ~ 27500 years, ambient density ~ 0.019 cm $^{-3}$, initial explosion energy of $\sim 0.18 \times 10^{51}$ erg and a luminosity $L_x \sim 9.9 \times 10^{34}$ erg s $^{-1}$. The swept-up mass amounts to $\sim 45 M_\odot$.

6.3.3 Summary and Discussion

The spatial and spectral properties of G 65.3+5.7 have been studied in X-rays using data from the ROSAT all-sky survey and pointed ROSAT PSPC. G65.3+5.7 shows a X-ray shell with an extent of 3.0×3.2 degree which is mainly dominant in the soft energy band below 1 keV. Bright extended objects are located within the remnant showing hard X-ray emission. Correlating the source positions with databases like NVSS and the optical DSS2 as well as with SIMBAD and NED and calculating the hardness ratio, enabled their identification as foreground or extragalactic objects.

The spectral analysis shows a slight increase of the plasma temperature towards the center of the remnant which is in agreement with the energy distribution in the energy image. For small X-ray bright regions within the remnant, spectral analyses were performed resulting in a variation of factor ~ 2 in temperature and factor ~ 4 in N_H . The overall spectrum of G 65.3+5.7 can be described by a two-temperature Raymond-Smith model. Using the Sedov analysis, G 65.3+5.7 has a radius of ~ 28 pc at a distance of 1 kpc, an initial explosion energy $E_0 \sim 0.18 \times 10^{51}$ erg, ambient density ~ 0.019 cm $^{-3}$ and an age of 27500 years. Since SNe Ia are thought to have low explosion energies ($E_0 \approx 0.5 \times 10^{51}$ erg) the determined value of E_0 is weak evidence for the progenitor of G 65.3+5.7 being a SN Ia. In addition, the distance estimate of both, the SNR and the pulsar do not agree within their errors. This would be in conflict with an assumed association of the remnant with the pulsar PSR J1931+30.

The radio pulsar PSR J1931+30, which is located within G 65.3+5.7, has an offset of $\sim 45'$ from the geometrical center of the remnant. Unfortunately, the position at the pulsar is not well determined. Published positions list an error box of $5'$. A first time derivative of the pulsar rotation period is also not available, leaving open the pulsar spin-down age and properties like spin-down flux and magnetic polar field. An association of the pulsar with the remnant based on age estimation from the radio data is therefore currently not possible. However, using the count rate upper limit in the X-ray data and assuming a Crab-like spectrum, an X-ray flux of $f_x \leq 3.93 \times 10^{-13}$ erg cm $^{-2}$ s $^{-1}$ was obtained. This flux value yields an upper limit of the X-ray luminosity of $L_x \leq 4.32 \times 10^{32}$ erg s $^{-1}$, using the dispersion based distance of 3 kpc (Camilo et al., 1996). The luminosity is comparable to the luminosities of the recently discovered 65 ms pulsar PSR J0205+6449 in 3C58 (Murray et al., 2002) and B0833-45 in the Vela SNR (cf. Becker & Truemper (1997) and references therein). Using the upper limit of the X-ray luminosity and applying the relation $L_x = 10^{-3} \cdot \dot{E}$ by Becker & Truemper (1997), \dot{P} could subsequently be calculated from $\dot{E} = 4\pi I \dot{P} P^{-3}$ with a moment of inertia $I \approx (2/5) MR^2 \approx 10^{45}$ g cm 2 and $P = 0.582219$ s. The lower limit of the characteristic age $\tau = P/2\dot{P}$ is about 1400 years according to the observational X-ray and radio parameters. In comparison, the remnants' age is about a factor 20

higher than the calculated age of the pulsar.

Further radio observations are necessary to determine the pulsar spin down age and the accurate position in order to clarify if the pulsar is associated with G 65.3+5.7 or not (cf. 3.5).

Appendix A

Source catalogues of the SNR candidates

The following tables include all SNR candidates, listed with their source properties, like position in R.A. and DEC (J2000.0), the extent in arcmin, count rate and the hardness ratio HR 1 as well as HR 2 which are defined in the following way:

$$HR1 = \frac{B - A}{B + A} \quad (\text{A.1})$$

$$HR2 = \frac{D - C}{D + C} \quad (\text{A.2})$$

where A: 11-41 channels, B: 52-201 channels, C: 52-90 channels and D:91-201 channels in the ROSAT PSPC.

All SNR candidates with an extent below $30'$ are considered separately and classified by five groups which contain:

- Objects which are identified as SNRs
- very promising SNR candidates
- good SNR candidates
- weak SNR candidates
- targets which are identified as extragalactic objects or X-ray bright stars

Because of the smaller number of large SNRs ($D > 30'$) a classification as described above was not performed. The SNR candidates with an extent larger than $30'$ are listed without such a classification. The corresponding images of all SNR candidates are listed in the appendix B according to this classification scheme.

Nr.	Source	RA hh:mm:ss	DEC dd:mm:ss	extent arcmin	count rate cts/s	HR1	HR2
1	G38.7-1.4	19:07:05	+04:31:11	13×10	0.07±0.02	+0.89	+0.43
2	G296.8-1.0	11:56:20	-63:09:34	14×8	0.19±0.04	+0.96	+0.44

Table A.1: Identified SNR

Nr.	Source	R.A. hh:mm:ss	DEC dd:mm:ss	extent arcmin	count rate cts/s	HR1	HR2
1	G80.7+6.8	20:08:15	+45:04:23	12×12	0.05±0.02	+0.21	0.00
2	G254.8-7.0	07:49:58	-40:11:42	18×12	0.07±0.03	+0.23	+0.33
3	G286.6-15.2	09:10:51	-70:39:47	18×13	0.09±0.03	+0.52	-0.27
4	G308.3-1.4	13:40:57	-63:43:37	10×9	0.35±0.04	+0.95	+0.43
5	G309.9-2.5	13:56:29	-64:30:49	24×13	0.18±0.05	+0.59	+0.61
6	G321.8-3.5	15:33:21	-60:15:56	25×25	0.20±0.07	+0.58	-0.68
7	G322.5+6.3	15:00:57	-51:35:10	14×9	0.40±0.05	+0.96	+0.42
8	G332.5-5.6	16:42:59	-54:32:09	17×16	0.45±0.08	+0.90	-0.53
9	G337.2+13.0	15:47:32	-37:55:09	15×15	0.15±0.03	-0.50	-0.29

Table A.2: Very promising SNR-candidates

Nr.	Source	R.A. hh:mm:ss	DEC dd:mm:ss	extent arcmin	count rate cts/s	HR1	HR2
1	G7.6+2.0	17:55:11	-21:23:24	13×7	0.33±0.06	+0.89	+0.88
2	G16.7+15.9	17:25:00	-06:33:54	12×7	0.17±0.04	+0.52	+0.54
3	G17.8-12.5	19:10:03	-19:03:30	7×7	0.06±0.03	+0.37	+0.18
4	G17.8-12.9	19:11:41	-19:10:18	9×7	0.70±0.05	+0.75	+0.85
5	G31.9-1.1	18:53:28	-01:26:35	11×7	0.28±0.06	+1.00	+0.56
6	G33.7+7.6	18:25:45	+04:08:40	5×5	0.13±0.03	-0.07	+0.24
7	G34.5-12.0	19:37:10	-04:02:27	9×6	0.05±0.02	+1.00	+0.33
8	G35.2+17.1	17:53:59	+09:37:01	8×8	0.09±0.03	+0.33	-0.10
9	G36.0+6.0	18:35:33	+05:24:45	12×8	0.08±0.03	+0.36	+0.22
10	G38.3+10.6	18:22:54	+09:30:10	8×8	0.09±0.03	+0.85	+0.30
11	G38.5+7.3	18:35:19	+08:13:58	15×15	0.10±0.04	+0.90	+0.18
12	G55.6+2.1	19:26:47	+21:02:39	11×8	0.09±0.03	+1.00	+0.23
13	G56.3-2.3	19:44:28	+19:32:47	8×8	0.12±0.03	+0.02	-0.25
14	G57.4+6.1	19:14 58	+24:32:24	7×7	0.07±0.02	+0.50	+0.28
15	G63.4+0.4	19:49:55	+27:02:02	8×8	0.10±0.03	+0.06	+0.33
16	G64.0-0.1	19:53:08	+27:15:35	12×10	0.04±0.02	+0.88	+0.75
17	G66.7-9.8	20:35:48	+24:11:13	11×8	0.08±0.03	+0.76	+0.16
18	G66.8-1.3	20:04:28	+29:04:09	13×8	0.07±0.02	+0.16	+0.09
19	G71.2-2.9	20:21:52	+31:48:15	22×15	0.08±0.02	+0.25	+0.10
20	G73.1+5.5	19:52:27	+37:58:28	12×8	0.15±0.03	+0.59	+0.15
21	G73.2-15.9	21:14:19	+25:22:57	8×6	0.18±0.02	+0.70	+0.04
22	G83.8+12.4	19:47:50	+50:30:45	10×9	0.05±0.02	+0.58	+0.47
23	G85.4+0.8	20:50:39	+45:22:24	18×12	0.10±0.03	+1.00	+0.31
24	G95.4-3.9	21:51:47	+49:09:50	5×5	0.05±0.02	0.00	+0.25
25	G103.5-8.8	22:50:16	+49:25:28	8×8	0.13±0.03	+0.50	+0.12
26	G105.6+13.6	21:17:10	+68:56:42	17×14	0.12±0.02	+0.51	+0.37
27	G118.9-15.4	00:28:32	+47:19:22	9×9	0.05±0.02	+1.00	+0.17
28	G124.6-5.4	01:03:33	+57:24:12	8×8	0.20±0.05	+0.07	-0.28
29	G125.4+10.0	01:23:50	+72:42:30	5×5	0.08±0.02	+0.95	+0.62
30	G141.7-0.7	03:15:30	+56:53:13	17×10	0.08±0.03	-0.15	-0.29
31	G151.9+11.7	05:15:22	+58:46:16	9×7	0.22±0.04	+0.79	+0.47
32	G153.3+3.8	04:37:32	+52:49:54	8×8	0.14±0.03	-0.61	-0.40
33	G162.9+13.9	06:06:01	+50:29:57	12×7	0.06±0.03	+1.00	+0.20
34	G176.0+2.7	05:46:49	+33:46:18	15×5	0.08±0.03	+1.00	+0.39
35	G178.9+16.0	06:50:40	+37:40:12	10×10	0.07±0.03	+0.75	+0.25
36	G179.0+6.5	06:09:42	+33:03:01	15×7	0.09±0.03	+1.00	+0.12
37	G187.7+0.4	06:04:13	+22:29:59	7×7	0.11±0.03	+0.14	+0.07
38	G188.1-3.3	05:51:37	+20:19:19	11×7	0.04±0.02	+0.60	+0.14
39	G193.0+12.4	07:01:24	+23:14:08	15×8	0.11±0.05	+0.76	+0.29
40	G198.7+4.0	06:39:51	+14:28:27	7×7	0.09±0.03	+0.29	-0.18
41	G219.4-14.6	06:10:22	-12:14:43	15×10	0.07±0.02	+0.29	+0.58
42	G221.8+1.5	07:12:51	-07:11:21	22×10	0.07±0.03	+0.26	+0.28

43	G226.0+0.5	07:17:24	-11:19:50	10×10	0.21±0.03	+0.92	+0.67
44	G229.2-17.2	06:16:20	-21:57:03	8×8	0.13±0.02	+0.90	+0.35
45	G255.5+10.8	09:03:28	-30:22:22	12×8	0.06±0.02	+0.56	+0.33
46	G258.4-7.5	07:57:28	-43:28:07	8×8	0.13±0.03	+0.46	+0.06
47	G259.4+10.9	09:15:36	-33:10:41	28×28	0.13±0.05	+0.92	-0.09
48	G260.3-9.6	07:52:22	-46:11:00	15×10	0.08±0.02	+0.37	+0.24
49	G261.6+15.5	09:38:29	-31:28:00	15×11	0.07±0.02	+0.03	-0.33
50	G262.8-9.1	08:02:42	-48:04:22	20×10	0.14±0.03	+0.32	+0.28
51	G265.2+8.1	09:25:24	-39:13:41	8×8	0.04±0.02	+0.74	+0.20
52	G265.8-7.1	08:22:19	-49:30:44	17×12	0.09±0.02	+1.00	-0.09
53	G266.0+9.6	09:34:05	-38:43:00	30×30	0.21±0.07	+0.06	-0.19
54	G271.6+2.8	09:30:35	-47:32:03	14×6	0.12±0.03	+0.41	-0.47
55	G276.2-7.7	09:01:46	-58:05:47	12×8	0.25±0.05	+0.29	+0.11
56	G278.0+12.4	10:32:36	-43:42:07	21×13	0.27±0.06	-0.10	0.00
57	G285.7+4.1	10:48:44	-54:38:55	8×7	0.09±0.04	+0.10	0.00
58	G286.8-0.1	10:41:30	-58:51:49	30×20	0.17±0.06	+0.27	-0.13
59	G288.1-0.1	10:50:24	-59:24:11	9×8	0.09±0.03	+1.00	+0.48
60	G290.4-2.0	11:01:15	-62:07:45	21×9	0.15±0.06	+0.24	+0.11
61	G290.9-1.1	11:07:44	-61:30:11	22×22	0.20±0.06	+0.36	+0.32
62	G294.8-0.3	11:40:56	-61:59:52	7×7	0.12±0.03	+0.09	-0.04
63	G295.4-3.0	11:40:06	-64:47:52	12×7	0.08±0.03	+0.50	-0.28
64	G296.8-1.0	11:56:20	-63:09:35	12×7	0.13±0.03	+1.00	+0.70
65	G299.5-0.6	12:20:27	-63:12:44	8×7	0.32±0.08	0.00	+0.29
66	G307.5+5.0	13:25:30	-57:32:20	6×6	0.70±0.09	+1.00	+0.70
67	G310.8-1.2	14:01:54	-62:58:29	10×7	0.07±0.03	+1.00	-0.11
68	G312.4+4.8	14:01:14	-56:49:20	17×12	0.16±0.07	+0.47	+0.68
69	G314.6+13.6	13:59:08	-47:42:29	18×8	1.23±0.14	+0.74	+0.33
70	G314.7-1.2	14:33:30	-61:40:18	25×20	0.11±0.04	+0.91	+0.64
71	G317.5+18.3	14:07:01	-42:26:33	20×20	0.26±0.14	+1.00	+0.02
72	G328.1+15.8	15:01:49	-40:37:13	8×8	0.26±0.05	+1.00	+0.23
73	G338.3+15.3	15:44:19	-35:23:56	10×7	0.12±0.04	+0.44	+0.16
74	G342.4-1.9	17:04:06	-44:33:30	15×10	0.14±0.05	+1.00	+0.31
75	G349.1+13.0	16:28:09	-29:50:19	10×10	0.09±0.03	-0.19	-0.32
76	G353.6-0.8	17:32:36	-34:44:54	30×15	0.38±0.08	+0.92	+0.81
77	G353.2+0.9	17:24:42	-34:13:03	12×7	0.15±0.04	+1.00	+0.76
78	G359.8-14.1	18:44:13	-35:40:05	8×8	0.18±0.05	+0.59	+0.07

Table A.3: Good SNR-candidates

Nr.	Source	R.A. hh:mm:ss	DEC dd:mm:ss	extent arcmin	count rate cts/s	HR1	HR2
1	G0.4-7.9	18:18:27	-32:29:36	7×5	0.05±0.05	-	-
2	G1.1-0.8	17:51:33	-28:24:08	30×12	0.52±0.09	+0.81	+0.49
3	G7.9-6.4	18:27:52	-25:06:37	13×10	0.12±0.07	+1.00	-0.54
4	G13.0-14.9	19:11:19	-24:13:58	30×12	-	-	-
5	G13.0+6.3	17:51:10	-14:33:11	20×20	0.11±0.05	+0.78	-0.78
6	G15.9-3.9	18:34:10	-16:54:40	20×20	0.09±0.05	+1.00	+0.38
7	G23.6-4.2	18:49:26	-10:13:25	10×10	0.10±0.04	+1.00	+0.13
8	G26.6+1.8	18:33:14	-04:50:15	8×8	0.04±0.02	+0.82	+0.84
9	G31.4-0.4	18:49:52	-01:33:18	5×5	1.21±0.07	-0.03	0.00
10	G31.9-1.1	18:53:28	-01:26:35	11×7	0.28±0.06	+1.00	+0.56
11	G35.1+17.1	17:53:59	+09:34:26	10×8	0.08±0.03	+0.51	+0.19
12	G35.6-5.8	19:16:55	-00:17:18	16×12	0.11±0.04	+0.66	-0.08
13	G42.0-11.4	19:48:38	+02:40:11	15×15	0.05±0.03	+0.93	+0.54
14	G46.7-12.7	20:01:59	+06:04:50	8×7	0.07±0.02	+0.60	+0.23
15	G46.8-2.2	19:24:53	+11:15:41	10×10	0.04±0.02	-0.20	+1.00
16	G56.2+8.2	19:04:31	+24:23:54	10×10	0.03±0.02	+1.00	+0.20
17	G57.0+4.3	19:20:56	+23:18:19	11×9	0.09±0.04	+0.09	+0.22
18	G67.4+10.7	19:16:11	+35:24:11	8×8	0.16±0.02	+0.88	+0.49
19	G70.5+1.6	20:02:22	+33:40:25	8×8	0.10±0.03	+0.67	+0.06
20	G72.2+9.2	19:33:33	+38:56:05	9×7	0.05±0.02	+1.00	+0.20
21	G74.1+0.3	20:17:23	+36:03:40	10×7	0.08±0.02	+0.44	-0.15
22	G75.8+8.1	19:47:21	+41:33:24	7×6	0.03±0.02	+0.33	+0.55
23	G75.9+15.6	19:10:51	+44:55:59	7×6	0.09±0.03	+0.78	-0.12
24	G76.3+0.4	20:23:07	+37:55:12	17×17	0.05±0.01	+0.61	+0.08
25	G78.0+5.3	20:06:41	+42:00:09	12×8	0.05±0.02	+1.00	-0.06
26	G83.7+10.3	19:59:05	+49:27:54	20×18	0.04±0.02	+0.22	+0.18
27	G84.6-0.1	20:51:49	+44:14:34	25×25	0.10±0.04	+0.95	+0.35
28	G85.7+10.6	20:03:22	+51:15:54	16×11	0.12±0.02	+0.74	+0.31
29	G88.6+6.0	20:38:10	+51:04:33	5×5	0.05±0.02	+0.14	-0.17
30	G94.8-4.9	21:52:59	+47:56:58	30×30	0.18±0.05	+1.00	-0.08
31	G100.0-2.7	22:10:46	+52:55:16	23×13	0.13±0.03	+0.69	+0.10
32	G103.5-8.8	22:50:16	+49:25:29	11×9	0.16±0.04	+0.51	+0.15
33	G106.0+13.2	21:23:01	+68:53:30	13×13	0.08±0.02	+0.33	-0.01
34	G108.0-1.2	22:53:56	+58:13:28	30×20	0.08±0.03	-	-
35	G110.9+2.8	23:02:12	+63:03:20	25×20	0.17±0.03	+0.67	+0.44
36	G116.8-1.1	00:00:09	+61:10:43	30×30	0.18±0.03	-	-
37	G118.8-11.5	00:25:21	+51:07:49	10×8	0.04±0.02	+0.60	+0.18
38	G127.4-0.7	01:29:09	+61:49:00	8×8	0.08±0.02	-0.17	+0.35
39	G128.2+2.6	01:41:46	+64:57:11	8×8	0.02±0.01	-	-
40	G129.5-2.8	01:43:09	+59:24:10	30×25	0.08±0.04	-0.34	+0.39
41	G135.2-1.7	02:28:15	+58:49:43	25×12	0.09±0.03	+0.25	+0.24
42	G138.9-12.5	02:24:52	+47:25:42	9×9	0.04±0.02	+1.00	+0.10

43	G141.5+0.5	03:18:58	+57:56:21	16×10	0.06±0.02	+0.66	+0.89
44	G141.6+2.1	03:26:10	+59:14:12	14×9	0.04±0.03	+1.00	+0.26
45	G142.7+9.0	04:09:39	+63:56:05	13×13	0.07±0.03	+0.07	-0.12
46	G142.8-8.3	02:56:43	+49:43:56	18×12	0.07±0.03	+0.90	+0.29
47	G146.1+12.1	04:50:39	+63:33:23	7×7	0.05±0.02	+0.25	+0.08
48	G148.3-13.1	03:10:13	+42:49:51	12×12	0.08±0.02	+0.71	+0.09
49	G149.2+15.1	05:27:52	+62:46:57	20×14	0.08±0.04	+1.00	-0.13
50	G173.2-0.1	05:27:56	+34:39:22	12×10	0.06±0.02	+0.71	+0.60
51	G173.9+0.3	05:31:23	+34:12:06	11×8	0.06±0.02	+0.71	+0.79
52	G176.0-11.8	04:51:50	+25:30:57	15×10	0.08±0.03	+1.00	+0.38
53	G178.2-3.3	05:28:37	+28:39:53	8×7	0.04±0.02	+0.58	-0.28
54	G203.4+9.0	07:06:23	+12:31:56	12×9	0.12±0.03	+1.00	+0.31
55	G218.6-15.7	06:04:59	-12:01:53	8×8	0.09±0.03	+0.52	+0.63
56	G222.0+14.4	07:59:17	-01:18:22	12×10	0.17±0.04	+0.42	+0.07
57	G223.7-0.1	07:11:00	-09:35:40	15×12	0.07±0.03	+0.12	+0.48
58	G238.5-6.4	07:16:01	-25:40:04	9×9	0.06±0.02	+1.00	+0.57
59	G253.0+15.5	09:12:14	-25:26:10	25×25	0.16±0.04	+0.35	-0.21
60	G253.0+13.7	09:06:19	-26:38:23	12×12	0.07±0.02	+0.28	+0.22
61	G254.4+10.3	08:58:26	-29:53:18	10×8	0.07±0.02	+0.33	+0.18
62	G256.7-6.7	07:56:23	-41:38:18	18×7	0.14±0.05	+0.69	+0.24
63	G258.3+1.5	08:36:31	-38:25:01	15×15	0.07±0.03	+1.00	+0.87
64	G259.1+11.8	09:17:44	-32:22:12	28×20	0.09±0.04	+0.77	-0.08
65	G266.4+9.7	09:35:40	-38:56:09	10×10	0.06±0.03	+0.28	+0.24
66	G272.2-9.0	08:36:24	-55:47:50	16×10	0.10±0.03	+0.62	+0.09
67	G292.3+0.6	11:23:25	-60:26:19	9×6	0.12±0.05	-0.08	+0.67
68	G294.9-1.6	11:38:47	-63:20:30	13×11	0.27±0.05	+0.75	+0.16
69	G305.5-1.9	13:15:17	-64:41:02	30×30	0.34±0.09	+0.56	-0.18
70	G315.5+0.4	14:34:09	-59:59:30	19×18	0.17±0.05	+0.39	+0.16
71	G319.8-2.1	15:14:20	-60:10:02	23×15	0.04±0.02	+0.63	-0.10
72	G328.1+15.8	15:01:49	-40:37:13	5×5	0.24±0.05	+1.00	+0.02
73	G332.9+1.9	16:10:10	-49:04:02	13×8	0.08±0.04	+0.38	+0.57
74	G334.1-8.9	17:08:10	-55:19:51	12×9	0.19±0.08	+0.22	-0.08
75	G334.5-9.3	17:12:02	-55:20:04	17×12	0.10±0.05	+0.04	+0.17
76	G336.0-4.4	16:51:40	-51:09:33	20×10	0.08±0.06	+0.26	+1.00
77	G353.7+17.7	16:25:37	-23:26:09	11×6	0.26±0.04	+0.81	+0.63
78	G353.7+16.0	16:31:22	-24:31:43	7×5	0.10±0.03	+0.56	+0.44
79	G355.7+10.6	16:55:01	-26:25:12	20×12	0.20±0.05	+0.90	+0.51
80	G355.8-7.1	18:04:47	-36:08:19	15×15	0.16±0.08	+0.68	+0.05
81	G358.2+6.5	17:16:25	-26:54:12	12×7	0.10±0.05	+0.65	-0.01
82	G359.8-14.1	18:44:13	-35:40:05	8×8	0.19±0.05	+0.65	+0.10

Table A.4: Weak candidates with poor evidence for SNRs

Nr.	Source	R.A. hh:mm:ss	DEC dd:mm:ss	extent arcmin	count rate cts/s	HR1	HR2	probable source
1	G0.55+9.27	17:12:24	-23:23:22	11×10	6.77±0.16	+0.98	+0.60	Star/PN
2	G6.1-1.3	18:04:23	-24:22:07	22×10	0.49±0.05	+0.98	+0.43	HII
3	G7.2+1.4*	17:56:31	-22:00:37	10×7	0.18±0.04	+0.63	+0.35	Star
4	G10.9-16.9*	19:15:47	-26:54:46	8×8	0.16±0.04	+0.80	0.00	Gal
5	G11.3-15.8*	19:11:50	-26:04:32	7×7	0.19±0.06	+0.08	-0.40	Gal
6	G12.7-14.1	19:07:34	-24:07:21	20×12	0.08±0.06	-0.57	-0.92	Moon
7	G13.3-16.4	19:17:48	-24:34:12	16×12	0.07±0.03	+0.82	+0.40	Gal
8	G14.9+5.1	17:59:08	-13:31:46	7×7	0.13±0.03	+0.69	+0.60	Gal
9	G14.12-0.01	18:16:09	-16:41:00	70×60	3.92±0.21	+1.00	+0.18	H II/Gal
10	G17.7-16.3	19:24:26	-20:36:06	13×5	0.11±0.05	+0.62	0.00	Gal
11	G17.4+13.2	17:35:44	-07:23:09	8×8	0.17±0.03	+1.00	+0.72	Gal
12	G26.3-9.8	19:14:43	-10:16:00	15×15	0.13±0.05	+0.76	+0.67	Gal
13	G30.7+9.4	18:14:01	+02:18:58	9×9	0.29±0.04	+1.00	+0.38	Gal
14	G34.9+17.6*	17:51:38	+09:37:03	8×7	0.06±0.02	+0.89	+0.13	Quasar
15	G39.1+8.7	18:31:16	+09:26:09	17×8	0.11±0.03	+0.83	+0.20	Gal
16	G41.1-11.2	19:46:06	+02:03:49	12×8	0.13±0.03	+1.00	+0.60	Gal
17	G61.4+12.1	18:58:20	+30:43:26	19×11	0.10±0.02	+0.91	+0.48	Gal
18	G68.4+1.9	19:55:46	+32:05:09	12×8	0.11±0.03	+1.00	+0.57	HMXB
19	G72.9+2.0	20:06:22	+35:58:17	10×10	0.29±0.02	-0.31	-0.14	Star
20	G76.5+8.0	19:50:08	+42:05:03	15×15	0.90±0.04	+1.00	+0.25	Gal
21	G78.7+9.9	19:46:21	+44:56:33	5×5	0.09±0.02	+0.10	+0.11	Star
22	G85.4+9.3	20:09:36	+50:22:53	8×7	0.04±0.01	+1.00	+0.23	Gal
23	G92.5-3.7	21:37:56	+47:26:12	8×8	0.11±0.02	+1.00	+0.75	Gal
24	G94.6+8.9	20:47:05	+57:33:40	8×7	0.09±0.02	+1.00	+0.61	Gal
25	G104.1+14.1*	21:02:17	+68:06:33	11×8	0.07±0.02	+1.00	+0.25	Star
26	G104.2-5.11	22:42:56	+53:01:24	10×8	0.15±0.03	+0.84	+0.55	Gal
27	G104.7-4.9	22:44:59	+53:27:38	10×7	0.12±0.03	+0.79	+0.31	Gal
28	G105.1-5.4	22:48:49	+53:09:39	10×7	0.18±0.04	+1.00	+0.40	Gal
29	G116.9-6.9	00:08:41	+55:30:25	7×6	0.08±0.01	+0.11	+0.39	Star
30	G120.4+0.9	00:28:39	+63:40:49	6×6	0.31±0.04	+0.11	+0.18	Star
31	G129.9+8.9	02:16:43	+70:38:34	8×8	0.16±0.02	+0.69	+0.69	Gal
32	G131.8-9.4	01:49:28	+52:31:04	25×8	0.17±0.04	+0.40	-0.16	Gal
33	G134.3-6.5	02:10:33	+54:36:18	15×13	0.12±0.03	+0.69	+0.37	Gal
34	G135.2+6.4	02:57:36	+66:12:45	11×8	0.13±0.03	+0.68	+0.84	Gal
35	G142.7-4.2	03:08:48	+53:19:20	8×7	0.07±0.02	+1.00	+0.88	Gal
36	G146.4-10.0	03:09:59	+46:26:28	7×4	0.07±0.02	+0.85	+0.33	Gal
37	G146.6-13.0	03:02:32	+43:43:22	15×15	2.26±0.07	+0.90	+0.44	Gal
38	G154.5-9.6	03:48:06	+42:14:34	10×9	0.10±0.03	+1.00	+0.40	Gal
39	G172.7-8.1*	06:01:53	+39:20:49	10×5	0.19±0.03	+0.69	-0.03	Star
40	G178.1-3.0	05:29:30	+28:59:08	7×7	0.08±0.02	+1.00	+0.65	Star
41	G181.6-2.5	05:39:46	+26:14:33	7×7	0.23±0.03	+0.90	+0.67	Star

42	G200.0+4.7	06:44:37	+13:41:01	7×5	0.05±0.02	+1.00	+0.61	Gal
43	G224.4+5.2	07:31:12	-07:44:18	35×30	0.62±0.07	+0.51	+0.14	ClG
44	G226.0+0.5	07:17:24	-11:19:50	10×10	0.17±0.03	+0.88	+0.65	Gal
45	G235.0-9.9	06:54:10	-23:55:55	8×7	0.09±0.02	+1.00	+0.38	Star
46	G237.0+3.8	07:51:32	-19:19:39	10×8	0.08±0.03	+0.84	+0.39	Gal
47	G238.3+9.8	08:15:55	-17:21:28	7×4	0.23±0.06	+0.42	+0.36	Gal
48	G240.0+3.8	07:58:06	-21:57:15	8×6	0.21±0.05	+1.00	+0.48	Gal
49	G241.7+4.9	08:05:57	-22:51:01	10×8	0.16±0.04	+0.82	+0.32	Gal
50	G253.3+11.8	09:00:44	-28:07:00	12×7	0.06±0.02	+1.00	+0.21	Quasar
51	G265.2+10.5	09:33:57	-37:28:05	13×8	0.10±0.03	+0.87	+0.47	Gal
52	G272.1-11.5	10:04:03	-41:09:36	8×8	0.22±0.03	+0.96	+0.51	Gal
53	G287.59-0.79	10:44:25	-59:49:22	100×70	14.89±0.35	+0.93	-0.08	H II/OpC
54	G292.5-10.6	10:41:14	-70:45:24	9×9	0.16±0.02	+0.89	+0.39	ClG
55	G318.1+17.9	14:10:36	-42:39:30	8×7	0.48±0.11	+1.00	+0.37	Gal
56	G323.6-8.7	16:14:04	-63:07:59	10×10	0.21±0.05	+0.90	+0.05	ClG
57	G329.3-9.9	16:53:02	-59:46:09	10×8	0.78±0.14	+0.89	+0.54	Gal
58	G329.7+7.2	15:35:17	-46:59:32	8×7	0.14±0.03	+0.64	-0.15	Gal

Table A.5: Targets which are identified as extragalactic objects or X-ray bright stars. Targets which are flagged with a * were identified by a pointed ROSAT HRI or PSPC observation, respectively. The last column denotes the nature of the targets where PN: Planetary Nebula, Gal: Galaxy, ClG: Cluster of Galaxies, OpC: Open (galactic) cluster and HMXB: High Mass X-ray Binary.

Nr.	Source	R.A. hh:mm:ss	DEC dd:mm:ss	extent arcmin	count rate cts/s	HR1	HR2
1	G22.39+9.50	17:58:15	-04:53:46	40×40	0.51±0.11	+0.23	+0.01
2	G24.07-0.28	18:36:11	-08:00:36	35×20	0.32±0.07	+1.00	+0.60
3	G77.88-4.63	20:47:54	+36:08:54	50×50	0.46±0.10	+1.00	+0.24
4	G79.43-4.89	20:53:47	+37:10:49	50×50	0.44±0.09	+0.23	-0.45
5	G80.76+2.84	20:25:58	+42:57:04	50×45	0.62±0.08	+0.74	+0.18
6	G81.16-1.13	20:44:21	+40:53:29	40×40	0.56±0.06	+1.00	+0.21
7	G98.57-5.67	22:14:11	+49:36:58	35×35	0.16±0.06	+1.00	+0.04
8	G104.74+9.91	21:38:03	+65:41:38	45×35	0.24±0.05	+1.00	-0.42
9	G197.45+0.07	06:22:54	+13:46:36	40×40	0.54±0.09	-1.00	0.00
10	G253.83-3.00	08:05:09	-37:16:57	50×35	0.40±0.08	-0.26	-0.46
11	G320.47-1.67	15:17:00	-59:29:29	35×35	0.45±0.08	+0.82	+0.17
12	G333.48-2.28	16:31:01	-51:37:43	45×45	1.08±0.14	-0.01	-0.49
13	G334.44-3.19	16:39:30	-51:32:03	40×40	0.31±0.11	+1.00	+0.11
14	G335.31+10.60	15:48:02	-40:54:51	55×50	0.63±0.14	+0.57	-0.34
15	G335.56-1.59	16:36:43	-49:37:58	60×60	0.69±0.15	+0.69	+0.10
16	G351.17+6.64	16:56:53	-32:25:00	40×30	0.61±0.11	+0.78	-0.10

Table A.6: SNR candidates with an extent of $30' \leq D \leq 60'$

Nr.	Source	R.A. hh:mm:ss	DEC dd:mm:ss	extent arcmin	count rate cts/s	HR1	HR2
1	G7.48-1.51	18:08:10	-23:13:36	70×50	6.54±0.24	+0.87	+0.03
2	G24.01+6.12	18:13:15	-05:05:08	120×120	3.22±0.21	+1.00	-0.07
3	G25.12-1.80	18:43:34	-07:46:22	80×60	1.99±0.15	+0.91	-0.25
4	G43.72+2.60	19:01:55	+10:46:58	120×90	1.40±0.17	+0.90	+0.17
5	G75.43-0.22	20:23:02	+36:49:58	80×50	1.52±0.14	+0.72	+0.39
6	G77.56+3.43	20:13:41	+40:38:42	90×90	6.77±0.13	+0.44	+0.15
7	G105.37-8.32	22:59:00	+50:40:39	160×160	1.31±0.31	-0.09	-0.15
8	G207.73+1.55	06:47:28	+05:20:13	90×90	4.19±0.25	-0.83	-1.00
9	G287.59-0.79	10:44:25	-59:49:22	100×70	14.89±0.35	+0.93	-0.08

Table A.7: SNR candidates with an extent of $60' \leq D \leq 120'$

Nr.	Source	R.A. hh:mm:ss	DEC dd:mm:ss	extent arcmin	count rate cts/s	HR1	HR2
1	G1.85-2.52	17:59:49	-28:37:32	330×180	65.82± 1.17	+1.00	+0.13
2	G10.71+6.28	17:46:18	-16:32:28	260×260	23.13±0.60	+1.00	+1.00
3	G11.61+3.96	17:56:34	-16:56:21	240×240	11.6±0.58	+1.00	-0.12
4	G12.71+8.28	17:43:23	-13:48:50	240×240	23.80±0.60	+1.00	-0.23
5	G16.35-8.78	18:53:11	-18:42:03	180×160	9.60±0.45	+1.00	-0.35
6	G17.03-3.48	18:34:35	-15:43:45	250×250	6.51±0.62	+0.76	+0.10
7	G26.73-3.61	18:53:01	-07:09:45	180×180	6.58±0.43	+0.88	+0.01
8	G27.48-0.25	18:42:22	-04:57:57	180×180	3.88±0.31	+1.00	+0.14
9	G69.45+1.19	20:01:18	+32:36:45	160×60	12.88±0.32	+0.93	-0.05
10	G76.60-4.01	20:41:36	+35:31:45	180×180	1.75±0.29	+1.00	-0.24
11	G107.46+9.67	22:00:07	+67:14:27	240×240	5.05±0.11	+0.14	-0.44
12	G253.54-1.36	08:11:16	-36:09:06	240×240	7.48±0.45	-0.94	-0.87
13	G309.61-3.03	13:55:24	-65:04:10	220×180	21.18±0.89	+0.92	+0.01
14	G312.09+4.20	14:00:04	-57:26:48	240×140	12.72±0.45	+0.83	-0.18
15	G331.13-4.84	16:32:52	-55:05:22	260×140	24.00±0.62	+0.02	-0.32
16	G333.54+8.14	15:49:05	-43:55:29	180×180	7.29±0.31	+0.84	-0.34
17	G337.51+12.70	15:49:44	-37:55:25	180×180	4.59±0.42	+0.11	-0.36
18	G343.75+3.99	16:43:46	-39:48:19	270×240	15.30±0.59	+0.69	-0.59

Table A.8: SNR candidates with an extent of $120' \leq D$

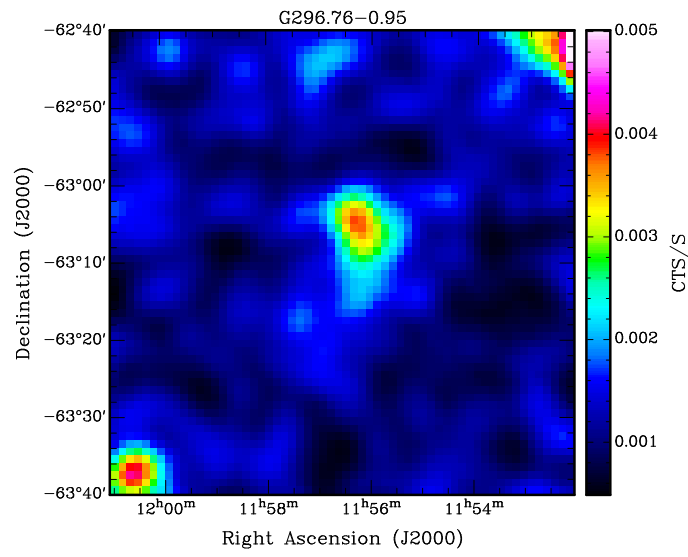
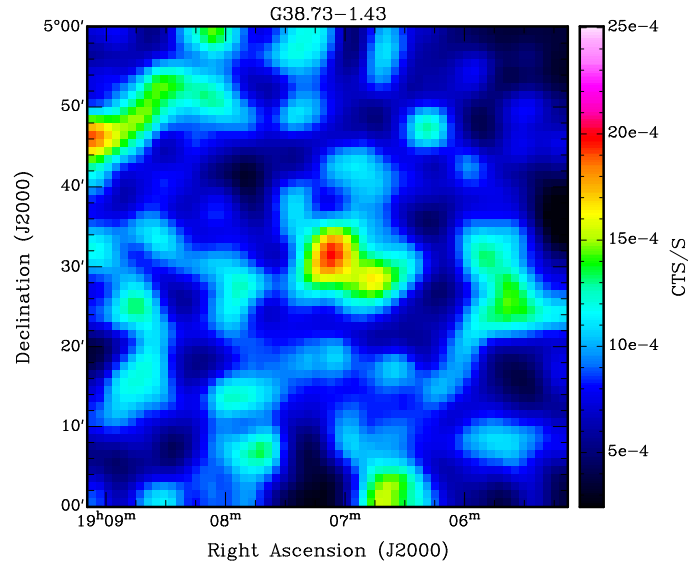
Appendix B

RASS images of the SNR candidates

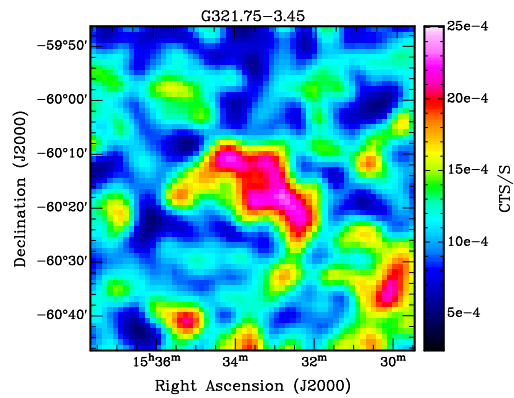
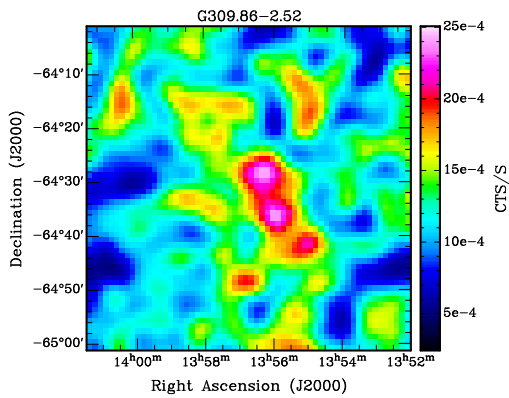
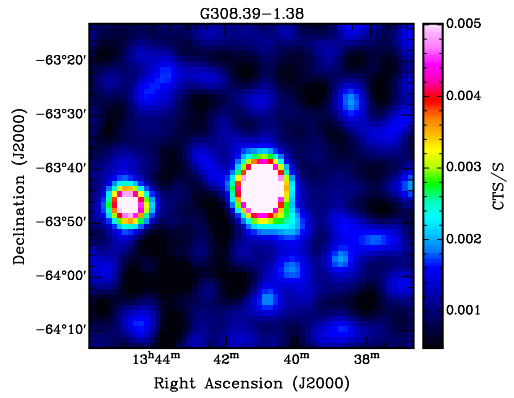
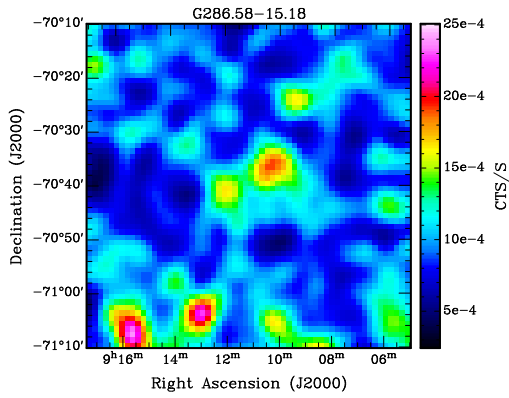
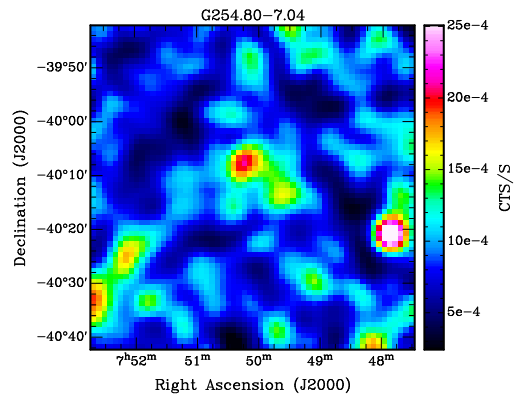
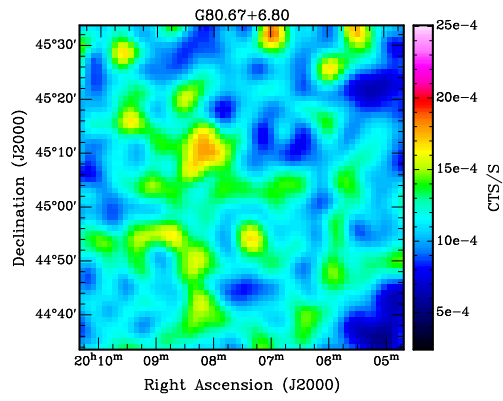
The RASS images of all SNR candidates are shown here according the Tab. A.1 - A.8. They are listed with increasing galactic coordinates and extent. The images have been exposure corrected and hence show a count rate map of the SNR candidates. All images have been binned with $1'$ and smoothed with a gaussian filter of $5'$ in order to reduces the variance of the noise but to keep a moderate resolution. Two different count rate ranges (0.0005 - 0.005 cts/s) and (0.00025 - 0.0025 cts/s) have been used due to different source strengths.

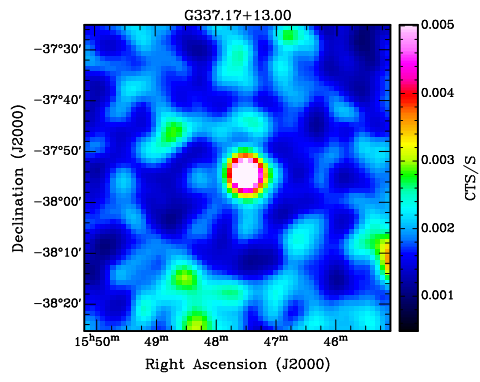
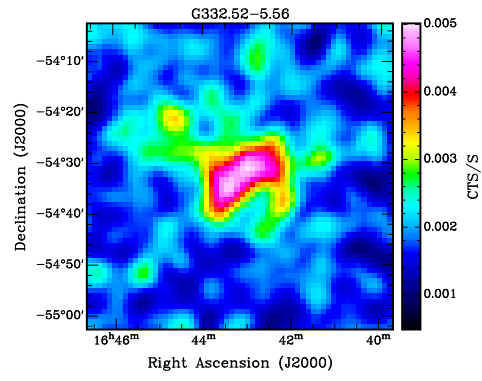
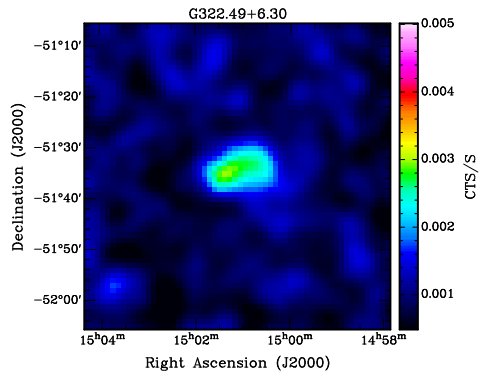
The images of the SNR candidates with an extent below $30'$ have a size of $1^\circ \times 1^\circ$, the images of the candidates with $30' \leq D \leq 60'$ have a size of $1.5^\circ \times 1.5^\circ$, the images of the candidates with $60' \leq D \leq 120'$ have a size of $3^\circ \times 3^\circ$ and the images of the candidates with $120' \leq D$ have a size of $6^\circ \times 6^\circ$, respectively.

Identified SNRs (cf. A 1)

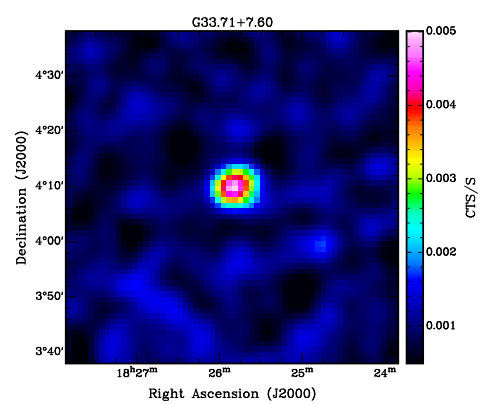
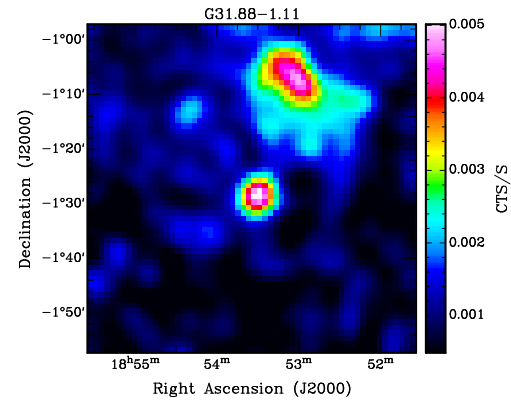
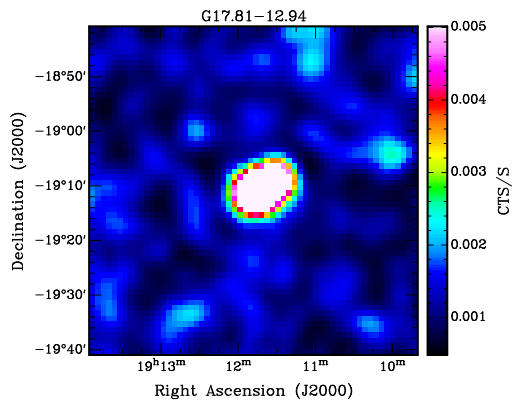
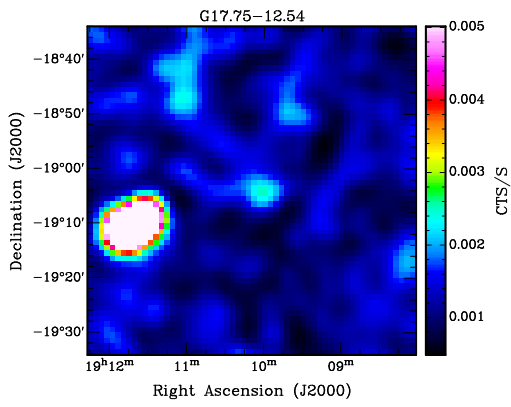
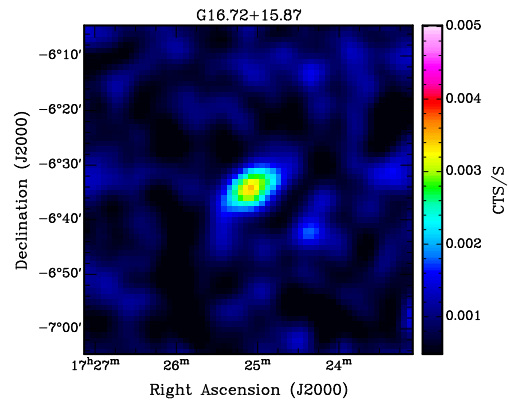
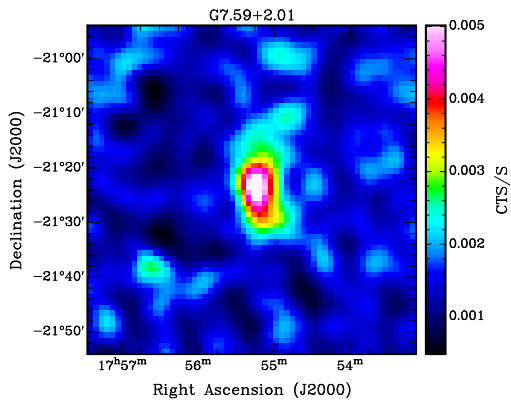


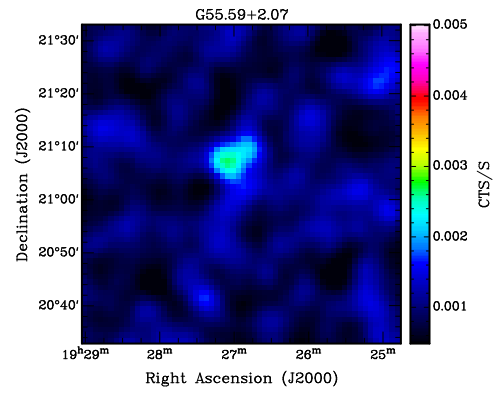
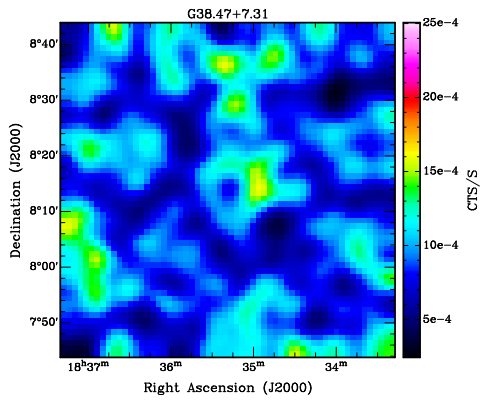
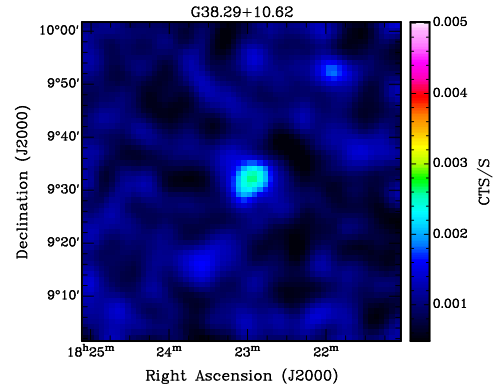
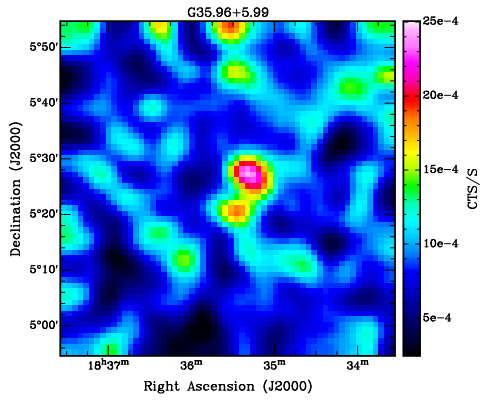
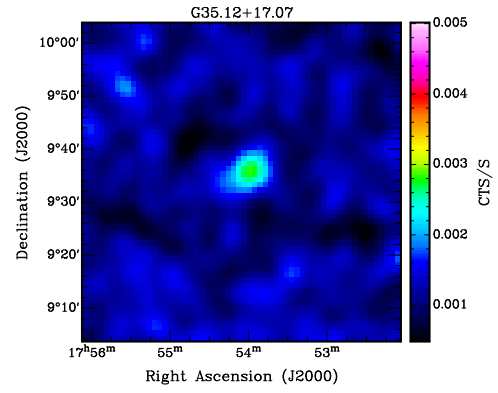
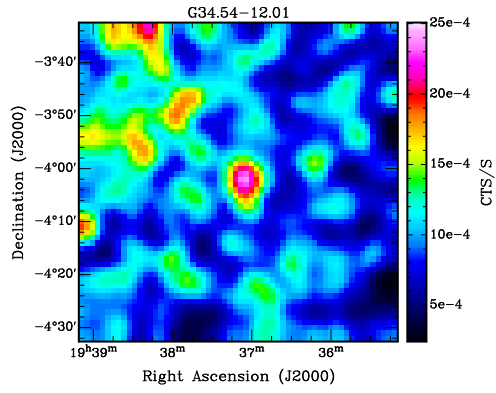
Most promising SNR candidates (cf. A 2)

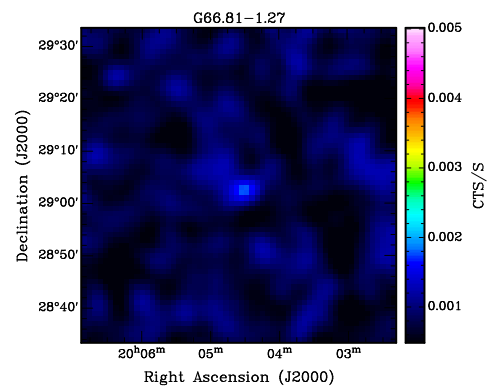
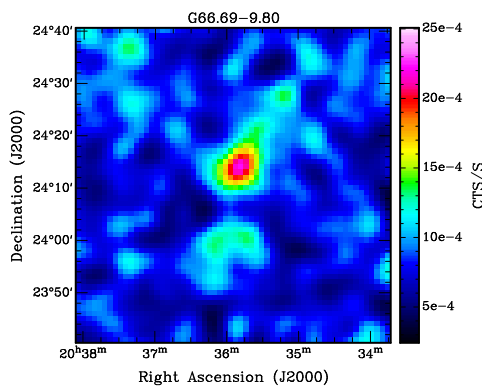
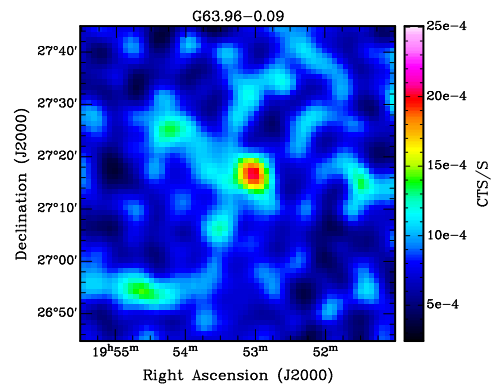
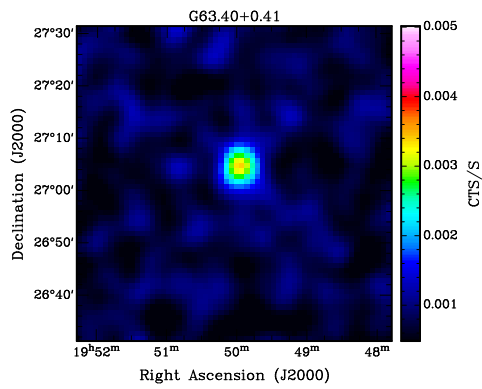
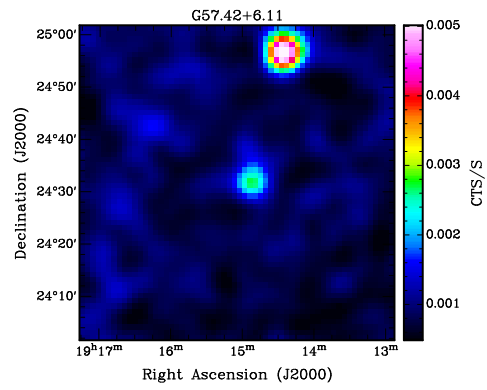
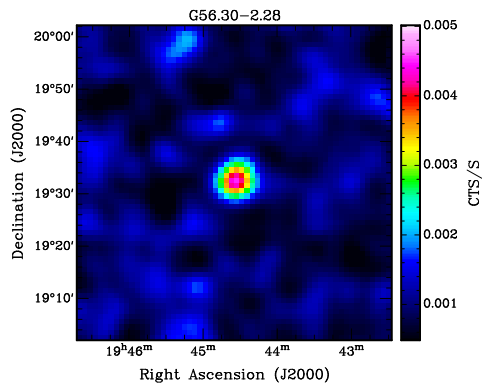


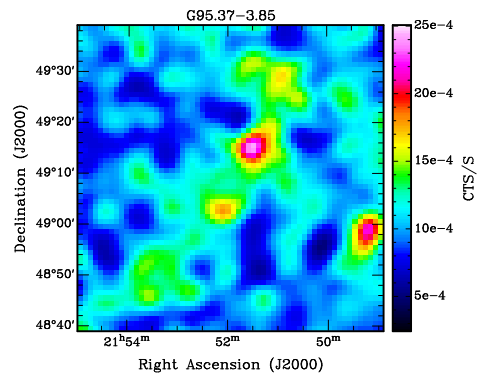
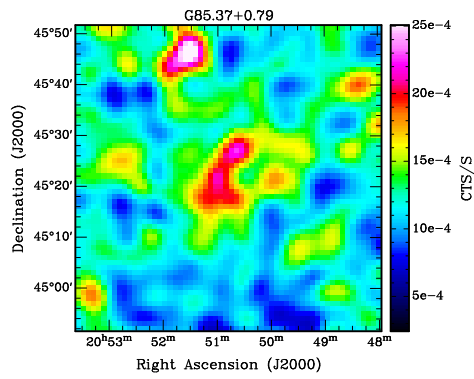
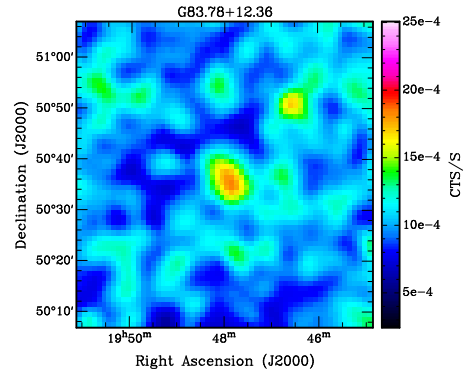
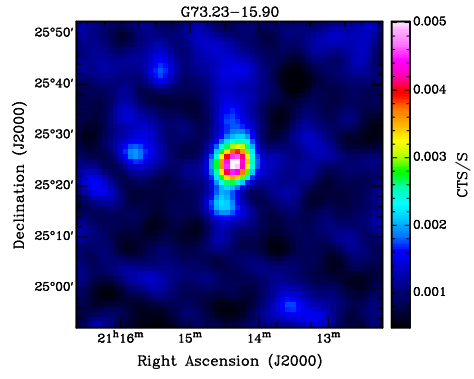
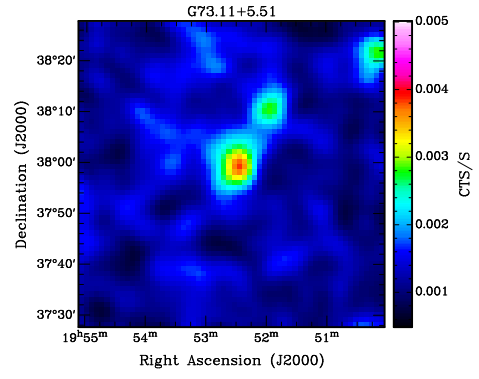
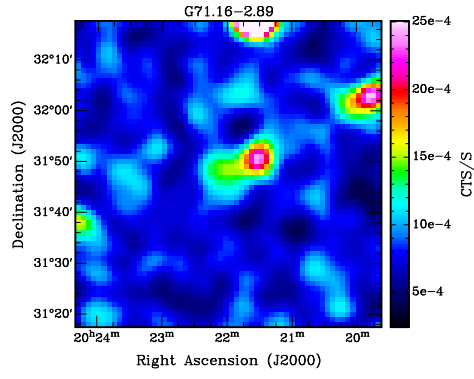


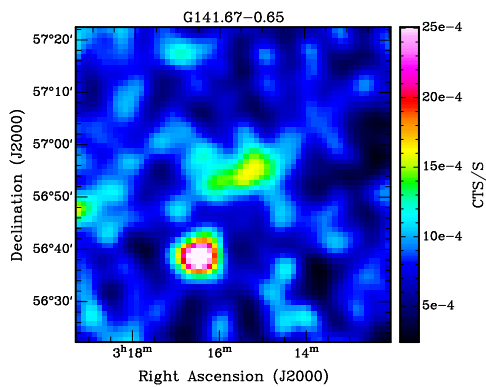
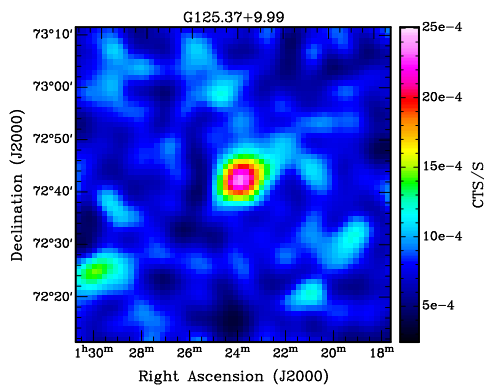
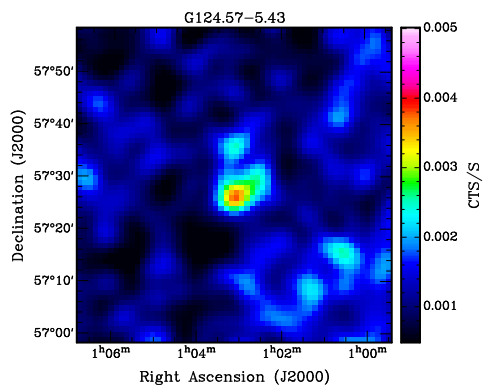
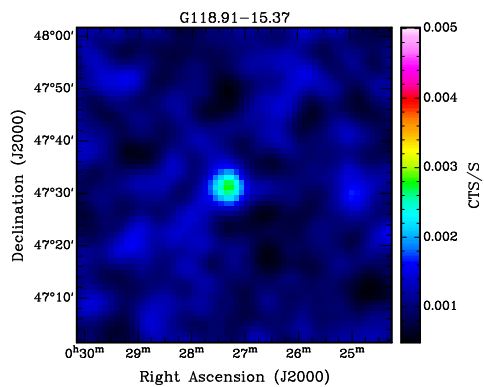
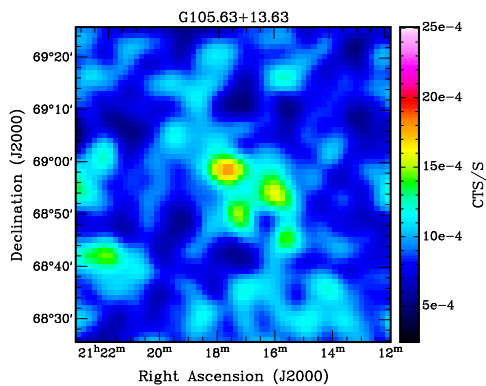
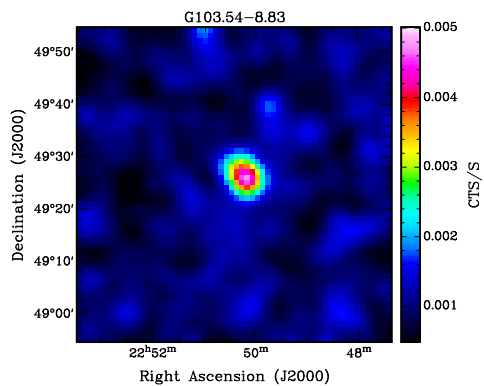
Good SNR candidates (cf. A 3)

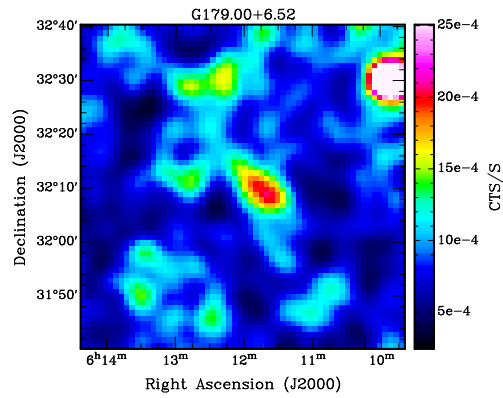
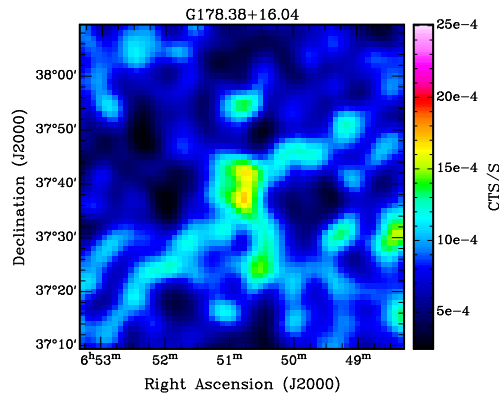
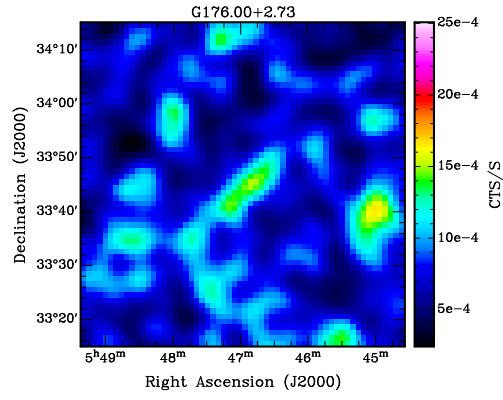
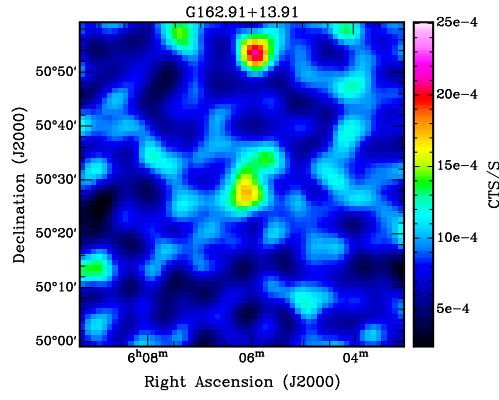
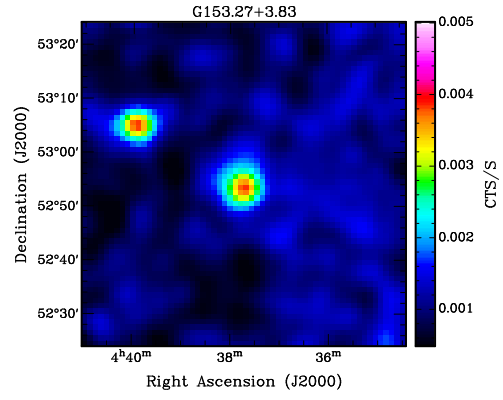
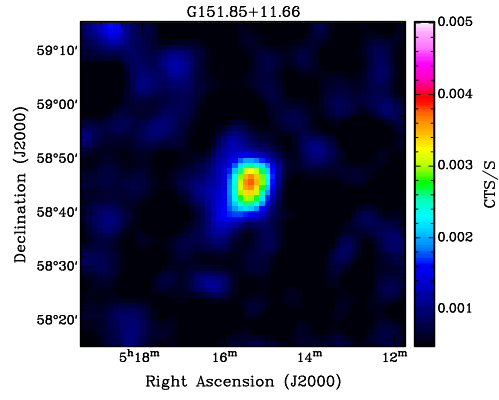


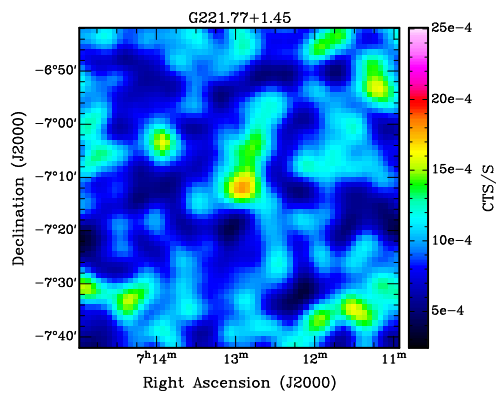
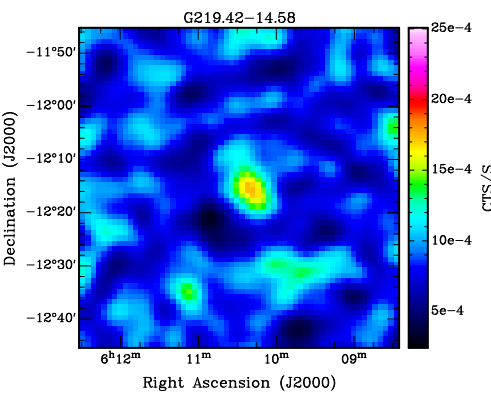
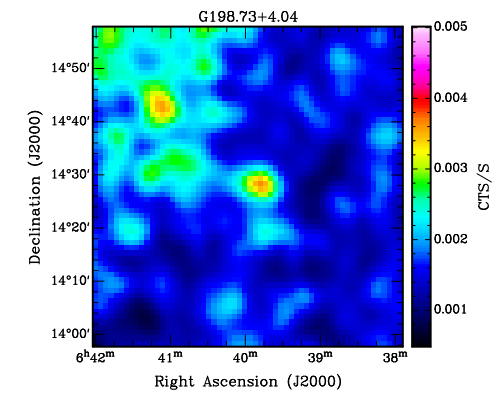
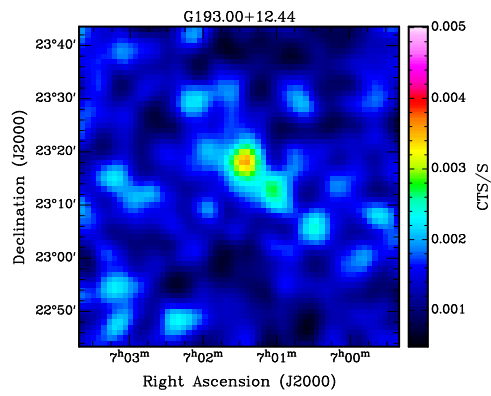
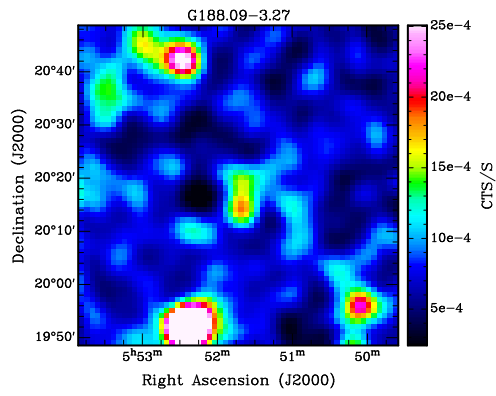
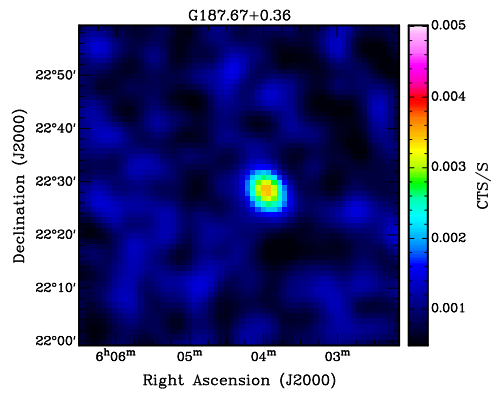


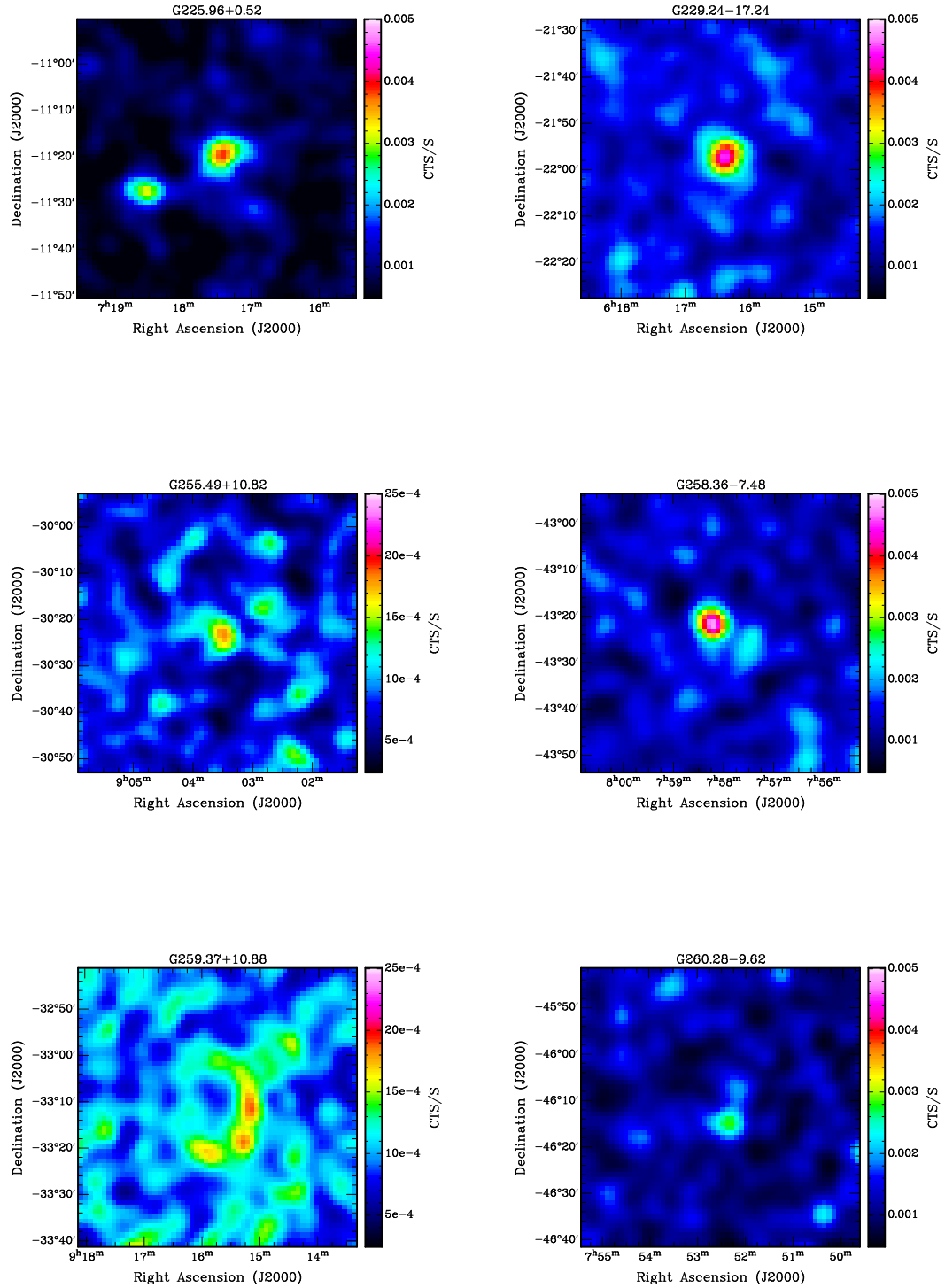


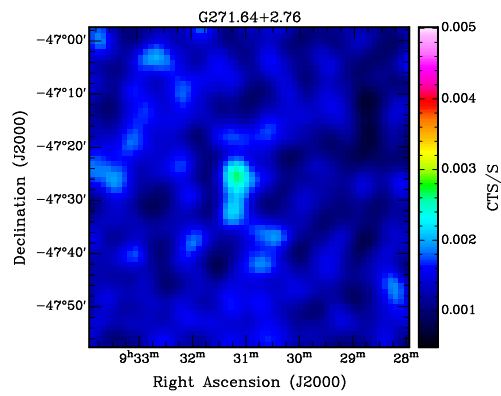
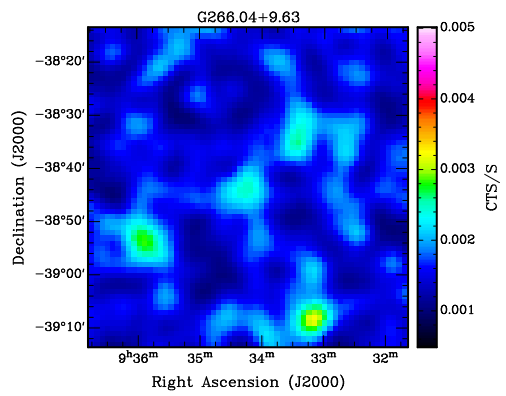
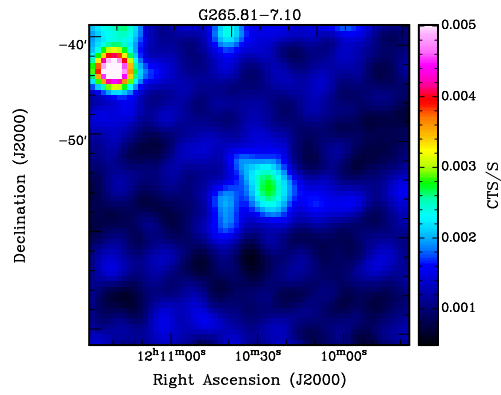
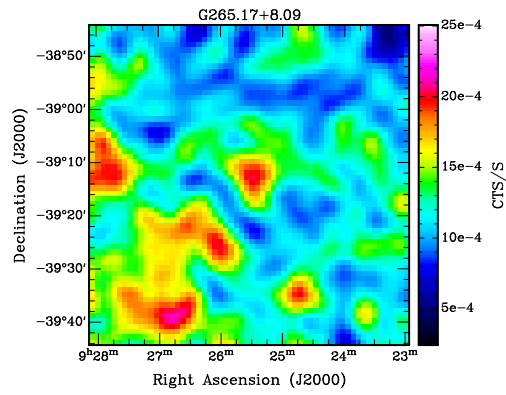
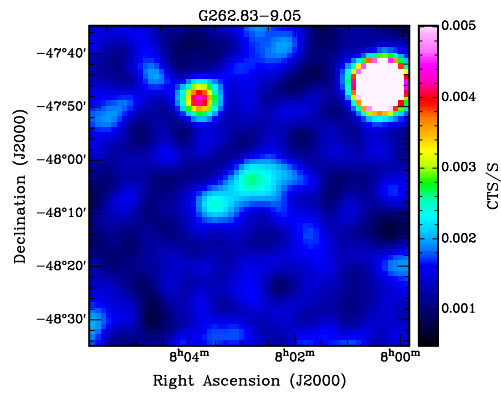
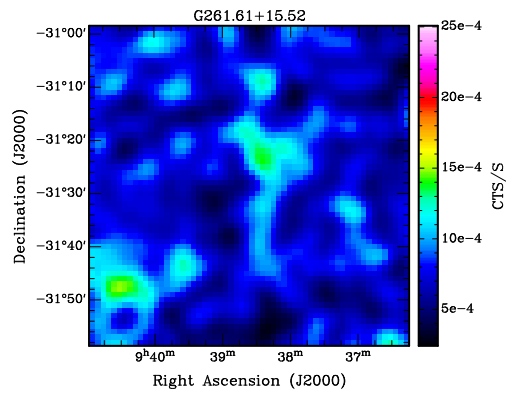


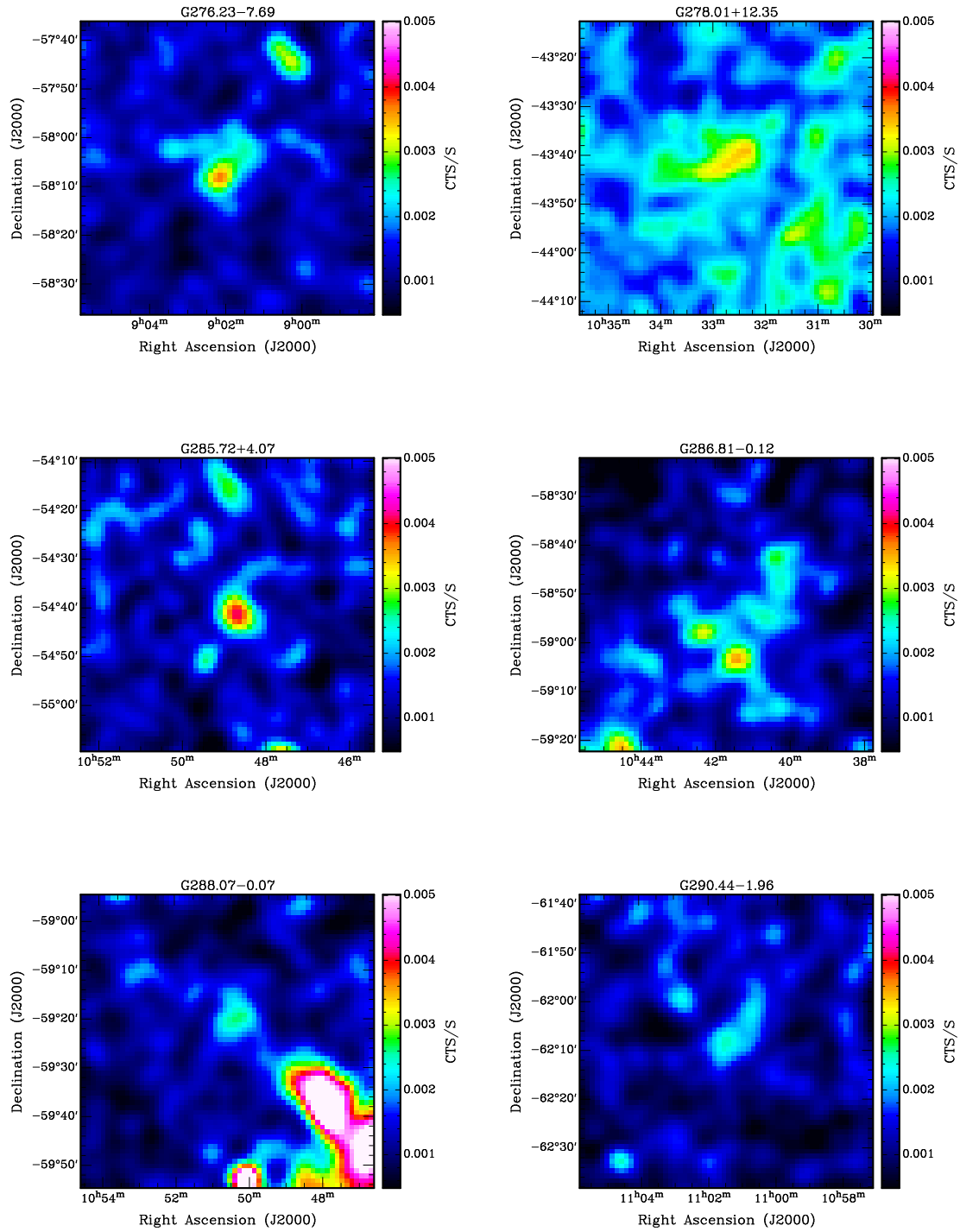


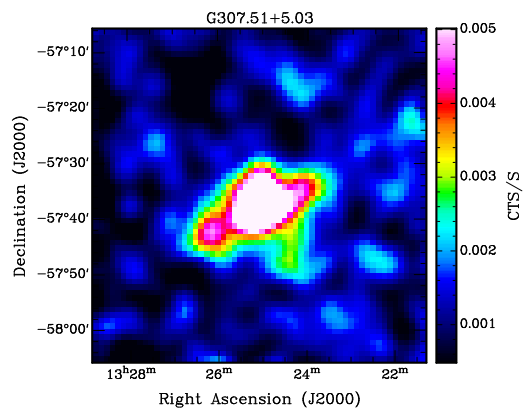
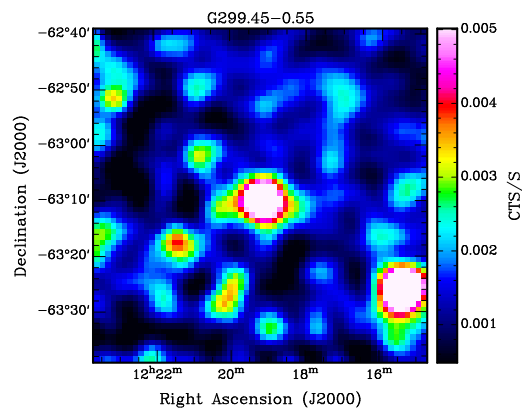
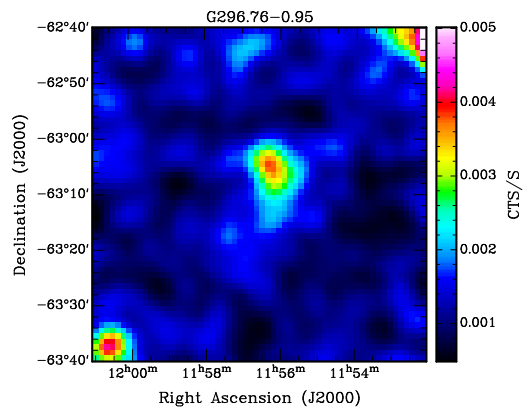
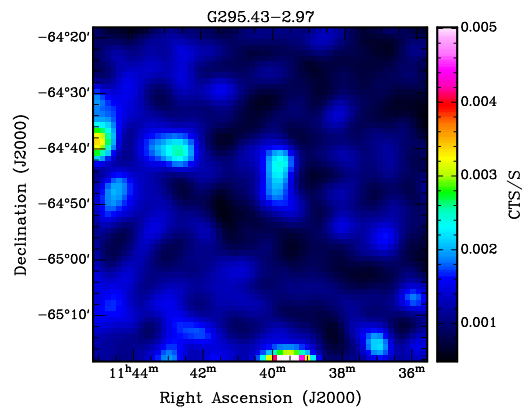
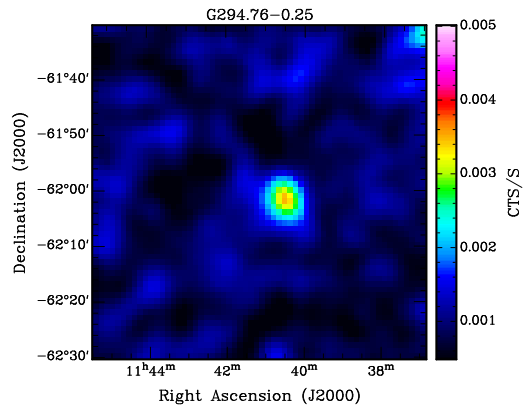
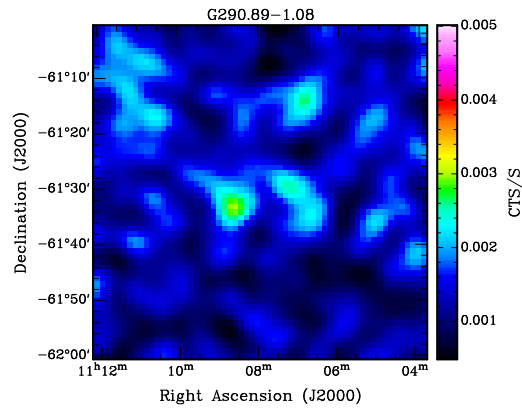


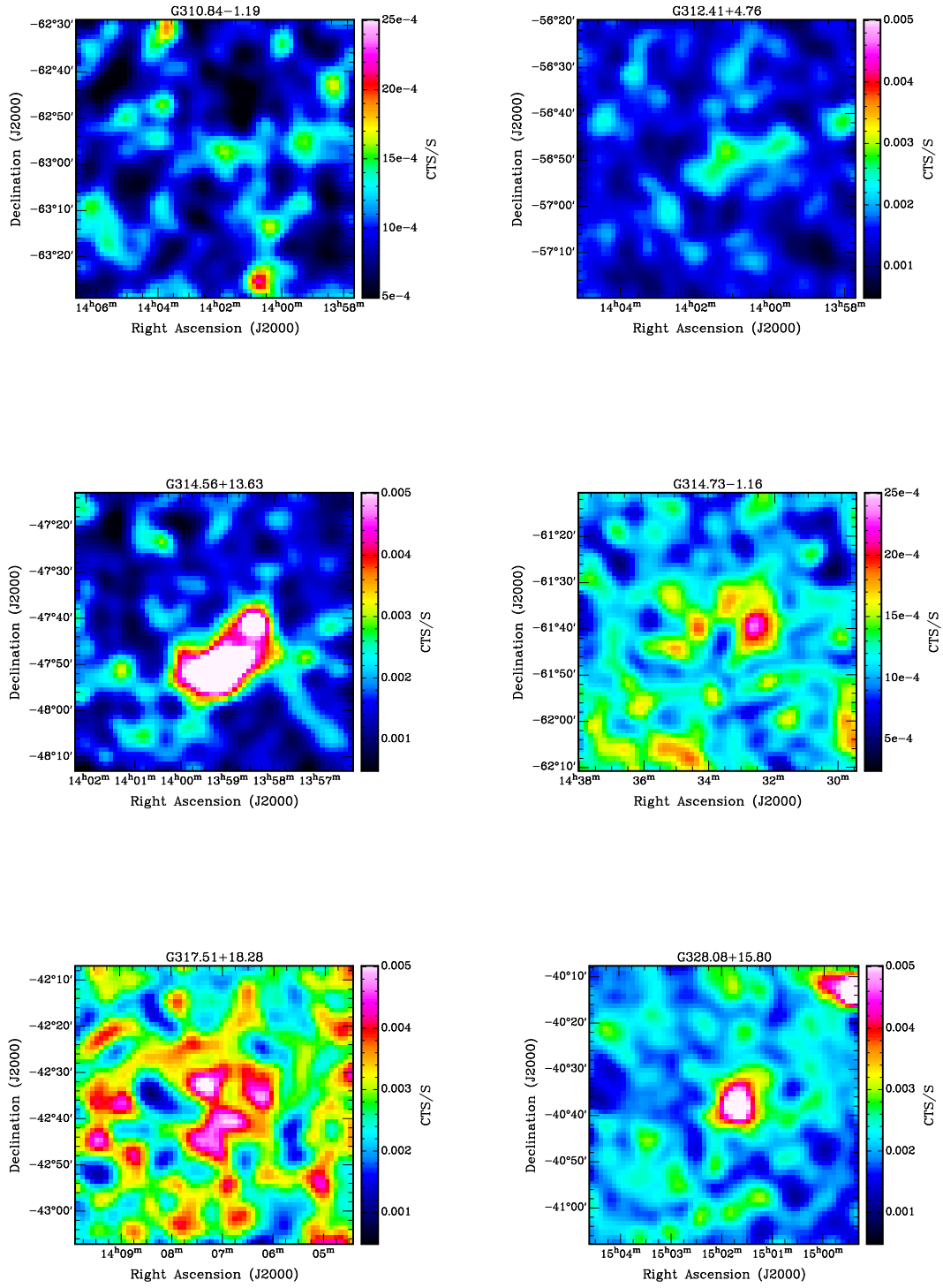


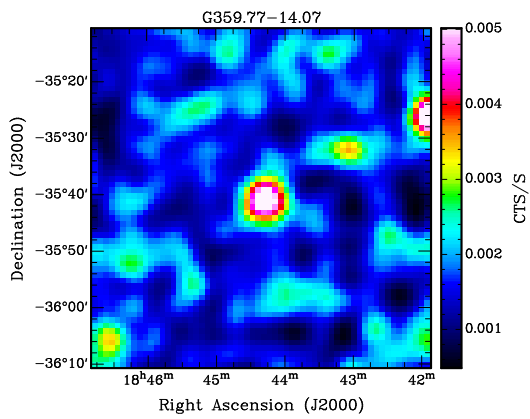
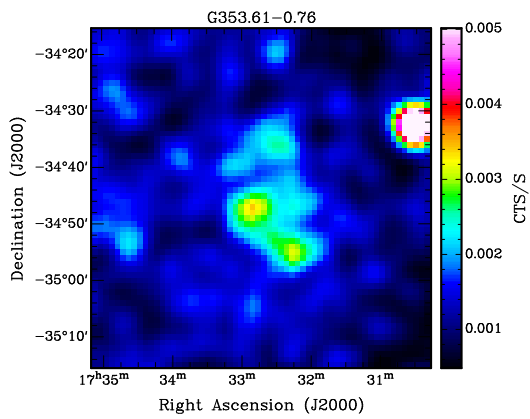
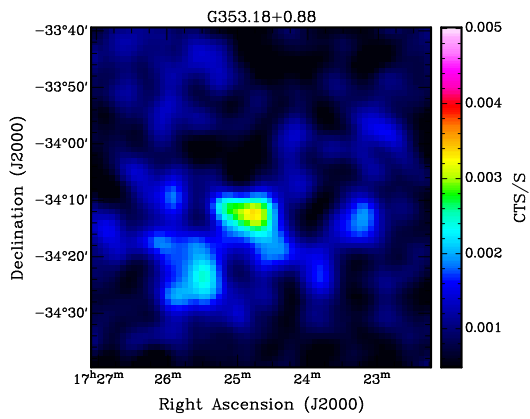
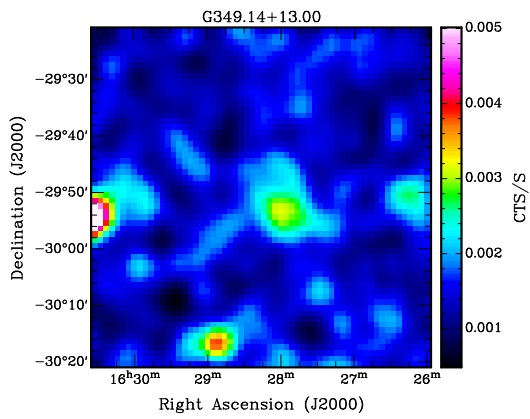
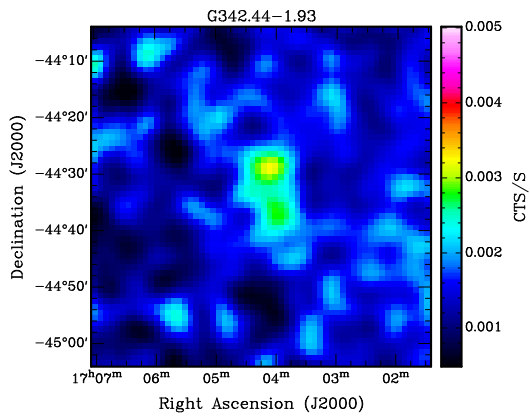
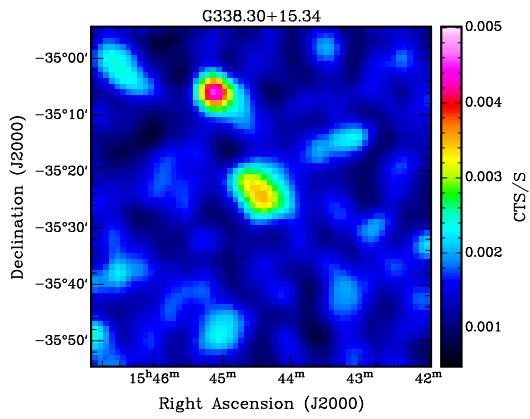




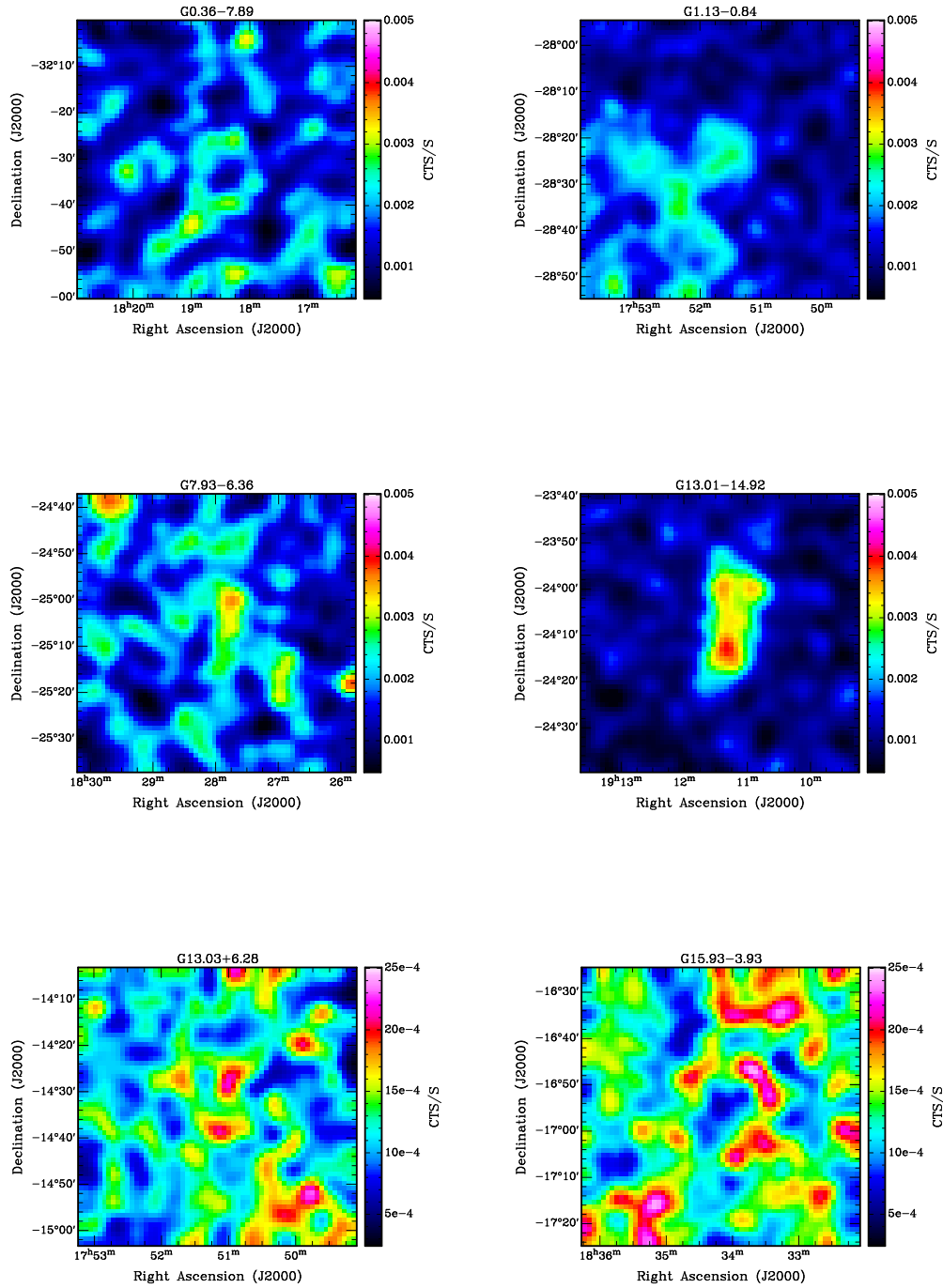


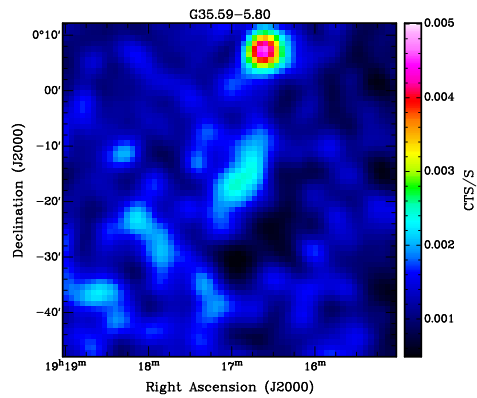
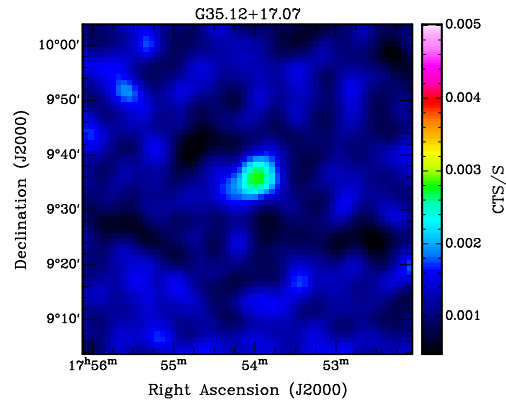
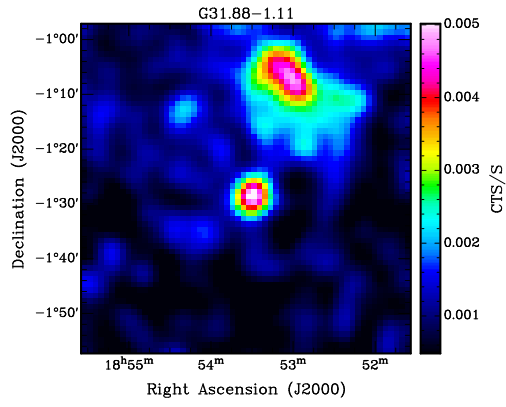
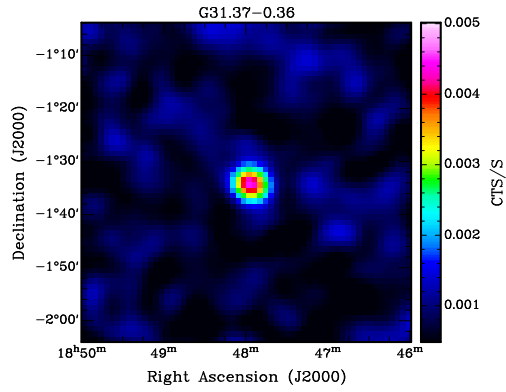
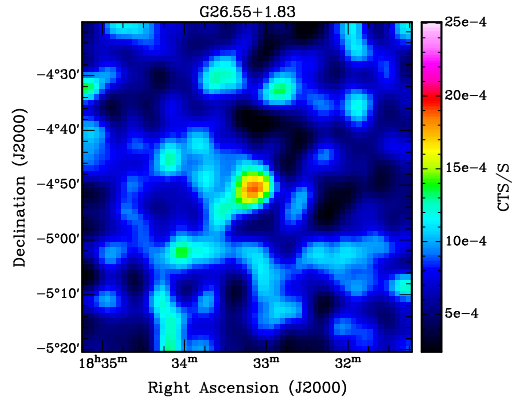
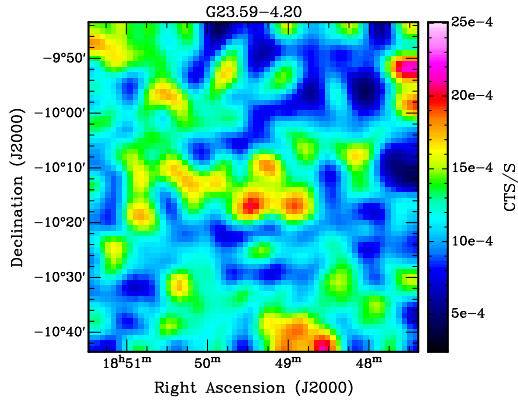


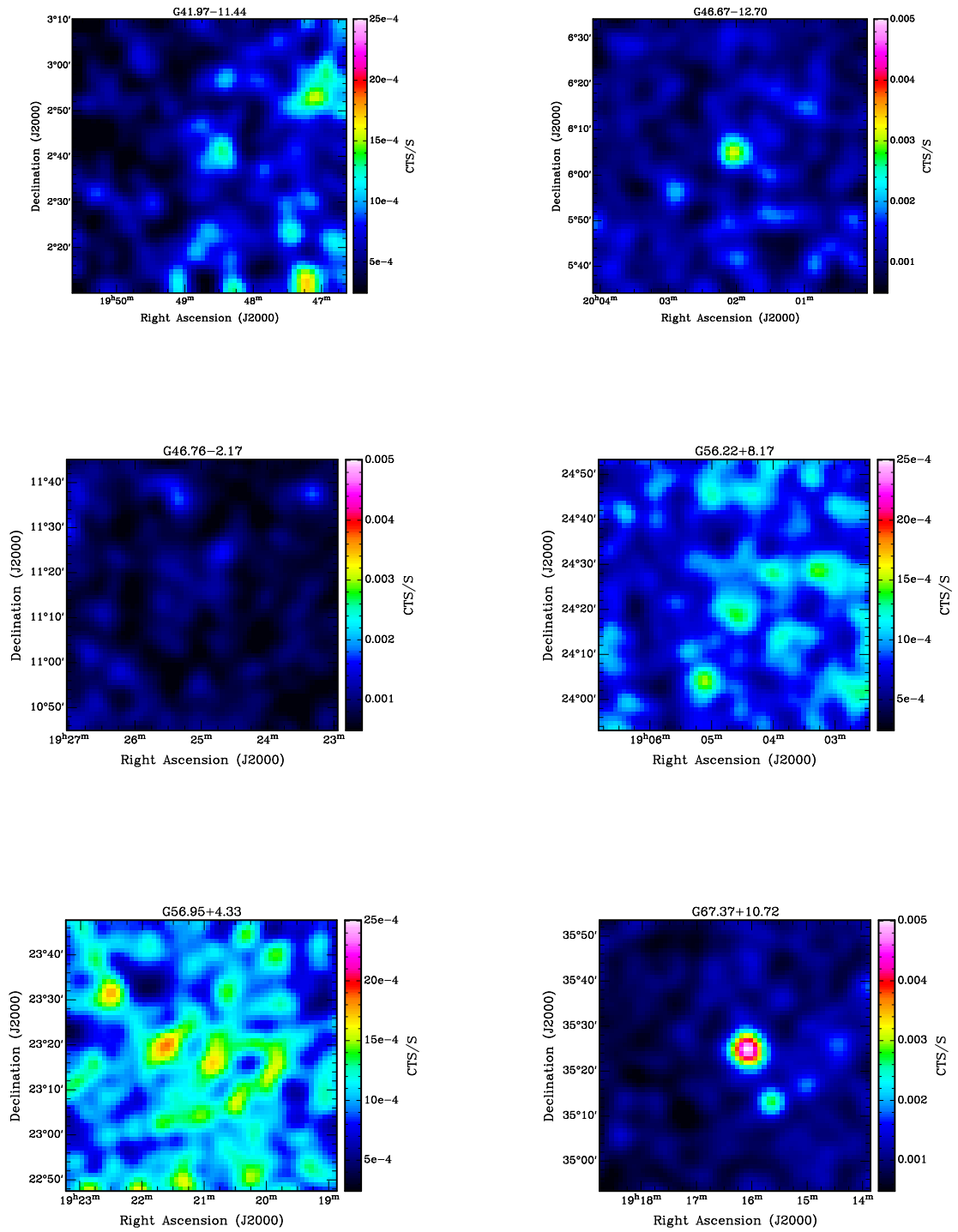


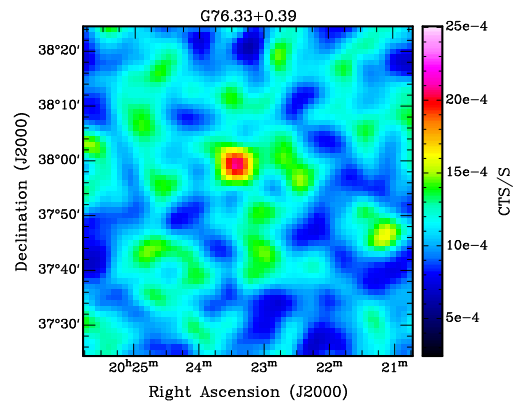
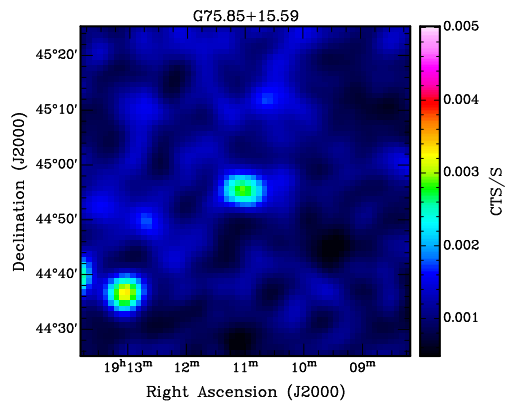
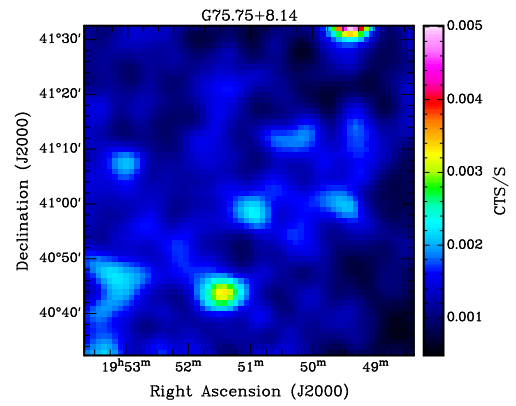
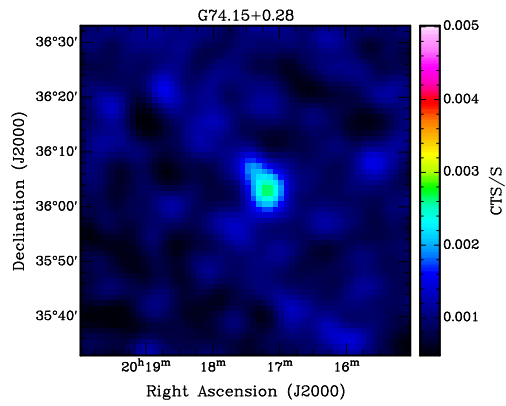
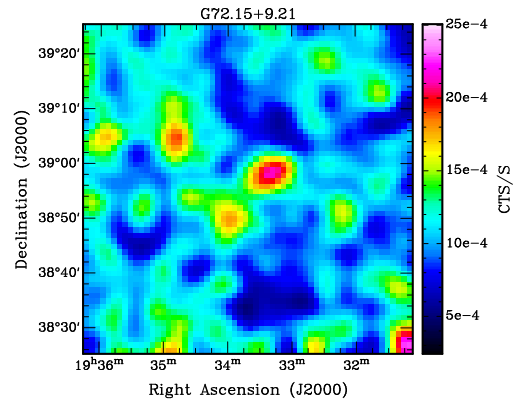
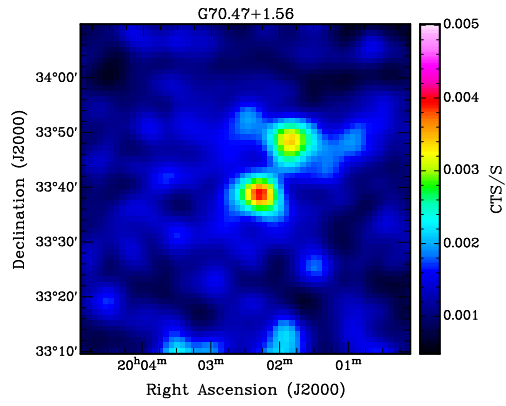


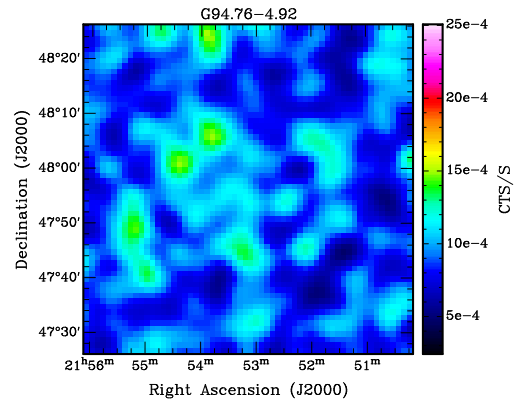
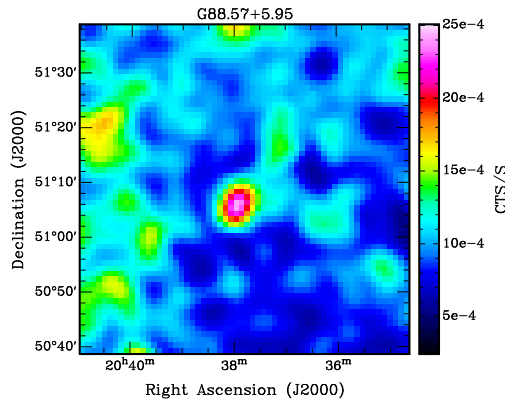
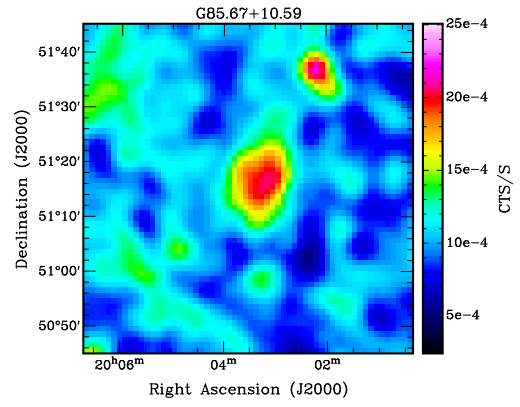
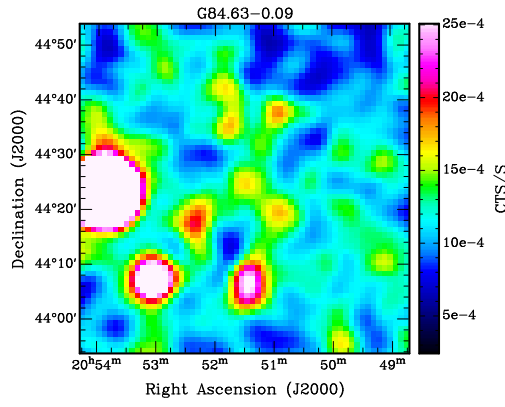
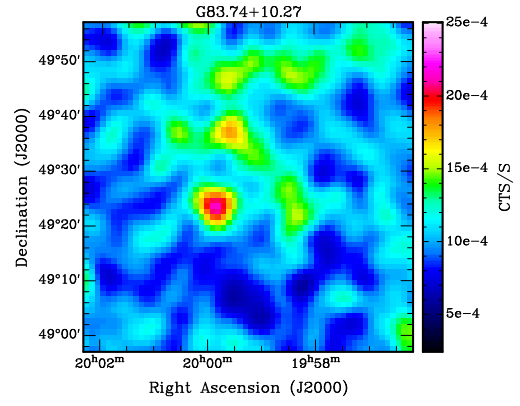
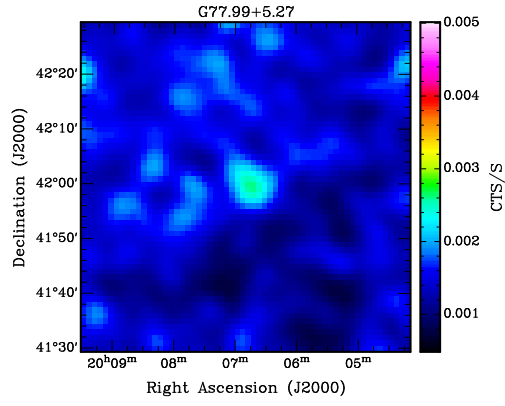
Weak candidates (cf. A 4)

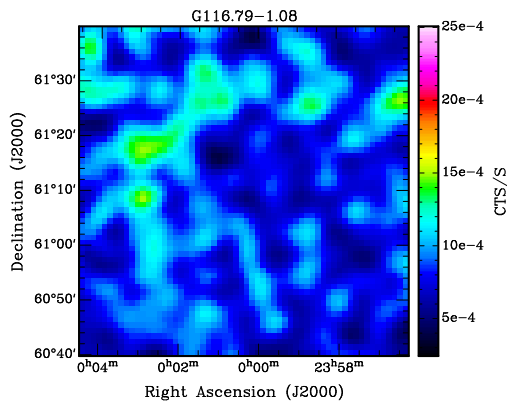
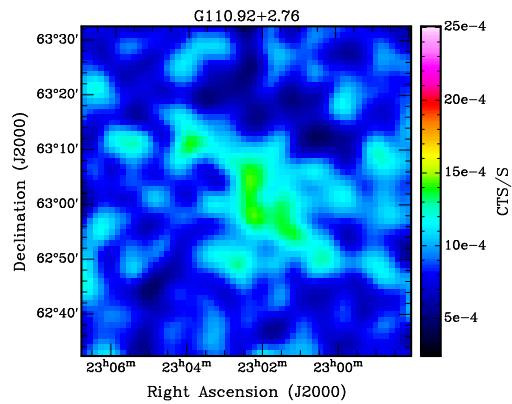
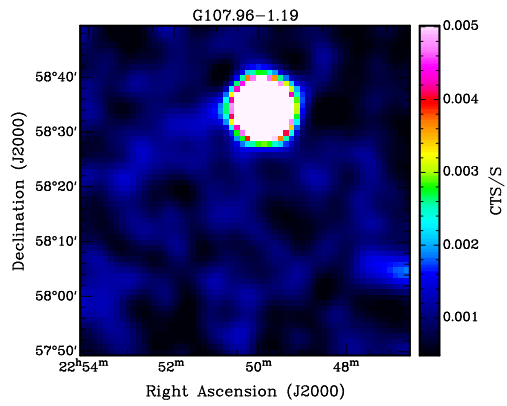
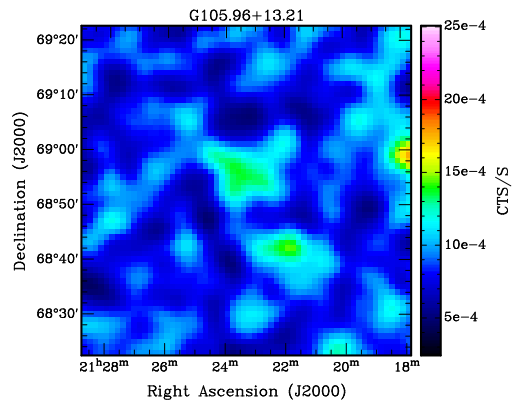
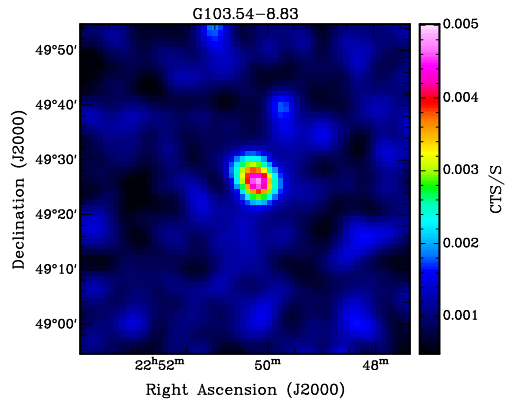
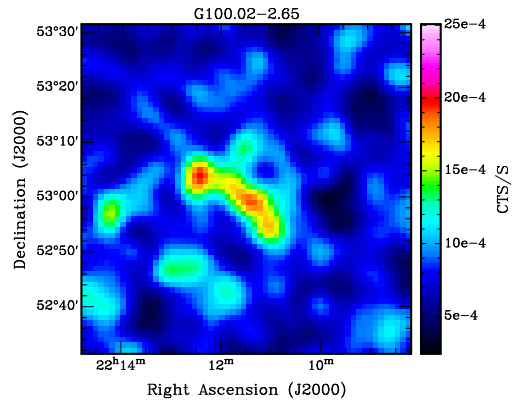


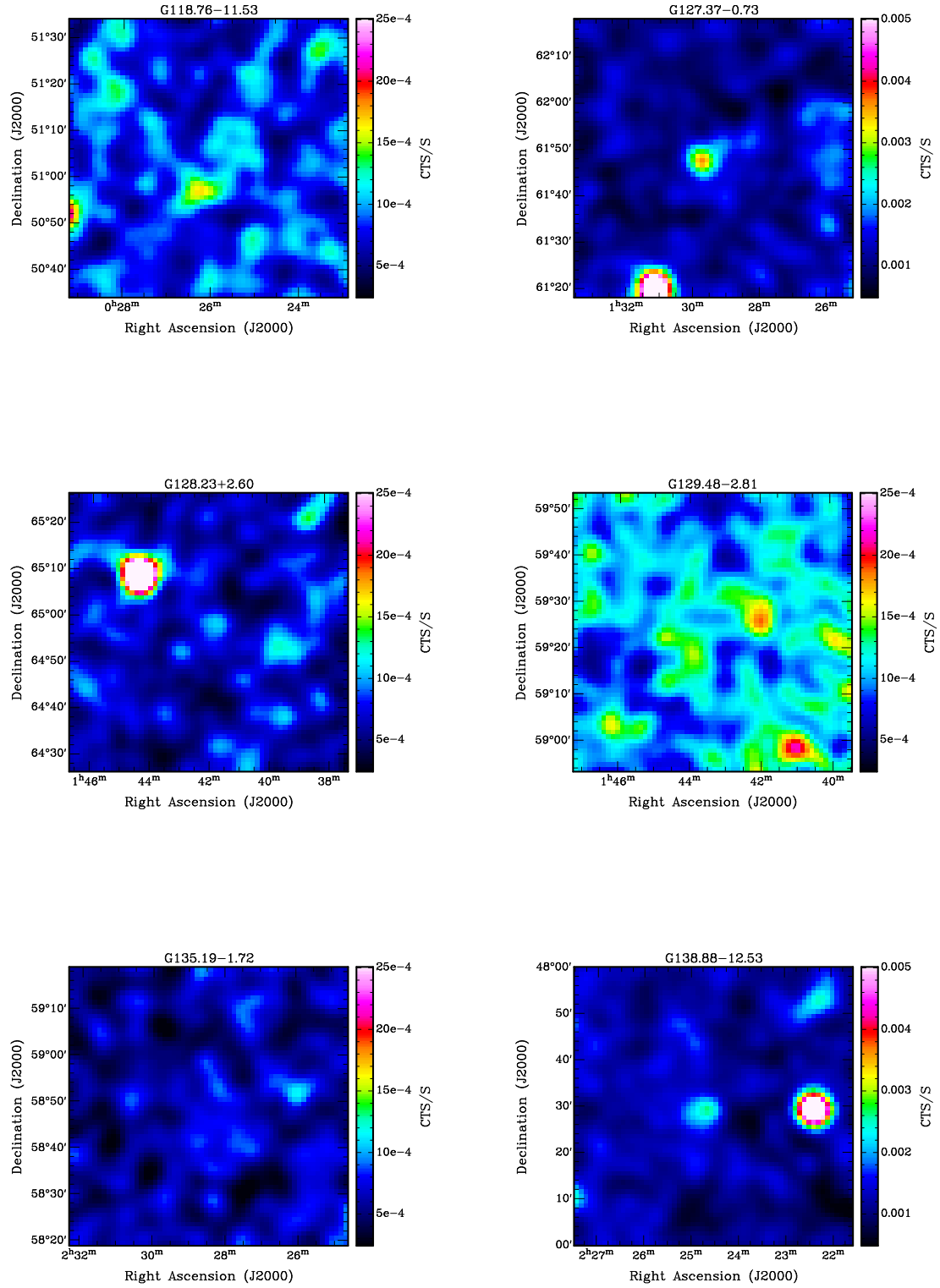


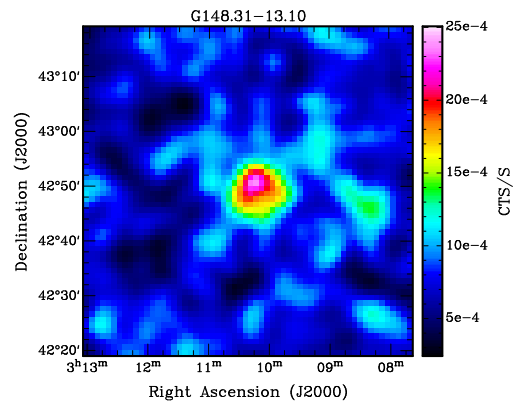
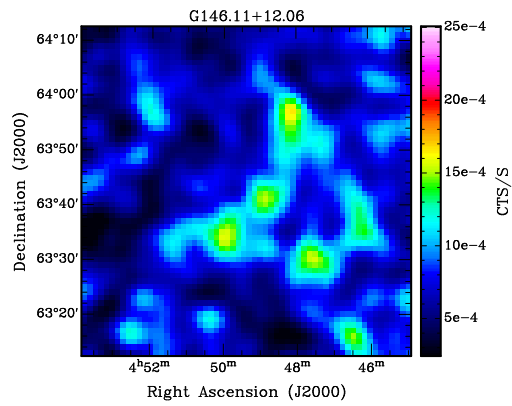
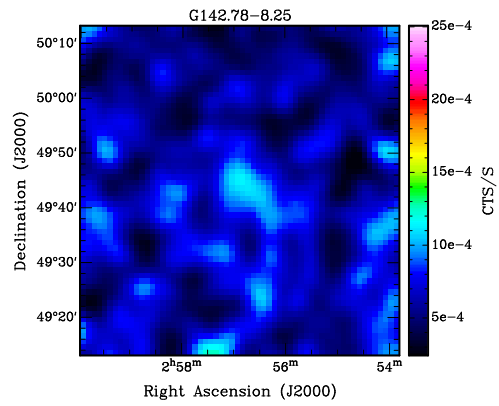
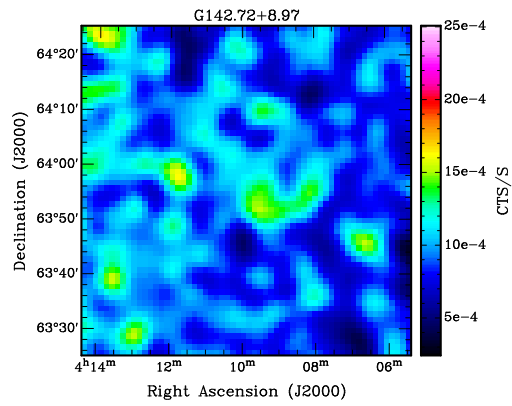
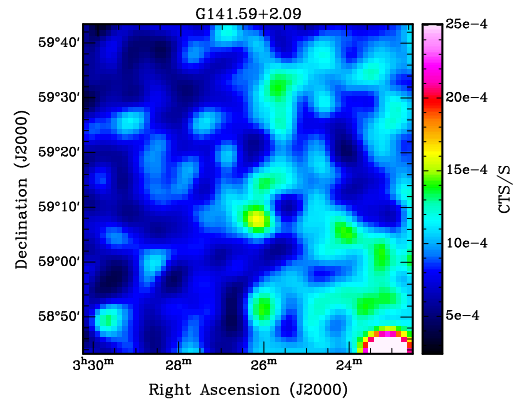
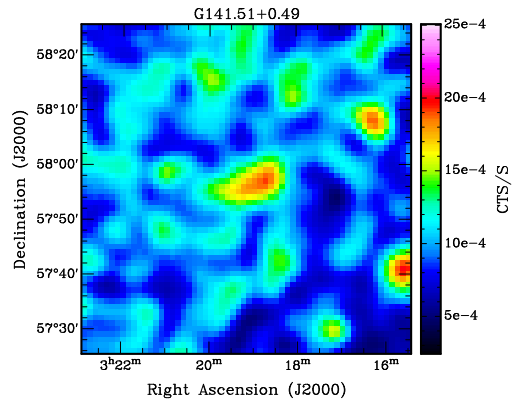


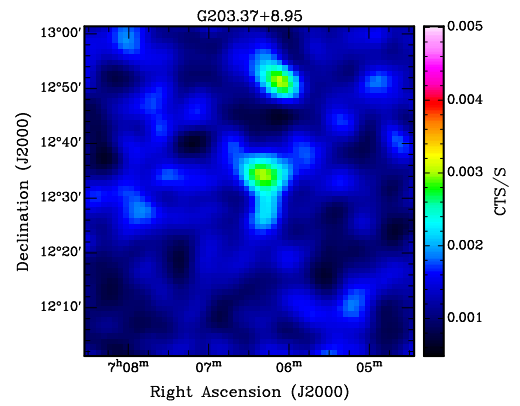
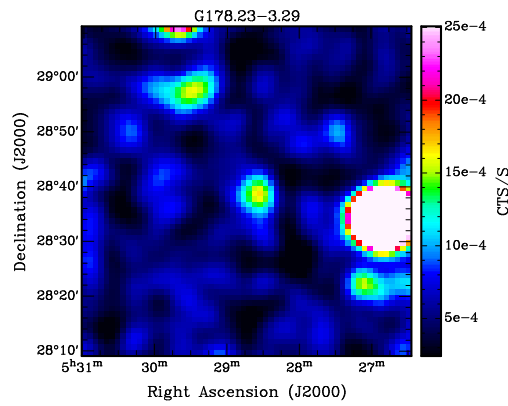
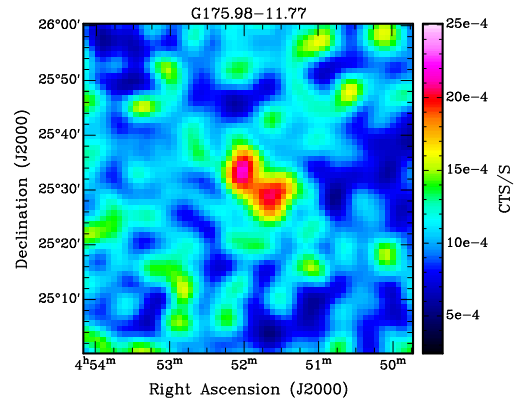
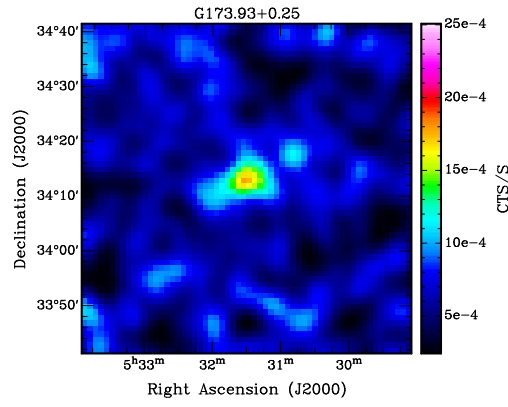
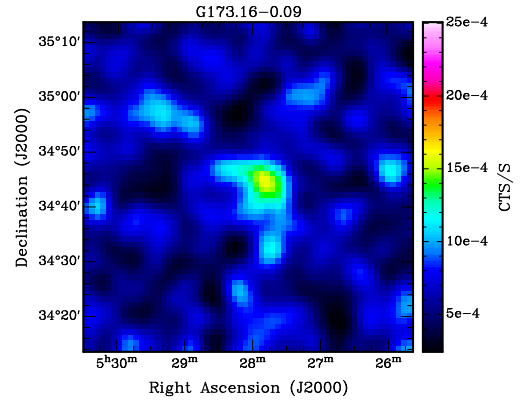
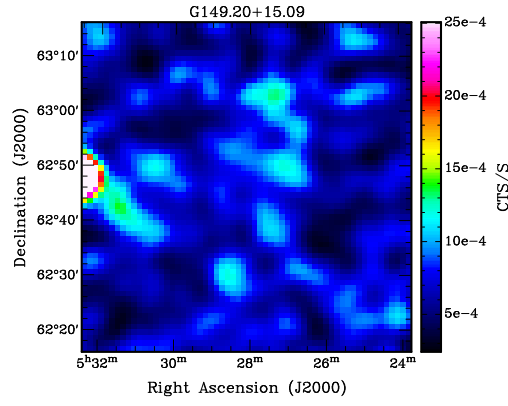


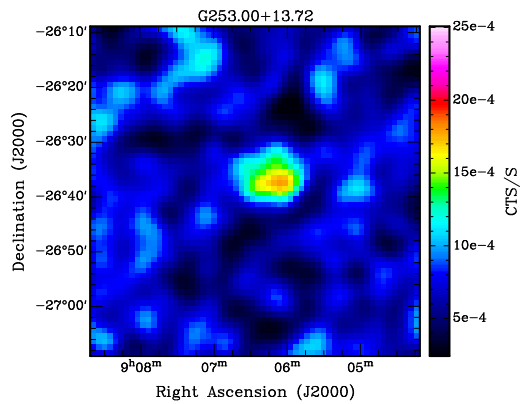
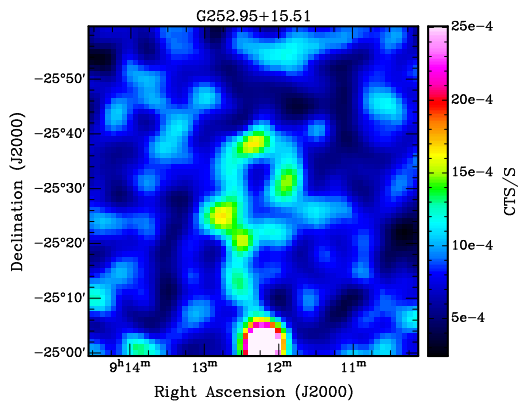
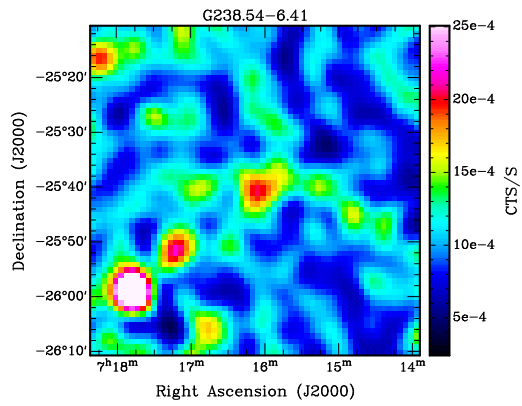
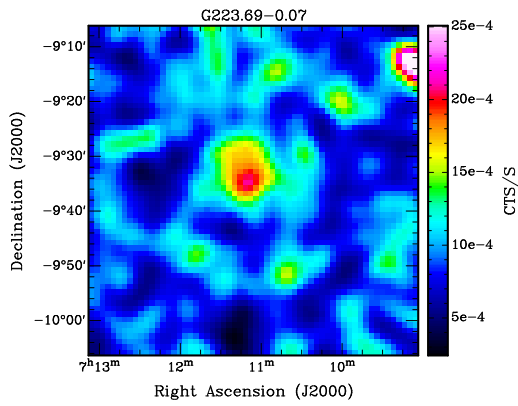
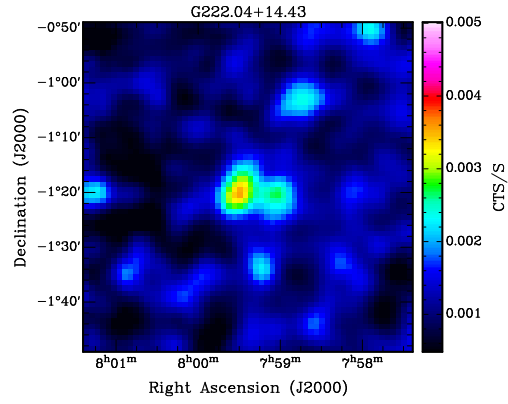
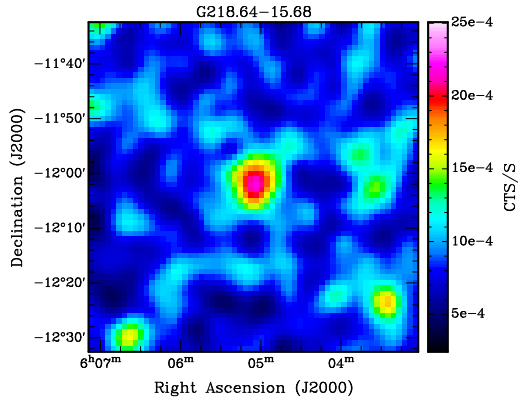


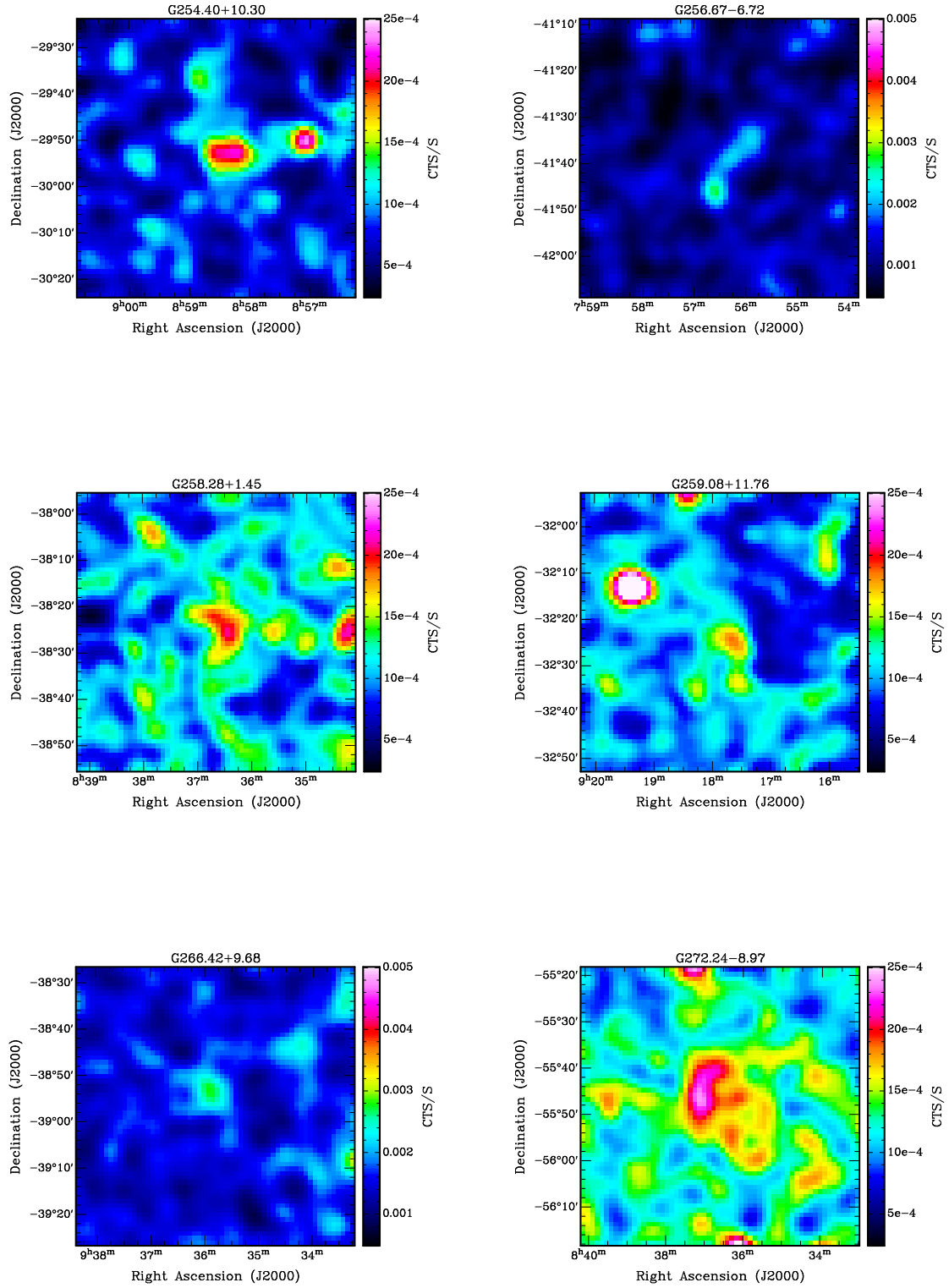


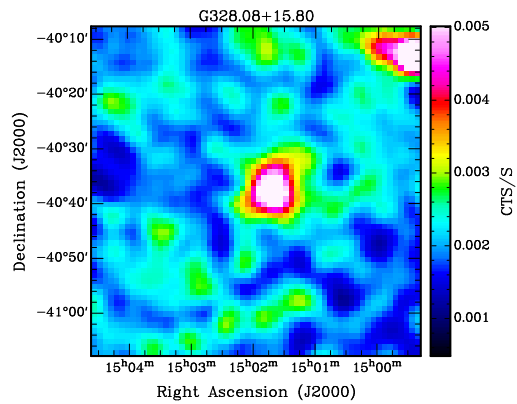
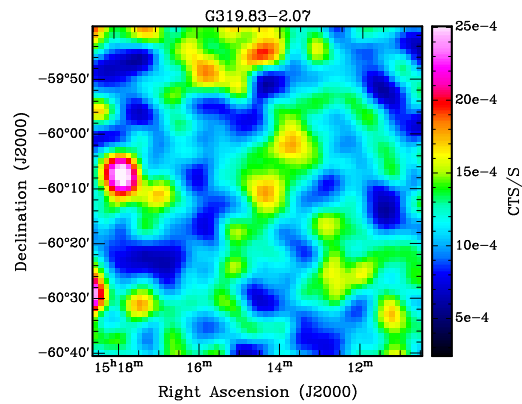
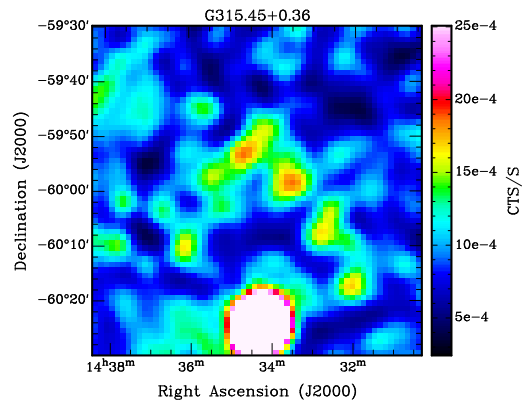
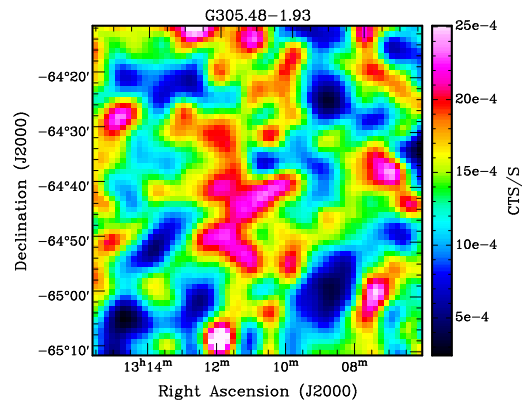
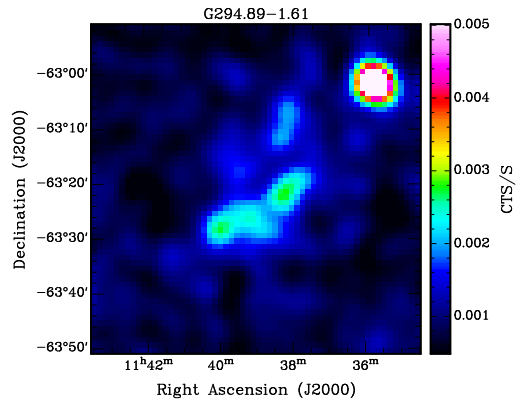
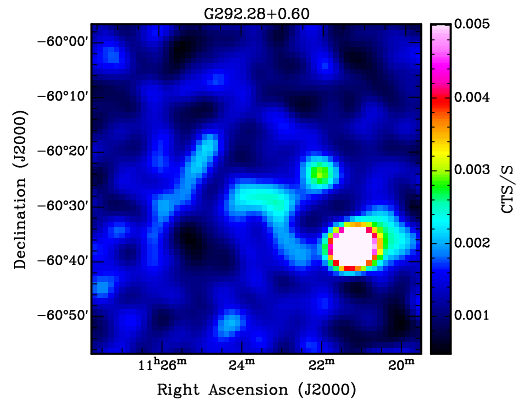


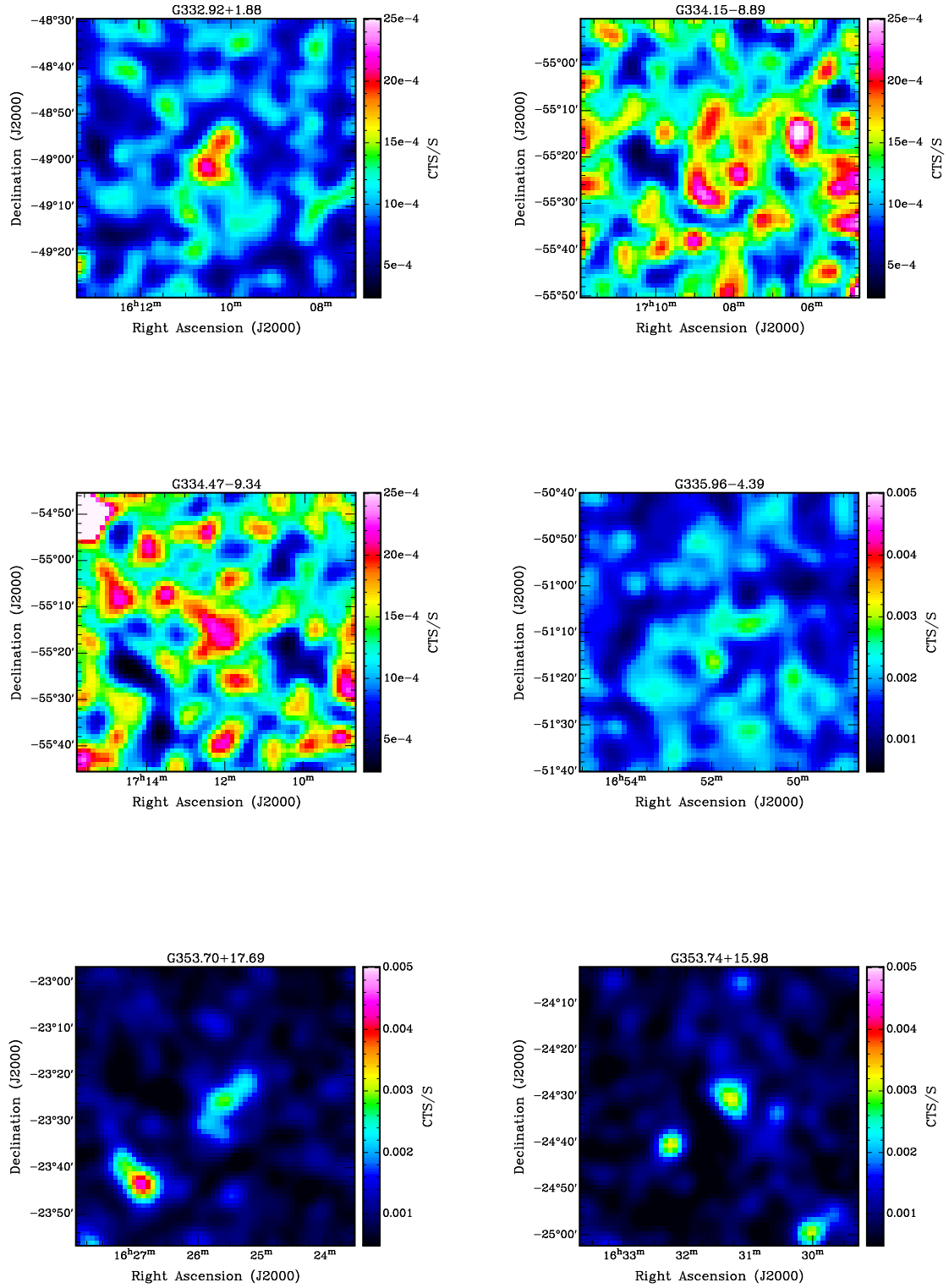


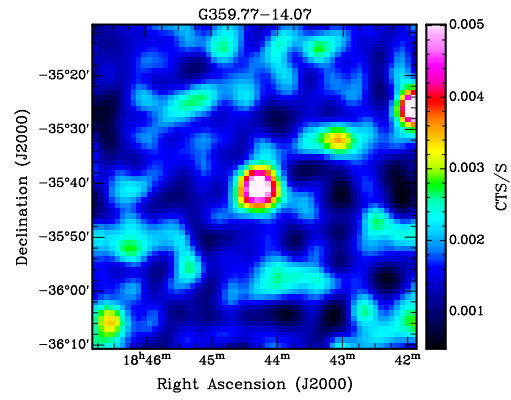
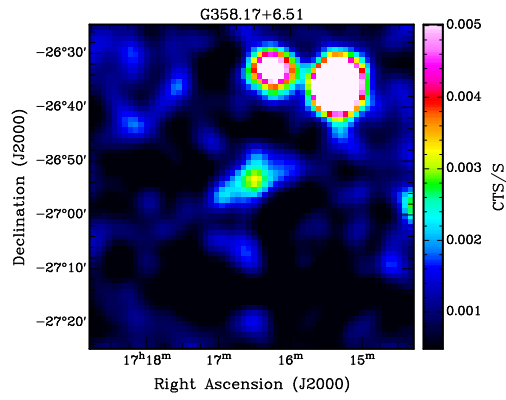
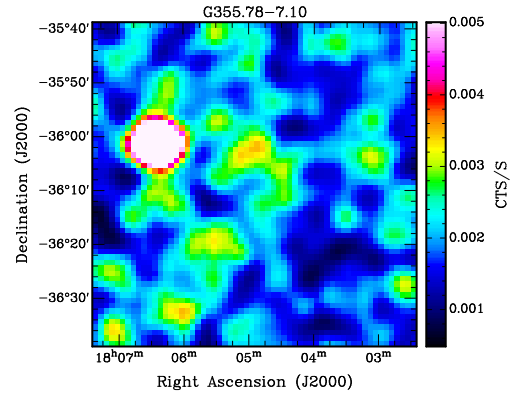
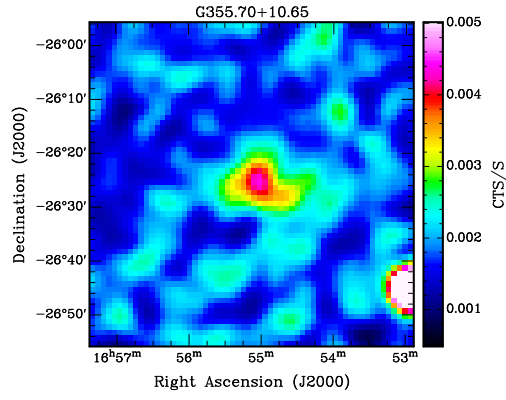




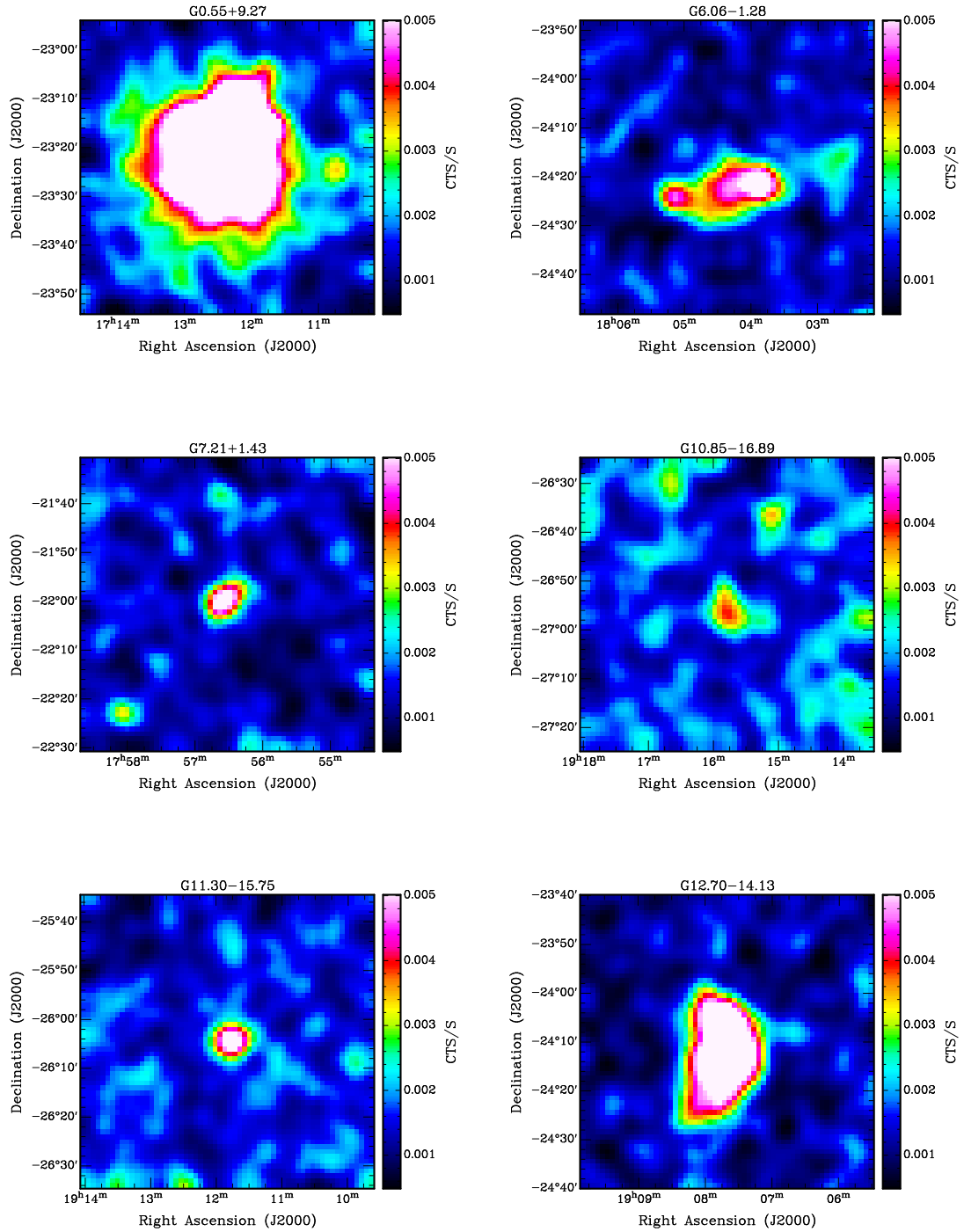


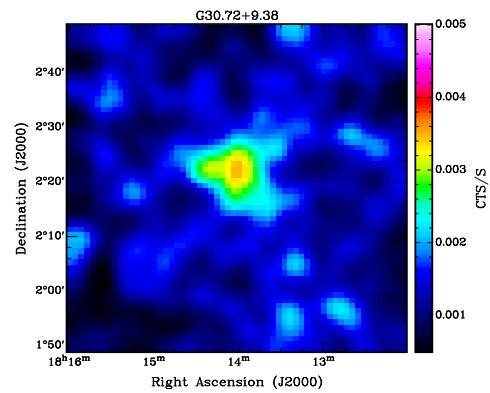
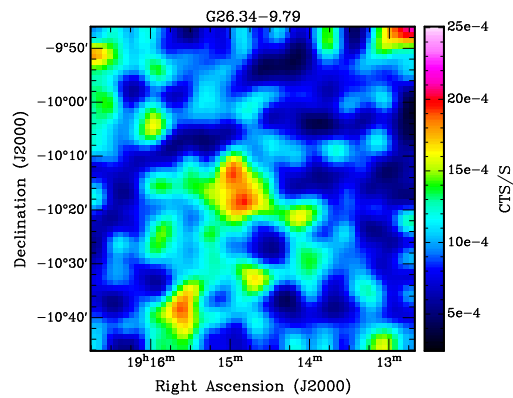
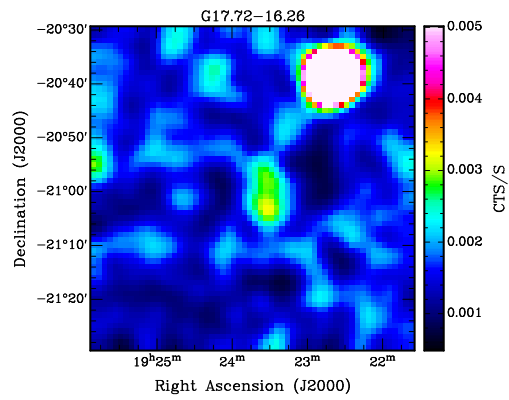
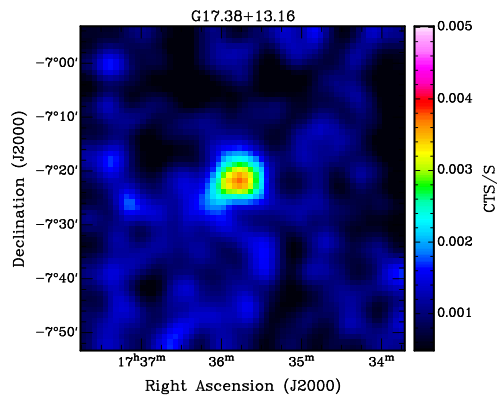
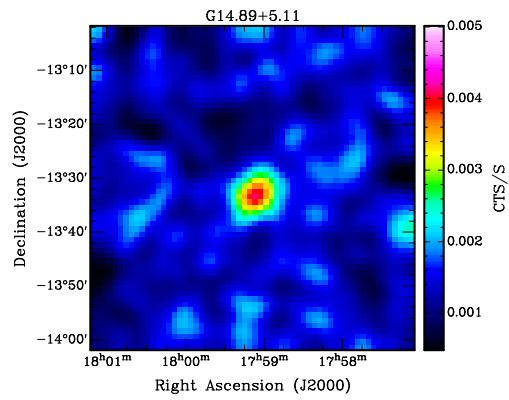
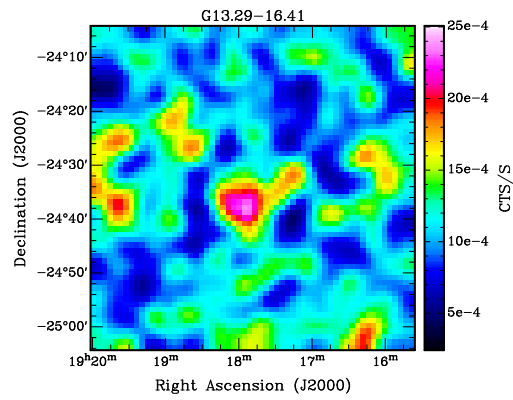


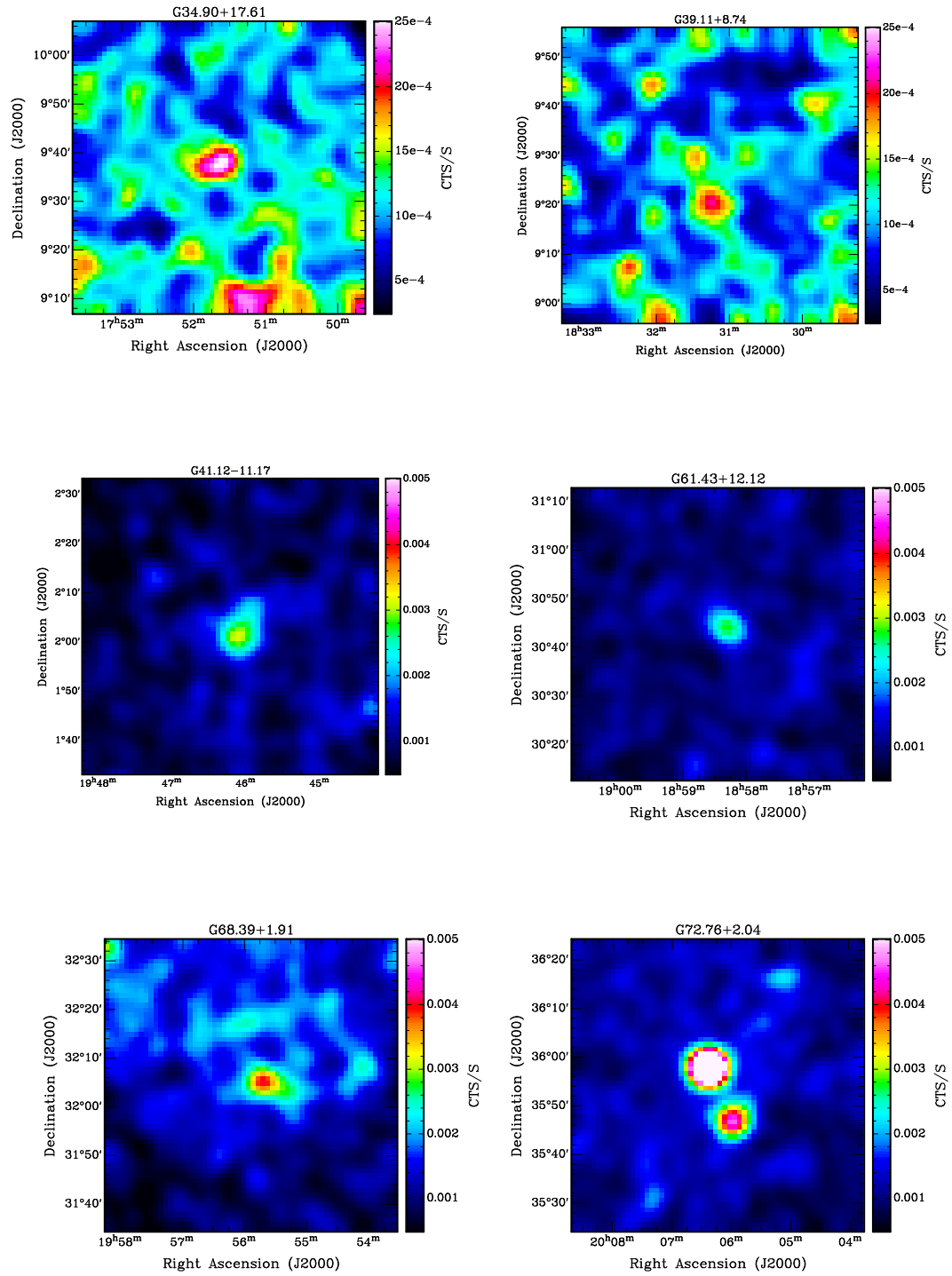


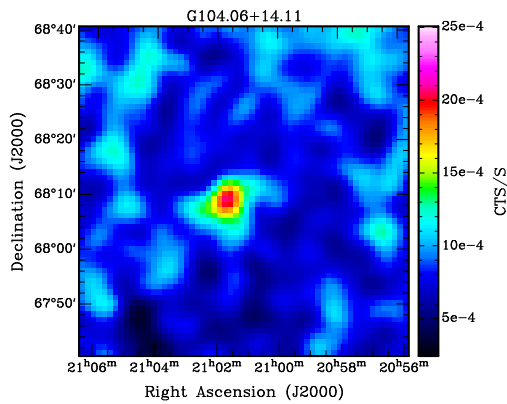
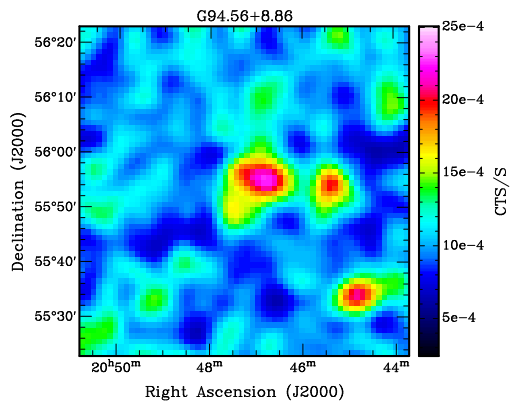
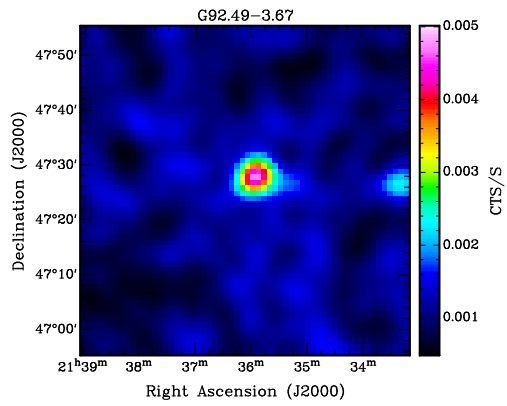
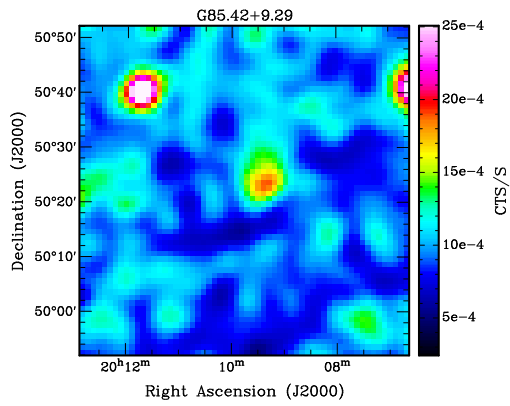
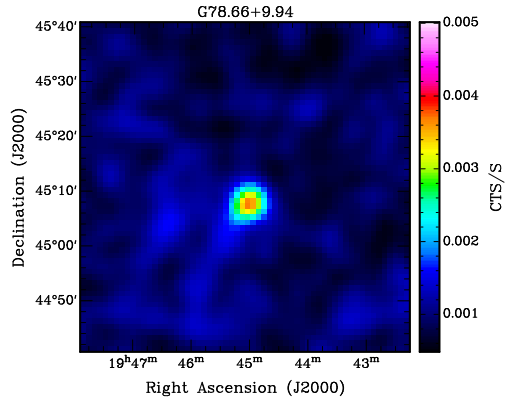
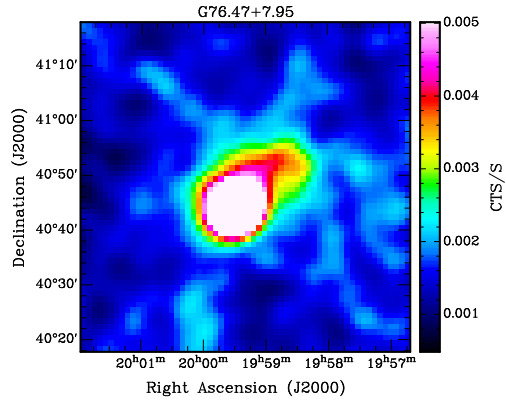


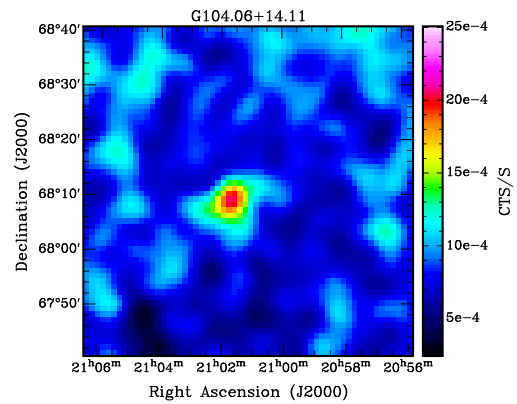
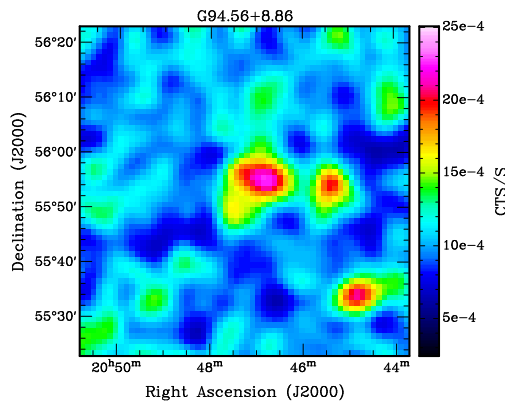
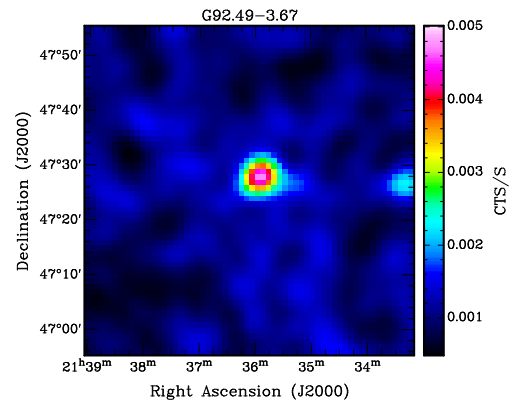
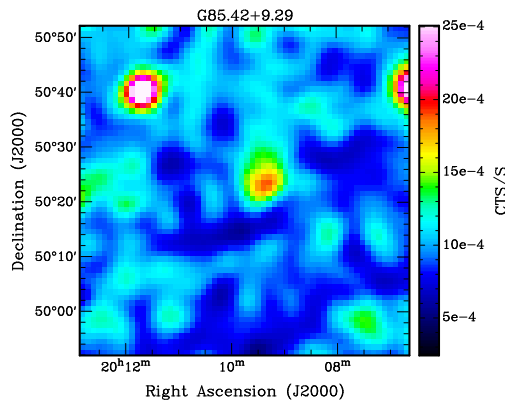
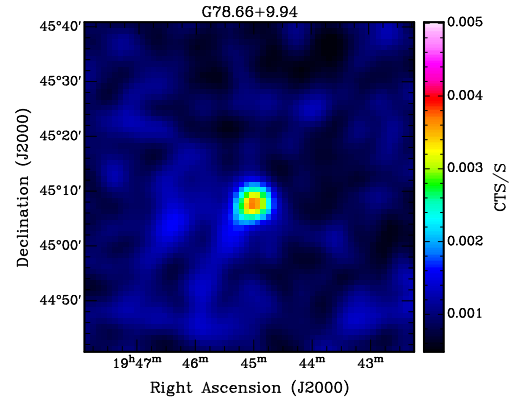
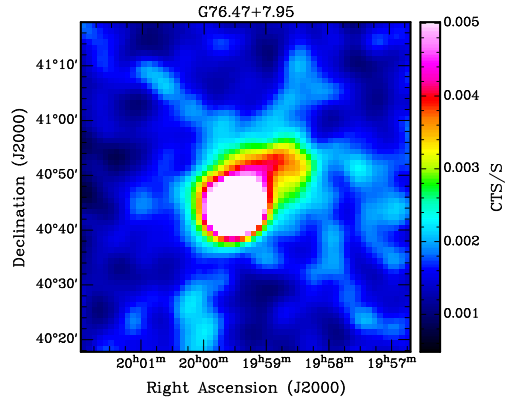
Targets which are probably of extragalactic origin (cf. A 5)

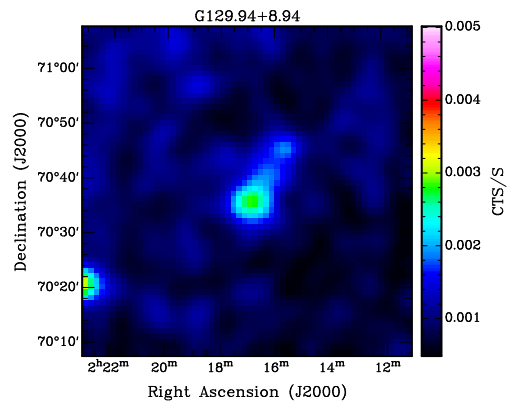
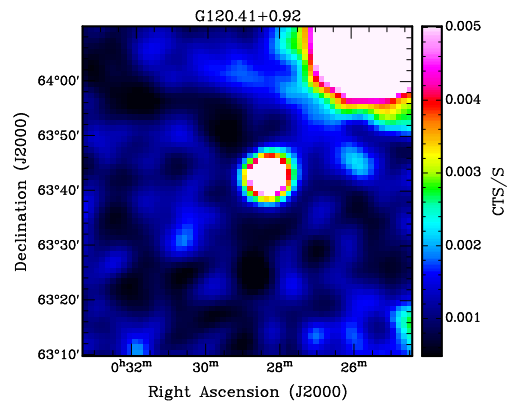
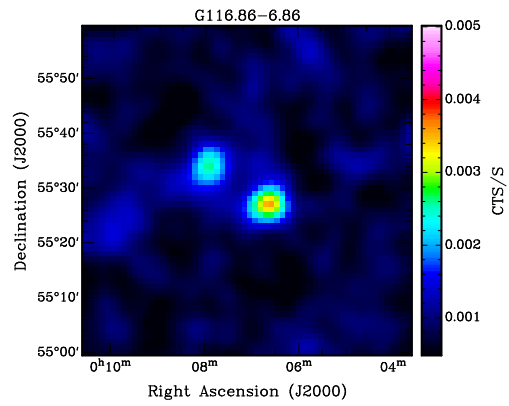
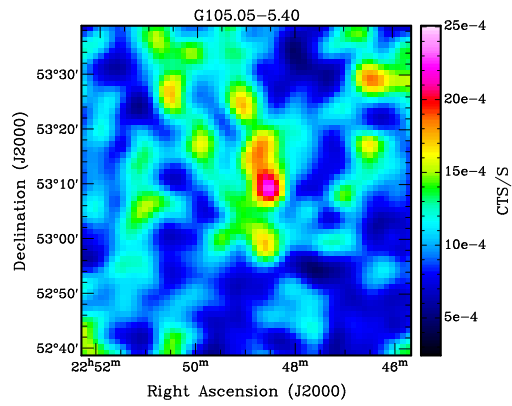
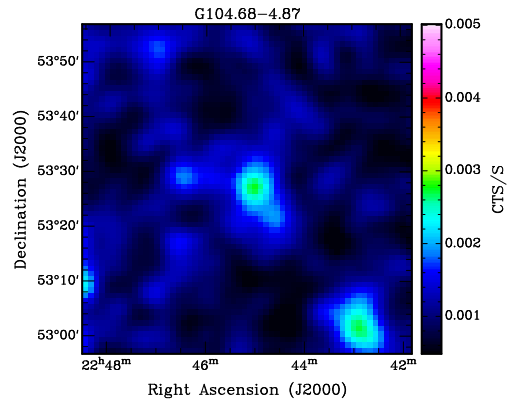
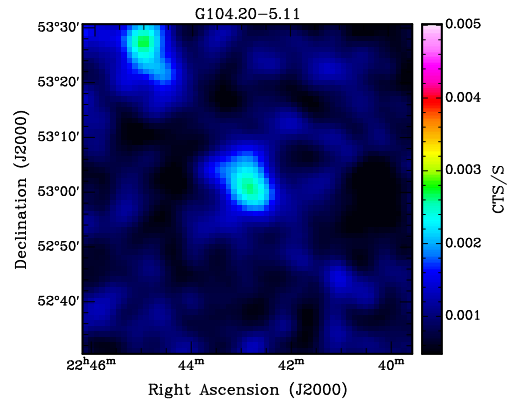


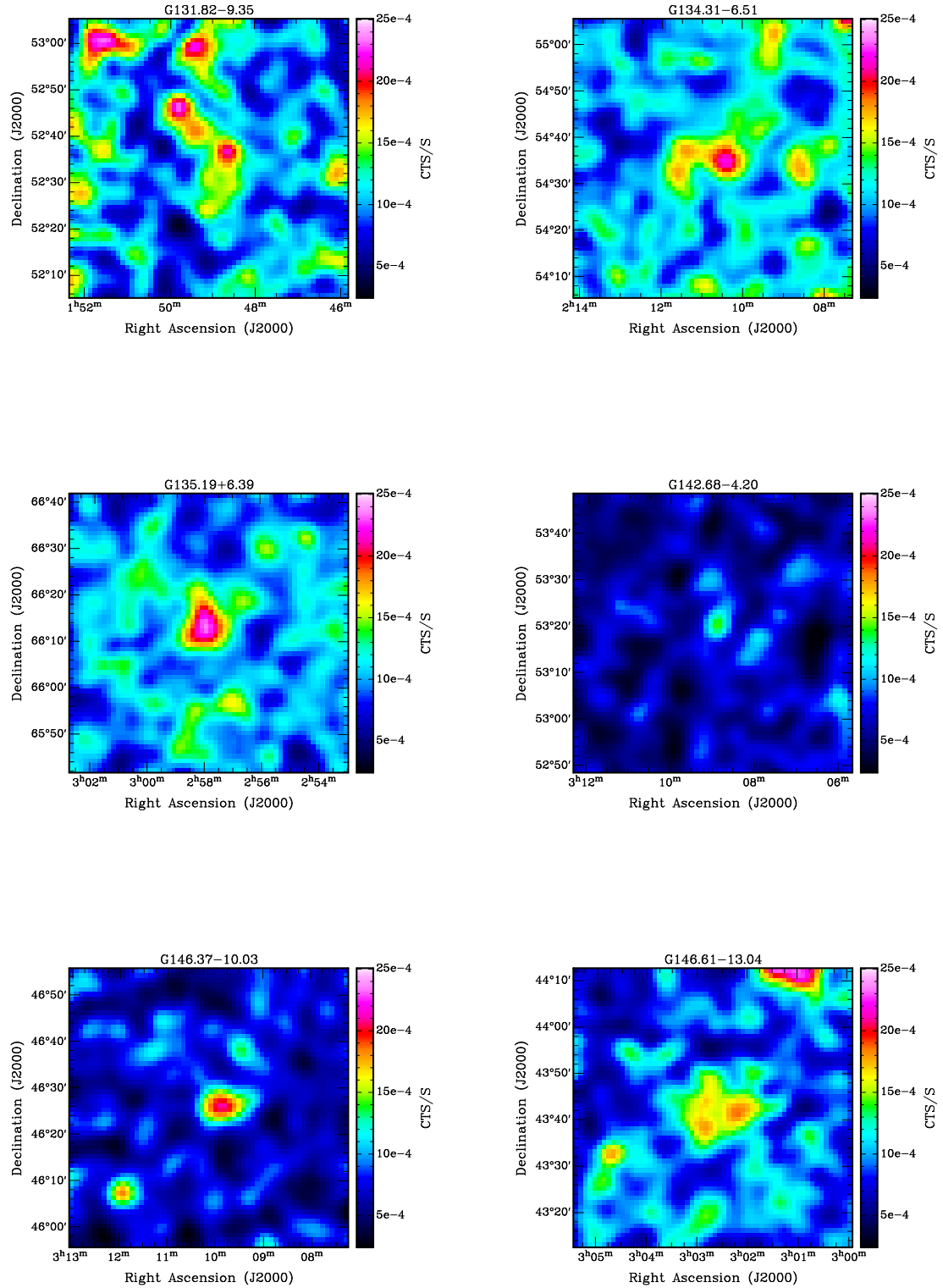


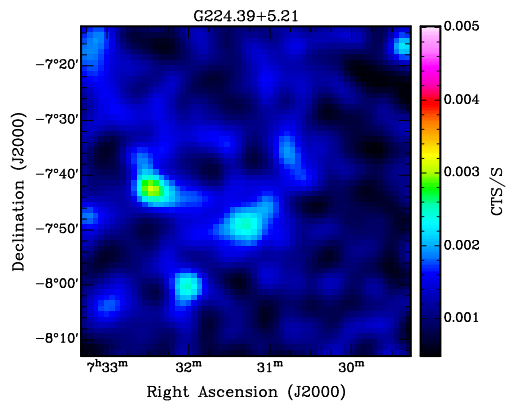
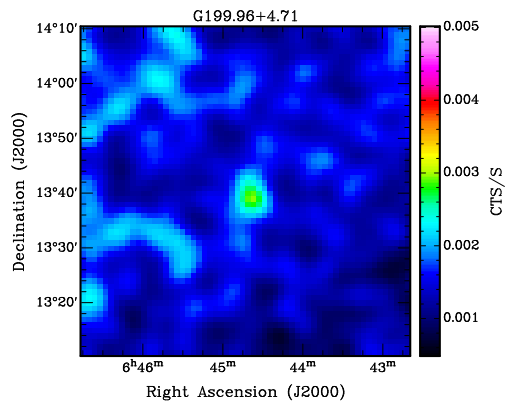
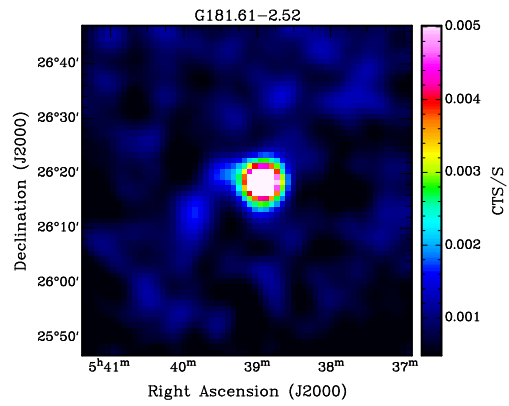
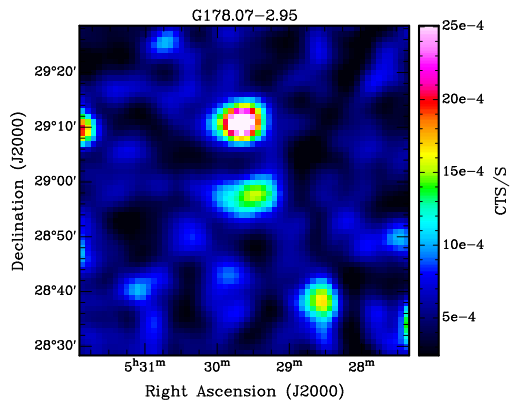
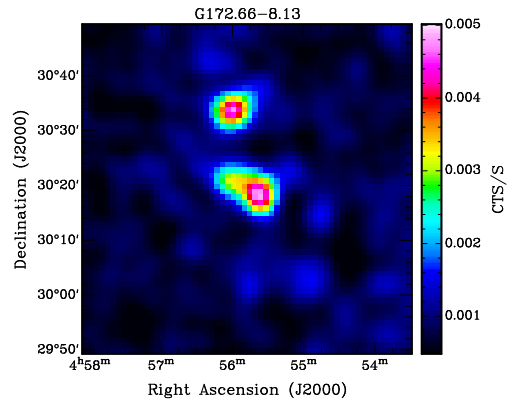
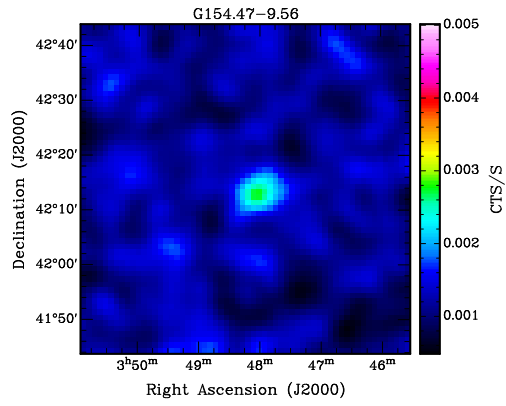


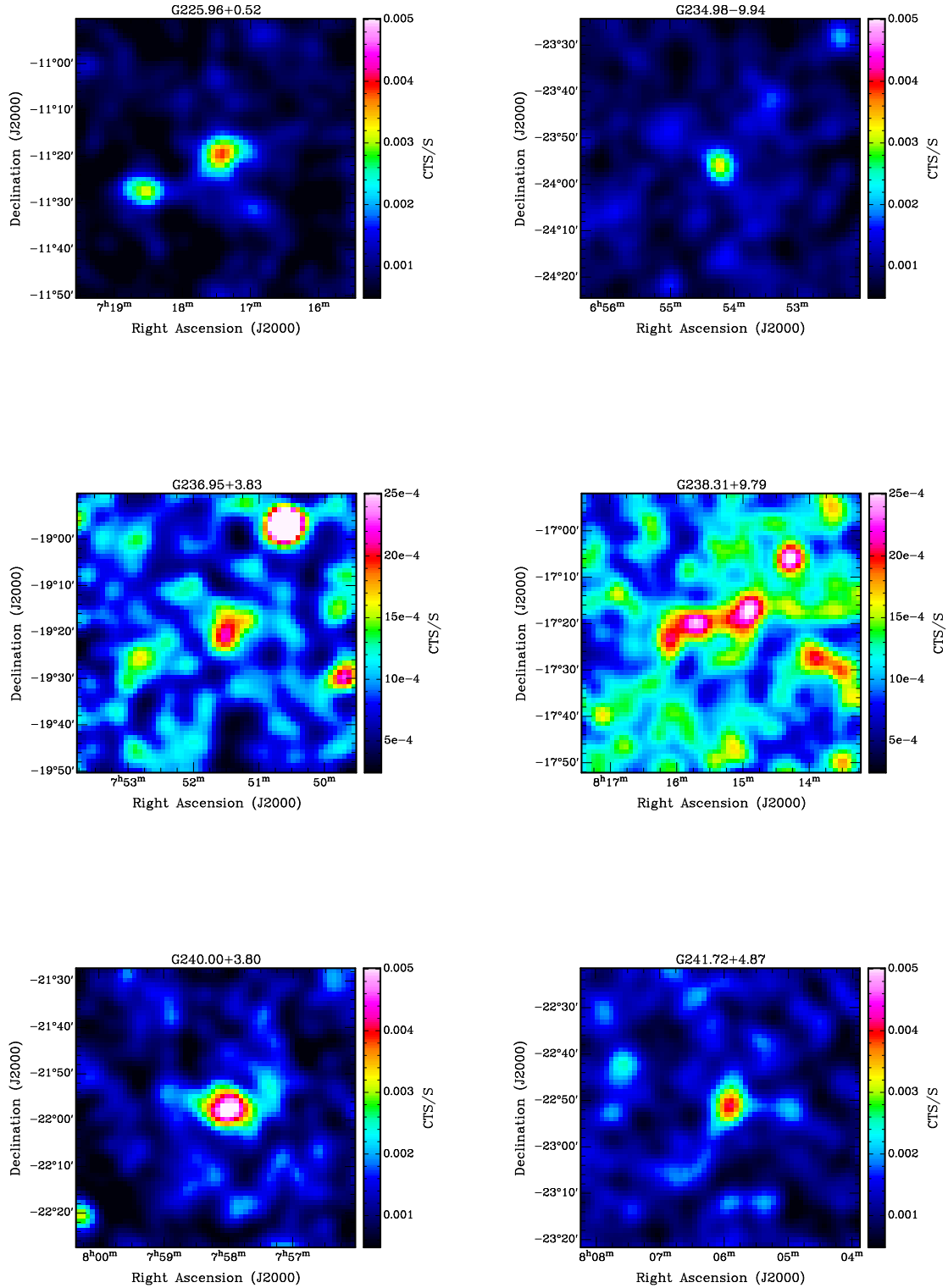


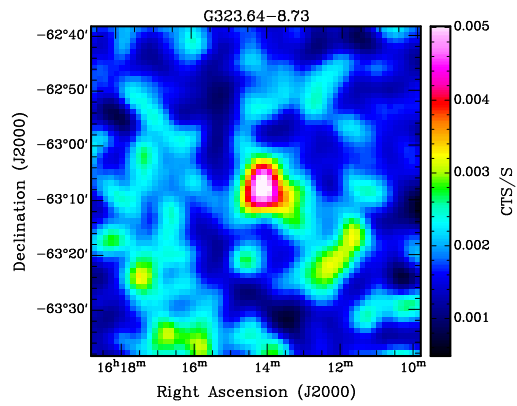
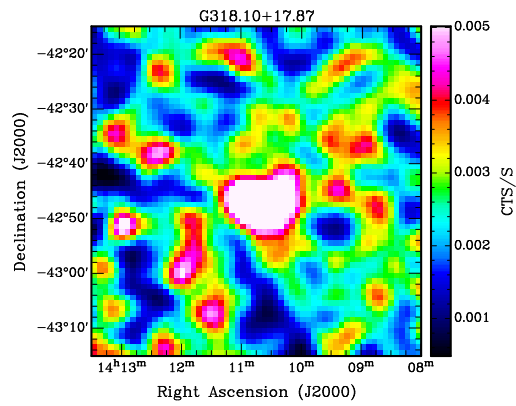
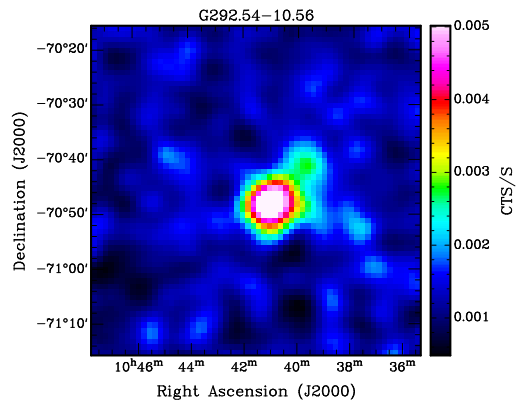
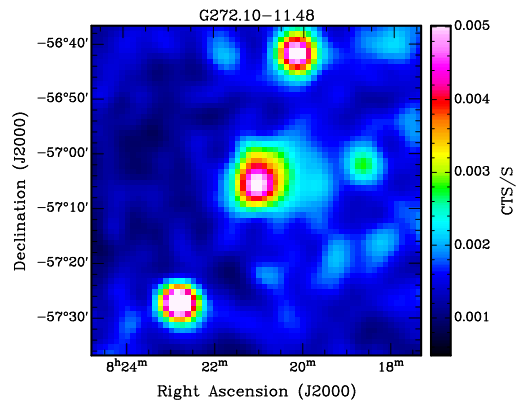
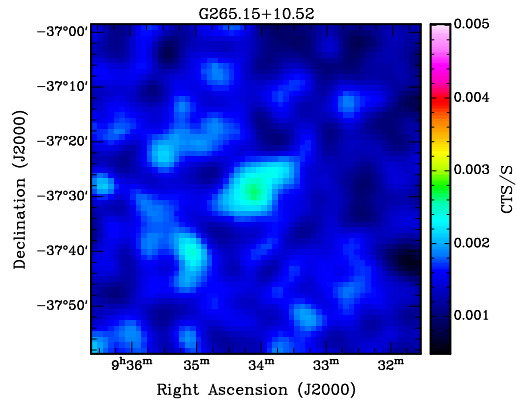
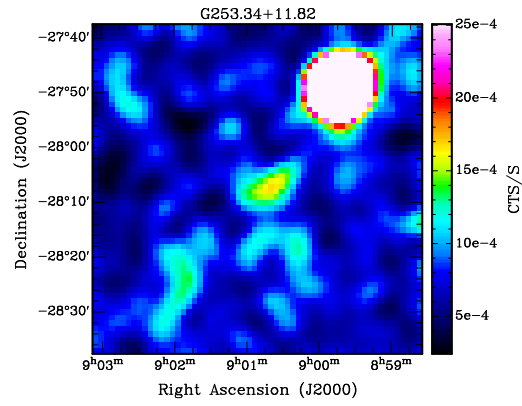


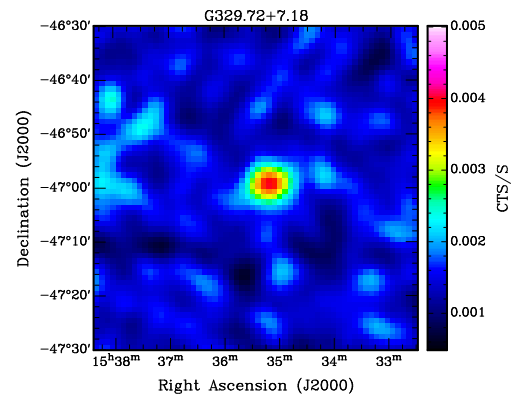
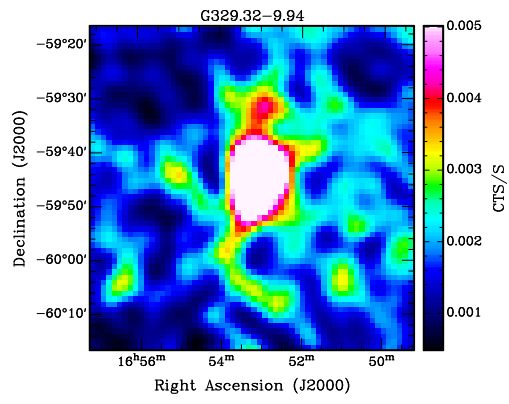




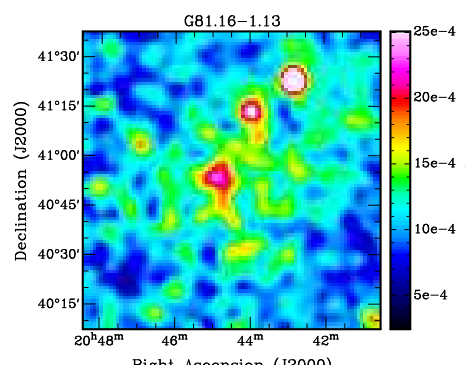
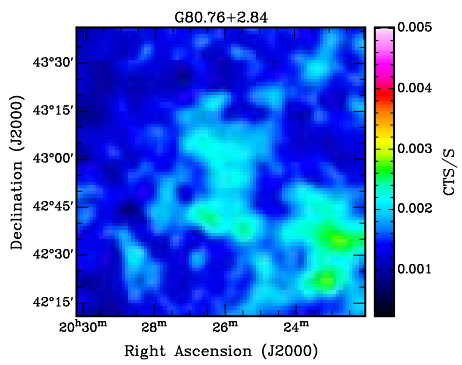
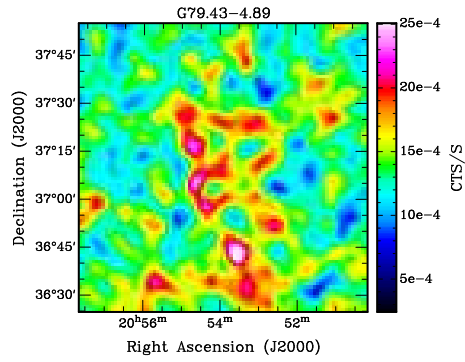
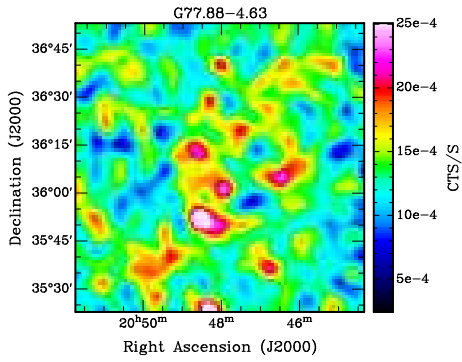
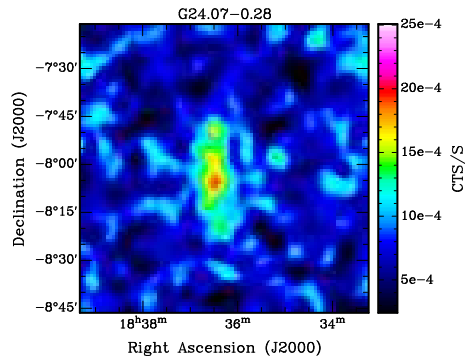
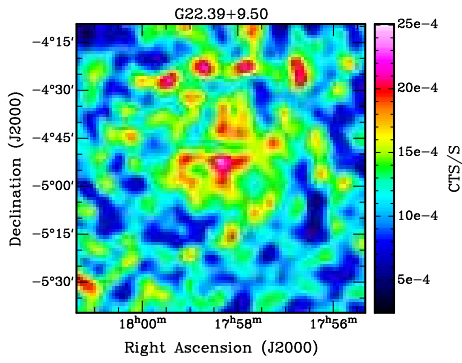


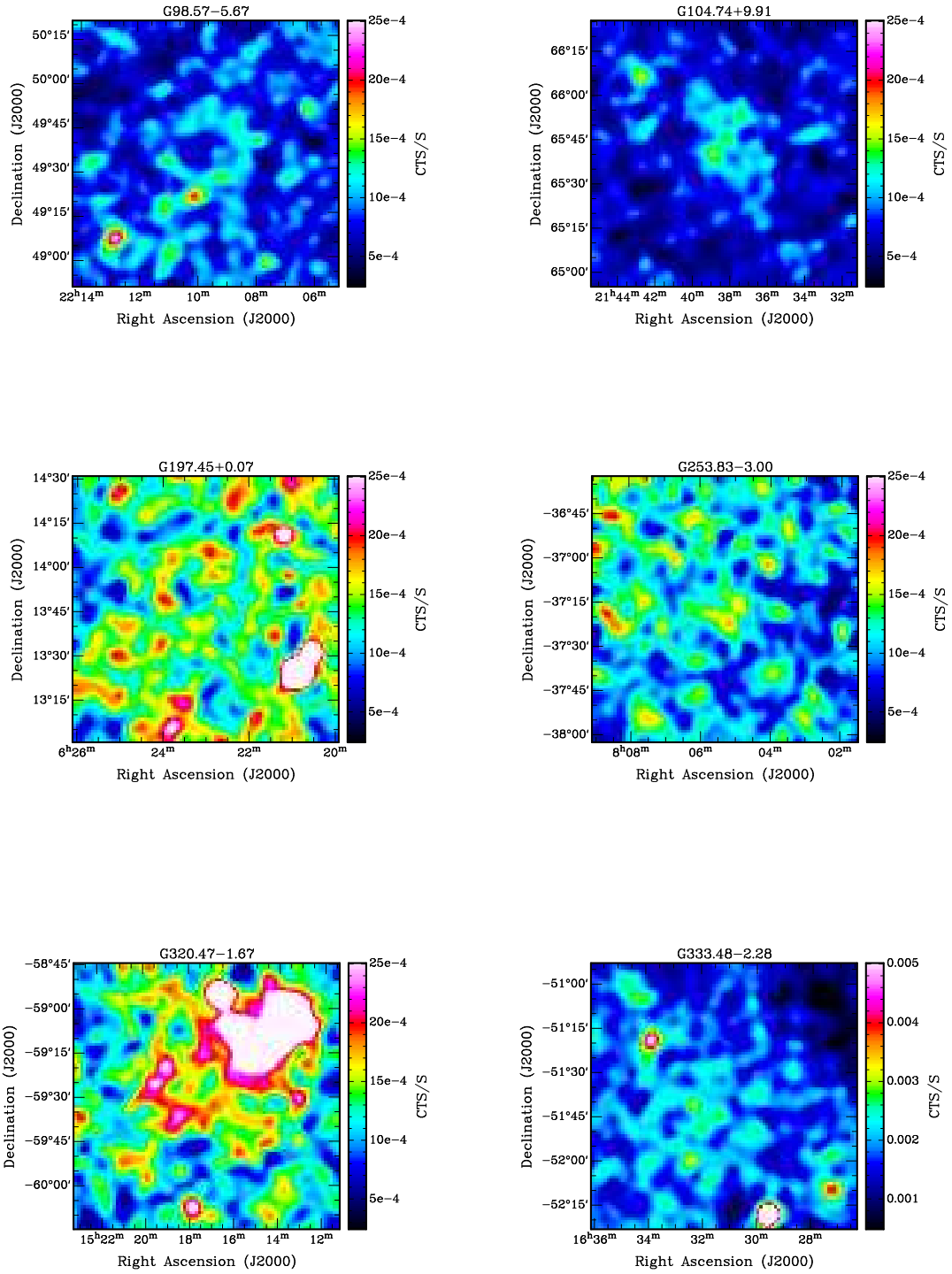


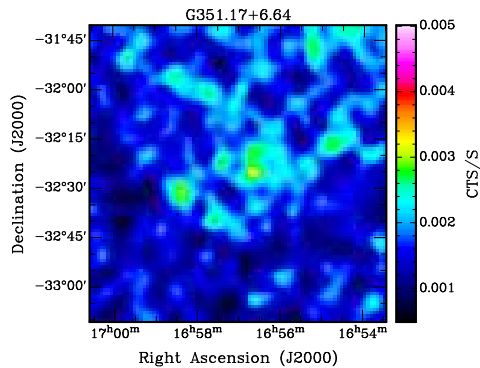
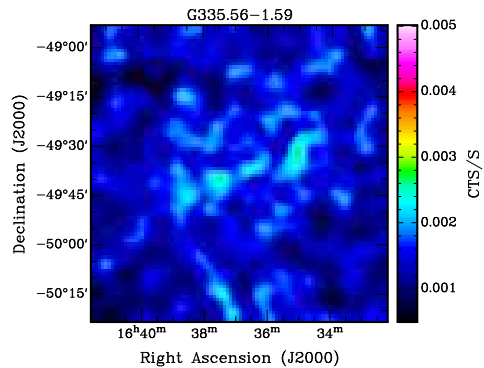
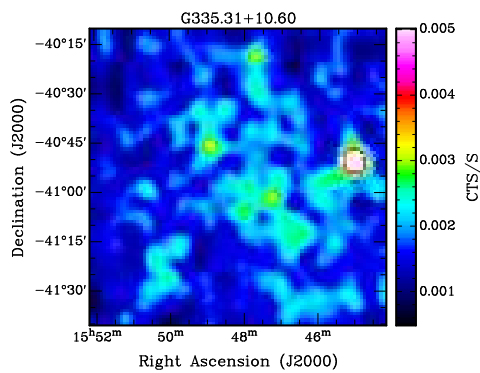
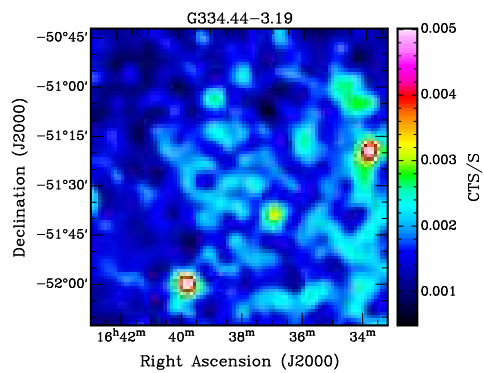


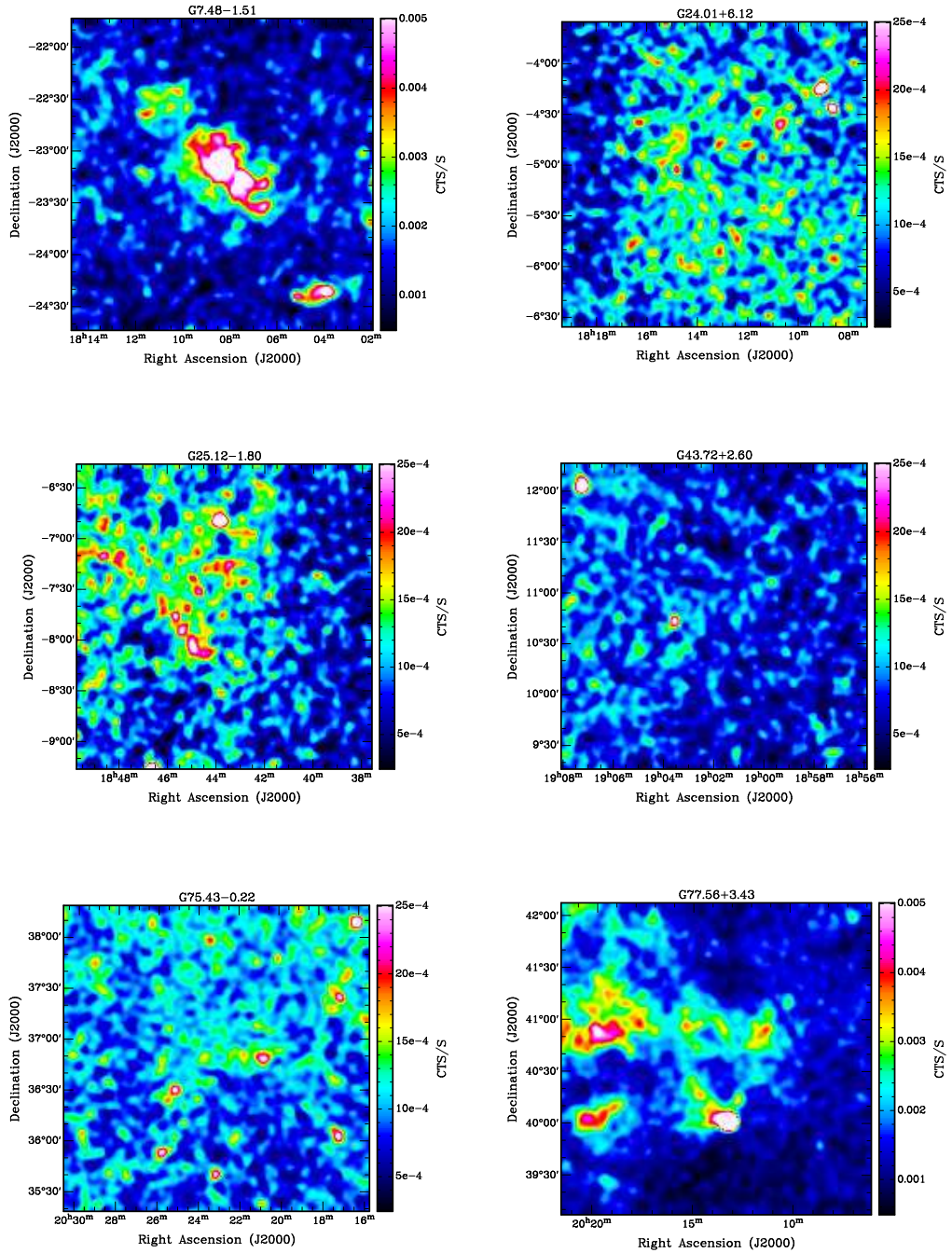


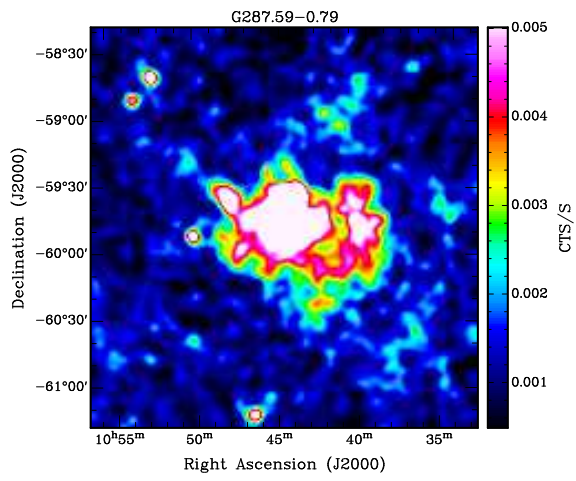
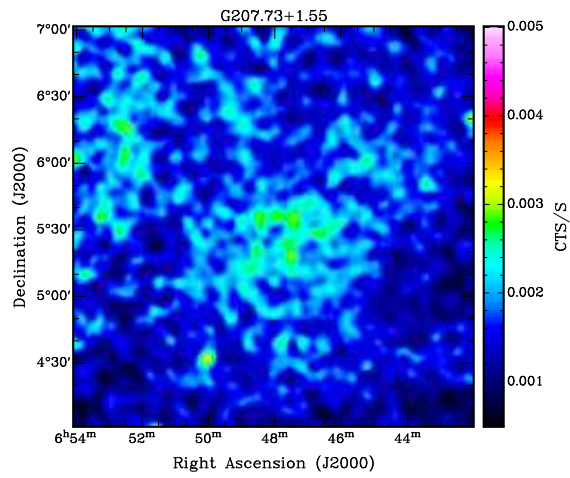
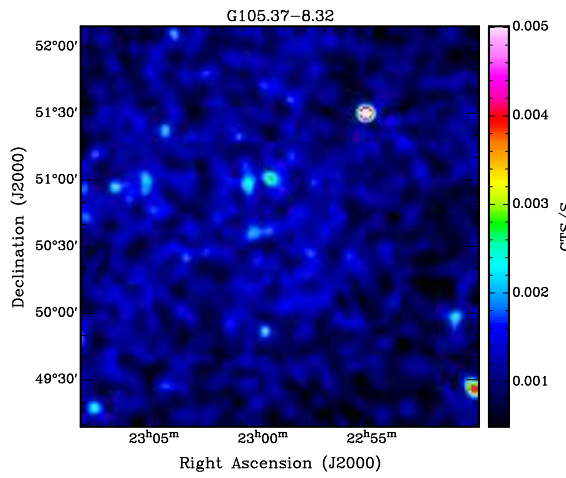
SNR candidates with an extent of $30' \leq D \leq 60'$ (cf. A 6)

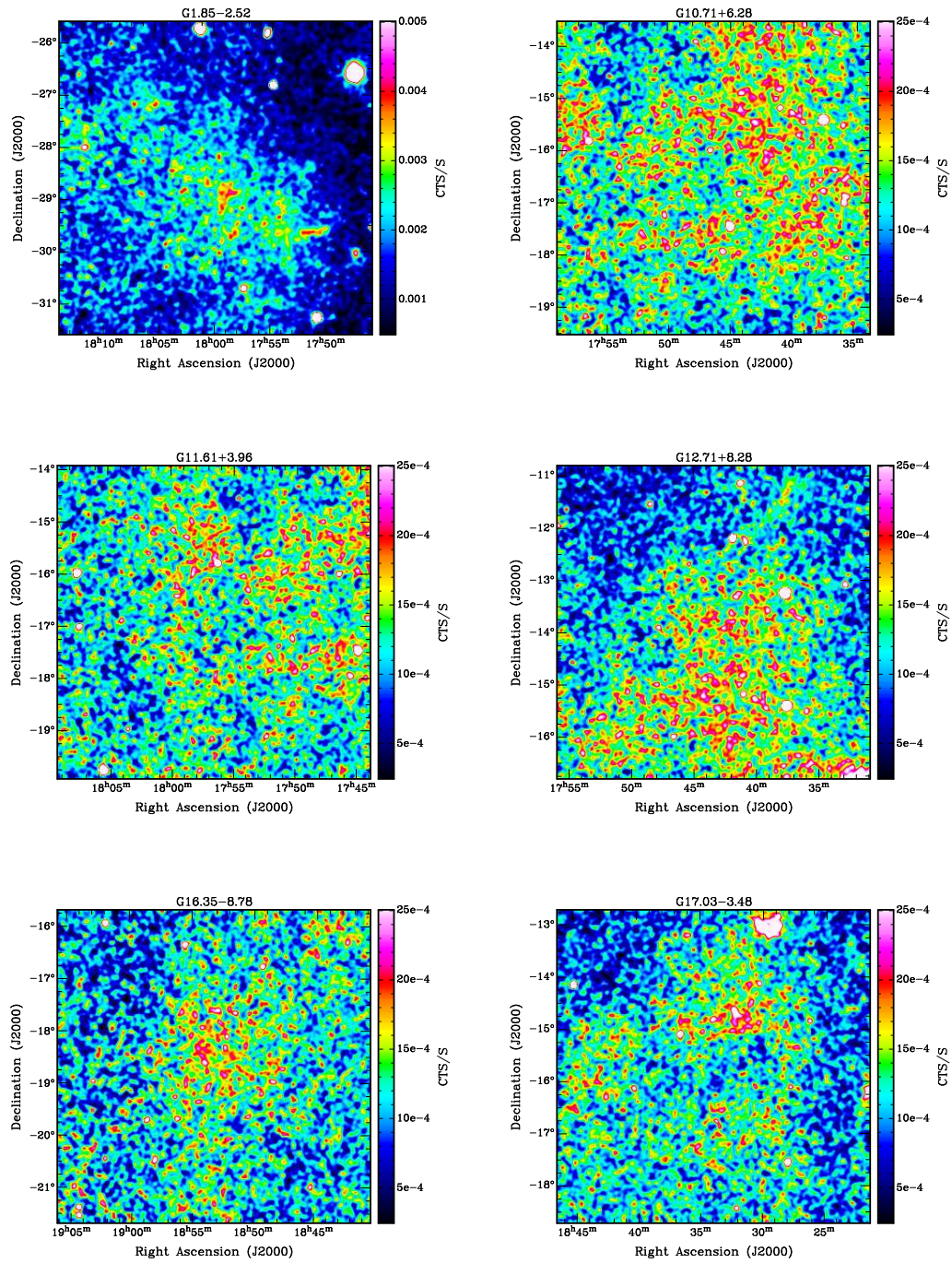


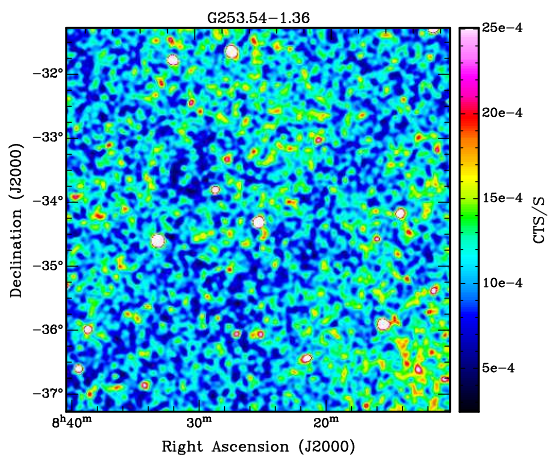
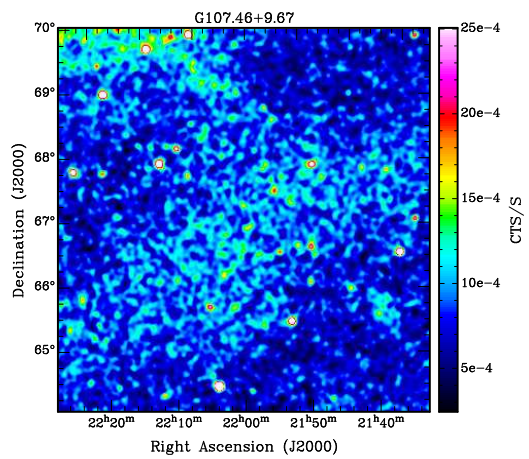
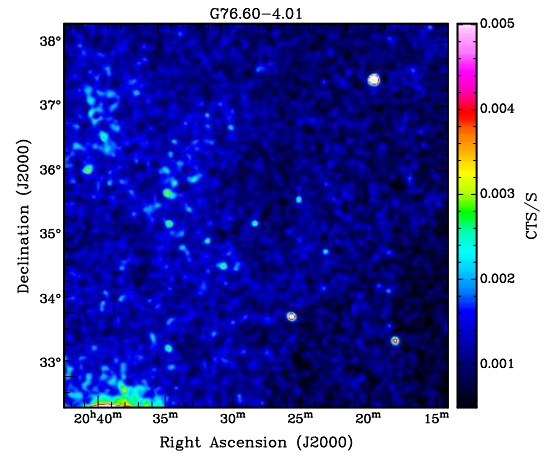
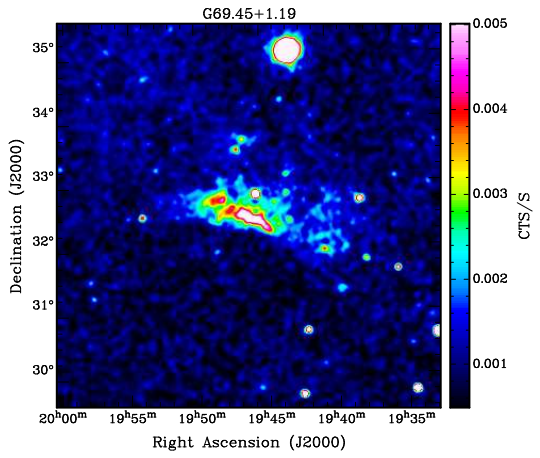
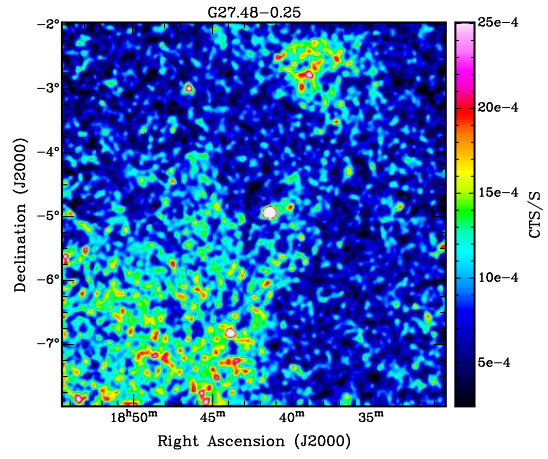
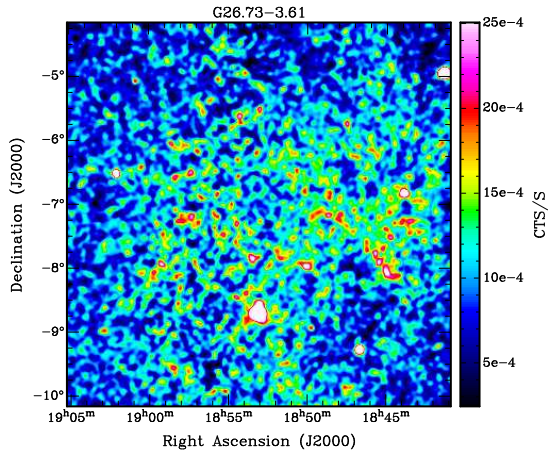


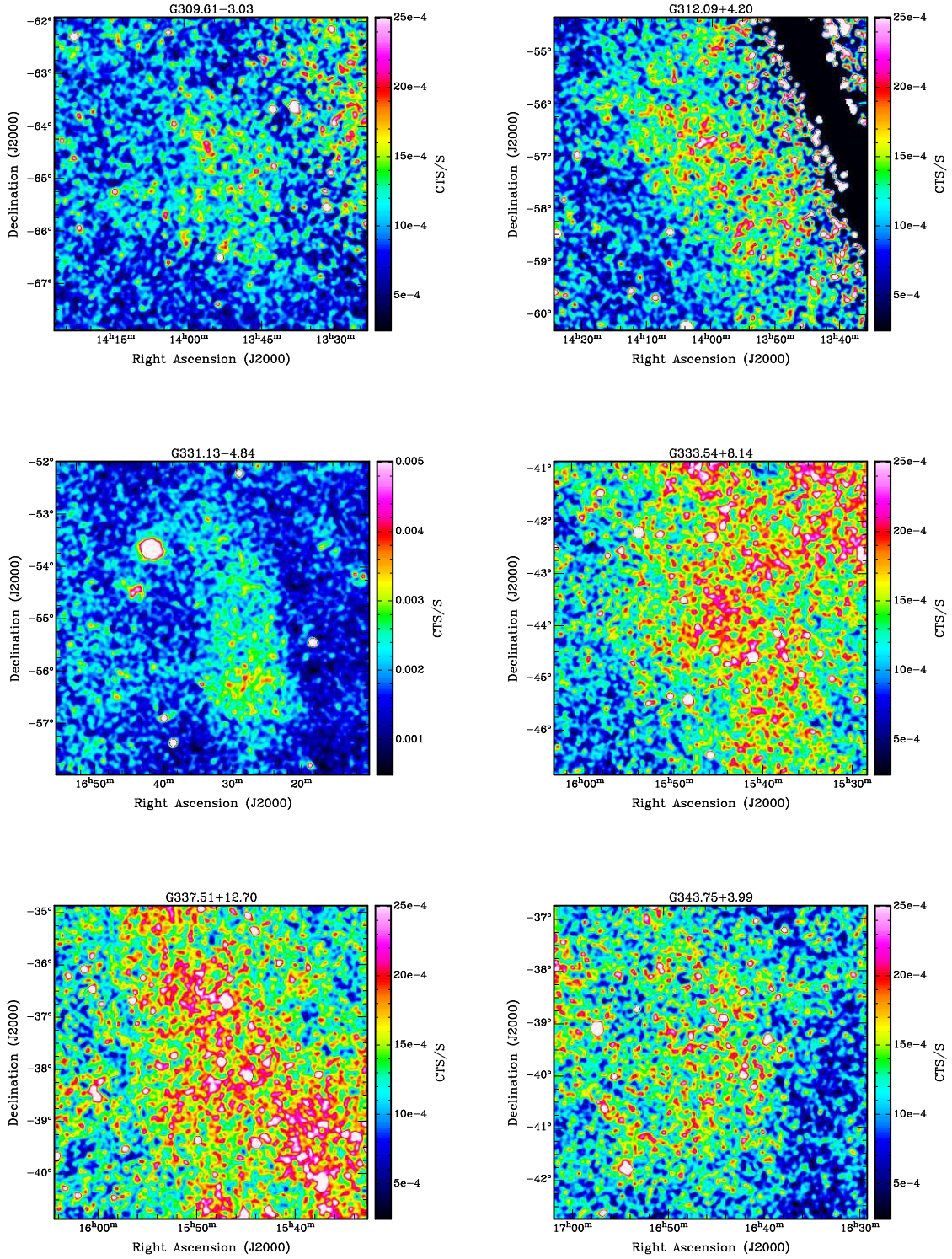


SNR candidates with an extent of $60' \leq D \leq 120'$ (cf. A 7)



SNR candidates with an extent of $120' \leq D$ (cf. A 8)





Bibliography

- Alfvén, H. & Herlofson, N. 1950, *Phys.Rev.*, 78, 616
- Anderson, M. C. & Rudnick, L. 1993, *ApJ*, 408, 514
- Arons, J. & Tavani, M. 1994, *ApJS*, 90, 797
- Aschenbach, B. 1985, *Reports of Progress in Physics*, 48, 579
- . 1987, Presented at the 31st SPIE Annual International Symposium, San Diego, Calif., Aug. 1987, 88, 22836
- Aschenbach, B. 1996, in *Roentgenstrahlung from the Universe*, 213–220
- Aufderheide, M. B., Brown, G. E., Kuo, T. T. S., et al. 1990, *ApJ*, 362, 241
- Austin, S. M., Trentelman, G. F., & Kashy, E. 1971, *ApJ*, 163, L79
- Baade, W. & Zwicky, F. 1934, *Proceedings of the National Academy of Science*, 20, 254+
- Bandiera, R. & Bocchino, F. 2003, *Proc. of COSPAR-2002 (10-19 October 2002, Houston, TX, USA)* in press, L115
- Baring, M. G., Ellison, D. C., Reynolds, S. P., et al. 1999, *ApJ*, 513, 311
- Baring, M. G. & Harding, A. K. 1998, *ApJ*, 507, L55
- Becker, R. H. & Szymkowiak, A. E. 1981, *ApJ*, 248, L23
- Becker, W. & Aschenbach, B. 2001, *Proceedings of the 270.WE-Heraeus Seminar on Neutron Stars, Pulsars and Supernova Remnants*, eds W. Becker, H. Lesch & J. Truemper. Proceedings available as MPE-Report 278 (astrp-ph/0208466), p. 64
- Becker, W. & Pavlov, G. 2001, *Pulsars and Isolated Neutron Stars in "The Century of Space Science"*, ed. Johan Bleeker, Johannes Geiss and Martin Huber (Kluwer Academic Publishers)
- Becker, W. & Truemper, J. 1997, *A&A*, 326, 682
- Biggs, J. D. & Lyne, A. G. 1996, *MNRAS*, 282, 691

- Blair, W. P., Raymond, J. C., Danziger, J., et al. 1988, in *A Decade of UV Astronomy with the IUE Satellite*, Volume 1, Vol. 1, 117–120
- Blondin, J. M., Wright, E. B., Borkowski, K. J., et al. 1998, *ApJ*, 500, 342+
- Bodansky, D., Clayton, D. D., & Fowler, W. A. 1968, *ApJS*, 16, 299
- Branch, D. & Miller, D. L. 1993, *ApJ*, 405, L5
- Broadbent, A., Osborne, J. L., & Haslam, C. G. T. 1989, *MNRAS*, 237, 381
- Brogan, C. L., Frail, D. A., Goss, W. M., et al. 2000, *ApJ*, 537, 875
- Busser, J. U. Z. 1998, Thesis, Ludwig-Maximilian Universität München
- Camilo, F., Nice, D. J., Shrauner, J. A., et al. 1996, *ApJ*, 469, 819+
- Canto, J. 1977, *A&A*, 61, 641
- Cappellaro, E., Turatto, M., Tsvetkov, D. Y., et al. 1997, *A&A*, 322, 431
- Case, G. L. & Bhattacharya, D. 1998, *ApJ*, 504, 761+
- Chevalier, R. A. 1974, *ApJ*, 188, 501
- Chin, Y. N. & Huang, Y. L. 1994, *Nature*, 371, 398
- Cioffi, D. F., McKee, C. F., & Bertschinger, E. 1988, *ApJ*, 334, 252
- Clark, D. H. & Stephenson, F. R. 1976, *QJRAS*, 17, 290
- Condon, J. J., Cotton, W. D., Greisen, E. W., et al. 1998, *AJ*, 115, 1693
- Corcoran, M. F. 1999, in *Revista Mexicana de Astronomia y Astrofisica Conference Series*, Vol. 8, 131–136
- Cornwell, T. J. & Evans, K. F. 1985, *A&A*, 143, 77
- Cowsik, R. & Sarkar, S. 1984, *MNRAS*, 207, 745
- Danzmann, K. 2000, *Advances in Space Research*, 25, 1129
- Davelaar, J., Smith, A., & Becker, R. H. 1986, *ApJ*, 300, L59
- de Jager, O. C. 1995, in *Currents in High-Energy Astrophysics. Proceedings of the NATO Advanced Study Institute and Ninth Course of the International School of Cosmic Ray Astrophysics on Currents in High-Energy Astrophysics*, held at Ettore Majorana Centre, Erice, Sicily, Italy, May 7-18, 1994. Editors, Maurice M. Shapiro, Rein Silberberg, John P. Wefel; Publisher, Kluwer Academic Publishers, Dordrecht; Boston, 1995. LC # QB463 .C87 1995. ISBN # 0-7923-3354-3., p.225, 225+

-
- den Herder, J. W., Brinkman, A. C., Kahn, S. M., et al. 2001, *A&A*, 365, L7
- D’Ercole, A. 1992, *MNRAS*, 255, 572
- Dermer, C. D. 1986a, *ApJ*, 307, 47
- . 1986b, *A&A*, 157, 223
- Dickel, J. R. 1999, in *Perspectives on Radio Astronomy-Science with Large Antenna Arrays*, Netherland Foundation for Research in Astronomy, M. P. van Haarlem; Eds.
- Dickel, J. R., Green, A., Ye, T., et al. 1996, *AJ*, 111, 340+
- Dickel, J. R. & Milne, D. K. 1976, *Australian Journal of Physics*, 29, 435
- Dickey, J. M. & Lockman, F. J. 1990, *ARA&A*, 28, 215
- Dopita, M. A., Binette, L., & Tuohy, I. R. 1984, *ApJ*, 282, 142
- Douvion, T., Lagage, P. O., Cesarsky, C. J., et al. 2001, *A&A*, 373, 281
- Dragicevich, P. M., Blair, D. G., & Burman, R. R. 1999, *MNRAS*, 302, 693
- Droege, W., Lerche, I., & Schlickeiser, R. 1987, *A&A*, 178, 252
- Drury, L. O., Aharonian, F. A., & Voelk, H. J. 1994, *A&A*, 287, 959
- Duncan, A. R., Stewart, R. T., Haynes, R. F., et al. 1997, *MNRAS*, 287, 722
- Ekers, R. 1999, in *Looking Deep in the Southern Sky*, 146—+
- Ellison, D. C., Berezhko, E. G., & Baring, M. G. 2000, *ApJ*, 540, 292
- Ellison, D. C., Slane, P., & Gaensler, B. M. 2001, *ApJ*, 563, 191
- Emerson, D. T. & Graeve, R. 1988, *A&A*, 190, 353
- Evans, R. 1994, *Proceedings of the Astronomical Society of Australia*, 11, 7
- . 1997, *Publications of the Astronomical Society of Australia*, 14, 204
- Fermi, E. 1949, *Phys.Rev.*, 75, 1169
- Fesen, R. A., Blair, W. P., & Kirshner, R. P. 1985, *ApJ*, 292, 29
- Fesen, R. A., Gull, T. R., & Ketelsen, D. A. 1983, *ApJS*, 51, 337
- Fesen, R. A. & Hurford, A. P. 1996, *ApJS*, 106, 563+
- Fowler, W. A., Caughlan, G. R., & Zimmerman, B. A. 1975, *ARA&A*, 13, 69
- Frater, R. H., Brooks, J. W., & Whiteoak, J. B. 1992, *Journal of Electrical and Electronics Engineering Australia*, 12, 103

- Furst, E., Reich, W., Reich, P., et al. 1990, *A&AS*, 85, 691+
- Gaensler, B. M., Slane, P. O., Gotthelf, E. V., et al. 2001, *ApJ*, 559, 963
- Gagne, M., Caillault, J., & Stauffer, J. R. 1995, *ApJ*, 450, 217+
- Garmire, G. P. & Tuohy, I. R. 1979, *BAAS*, 11, 723
- Garmire, A. B., Pavlov, G., & Burrows, D. N. 2001, in *Two Years of Science with Chandra*, Abstracts from the Symposium held in Washington, DC, 5-7 September, 2001.
- Garmire, G. P. 1997, *Bulletin of the American Astronomical Society*, 29, 823
- Gotthelf, E. V. 1998, *Memorie della Societa Astronomica Italiana*, 69, 831+
- Gotthelf, E. V., Petre, R., & Hwang, U. 1997, *ApJ*, 487, L175
- Green, A. J. 1997, *Publications of the Astronomical Society of Australia*, 14, 73
- Green, D. A. 1991, *PASP*, 103, 209
- Green, D. A. 1996, in *IAU Colloq. 145: Supernovae and Supernova Remnants*, 341+
—, 2002, *VizieR Online Data Catalog*, 7211, 0+
- Gregory, P. C., Vavasour, J. D., Scott, W. K., et al. 1994, *ApJS*, 90, 173
- Griffith, M. R. & Wright, A. E. 1993, *AJ*, 105, 1666
- Gull, T. R., Kirshner, R. P., & Parker, R. A. R. 1977, *ApJ*, 215, L69
- Gvaramadze, V. V. 2001, in *Astronomische Gesellschaft Meeting Abstracts*, Vol. 18, 102+
- Hachenberg, O. 1970, *S&T*, 40, 338+
- Hamaker, J. P. & Bregman, J. D. 1996, *A&AS*, 117, 161
- Hamuy, M. & Pinto, P. A. 2002, *ApJ*, 566, L63
- Hartman, R. C., Bertsch, D. L., Bloom, S. D., et al. 1999, *ApJS*, 123, 79
- Hashimoto, M., Iwamoto, K., & Nomoto, K. 1993, *ApJ*, 414, L105
- Helfand, D. J., Gotthelf, E. V., & Halpern, J. P. 2001, *ApJ*, 556, 380
- Hillebrandt, W. & Niemeyer, J. C. 2000, *ARA&A*, 38, 191
- Holland, A. D., Turner, M. J., Abbey, A. F., & Pool, P. J. 1996, in *Proc. SPIE Vol. 2808*, p. 414-420, *EUV, X-Ray, and Gamma-Ray Instrumentation for Astronomy VII*, Oswald H. Siegmund; Mark A. Gummin; Eds., 414-420

-
- Iben, I. & Tutukov, A. V. 1984, *ApJS*, 54, 335
- Ilovaisky, S. A. & Lequeux, J. 1972, *A&A*, 18, 169+
- Jansen, F., Lumb, D., Altieri, B., et al. 2001, *A&A*, 365, L1
- Johnston, S. 1994, *Proceedings of the Astronomical Society of Australia*, 11, 80+
- Jun, B. & Norman, M. L. 1996, *ApJ*, 465, 800+
- Kaastra, J. S. 1992, *An X-Ray Spectral Code for Optically Thin Plasmas* (Internal SRON-Leiden Report, updated version 2.0)
- Kalberla, P. M. W., Mebold, U., & Reich, W. 1980, *A&A*, 82, 275
- Kashyap, V. & Drake, J. J. 1999, *ApJ*, 524, 988
- Kaspi, V. 1998, *Neutron Stars and Pulsars: Thirty years after the Discovery* (N.Shibazaki, N.Kawai, S.Shibata, Tokyo: Universal Academy Press , 401)
- Kaspi, V. M. 1996, in *ASP Conf. Ser. 105: IAU Colloq. 160: Pulsars: Problems and Progress*, 375+
- Kenter, A. T., Gomes, J., Murray, S. S., Moore, R. W., Roll, R. K., & Zombeck, M. V. 1994, in *Proc. SPIE Vol. 2280, p. 69-88, EUV, X-Ray, and Gamma-Ray Instrumentation for Astronomy V*, Oswald H. Siegmund; John V. Vallerga; Eds., 69–88
- Kodaira, K. 1974, *PASJ*, 26, 255+
- Koyama, K., Petre, R., Gotthelf, E. V., et al. 1995, *Nature*, 378, 255
- Lasker, B. M., Greene, G. R., Lattanzi, M. J., et al. 1998, in *Astrophysics and Algorithms*
- Liedahl, D. A., Osterheld, A. L., & Goldstein, W. H. 1995, *ApJ*, 438, L115
- Liu, Q. Z., van Paradijs, J., & van den Heuvel, E. P. J. 2001, *A&A*, 368, 1021
- Lockman, F. J. 1989, *ApJS*, 71, 469
- Longair, M. S. 1994, *High Energy Astrophysics* (Cambridge UP, 1994)
- Lorimer, D. R., Bailes, M., & Harrison, P. A. 1997, *MNRAS*, 289, 592
- Lorimer, D. R., Lyne, A. G., & Camilo, F. 1998, *A&A*, 331, 1002
- Lorimer, D. R. & Xilouris, K. M. 2000, *ApJ*, 545, 385
- Lou, Y. 1994, *ApJ*, 428, L21

- Maccacaro, T., Gioia, I. M., Wolter, A., et al. 1988, *ApJ*, 326, 680
- Marsh, K. A. & Richardson, J. M. 1987, *A&A*, 182, 174
- Mason, K. O., Breeveld, A., Much, R., et al. 2001, *A&A*, 365, L36
- Matheson, T., Filippenko, A. V., Li, W., et al. 2001, *AJ*, 121, 1648
- Mathewson, D. S., Ford, V. L., Dopita, M. A., et al. 1983, in *IAU Symp. 101: Supernova Remnants and their X-ray Emission*, Vol. 101, 541–549
- Matteucci, F. & Francois, P. 1989, *MNRAS*, 239, 885
- Mattox, J. R., Bertsch, D. L., Chiang, J., et al. 1996, *ApJ*, 461, 396
- Mavromatakis, F., Boumis, P., Papamastorakis, J., et al. 2002, accepted in *A&A*
- Mavromatakis, F., Papamastorakis, J., Ventura, J., et al. 2001, *A&A*, 370, 265
- Mazzarella, J. M., Madore, B. F., & Helou, G. 2001, in *Proc. SPIE Vol. 4477*, p. 20-34, *Astronomical Data Analysis*, Jean-Luc Starck; Fionn D. Murtagh; Eds., Vol. 4477, 20–34
- McMillan, R. J. & Ciardullo, R. 1996, *ApJ*, 473, 707
- Mewe, R., Kaastra, J. S., & Liedahl, D. A. 1995, *Legacy*, 6, 16
- Morsi, H. W. & Reich, W. 1987, *A&AS*, 69, 533
- Murray, S. S., Slane, P. O., Seward, F. D., et al. 2002, *ApJ*, 568, 226
- Nugent, J. J., Pravdo, S. H., Garmire, G. P., et al. 1984, *ApJ*, 284, 612
- Oegerle, W. R. & Hill, J. M. 2001, *AJ*, 122, 2858
- Ohashi, T., Kikuchi, K., Matsushita, K., et al. 2000, *Advances in Space Research*, 25, 593
- Oliva, E., Moorwood, A. F. M., Drapatz, S., et al. 1999, *A&A*, 343, 943
- Oort, J. H. 1951, in *Problems of Cosmical Aerodynamics; Proceedings of a Symposium on the Motion of Gaseous Masses of Cosmical Dimensions held at Paris, August 16-19, 1949*. UNESCO meeting jointly sponsored by the International Astronomical Union and the International Union of Theoretical and Applied Mechanics, 1951., p.118, 118+
- Pérez-Torres, M. A., Alberdi, A., & Marcaide, J. M. 2001, *A&A*, 374, 997
- Parker, Q. A., Phillipps, S., & Morgan, D. H. 1999, in *ASP Conf. Ser. 168: New Perspectives on the Interstellar Medium*, 126–+

-
- Petre, R. & Gotthelf, E. V. 1998, *Memorie della Societa Astronomica Italiana*, 69, 837+
- Petschek, A. 1990, *Supernovae (Astronomy and Astrophysics Library, New York: Springer, 1990)*
- Pfeffermann, E. & Briel, U. G. 1986, in *X-ray instrumentation in astronomy; Proceedings of the Meeting, Cannes, France, December 2-4, 1985 (A87-19722 07-35)*. Bellingham, WA, Society of Photo-Optical Instrumentation Engineers, 1986, p. 208-212., Vol. 597, 208–212
- Pfeffermann, E., Briel, U. G., Hippmann, H., et al. 1987, in *Soft X-ray optics and technology; Proceedings of the Meeting, Berlin, Federal Republic of Germany, Dec. 8-11, 1986*, Bellingham, WA, Society of Photo-Optical Instrumentation Engineers, Volume 733, 1987, p. 519., Vol. 733, 519–+
- Popov, S. B. 1998, *Astronomical and Astrophysical Transactions*, 17, 35+
- Prigozhin, G. Y., Kissel, S. E., Bautz, M. W., et al. 2000, in *Proc. SPIE Vol. 4140, p. 123-134, X-Ray and Gamma-Ray Instrumentation for Astronomy XI*, Kathryn A. Flanagan; Oswald H. Siegmund; Eds., Vol. 4140, 123–134
- Rüdiger, A. 2000, *Advances in Space Research*, 25, 1157
- Ratnatunga, K. U. & van den Bergh, S. 1989, *ApJ*, 343, 713
- Raymond, J. C. 2001, *Space Science Reviews*, 99, 209
- Reach, W. T. & Rho, J. 2000, *ApJ*, 544, 843
- Reich, P., Reich, W., & Fuerst, E. 1997, *A&AS*, 126, 413
- Reich, W., Berkhuijsen, E. M., & Sofue, Y. 1979, *A&A*, 72, 270
- Reich, W., Fuerst, E., Reich, P., et al. 1990a, *A&AS*, 85, 633
- Reich, W., Reich, P., & Fuerst, E. 1990b, *A&AS*, 83, 539
- Reinecke, M., Niemeyer, J. C., & Hillebrandt, W. 2002, *New Astronomy Review*, 46, 481
- Reynolds, S. P. & Ellison, D. C. 1992, *ApJ*, 399, L75
- Rho, J. 1996, PhD thesis, University of Maryland
- Riess, A. G., Filippenko, A. V., Li, W., et al. 1999, *AJ*, 118, 2675
- Robertson, J. G. 1991, *Australian Journal of Physics*, 44, 729
- Rohlf, K. & Wilson, T. L. 1996, *Tools of Radio Astronomy (Astronomy and Astrophysics Library, Berlin Heidelberg: Springer, 1996)*

- Roman, A. T., Iwata, I., & Saitō, M. 2000, *ApJS*, 127, 27
- Rosado, M., Le Coarer, E., & Georgelin, Y. P. 1994, *Revista Mexicana de Astronomia y Astrofisica*, vol. 29, 29, 97
- Russeil, D. 1997, *A&A*, 319, 788
- Sanwal, D., Garmire, G. P., Garmire, A., et al. 2002, American Astronomical Society Meeting, 200, 0+
- Sault, R. J., Teuben, P. J., & Wright, M. C. H. 1995, in *ASP Conf. Ser. 77: Astronomical Data Analysis Software and Systems IV*, Vol. 4, 433–+
- Scheffler, H. & Elsässer, H. 1990, *Physik der Sterne und der Sonne* (BI Wissenschaftsverlag: Mannheim 1990)
- Schönfelder, V. 2001, *The Universe in Gamma Rays* (Astronomy and Astrophysics Library, Berlin, Heidelberg: Springer 2001)
- Sedov, L. I. 1959, *Similarity and Dimensional Methods in Mechanics* (Similarity and Dimensional Methods in Mechanics, New York: Academic Press, 1959)
- Seward, F. D. 1990, *ApJS*, 73, 781
- Shaver, P. A. & Goss, W. M. 1970, *Australian Journal of Physics Astrophysical Supplement*, 14, 133+
- Shigeyama, T., Iwamoto, K., Hachisu, I., et al. 1996, in *Proc. IAU Coll. 145*, 129
- Simonetti, J. M. 1992, *ApJ*, 386, 170
- Slane, P. 2002, to appear in the proceedings of the XXII Moriond Astrophysics Meeting "The Gamma-Ray Universe", eds. A. Goldwurm, D. Neumann, and J. Tran Thanvan
- Slane, P., Chen, Y., Schulz, N. S., et al. 2000, *ApJ*, 533, L29
- Smith, D. A., Wilson, A. S., Arnaud, K. A., et al. 2002, *ApJ*, 565, 195
- Sofue, Y. & Reich, W. 1979, *A&AS*, 38, 251
- Spruit, H. C. & Phinney, E. S. 1998, *Nature*, 393, 139+
- Stadlbauer, T. & Aschenbach, B. 2001, *Astronomische Gesellschaft Abstract Series*, Vol. 18.
- Strüder, L., Briel, U., Dennerl, K., et al. 2001, *A&A*, 365, L18
- Strom, R. 1990, in *Kundt W., ed., Neutron Stars and Their Birth Events*. Kluwer, Dordrecht, p.253
- Sung, H., Chun, M., & Bessell, M. S. 2000, *AJ*, 120, 333

-
- Takizawa, M. 2002, PASJ, 54, 363
- Tammann, G. A., Loeffler, W., & Schroeder, A. 1994, ApJS, 92, 487
- Tamura, M. 1999, in Star Formation 1999, Proceedings of Star Formation 1999, held in Nagoya, Japan, June 21 - 25, 1999, Editor: T. Nakamoto, Nobeyama Radio Observatory, p. 212-216, 212–216
- Taylor, A. R., Wallace, B. J., & Goss, W. M. 1992, AJ, 103, 931
- Taylor, J. H., Manchester, R. N., & Lyne, A. G. 1993, ApJS, 88, 529
- Terasawa, M., Sumiyoshi, K., Kajino, T., et al. 2001, ApJ, 562, 470
- Thompson, C. & Duncan, R. C. 1995, MNRAS, 275, 255
- . 1996, ApJ, 473, 322+
- Thorne, K. S. 1997, in Critical Problems in Physics, Proceedings of a Conference Celebrating the 250th Anniversary of Princeton University held in Princeton, NY, 31 Oct - 2 Nov, 1996. Edited by Val L. Fitch, Daniel R. Marlow, and Margit A. E. Dementi. Princeton, p.167, 167+
- Torres, D. F., Romero, G. E., Combi, J. A., et al. 2001, A&A, 370, 468
- Townsley, L. K., Broos, P. S., Garmire, G. P., & Nousek, J. A. 2000, ApJ, 534, L139
- Truemper, J. 1982, Advances in Space Research, 2, 241
- Tsujimoto, T., Nomoto, K., Yoshii, Y., et al. 1995, MNRAS, 277, 945
- Tuohy, I. & Garmire, G. 1980, ApJ, 239, L107
- Turner, M. J. L., Abbey, A., Arnaud, M., et al. 2001, A&A, 365, L27
- van den Bergh, S. 1978, ApJS, 38, 119
- . 1988, PASP, 100, 205+
- van den Bergh, S. & Tammann, G. A. 1991, ARA&A, 29, 363
- van der Laan, H. 1962, MNRAS, 124, 179
- van Speybroeck, L. P. 1997, Bulletin of the American Astronomical Society, 29, 823
- Voges, W. 1993, Advances in Space Research, 13, 391
- . 1994, in "Basic Space Science", ed. H.J. Haubold and L.I. Onuora (new York: AIP), 212
- von Hoerner, S. 1975, A&A, 41, 301

- Walsh, A. J., Burton, M. G., Hyland, A. R., et al. 1998, MNRAS, 301, 640
- Warwick, R. S., Bernard, J.-P., Bocchino, F., et al. 2001, A&A, 365, L248
- Weiler, K. W. & Sramek, R. A. 1988, ARA&A, 26, 295
- Weisskopf, M. C., Tananbaum, H. D., Van Speybroeck, L. P., et al. 2000, in Proc. SPIE Vol. 4012, p. 2-16, X-Ray Optics, Instruments, and Missions III, Joachim E. Truemper; Bernd Aschenbach; Eds., Vol. 4012, 2–16
- Wenger, M., Ochsenbein, F., Egret, D., et al. 2000, A&AS, 143, 9
- Whiteoak, J. B. Z. 1992, A&A, 262, 251
- Whiteoak, J. B. Z. & Green, A. J. 1996, A&AS, 118, 329
- Willingale, R., Aschenbach, B., Griffiths, R. G., et al. 2001, A&A, 365, L212
- Wilms, J., Allen, A., & McCray, R. 2000, ApJ, 542, 914
- Wilson, T. L., Mezger, P. G., Gardner, F. F., et al. 1970, A&A, 6, 364
- Woltjer, L. 1972, ARA&A, 10, 129+
- Woosley, S. E. & Weaver, T. A. 1986, BAAS, 18, 1016+
- Woudt, P. A. & Kraan-Korteweg, R. C. 2001, A&A, 380, 441
- Yungelson, L. & Livio, M. 1998, ApJ, 497, 168
- Zhang, B., Xu, R. X., & Qiao, G. J. 2000, ApJ, 545, L127

Acknowledgements

During the last three years I have benefitted from many people in the MPE and also from outside to plan and organize as well as realize this labor-intensive work. Therefore, I would like to express my gratitude to all of them.

Primarily I want to thank Prof. Dr. Joachim Trümper for giving me the opportunity to work in the X-ray group at the Max-Planck-Institut für extraterrestrische Physik and to participate at several conferences and workshops.

Special thanks go to Dr. Werner Becker who advised my PhD thesis and was my first contact person in all scientific, but also organizational questions regarding the analysis of the X-ray data as well the process of this work. As the Principle Investigator of most of the X-ray and radio proposals he made me available all the data. He also encouraged me to participate in several very interesting international conferences and workshops.

Thanks go also to Dr. Bernd Aschenbach who spent a lot of time for fruitful discussions regarding the spectra of SNRs.

Dr. Peter Schücker had always time for interesting discussions in astronomy and general physics and gave me a lot of scientific advices about clusters of galaxies.

Dr. Wolfgang Reich made possible two short research visits to the Max-Planck-Institut für Radioastronomie in Bonn, Germany and brought me in the field of radio supernova remnants. He also spent a lot of time to show me the Effelsberg radio telescope.

Dr. Miroslav Filipovic was my collaborator in radio astronomy on the southern hemisphere. I am grateful for the fruitful discussions about the analysis of the ATCA data and the observed sources.

Dr. Martin Weisskopf and collaborators from the Marshall Space Flight Center in Huntsville, USA, provided me the Chandra data and gave me useful advices about the analysis of these data.

Dr. Jakob Englhauser spent a lot of time to make the RASS-I data available to me.

Thanks go also to Dr. Michael Freyberg, Dr. Dieter Breitschwerdt and Dr. Frank Haberl for their help.

Harald Baumgartner, Achim Bohnet, Lars Klose and Joachim Paul could solve all computer and network problems in a very short time and made an efficient work possible.

Thanks go to Barabara Mory for providing me with nice colour plots.

Helmut Dannerbauer, Thomas Stadlbauer, Manami Sasaki, Ralf Keil, Frank Pf-

efferkorn as well as Brigitte König, Dr. Viki Jörgens, Dr. Thomas Reiprich and Dr. Beate Stelzer were not only partners for scientific discussions but also for nice coffee time conversations.

My thanks go also to my officemates Elisa Costantini and Paulo Mendes for scientific and wordly discussions and the friendly relation. Beside astronomy Elisa made for a nice italian atmosphere in our office.

I thank Prof. Dr. Antonio Bianchini from the University of Padova for the friendly relation during the last years and his interest in my PhD thesis.

I thank Linda Pittroff, Luigi Gallo and Paul Lynam for reading this manuscript.

I am deeply grateful to my girlfriend Elke Panzl and my parents Christel and Walter Schaudel for their patience and support.

Finally I want to thank everyone who accompanied me during my work.

Curriculum Vitae

Name: Daniel Schaudel
Date of Birth: January, 28, 1973
Place of Birth: Ettenheim, Germany
Nationality: German

Education:

1979 - 1983: Primary School, Ettenheim
1983 - 1992: Städtisches Gymnasium, Ettenheim
Abitur
1992 - 1993: Civil Service in the hospital Ettenheim, Germany
1993 - 1995: Study of Physics at the Albert-Ludwigs-Universität Freiburg, Germany
1995 - 1996: Study of Physics and Astronomy at the University of Padova, Italy
1996 - 1997: Study of Physics at the Ruprecht-Karls-Universität Heidelberg, Germany
1997 - 1999: Study of Physics at the Ludwig-Maximilians-Universität München, Germany

Diploma Thesis:

1998 - 1999: Max-Planck-Institut für Quantenoptik in Garching, Germany
Supervisor: Prof. Dr. Herbert Walther
Title: "UV-High Finesse Cavity for an Ion-Trap-Laser"

Current Position:

1999 - 2003: Research Assistant at the Max-Planck-Institut für extraterrestrische Physik in Garching, Germany

List of Publications

Warwick, R. S., Bernard, J.-P., Bocchino, F., Decourchelle, A., Ferrando, P., Griffiths, R. G., Haberl, F., La Palombara, N., Lumb, D., Mereghetti, S, Read, A. M., Schaudel, D., Schurch, N., Tiengo, A. & Willingale, R.

“The extended X-ray halo of the Crab-like SNR G21.5-0.9”

Astronomy & Astrophysics, 365, p. L248-L253 (2001)

Mavromatakis, F., Papamastorakis, J., Ventura, J., Becker, W., Paleologou, E. & Schaudel, D.

“The supernova remnants G 67.7+1.8, G 31.5-0.6 and G 49.2-0.7”

Astronomy & Astrophysics, 370, p.265-272 (2001)

Schaudel, D., Becker, W., Voges, W., Aschenbach, B., Reich, W. & Weisskopf, M.

“Galactic SNR Candidates in the ROSAT All-Sky Survey”

Neutron Stars in Supernova Remnants, ASP Conference Series, Vol. 271, held in Boston, MA, USA, 14-17 August 2001. Edited by Patrick O. Slane and Bryan M. Gaensler. San Francisco: ASP, 2002., p.391

Schaudel, D., Becker, W., Aschenbach, B., Trümper, J., Reich, W. & Weisskopf, M.

“Galactic SNR candidates in the ROSAT all-sky survey”

Proceedings of the 270. WE-Heraeus Seminar on Neutron Stars, Pulsars, and Supernova Remnants. MPE Report 278. Edited by W. Becker, H. Lesch, and J. Trümper. Garching bei München: Max-Planck-Institut für extraterrestrische Physik, 2002., p.26

